Implementing Liquid Lubrication in Micro-Electro-Mechanical Systems

By

Peng Wang

A thesis submitted to Imperial College London in fulfilment of the requirements for the Degree of Doctor of Philosophy (PhD) and the Diploma of Imperial College (D. I. C.)

January 2020

Tribology Group

Department of Mechanical Engineering

Imperial College London

Abstract

Even though there are many types of micro-electro-mechanical devices (MEMS), few commercialized MEMS devices can achieve functions requiring rotation. This is a result of a lack of methods providing efficient lubrication for the micro sliding contacts. Liquid hydrodynamic bearings which are commonly used in the macro sliding contacts could still be efficient in micro sliding contacts if appropriate bearing design and lubricants are applied. This thesis reports on the research focused on miniaturizing liquid hydrodynamic bearings thereby improving the performance of the micro sliding contacts in MEMS devices.

A finite volume model considering mass-conservation and cavitation has been developed to investigate the performance of the micro pocketed parallel thrust bearings. Simulation results show that the micro thrust bearing performance is largely affected by cavitation. It also shows that micro pocketed parallel thrust bearings with appropriate pocket shapes can generate sufficient load support and operate in the low friction coefficient full-film lubrication regime when low viscosity lubricant is supplied (*e.g.* hexadecane).

Micro fabrication process has been developed to manufacture the micro pocketed parallel thrust bearings. The manufactured micro bearings have been examined both on a MEMS tribometer and on a prototype micro energy harvesting turbine. Test results show that low friction coefficient, torque and power loss can be achieved in a wide rotational speed range from the micro bearings with proper design and lubricated by low viscosity and low surface tension liquid (*e.g.* hexadecane).

Effects of friction modifiers and partial surface textures on the micro liquid hydrodynamic bearings performance have also been investigated. Results indicate that both methods are still efficient in friction reduction.

As a conclusion, miniaturized liquid hydrodynamic bearings with appropriate bearing design and lubricants are efficient to achieve low friction coefficient and wear rate for the micro sliding contacts in a wide rotational speed range.

Acknowledgement

I would like to express my sincere gratitude to the following people:

- My supervisors, Dr. Tom Reddyhoff and Prof. Andrew Holmes. They not only always guide and help me with great patience and enthusiasm during this research but also encourages me when I felt upset in my Ph.D student life.
- Prof. Daniele Dini and Dr. Francisco Profito. They gave me help and lots of crucial suggestions on the numeric model development.
- Dr. Guangbin Dou. He taught me how to design the masks for micro fabrication and how to use the chemicals and equipment for micro fabrication.
- My parents. For my whole life, especially the tough Ph.D life period, they always unconditionally give me their support and encourage me once and once again to bravely chase my goals. They are the best parents over the world.
- My girlfriend. She accompanied me throughout my tough Ph.D life period and encouraged me not to give up even in the most difficult time. Without her accompany, my research would not be possible to be completed.

Declaration and Copyright

The author claims that the work reported in this thesis is his own and the work by other researchers which is also shown in this thesis is appropriately referenced.

Table of Contents

List of Figures

List of Tables

Nomenclature

r_{out}	:	Outside radius of the bearing	T	:	Frictional torque
r_{pad}	:	Radius of the central flat region	τ	:	Shear stress of the flow
r_{rim}	:	Radius of the rim of the bearing	μ	:	Friction coefficient of the bearing
θ_{land}	:	Angular width of un-recessed land	W_h	:	Integrated bearing hydro-force
θ_{pock}	:	Angular width of recessed pocket	W_a	:	Force from atmospheric pressure
h_{min}	:	Minimum film thickness of bearing	W_n	:	Net supporting force of the bearing
h_{step}	:	Depth of the recessed pocket	LCC	:	Load support with unit: $g \cdot f$
ω	:	Rotational speed of the bearing	$g \cdot f$	:	Unit defined as gram force
p	:	Pressure value	TE_{θ}	:	Circumferential direction pocket extent
S	:	Film fraction value	TE_r	:	Radial direction pocket extent
ρ	:	Density of the lubricant	γ	:	Ratio defined as h_{min}/r_{outer}
η	:	Dynamic viscosity of the lubricant	δ	:	Ratio defined as h_{min}/h_{step}
g	:	Acceleration of gravity	ε	:	Ratio defined as h_{step}/r_{outer}
u_{θ}, u_r	:	Circumferential and radial flow speed	$P, \overline{W}, \overline{T}, H$	:	Normalized pressure, force, frictional torque, film thickness
$\dot{m}_{\theta}, \dot{m}_r$	:	Circumferential and radial mass flow rate	e, w, n, s	:	Indices denoting east, west, north and south

Chapter 1: Introduction

The background introduction and the objectives of this research together with the layout of the thesis are presented in this chapter

1.1 Research Background and Aims

Micro-electro-mechanical systems (MEMS) are micro machines/devices with the size ranging from 1 to 1000 microns. Due to their nature of tiny size and ability to combine microprocessors, micro actuators and sensors together, MEMS have many unique functions and a wide range of applications (MEMS sensors including accelerometers, gyroscopes and tilt sensors, etc. MEMS actuators including inkjet printers, micro switches, micro pumps and micro grippers). [1] However, further development of MEMS has been hindered by the difficulties in lubricating the micro contacts in MEMS. Difficulties in MEMS lubrication are mainly resulted from two effects:

i. As the overall dimensions of MEMS are in mm/μm range, surface forces (usually function as stiction or traction forces in MEMS) such as capillary force, van der Waals force and viscous dragging force become dominant compared to body (inertia) forces such as gravity, centrifugal force and electric/magnetic field force.
ii. The most commonly used material for MEMS fabrication, silicon, is very brittle.

Therefore, micro contacts in MEMS are vulnerable to the problems such as adhesion, high friction and high wear rate, which hinders the invention of rotating or sliding MEMS devices.

Several lubricating methods such as applying diamond-like carbon or fluorinated organic surface coatings (to reduce surface wettability) and building self-assembled mono lubricant layers over the contact surfaces (to make the surface slippery) have been proposed in various researches to solve the MEMS lubrication problems. These methods are effective in improving lubrication performance for micro contacts with small amount of applied sliding, but they are not endurable with prolonged sliding motion as both the hydrophobic coatings and the slippery monolayers will be worn out when large amount of sliding is applied.

Liquid lubrication is a cheap, reliable and efficient approach used in the lubrication of macro-scale rolling and sliding contacts. Due to the high surface to volume ratio in micro scale, liquid lubrication was believed not to be feasible at first in micro scale applications as the viscous drag force might dominate in micro systems and cause problems such as overdamping. [2]

However, Reddyhoff and Ku [3] found through lab experiments that liquid lubrication is still effective in lubricating a millimetre-scale flat to flat contact with high applied sliding speed. Low friction coefficient and low wear rate are achieved when the tested millimetre-scale contact is lubricated with low viscosity liquid (hexadecane). Therefore, developing miniatured liquid bearings with low friction coefficient and low wear rate could be a high-efficiency solution to improve the performance and reliability for the potential MEMS devices with sliding contacts.

Liquid bearings can be classified into two types which are hydrodynamic and hydrostatic thrust bearings. Operation of both type of bearings relies on the pressurized liquid film which helps to support the applied load. When the applied load is totally supported by the pressurized liquid film, the contact surfaces of the bearings will be separated hence achieving low friction coefficient and wear rate. The pressurized liquid film of hydrostatic bearings is formed by external pressurization (pump) whereas the load-supporting pressure of the liquid film of hydrodynamic bearings is developed when the liquid flowing through bearing surfaces with convergent profiles at high speed. [4]

Compared to hydrostatic liquid thrust bearings, the hydrodynamic bearings are able to entrain lubricants into the bearing and pressurize the entrained liquid automatically without any external pressurization equipment and are more suitable for applications operating at high speed. In addition, the design of liquid hydrodynamic thrust bearing is relatively simpler compared to that of hydrostatic bearings as the operation of liquid hydrodynamic bearings does not rely on external pumps to supply lubricant fluids, hence the cost of this type of bearing is lower especially when the bearings are miniaturized. Therefore, hydrodynamic bearings are more suitable to be miniaturized and used in MEMS devices.

One of the potential MEMS applications with high sliding contacts that might benefit from the liquid lubrications is the turbine-type micro energy harvester. Micro energy harvesters are very important applications of MEMS. They can capture energy from external sources such as solar

power, flow power and vibration power and store and generate electrical power for other micro autonomous devices. While the large-scale energy generators use fuels as energy resources, micro energy harvesters capture energy that exists in surrounding environments and cost free (e.g. air flow, vibration energy). Micro energy harvesting turbine is essentially a micro air flow-driven electrical generator. The rotor of the micro turbine is driven by the air flow and rotates thereby capturing the energy from air flow and transferring it to mechanical energy of the rotor. The mechanical energy is then used to generate electrical power by the integrated micro generator and provide the generated electrical power for applications located in places where usage and change of supplement batteries are challenging (e.g. wireless sensors in air conditioning systems or remote gas pipelines) [5]. However, the efficiency of the micro-turbine harvester is limited by the frictional torque generated in the sliding contact between the turbine rotor and stator. Furthermore, the effect of frictional torque applied in surface would increase with decreasing size of the device, which may even result in in-use stiction. In addition, the range of the flow speed within which the micro energy harvesting turbine can operates normally is also limited by high frictional torque.

The prototype micro energy harvesting turbine on which the efficiency of the developed micro liquid hydrodynamic bearings will be installed and tested in this research was developed by Howey and co-researchers [6]. The diameter of the miniature shrouded wind turbine is only 2 cm. The energy harvester can operate at air speeds in the range of 3-7 ms-1 and generate electrical power between 80 μW and 2.5 mW. Currently, a pair of jewel V bearings are used to bear the axial and radial load. However, the performance of the jewel V bearings is not satisfactory especially at low speed (over 80% of the generated power is lost in the sliding contacts). The efficiency of the sliding contacts of the prototype energy harvesting turbine is expected to be improved by replacing the jewel V bearings with developed liquid hydrodynamic bearings. A picture of the prototype energy harvesting turbine used in this research is shown in figure 1-1.

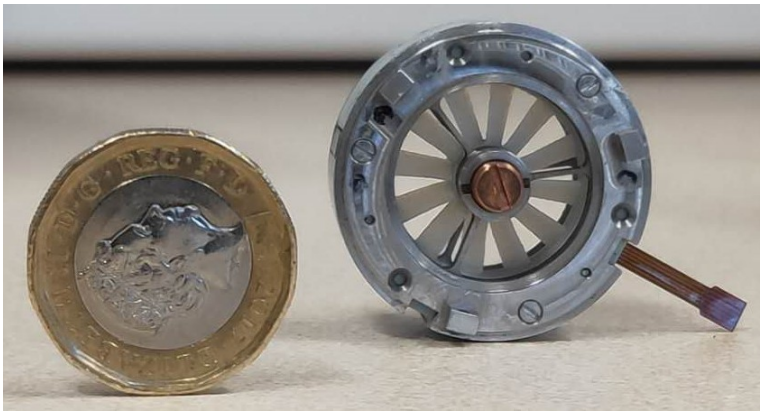

Figure 1-1. Size comparison between a one-pound coin and the prototype micro energy harvesting turbine

For each sliding contact of the micro energy harvesting turbine, a journal bearing to support the radial direction load and a thrust bearing to support the axial direction load are needed. The liquid hydrodynamic thrust bearing can be roughly divided into 3 categories: tapered land thrust bearing, tilted thrust bearing and step thrust bearing based on the profiles of the bearing pad surfaces [7]. Among all types of thrust bearings, step thrust bearings are more commonly used due to its ability to generate sufficient load carrying capacity in wide dimension scales and the low cost in design and manufacturer [7]. In addition, the fabrication difficulty for miniatured step thrust bearing is much lower than that of other two types of bearings as it is extremely difficult to accurately construct wedged surfaces in micro scale. As to the micro journal bearing for the high sliding MEMS devices, micro ruby ring could be an appropriate choice as the lubrication properties of ruby are good (low kinetic friction coefficient, long lifetime, high anti-wear ability) [8, 9].

The correlations between the performance of the liquid lubricated bearings, especially the micro step thrust bearings, and the bearing design and operational conditions are of great importance as they are necessary for micro bearing development, usage and modification. This could be achieved by developing a numeric model of the bearing that correctly describes the liquid behaviours within the simulated micro bearings.

The overall aim of this project is to develop a pair of micro liquid hydrodynamic bearings with low friction coefficient and wear rate based on the findings of liquid lubrication from the lab tests [3] and install the developed micro bearings on a prototype energy harvesting turbine to improve its efficiency and reliability. Understanding of the micro bearing behaviours and

bearing performance optimization are also achieved by developing a numeric bearing model. Other methods to improve the micro liquid bearing performance are also investigated in this research (including applying additives and surface texture with different lubricants).

1.2 Research Objectives

To achieve the aims set for this research which are described in the previous section, several objectives are required to be completed.

i. Developing a finite volume model based on the solution of the mass-conservation considering Reynold's equation to simulate the lubrication behaviours of the micro thrust step bearings.

ii. Using the developed numeric model to investigate the correlations between the micro thrust step bearing performances and the bearing graphics and operational conditions, and to modify the bearing design.

iii. Developing micro fabrication recipes for the micro thrust step bearings and completing manufacturing work of the micro thrust bearings with different graphic designs.

iv. Testing the performance of the micro thrust bearings on a MEMS tribometer when they are lubricated with different liquids.

v. Assembling the micro thrust bearing and journal bearings and testing the performance of the micro bearings when they are installed on the prototype micro energy harvesting turbine.

vi. Investigating the effects of micro surface texture and friction modifier on the friction reduction of the micro thrust bearings.

1.3 Thesis Layout

The thesis is composed of nine chapters, brief summary for each of the chapters is presented as follows:

Chapter 1 demonstrates the background, aims and the objectives of this research, layout of the thesis is also given in this chapter.

Chapter 2 presents a brief literature review on the MEMS development, lubrication problems of MEMS devices and different types of lubrication methods of MEMS devices.

Chapter 3 describes the liquid mechanics and development process of the finite volume micro thrust bearing model. Validation cases of the developed model are also shown in this chapter.

Chapter 4 presents the simulated results demonstrating the performance of micro thrust bearings with different graphic parameters operating under different conditions.

Chapter 5 presents the fabrication processes of the micro thrust bearings. Detailed experimental setups of the micro thrust bearing assessment on the MEMS tribometer including the rig operation mechanism, rig calibration procedures, tested bearing parameters and the tested lubricants details are also demonstrated in this chapter.

Chapter 6 demonstrates the performance of the micro thrust bearings lubricated with different liquids obtained from tests on the MEMS tribometer.

Chapter 7 shows the performance of the micro thrust bearings and journal bearings when they operate on the micro energy harvesting turbine. How the micro thrust bearings and journal bearings are assembled and installed on the micro turbine is also presented in this chapter. In addition, detailed introduction on the MEMS energy harvesting turbine and test methods of the micro turbine are given in this chapter.

Chapter 8 shows the influence of micro surface texture on the lubrication behaviours of the thrust bearing.

Chapter 9 summarizes the key findings of this research and possible future work.

References lists all the references used in the whole thesis.

The list of published work and an **Appendix** containing the code of the numeric model and are given in the end of the thesis.

Chapter 2: Literature Review

A brief literature review of micro-electro-mechanical systems (MEMS) and the lubrication implementation on MEMS contacts are presented in this chapter. The review can be divided into four parts. The first part summarizes the developments and applications of MEMS, a detailed review on MEMS energy harvesters and the advantages of energy harvester with sliding or rotating contacts is also presented in this part. Problems in MEMS lubrication and the causes of the problems are reviewed in the second part. In the third part, lubrication methods for MEMS including dry lubrication, vapour phase lubrication and liquid lubrication methods are briefly reviewed. The final part briefly summarizes the fabrication techniques of MEMS devices.

2.1 Introduction on Micro-Electro-Mechanical Systems (MEMS)

Microelectromechanical systems (MEMS) are tiny devices consisting of small electrical and mechanical components, the feature sizes of MEMS typically range from 1 μm to 1000 μm. These devices are mostly fabricated from semiconductor materials by applying the processing techniques that are similar to the fabrication techniques used in batch fabrication of integrated circuits (IC). Because of their size, MEMS can accurately sense, actuate and control various micro scale physical quantities. After being integrated into macro scale systems MEMS can generate effects on macro scale devices hence achieving some high-accuracy functions in different fields (e.g. accelerometers in automobiles, inkjet printer heads and high accuracy micro spectrometers). [10-13]

With the development of semiconductor device manufacturing techniques such as dry etching, wet etching and micromachining, more and more types of MEMS with different practical functions have been developed and MEMS have already upgraded many types of consumer products and have changed our lifestyles. The global market for commercialized micro-electro-mechanical systems is also growing drastically. In 2012, the MEMS market totalled $12.6 billion and is estimated to rise to $24 billion in 2019. [14]

Many advantages could be drawn from the tiny size of MEMS. For example, because of the low inertia, the MEMS accelerometers are able to measure much higher acceleration than their macro scale counterparts; MEMS switches which function as parts of communication circuits can achieve signal switching much faster than the switches with much larger size. Power saving and low manufacture cost are also the advantages that can be gained from MEMS. [15]

However, problems attributed to the tiny size of MEMS also exist. In micro-scale, surface forces such as capillary force, Vander Waals force, adhesion and friction may dominate over inertia forces, which makes the design method of MEMS different from that of the macro devices. High surface forces may also result in severe wear and fast failures of MEMS especially the devices involving rotation and sliding. Figure 2-1 below demonstrates how tiny the MEMS could be by comparing the size of a spider mite and the size of a MEMS mirror assembly.

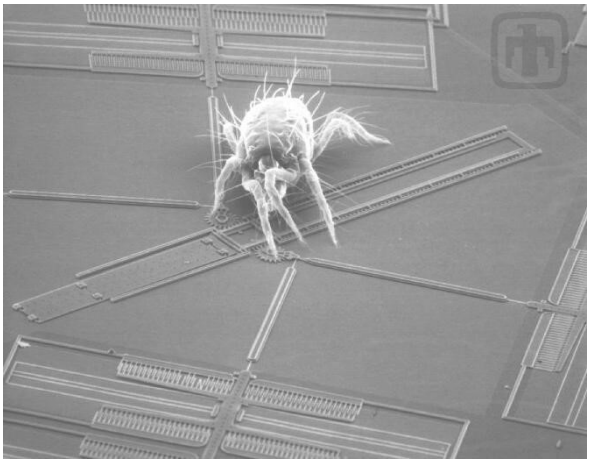

Figure 2-1. Spider mite on a MEMS mirror assembly [16]

2.1.1 Brief Development History of MEMS

Since 1950s, MEMS have been moving forward fast with more and more micro scale fabrication techniques being developed and various of devices which are built in lab researches being commercialized. A brief introduction on the development of MEMS is given below.

In 1959, Richard Feynman made a lecture: “There is plenty of room at the bottom” at California Institute of Technology and encouraged the development of MEMS technology. Micromachining, one of the most important fabrication methods, was invented in the 1960s. In 1970s, the first silicon accelerometer and inkjet head fabricated by micromachining was demonstrated in public. During 1980s to 1990s, more advanced MEMS fabrication methods

such as deep reactive ion etching (DRIE), and stencil lithography were developed, and an increasing number of researches were focused on MEMS issues. In the first decade of twenty first century, a lot of devices such as tri-axis accelerometers and MEMS gyros became commercialized and were sold in the market. MEMS have also been applied to more fields recently such as bioengineering, medical engineering and information & communication engineering. Currently, MEMS have already become an important part in our daily life.

2.1.2 MEMS Devices Types and Operation Mechanisms

MEMS devices can be roughly categorized two types which are micro sensors and micro actuators. Brief reviews on each type of MEMS devices and their mechanisms are presented below.

Micro Sensors

An important type of applications of MEMS are the MEMS sensors. MEMS sensors have the advantage of the small size that enables them to be easily integrated into associated systems.

Piezo-electric effect, piezo-resistive effect and capacitive effect are three most commonly used mechanisms in micro sensor designs. [16-18] Piezoelectric micro sensors consist of micro crystal structures which are able to generate electric voltage signal when they get pressurized. Piezo-resistive micro sensors are made of highly piezo-resistive materials (some semiconductor materials) whose resistivity changes when stresses are applied. The working mechanism of capacitive micro sensors is that the capacity of the micro sensors changes when stresses are applied (by changing the distance between the plates of the capacitor) or the properties of the dielectric (e.g. humidity) of the capacitor is changed. The detected changes of the properties of the MEMS sensors can be therefore used to quantify some physical input such as accelerate forces, stresses, deformation and humidity.

Micro accelerometer is a typical example of the MEMS sensors, explanation of the mechanism of a capacitive effect based one-axis accelerometer is given here. Figure 2-2 demonstrates the structure of the one-axis accelerometer. It consists of a proof mass (m) which is connected with an elastic suspension system and a capacity plate. Applied acceleration (a) would result in the deflection of the suspension system (x). [19]

$$m \cdot a = F = k \cdot x \tag{2-1}$$

The deflection x would result in the change of the capacitance (ΔC)

$$x = d\frac{\Delta C}{C_0} \tag{2-2}$$

where d is the distance between the moveable plate and the fixed plate of the capacitor and C_0 is the original capacitance value. The resulted capacitance change can be measured from the voltage output of the connecting electric circuits:

$$V_{out} = V_o \cdot \frac{\Delta C}{C_0} \tag{2-3}$$

Substituting equation (2) and (3) into equation (1), the applied acceleration can be obtained using the following equation:

$$a = \frac{k \cdot d \cdot V_{out}}{m \cdot V_o} \tag{2-4}$$

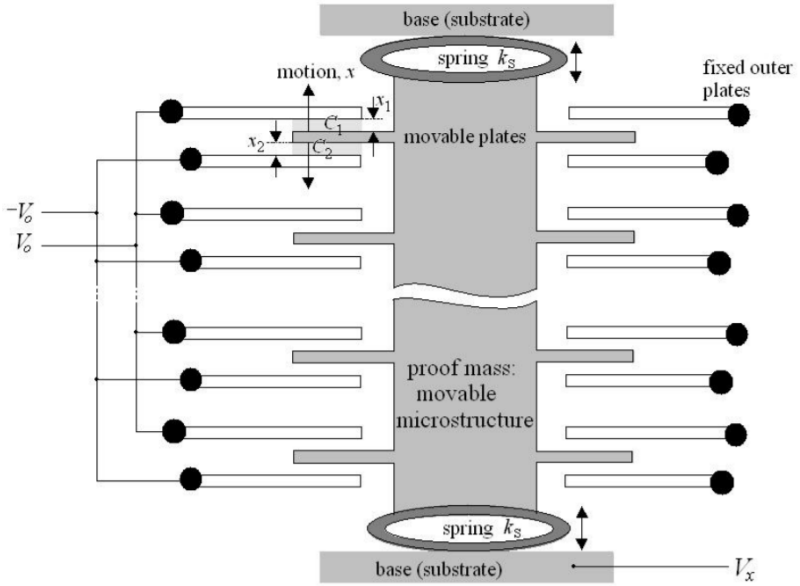

Figure 2-2 Structure of one axis accelerometer [19]

Micro accelerometers are widely used in electronic systems and devices such as airbags of the automotive and smartphones.

Actuation Systems

It is challenging but necessary to achieve actuation functions in MEMS. The commonly used actuation mechanisms in macro scale applications such as hydraulics, combustion engine and electric motor are not feasible in micro scale applications because the fabrication process would be extremely complicated and expensive and the performance would be low (resulting from the scale effect). The actuation mechanisms which suits for MEMS actuators are thermal

driving, electrostatic driving, piezoelectric driving and magnetic driving [20]. Table 2-1 below demonstrates the approximate driving energy density values with the actuation mechanisms above.

Table 2-1. Energy density by different actuation mechanisms [20]

Actuation	*Max. Energy Density*	*Physical and Material Parameters*	*Estimated Conditions*	*Approximate Order (J/cm^3)*
Electrostatic	$\frac{1}{2}\,\varepsilon_0 E^2$	E = electric field ε_0 = dielectric permittivity	5 V/μm	~ 0.1
Thermal	$\frac{1}{2}\,Y(\alpha\,\Delta T)^2$	α = coefficient of expansion ΔT = temperature rise Y = Young's modulus	3×10^{-6} /°C 100°C 100 GPa	~ 5
Magnetic	$\frac{1}{2}\,B^2/\mu_0$	B = magnetic field μ_0 = magnetic permeability	0.1 T	~ 4
Piezoelectric	$\frac{1}{2}\,Y(d_{33}\,E)^2$	E = electric field Y = Young's modulus d_{33} = piezoelectric constant	30 V/μm 100 GPa 2×10^{-12} C/N	~ 0.2

Detailed reviews on different actuation mechanisms are given in the following sections.

i Thermal Actuation

An important property of materials is the thermal expansion coefficient, materials would deform when temperature change occurs. The resultant deformation is proportional to the thermal expansion coefficient. Several methods are applied in MEMS to amplify the deflection hence achieving actuation functions.

The first method is to bond two layers of different materials together. The two bonded layers should have largely different thermal expansion coefficients. When temperature change occurs, the layer with higher thermal expansion coefficient would expand more than the other layer hence leading to bending deflection to achieve actuation function. The amount of deflection depends on the difference between thermal expansion coefficients of the two bonded layers and the temperature change. This method might be limited to be used only in a certain temperature range, the fabrication processes for this type of MEMS actuators are also complicated and the bonded layers might get separated during usage. Figure 2-3 below demonstrates the structure of a bimetallic plates. [21-23]

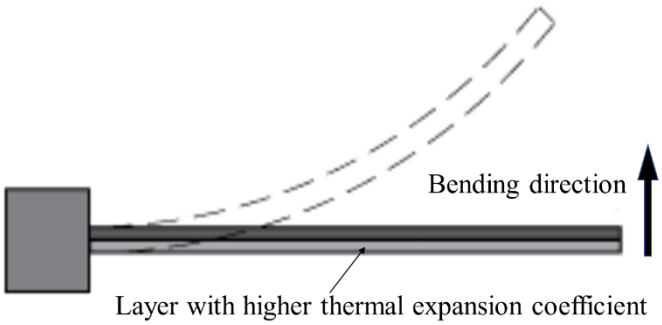

Figure 2-3. Structure of a bimetallic plates [21]

Thermal actuation can also be achieved by a specially designed single-layer beam made from single material. The beam is structured with a thinner arm and a thicker arm. The beam can be heated with current and temperature difference would be generated when the applied current passes the thinner and thicker arms of the beam. The temperature difference between the two arms would result in bending motion at the free end. Figure 2-4 below illustrates the structure of this kind of beam. [22, 23]

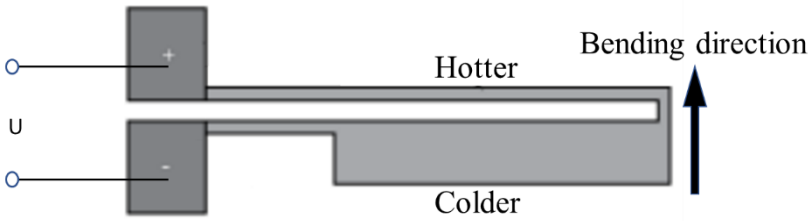

Figure 2-4. Structure of a single layer thermal actuation beam [22]

Another thermal actuation method is achieved by filling a sealed cavity with liquid. When the liquid-containing cavity is heated, forces against cavity wall would be generated from the rise of the liquid pressure hence making the compliant wall deflect. MEMES valves normally apply this kind of method.

ii Electrostatic Actuation

The electrostatic force between two charges is inversely proportional to the square of the distance between the charges. This force is negligible in macro scale. However, electrostatic force can be used to generate mechanical motions for MEMS devices as the gaps in these micro devices are very small. For example, the simplest electrostatic actuator consists of a movable electrode plate which is connected to a micro spring and a fixed electrode plate. When voltage

difference is applied on the structure, electrostatic force would pull the moveable plates towards the fixed plate. This application only requires little power supply [24].

iii Piezoelectric Actuation

Certain materials can generate electric charges when mechanical stress is applied, this phenomenon is defined as the piezoelectric effect. This process can be reversible for some materials, which means when electrical field is applied, accurate mechanical strains/stress can be generated. The reversal piezoelectric effect can then be used in MEMS actuators. For example, commercialized piezoceramic cylinders are able to generate force of a few newtons when voltage of a few hundred volts is applied. This actuation method also requires little power supply [25].

2.1.3 Micro Energy Harvester

The micro energy harvesters are devices which collect energy from ambient environment, generate electrical power using the captured energy and supply electrical power to the other low-power consumption devices. Normally, the devices powered by MEMS energy harvesters are not appropriate to be powered by batteries such as the implantable sensors and actuators and sensors located in pipes, tubes and ducts [26-28]. Recently, the development of micro energy harvesters has received more and more attention because of the advantages of energy renewable and environment friendly.

The energy sources that can be captured in nature are flow energy, thermal energy and solar energy [29]. For micro scale energy harvesters, solar energy is not preferable as the efficiency of solar energy harvesting is highly dependent on surface area of the harvester cells. In addition, solar energy might not be available in pipes and ducts. Thermal energy can be harvested through temperature difference between two different materials (e.g. thermal couple), the gained energy can also be used to generate electrical power [30]. However, the power obtained from thermal energy cannot reach a high value as big temperature difference is not feasible for micro scale devices [31].

Energy within flows especially the air flows is another energy source. One of the advantages of the flow energy source is that it is easily accessible from ambient environment (such as wind in nature/ liquid flow in tubes/ air flow in ducts). In addition, the power density of flow energy source is normally much higher than that of the thermal energy source (e.g. power density from

wind with 4.47 m/s speed can reach 10.4 mW/cm^3) [5]. Therefore, energy from flow (if accessible) is the preferable source for micro energy harvesters.

Based on the mechanism of the energy harvesting process, micro flow-energy harvesters can be divided into two types. The first type is the rotational energy harvesters, this kind of harvesters can harvester the energy from the flow and transfer the captured energy into mechanical energy of the rotor rotation. As shown in figure 2-5 (a), the rotor of the micro energy harvester turbine is rotated by the flow, the rotational speed of the rotor which determines the generated electrical power is dependent on the flow speed. The second type of micro flow-energy harvesters capture the energy within flow through vibration. As shown in figure 2-5 (b), when a mechanical resonator is immersed in the fluid flow, vortex would appear around the resonator and cause vibration of the resonator, the energy from the flow can be then harvested [6, 32, 33].

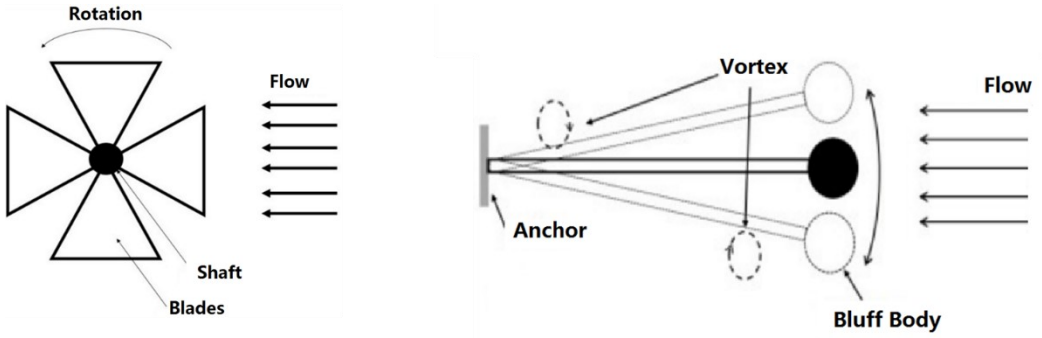

Figure 2-5 (a). Schematic of rotational flow-energy harvester; (b). Schematic of vibrational flow-energy harvester [32, 33]

Comparing the application range of the flow-energy harvesters with different energy capturing mechanisms it can be indicated that the rotational energy harvester can efficiently capture the energy from the flow in almost all directions whereas the vibrational flow-energy harvesters can only operate effectively when the flow direction is perpendicular to the resonator. [5]

For the rotational micro flow-energy harvesters (micro energy harvesting turbine), there are different options to transfer the harvestered flow energy to the electrical energy, which are piezoelectric method, electromagnetic method and electrostatic method. Priya and co-researchers [34] developed a piezoelectric micro energy harvesting turbine that could produce 10.2 mW-electrical power when the turbine rotational frequency is 6 Hz. Howey and co-researchers [6] developed an electromagnetic energy harvesting turbine with 2 cm outer diameter, it can generate 80 μW to 3.2 mW electrical power when it operates in the air flow

with 3-7 m/s flow speed. Recently, Perez et al [35] developed a 4 cm-diameter electrostatic energy harvesting turbine that could operate in the air flow with 1.5-10 m/s flow speed generat8ing 95 μW to 1.8mW electrical power.

Despite lots of development work by many researchers, there is no commercialized energy harvesting turbine yet. One of the main causes is that the cut-in flow speed at which the turbine can overcome the static friction and starts to operate is very high, the turbine would get stuck when the air speed is decreased to lower values. Howey [6] and co-researchers also reported the relationship between the efficiency of the bearing in the micro energy harvesting turbine and the air flow speed. They found that over 70% of the harvested energy is wasted on the micro sliding contacts when the flow speed is lower than 4m/s. That suggests that the efficiency improvement for the micro sliding contact is of great importance, it can further increase the efficiency of the micro energy harvesters and decrease the cut-in speed.

2.1.4 Summary of MEMS Development and Applications

As discussed above, MEMS technology has been improved drastically over the last few decades. A lot of commercialized MEMS applications have been used in various domains such as the micro devices in automobiles, smart phones and medical treatments. However, few commercialized applications are designed with sliding contacts which can enable rotational movements of MEMS devices to be achieved as adhesion and stiction might occur during operation and cause failure of the devices. One of the most promising MEMS that can benefit from designs with sliding contacts is the energy harvesting turbine which could be used to continuously supply electric power for applications located in places where usage of batteries is challenging (such as pipes and ducts). However, further development of energy harvesting turbine is limited by the low transmission efficiency and stiction problems of the micro sliding contacts between the rotors and stators. Solutions tackling this problem are investigated.

2.2 Tribological Problems of MEMS

The market of Micro-Electro-Mechanical Systems has already totalled millions of dollars with various kinds of successfully commercialized applications such as the accelerometers in the autos, inkjet printer heads, micromirrors in the display devices and gyroscopes in the mobile phones. However, a common feature of these successful commercialized MEMS applications

is that they involve no or few contacts with sliding. Excluding designs with sliding contacts limits the diversity of MEMS and restricts the development of MEMS with the functions based on surface interactions such as the micro motors and micro energy harvesting turbines. The main obstacles to the development of MEMS with sliding contacts are various tribological problems in the micro sliding contacts such as stiction, high friction, severe wear, short lifetime and in-use stuck. These problems are resulted from high surface forces. Surface forces such as capillary force, electrostatic force and Van der Waals force can be comparable to or even larger than the actuation forces in micro scale. The origins of the tribological problems are briefly explained in this part.

2.2.1 Scaling Law

In micro scale, the forces that we ignore in macro scale such as electrostatic forces and capillary forces might become dominant. The relationship between the physical parameters of an object and its size is the so-called scaling law. [36]

When the characteristic dimension of a device, L, decreases, the surface area of the device decreases in proportion to L^2 whereas the volume of the device decreases in proportion to L^3. The ratio between the surface area to the volume of the device increases with decreasing device size. Therefore, the force applied on the surfaces such as friction/ stiction force gradually become dominant with decreasing dimension of the device whereas the effects of body forces such as inertia force gradually become weaker.

Besides, some forces themselves are affected by the dimension scale; examples of such kind of forces are given as follows. The surface tension is proportional to L, the fluidic and electrostatic forces are proportional to L^2, the weight, inertia and electromagnetic forces are proportional to L^3. Therefore, in MEMS devices, the resistant forces such as surface tension and electrostatic forces might outweigh actuation forces, which would cause in-use stick or high friction, the devices might not operate in the way intended and the device lifetime might be very short. Figure 2-6 below demonstrates correlations between some common forces applied in MEMS and the MEMS device size.

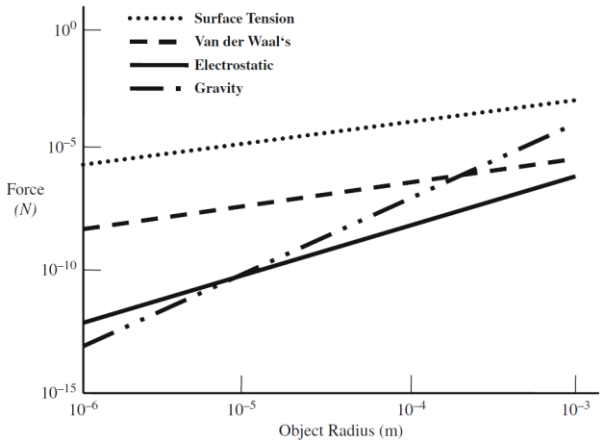

Figure 2-6. Relationships between some common forces and device size [37]

2.2.2 Origins of Adhesion and Frictional Forces in MEMS

Forces on the micro devices which might result in high resistance and adhesion on the micro sliding contacts are briefly reviewed in this section.

Capillary Force

One of the strongest forces causing adhesion and stiction in micro contacts is the capillary force. The water vapour would get condensed in the small gaps between the contacting surfaces and forms a thin water film, this phenomenon is the so-called capillary condensation. If the contact angle between the condensed liquid film layer and the solid surface θ_c is smaller than 90°, the pressure inside the liquid film is smaller than that outside the film. Therefore, for micro devices, the pressure difference results in adhesive force between the contacting plates hence holding the contacting surfaces together and causing adhesion and in-use stiction [38]. This pressure difference could be calculated using Laplace equation [38]:

$$\Delta p = \frac{2\gamma_{la}\cos\theta_c}{d} \tag{2-5}$$

Therefore, the external force required to separate the surfaces is:

$$F = \Delta pA = \frac{2A\gamma_{la}\cos\theta_c}{d} \tag{2-6}$$

Where the γ_{la} is the surface tension of liquid and air interface, d is the distance between the contacting surfaces and A is the wetted area. Therefore, the capillary force which holds the contacting surfaces in stiction F could be reduced by decreasing the liquid condensed area (wetting area) [39] (essentially, adhesion energy).

De Boer and co-researchers showed the dependency of adhesion energy on relative humidity by using a one end anchored micro-cantilever, the adhesion energy is quantified by the length of the part that is not stuck [40]. Deng and co-researchers also found that the maximum static friction of micro sliding contact is also strongly dependent on the relative humidity [41]. For a silicon against silicon contact with the roughness of 3nm, the adhesion energy which is resulted from water condensation could reach 0.14 Jm^{-2} under 100% relative humidity [42].

Figure 2-7 below demonstrates the liquid condensation when two surfaces are in contact under humid conditions.

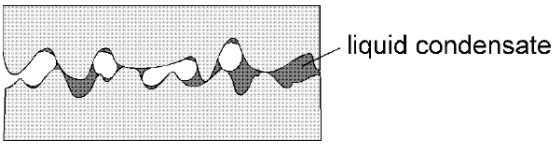

Figure 2-7. Liquid condensation in MEMS contacting surfaces [40]

Van der Walls Force

Van der Waals force between two contacting surfaces is a result of mutual electric interaction of the induced dipoles in the contacting surfaces [43]. The adhesion energy density caused by Van der Waals force can be calculated using the equation below:

$$E_{vdw} = -\frac{A_H}{12\pi d^2} \tag{2-7}$$

Where A_H is the Hamaker constant which normally ranges from 0.4-14$\times 10^{-19}$ J for polar molecules. *d* is the distance between the contacting bodies. In practice, the Van der Waals force drops much faster with increasing contact surfaces distance than it is predicted by equation above when the distance is larger than 20 nm [39]. The effect of Van der Waals force on adhesion almost disappear when the distance is larger than 20 nm. Normally, Van der Waals adhesion is much smaller than the capillary condensation adhesion and it is only dominant when the relative humidity is very low (<30%) or the contacting surfaces is water-repellent [38, 39]. The Van der Walls adhesion is mostly affected by the surface roughness.

Electrostatic Force

The differences in contact potential, the tribo-charging of sliding surfaces and the electrons trapped in the oxide layer of MEMS surfaces would together result in electrostatic forces within

the MEMS contact [44]. Theoretically, the electrostatic force obeys Coulomb's law and decreases with increasing distance between the contact surfaces. However, the charges often redistribute themselves according to the field [38, 39]. Normally, the stiction caused by electrostatic force is temporary as the non-equilibrium charging will relax with time.

Sliding

When sliding is applied within the contact, the high adhesion forces would lead to high friction and when the actuation force cannot overcome the in-use stiction occurs. In addition, silicon is a very brittle material, which means severe wear happens when large amount of sliding is applied especially when the friction is very high.

2.3 Lubrication Methods for MEMS

Currently, there are several different methods to reduce the adhesion and friction in MEMS devices, they could be roughly categorized into two categories based on the working mechanism. The first type of methods is to make the surfaces of MEMS devices more hydrophobic. The other type of methods is to separate the contact surfaces of MEMS devices by medium (solid, vapour or liquid) with which low adhesion and friction can be achieved.

2.3.1 Adhesion Reduction During Fabrication

As discussed above, liquid condensation and its resulting capillary force are the main causes of adhesion and stiction in MEMS devices. Liquid condensation is almost not avoidable as rinsing and drying processes are necessary for the fabrication of most MEMS devices. However, it has been found by researchers that the surface energy could be reduced by choosing appropriate low-surface-tension rinsing and drying liquid. Scheepers and co-researchers [45] found that the surface energy of a silicon nitride surface rinsed and dried using n-hexane (19 mJ m^{-2}) is much lower than the one which is rinsed and dried in DI water (73 mJ m^{-2}). Low surface energy of silicon wafers could also be achieved by using Fluorinert in rinsing and drying processes.

Mulhern and co-researchers [46] prevented liquid condensation by using a *supercritical drying process* where the liquid is transferred to vapor through the supercritical phase and no liquid-air interface exists during drying. Therefore, the liquid condensation is prevented.

There are other methods applied in micro fabrication processes to reduce the surface energy such as drying the MEMS devices under elevated temperature [47] and using sacrificial dioxide layers [48].

2.3.2 Stiction Reduction by Surface Treatments

As discussed in the previous section, capillary condensation is the main cause of the stiction of MEMS contact and it is determined by the environment humidity and the wetting area of the contact. Therefore, treatments changing the properties of the surfaces of MEMS devices to either make the surface more hydrophobic or reduce the real contact area are options to reduce the in-use stiction. The two commonly used methods are increasing the surface roughness and making the surface hydrophobic. [38, 39]

Hydrogen Termination on Silicon Surfaces

As most of the MEMS devices are made from silicon, lots of research has been conducted to investigate treatment on silicon surfaces to make the surface more hydrophobic. Hydrogen termination treatment on the silicon surfaces by passivating the surfaces by using chemicals such as the ammonium fluoride (NH_4F) or the hydrofluoric acid (HF) is an effective way to make the silicon surfaces hydrophobic. [49]

The bare silicon surface with almost no chemical termination is not hydrophilic, Arkles [50] and co-researchers measured the contact angle of a water droplet on a newly etched silicon surface, results show that the contact angle can reach 88 °. That is because water molecules cannot form hydrogen bond with the bare silicon atoms [51].

However, the bare silicon surface is very reactive because of the dangling bond terminated on the bare silicon surface, a thin layer of silicon dioxide (thickness lower than 1 nm) covering the silicon surface would form fast when the bare silicon is exposed to air [52, 53]. The silicon dioxides are vulnerable to hydroxyl group termination, the silicon surface in this case becomes very hydrophilic as hydrogen bonds forms between the hydroxyl groups terminated on the silicon surfaces and the water molecules. The contact angle in this case ranges from 35 ° to 48 ° [54].

Hydrofluoric acid (HF) and ammonium fluoride (NH_4F) can etch the thin silicon dioxide layer formed on the silicon surfaces together with the terminated hydroxyl groups. After the etching process, it can be found that the silicon surface is terminated with hydrogen [55-57]. Since the

dangling bond of bare silicon is terminated by hydrogens, the silicon surface is not passivated. The passivated silicon surfaces can be chemically stable for a few days when exposed to air [58]. Due to the low polarity of the silicon-hydrogen (Si-H) bond, hydrogen bond cannot be formed when water molecules are dropped on the passivated silicon surfaces. Figure 2-8 below demonstrates the hydrogen-terminated silicon surface

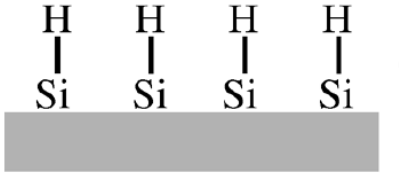

Figure 2-8 Wafer surface after hydrogen termination [59]

The properties of polycrystalline silicon surfaces after hydrogen termination treatment were tested by Houston and co-researchers through a series of investigations, and they validated that hydrogen termination treatment can make the silicon surfaces hydrophobic. They found that the contact angle between the water droplet and the hydrogen terminated silicon surface (by HF etching) is 61.0 °. The contact angle between the water droplet and the hydrogen terminated silicon surface (by NH_4F etching) can reach up to 85.5 °. [58-60]

However, as mentioned, the effect of passivation by hydrogen termination gradually vanishes with time and totally disappears in a few days. The silicon surfaces would be covered with hydrophilic silicon dioxide layer. That indicates that this method is not suitable for MEMS devices which are expected to be used for a long time.

Surface Roughening and Skewing

As discussed above, smaller wetting area can be achieved by reducing the real contact area. The adhesion forces including capillary force and Van der Waals force could be considerably decreased when the surface roughness is increased as the height of the gaps between two surfaces in contact, which can be indicated from equation (2-6) and equation (2-7). Two types of methods can be used to reduce the real contact area of the micro contacts, the first type is to fabricate micro bumps or holes over the surfaces and the second type is to roughen the surfaces directly. [39]

i Micro Dimples

Zhang and co-researchers [61] compared the friction coefficient of silicon samples with smooth surface and the silicon samples etched with micro dimples and confirmed that micro dimples are capable of friction reduction for micro sliding contacts through experiments. The micro dimples are etched regularly on the 4 mm X 4 mm silicon samples using lithography processes. The diameter of the dimple is 8.5 μm, the depth of the dimple is 60 nm, the distance between two neighbouring micro dimples is 6 μm. SEM images of a single micro dimple and the regularly dimpled silicon sample surface is demonstrated in figure 2-9 below.

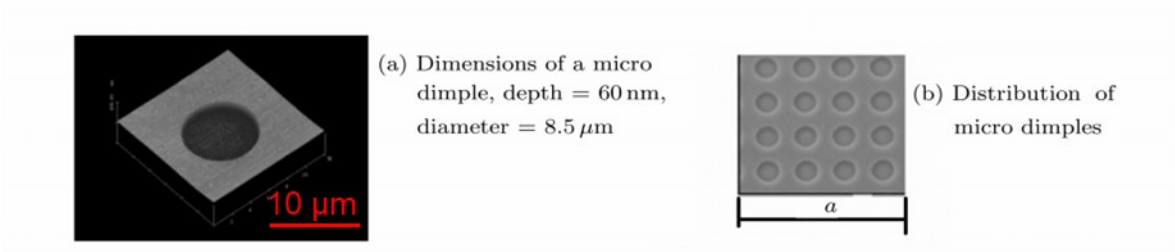

Figure 2-9 (a). SEM image of a single etched micro dimple; (b). SEM image of the regularly dimpled silicon surface [61]

Friction coefficient of the smooth silicon samples and the dimpled samples are measured under the test conditions of 314 μN load, 2.7 μm/s sliding speed and 85% relative humidity. The friction coefficient of the smooth samples is 0.4 whereas the friction coefficient of the dimpled samples is reduced to 0.3. [61]

ii Micro Bumps

Corresponding to micro dimples which are etched to a certain depth below the original surface, micro bumps are tiny features which are extruded to a certain height above the original surface. Therefore, the distance between the contact surfaces can be increased by the micro bumps hence reducing the capillary force and Van der Walls force. In addition, the shape of the micro bumps applied on MEMS device surfaces are normally hemispherical, so the real contact area can be reduced hence resulting in smaller stiction force.

Fan and co-researchers applied micro bumps to the parts surfaces of a micro electrostatic motor. [62] As shown in figure 2-10 below, the hemispherical micro bumps are fabricated on the bushing of the rotor which is fabricated from polycrystalline silicon. No in-use stuck happened

during the operation of the micro motor, which confirms that micro bumps are effective in stiction prevention [62].

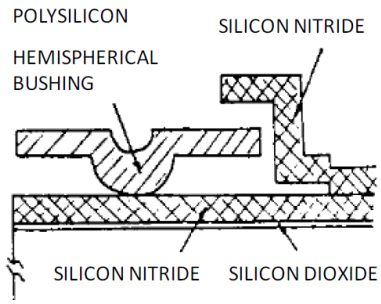

Figure 2-10. Micro-hemispherical bumps in micro rotor surface [62]

iii Direct Surface Roughening

The stiction problems of the micro contact can also be tackled by directly roughening the surfaces of the MEMS devices. Allison, Ando and co-researchers have investigated the pull-off force (adhesion force) of silicon-gold interfaces with four different combined surface roughness values (σ) through both experiments and numeric modelling [63, 64]. Combined surface roughness values and the measured pull-off forces are illustrated in table 2-2, the area of the micro contacts is all equal to 1000 μm^2.

Table 2-2. Pull-off forces of micro contacts with different surface roughness [63]

Combined Surfaces	A. Rough (σ=15.8nm)	B. Intermediate (σ=6.8nm)	C. Smooth (σ=1.4nm)	D. Super Smooth (σ=0.42 nm)
F^* (or $F / A_n E$)	2.35×10^{-9}	3.5×10^{-8}	5.8×10^{-5}	2.42×10^{-4}
F (μN) (A_n = 1000 μm^2)	0.12	1.7	2800	11813
$(h^*)_{max\ F}$ ($h^* < 3$ for contact)	5.0	4.9	2.3	1.7

It can be seen from table 2-2 that the adhesion force can be negligible when the surface roughness of the contact is 15.8 nm whereas the adhesion force is dominant when the surfaces of the contact are super smooth (0.42 nm combined surface roughness).

Even though the adhesion and high friction problems can be improved by changing the topography of the surfaces of micro devices by adding micro dimples, micromachining micro bumps and directly roughening the surfaces, problem of severe wear might occur on the surface

roughened micro contacts especially when large amount of sliding is applied. In addition, the structural parts of the micro devices might be too thin if surface roughening is overdone.

2.3.3 Dry Lubrication with Coatings

Coatings has been used to solve stiction problems of contacting surfaces since 1950s. Bowden and co-researchers [39] solved the stiction of a smooth substrate against indium ball contact by using molecular coating. From 1990s, coating was found to be useful in solving stiction problems resulted from capillary condensation in MEMS contacts. There are several methods to form coating films over the surfaces, but their working mechanisms are similar. The coating films cover the MEMS surfaces with long-chain molecules (typically hydrocarbon or fluorocarbon chains). Therefore, the surfaces of the micro contacts are not in direct contact, the coating films over the surfaces are hydrophobic, slippery and capable of protecting the contact surfaces. Two common lubricious coating films are briefly introduced below.

Self-Assembled Monolayer Coating (SAM)

Self-assembled monolayers are thin films of organic molecules which are formed on substrate surfaces in order through molecule adsorption [65, 66]. As most of MEMS devices are fabricated from silicon, deposition of SAM films on silicon (to be more precise, silicon dioxide) surfaces are briefly introduced in this section. A more detailed introduction on SAM issues can be found in the reference [67]. The structure of the self-assembled monolayer on the silicon substrate is demonstrated in figure 2-11.

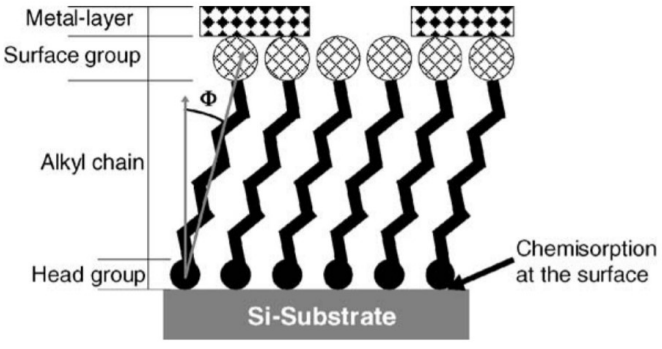

Figure 2-11. SAM structure on the silicon substrate surface [67]

It can be seen from figure 2-11 that the molecules which forms the SAM film consists of three parts: *(i)* The head group which is used to form chemical bond with the atoms on the silicon surface; *(ii)* The straight alkyl chain, Van der Walls interactions between the alkyl chains of

neighbouring molecules help the formation of the orderly and tightly packed structure of the SAM film; *(iii)* The terminal group at the tail end of the self-assembled monolayer molecules, the group can be replaced with different groups to achieve different functions [67].

To form SAM film on silicon device surfaces, thin silicon dioxide layer would be grown on the silicon surface first for the purpose of forming stronger interactions between the monolayer molecules and the device surfaces. Head groups that can be absorbed on the silicon dioxide surface are trichlorosilane group ($-SiCl_3$), trimethoxysilane group ($-Si(OCH_3)_3$) and triethoxysilane group ($-Si(OCH_2CH_3)_3$). However, the first head group is much more active than the other two head groups, which means the SAM formation process of the molecules with trichlorosilane is much shorter than that of the molecules with other two groups (hours compared to days). [67, 68]

To generate SAM film which is expected to reduce the stiction and protect the MEMS device surfaces, octadecyltricholorosilan (OTS) and perfluorodecyltrichlorosilane (FDTS) are commonly selected as the monolayer molecules. Their molecular formulas are: $CH_3-(CH_2)_{17}-Si-Cl_3$ (OTS) and $CF_3-(CF_2)_7-(CH_2)_2-Si-Cl_3$ (FDTS).

Figure 2-12 demonstrates the formation process of the formation processes of molecules with trichlorosilane group head ($-SiCl_3$). As demonstrated in figure 2-12, the molecules with trichlorosilane group head ($-SiCl_3$) contact with the hydroxyl group terminated silicon dioxide surface forming Si-O-Si bonds through hydrolysis reactions with the presence of water molecules. That enables the alkyltrichlorosilane molecules to be attached on the silicon dioxide layer surface. A condensation reaction would then happen among the hydroxyl attached silane parts of the molecules, covalent attachments and interactions bonding neighbouring molecules tightly together are achieved by the condensation reaction. [69-71]

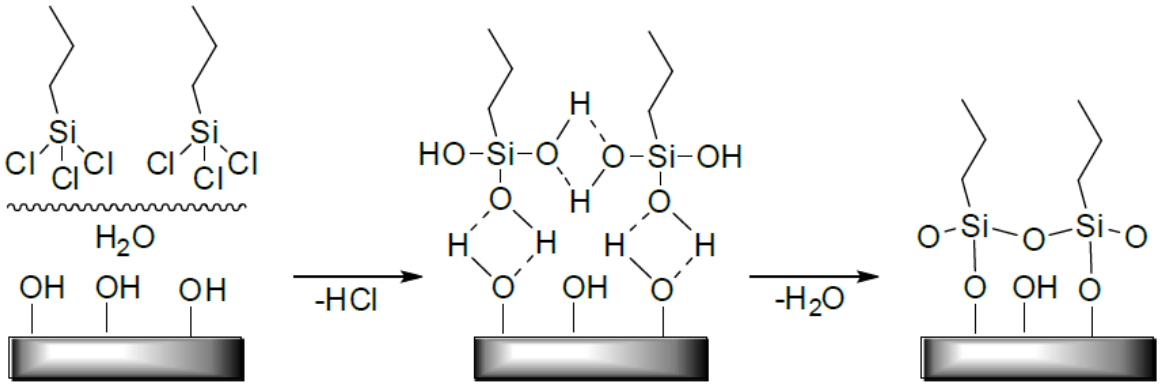

Figure 2-12. Self-assembled monolayer formation process of the alkyltrichlorosilane molecules on the silicon dioxide layer surface [69]

Boer and co-workers measured that the adhesion energy of OTS coated MEMS surface is about 30 μJ/m^2 and the adhesion energy of FDTS coated MEMS surface is around 8 μJ/m^2, the adhesion energy is significantly reduced compared to that of an untreated MEMS surface (around 56 mJ/m^2) [72]. Researchers have also compared the contact angles and friction coefficients of SAM coated MEMS devices and the uncoated silicon surfaces. Results show that water contact angle of a SAM coated MEMS surface is greater than 110° whereas the contact angle of an uncoated surfaces is smaller than 30°. The friction coefficient of the MEMS contacts is also reduced from bigger than unit to smaller than 0.1 (0.073) after OTS coating. [68, 72]

The disadvantages of this methods including that: firstly, the coating process requires strict control and there are other competing reactions happened simultaneously with the SAM film formation reaction. However, only one reaction is correct to form the coating film, the repeatability of the process is low [72]. Secondly, the molecules of the SAM coating film would degrade when ambient temperature is higher than 100°C, which may cause difficulties in packaging process. The coating molecules with fluorocarbon chain could withstand a higher temperature but it will degrade as well when it operates in humid conditions [39, 72].

Diamond Like Carbon Coating Films

Carbon-based solid film is widely used to coat the silicon MEMS devices surfaces. It can make the coated surface become highly hydrophobic. There are several different carbon-based solid films with different coating structures including: polymer like, graphite like and diamond like. The diamond like carbon-based film has the advantage of high hardness, which indicates that this type of coating film is able to resist wear under applied sliding [73]. The DLC film can be coated on the silicon surfaces with different methods including sputter coating, ion plating, etc. However, DLC coating film with the highest uniformity is conducted using the plasma enhanced chemical vapour deposition method (PECVD) [74].

In the PECVD process, the precursor gases molecules which are the sources of the carbon-based film would be activated by plasma, the plasma-activated precursor gases molecules, which typically consists of methane (CH_4) (other hydrocarbon gases are could also be used) and hydrogen gas (H_2), would be deposited on the silicon surfaces at high temperatures and

gradually forming the DLC coating layer. The temperature which is preferable for the growth of the carbon-based film ranges from 600 ℃ to 1000 ℃. By controlling the ratio between the hydrocarbon gas and the hydrogen gas which are supplied to the coating chamber, the surface roughness of the coated DLC film can then be manipulated in the range between 0.1 nm and 2 nm [75]. As illustrated in figure 2-13, the surface topography of the diamond like carbon-based coating film alters drastically with different precursor gases.

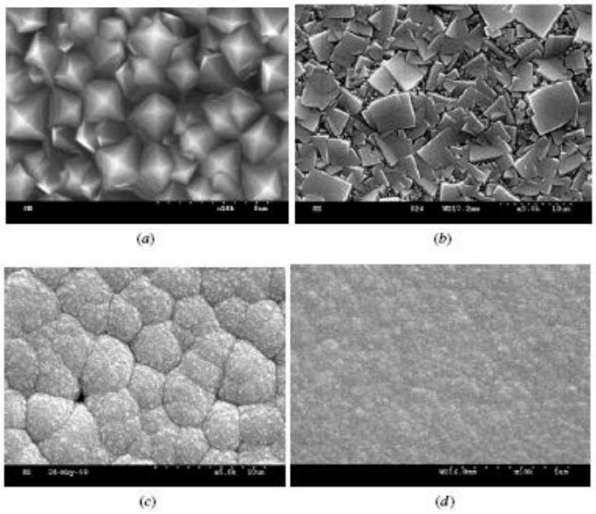

Figure 2-13 Pictures of diamond like carbon-based coating films constructed from precursor gases with four different hydrocarbon gas to hydrogen gas ratios. Ratios from figure (a) to (d) are: 2%mol CH_4 to 98%mol H_2, 3%mol CH_4 to 97%mol H_2, 4%mol CH_4 to 96%mol H_2 and 8%mol CH_4 to 92%mol H_2 respectively [75]

The surface energy of DLC coating is very low so the DLC coated surface is very hydrophobic. The water contact angle of a very finely deposited DLC coating could reach greater than 130° [76]. Stiction problem seldom occurs on the MEMS device surfaces with DLC coating film as the liquid droplet is much more confined to itself rather than to the MEMS device surface. Because the surface is very smooth and lubricious, the friction coefficient and the wear rate of DLC film coated surfaces are also very low. The friction coefficient of the DLC surface that is deposited with the gas of a 25:75 methane to hydrogen ratio could be as low as 0.003 [77].

The disadvantage of DLC is that even though the friction coefficient and wear rate is low, the coating cannot get replenished and will be totally worn out after large amount of sliding is applied. Besides, the friction properties of the DLC is largely affected by the environmental conditions including ambient air constituents, humidity. [74] When the humidity of the environment is high, the friction coefficient of the DLC film would ascend drastically. [78]

2.3.4 Vapor Phase Lubrication

Vapor phase lubrication is another effective lubrication method for MEMS devices. The working mechanism is similar to that of coating films on the surfaces to some extent. Lubricious films consisting of molecules from the supplied vapour form over the contacting surfaces either by chemical reaction or by surface absorption. Surface protection and low friction coefficient can then be achieved by the deposited films consisting of the molecules from the supplied vapour. The biggest difference from the film coating methods such as SAM coating and DLC coating to vapour phase lubrication methods is that the deposited film consisting of the molecules from the vapour can be self-replenished as the molecules of the vapour are continuously supplied; whereas the SAM or DLC coating films would be gradually worn out after large amount of sliding is applied.

Another advantage of vapour phase lubrication is that the vapour flow rate can be controlled so that the speed of film reformation equals the speed of film consumption, no excess lubricant is provided and the friction coefficient and wear rate can be continuously kept at a low level. Examples of micro silicon surfaces applied with vapour phase lubrication are given as follows.

Water Vapour on OTS Coated Surface

Patton and co-researchers [79] investigated the lubrication performance of the film consisting of water molecules from the water vapour deposited on the micro silicon surface which is previously coated with the OTS self-assembled monolayer. The researchers firstly developed an environment in which humidity can be controlled (water vapour is controlled this way) and tested the lifetime of a micro motor device whose sliding contacts were coated with OTS-SAM film. It was found that, comparing the lifetime of the motor operating in dry air where no water vapour is supplied, the lifetime of the micro motor became much larger when the humidity of the environment was kept between 30% to 50%. However, when the humidity is set over 50%, water condensation occurred hence causing stiction, in this case, the water molecules are no longer in vapour phase but in liquid phase. It was also found that water vapour lubrication is more effective when the rotation speed is lower as high rotation speed results in high water film wear rate.

Short-Chain Fatty Alcohols Vapour Lubrication

Several researchers investigated the performance of the vapour phase lubrication using alcohol molecules with short carbon chain length. Strawhecker and co-researchers [80] developed a test platform based on a gas handling machine that are able to control the supply rate of vapour. As demonstrated in figure 2-14 below, the test platform is composed of a gas supply source to provide inert gas or clean and dry air, bubblers with heating functions (two of them) and condensers (two of them) which are filled with alcohol molecules with short chain length are inserted into the bubblers. The supplied gas would firstly pass the bubblers (which are heated) at around 20 ℃ temperature so that the gas flow would be mixed with the alcohol molecules. The gas would then flow through condensers which are filled with the alcohol molecules to avoid supersaturation and liquid condensation issues that might happen when the flow reaches tested surfaces. The flow consists of dry air and alcohol vapour would finally enters a well-sealed chamber where the tests are conducted. Alcohol vapour partial pressure inside the sealed chamber is adjustable during tests. [79, 80]

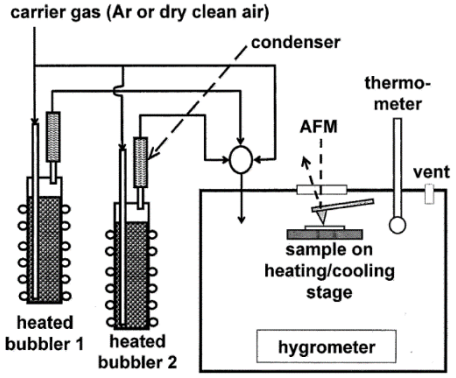

Figure 2-14. Structure of the vapour phase lubrication test system [80]

Strawhecker and coresearchers [80] investigated the lubrication performance of the propanol vapour and found that the friction coefficient of the lubricated sample surfaces (measured using the AFM pull-off force) was reduced from larger than 1 to around 0.4 when 50% propanol partial pressure was reached. However, when the propanol vapour pressure was further increased, no obvious further reduction in friction coefficient was observed, which indicates that only a few amounts of propanol molecules are required to form a complete lubricating layer over the surfaces.

Asay and co-researchers [81, 82] investigated the lubrication performance of pentanol vapour on MEMS contact by testing the friction coefficient and lifetime in the vapour phase lubrication

test system which is introduced in last paragraph. The silicon surfaces were firstly coated with hydrophobic film, pentanol vapour was supplied after that. The friction coefficient and lifetime results are demonstrated in figure 2-15 below. As shown in figure 2-15, the pentanol vapour is even capable of making the jammed micro contacts of which the previously coated lubricious coating film has already been worn out to rotate again. In addition, the previous failed contact could retain low level friction and could operate millions of cycles [82]. However, when the supply of pentanol vapour was stopped, the contacts got stuck again.

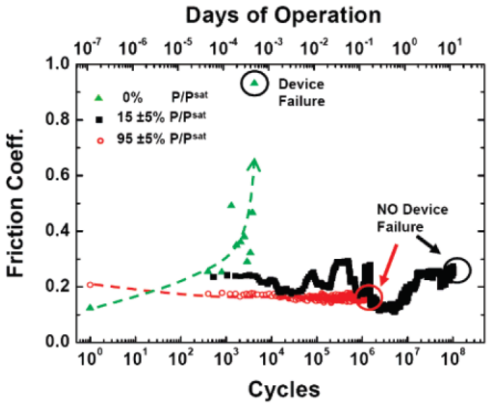

Figure 2-15. Friction coefficient and lifetime of pentanol vapour lubricated surfaces [82]

As demonstrated in figure 2-15, the hydrophobic film coated on the MEMS device surfaces before totally fails after approximately 3000 cycles when no vapour phase lubricant is supplied. When the MEMS contact was lubricated with pentanol (partial pressure reaches 95%), the friction coefficient stays stably at low level and the lifetime was increased by up to 4 orders of magnitude [81-84], no obvious wear occur. However, by-product from the reaction from the MEMS surface and pentanol molecules is generated during sliding and would accumulate hence resulting in possible overdamping and mechanical interference [85].

Challenges in Vapour Phase Lubrication

As discussed above, vapour phase lubrication behaves well under lab conditions where the test chamber is sealed, and constant vapour partial pressure can be precisely controlled. However, filling a sealed volume with certain amount of these kinds of lubricants with high vapour pressure in an actual MEMS device can be extremely challenging and expensive. In addition, the operation temperature range for vapour phase lubrication is limited to be small. Because temperature is important to keep a full protecting film consisting of the vapour molecules over the protected surfaces so that the wore part of the vapour molecule protection film can be

immediately replenished by adsorbing molecules in the environment. [85] For example, a contact lubricated with pentanol (partial pressure 10%) can only well operate at temperature ranging from 0 ℃ to 20 ℃.

2.3.5 Liquid Lubrication

Liquid lubrication is a prevalent lubrication method in macro scale devices. The liquid is entrained between the contacting surfaces and pressurized. The pressurized liquid would completely separate the contacting surfaces when sufficiently high speed is applied hence reducing the friction of the contact. Few early researchers have conducted investigations on the possibility of implementing liquid lubrication in micro-scale devices. Mehregany and co-researchers found that the frictional torque of micro motor lubricated with low di-electric constant is reduced [86]. Deng and co-researchers measured that the frictional torque of a micro motor using silicone oil as lubricant is one magnitude lower than that of the unlubricated case (0.1 pNm to 1 pNm) [2]. However, researchers found that the maximum rotation speed of the micro motor lubricated with liquid is restricted to a low value as viscous drag force would dominate when the speed is high, hence causing overdamping. Therefore, liquid lubrication is concluded to be inappropriate for micro lubrication by some researchers and not sufficient researches have been conducted.

However, Reddyhoff and co-researchers [3] have recently conducted frictional measurements of micro scale silicon surfaces lubricated with several liquids with very low viscosities (hexadecane, toluene silicone oil and water) on a custom-developed tribometer. It has been found that the friction coefficient of low viscosity liquid lubricated silicon surfaces could also be reduced to lower than 0.1 at high rotation speeds (524 $rad \cdot s^{-1}$), which indicates that low viscosity liquid lubrication is feasible for micro devices operating at high speeds. One problem of liquid lubrication is that liquid lubrication suffers from high friction when the speed is low and insufficient fluid is entrained within the contact to completely separate the surfaces. Reddyhoff and co-researchers [87] found that this problem can be solved by adding amine additives into the lubricant with low viscosity. The amine additives could form a solid like film over the contacting surfaces hence reducing friction and wear. This successful idea of solving the high friction at low speeds is similar to that of friction reduction in boundary lubrication for macro scale devices.

2.3.6 Summary of Lubrication Methods for MEMES Devices

As discussed above, most of the investigations on lubrication methods used in MEMS devices to reduce stiction and friction coefficient of the micro contacts are focused on modifying the properties of the surfaces, but they all have some disadvantages. For dry lubrication methods, the MEMS device surfaces are in direct contact so the coated protecting films like SAM or DLC would shear against each other and gradually degrade and fail after large amount of sliding is applied. In vapour phase lubrication, certain vapour molecules could get attached on the surfaces providing surface protection and low friction coefficient. When the protecting film is worn off, the film gets replenished from more vapour molecules in the environment. However, complex and expensive seal design is required as the friction increases fast when there is not sufficient vapour phase lubricant in the environment.

Liquid lubrication, the most effective and commonly used lubrication method in macro scale, has been ignored in small scale lubrication for a long time as researchers are concerned about the over viscous drag at high speeds and the stiction problems at low speeds. However, Reddyhoff and co-researchers [3] found that a 2-mm-diameter contacts could operate at high speeds (above 500 $rad \cdot s^{-1}$) with a low level of friction coefficient when lubricated with low viscosity lubricant in lab tests. That indicates the possibility of the development of a pair of hydrodynamic bearings used in micro contacts. With appropriate designed parameters, the friction coefficient of the bearings is possible to be minimized to a small value. The high friction problem at low operation speed might be solved by investigation appropriate additives surfaces.

2.4 Introduction on Micro Fabrication Techniques

Considering that the size of the micro bearings which are going to be fabricated and installed on the MEMS energy harvesting turbine in this research is only 1 millimetre or 2 millimetres and complicate pad shapes and textures with the feature size down to 1 micron are required to be patterned on the bearing surfaces, micro-fabrication techniques are selected as the method to fabricate the micro bearings. Micro fabrication techniques offer a way to achieve batch processing for the micro bearings with complicate and small features, design flexibility is also enabled by micro fabrication techniques so that micro bearings with different patterns can be produced in the same batch. Figure 2-16 below demonstrates a wafer that is being processed.

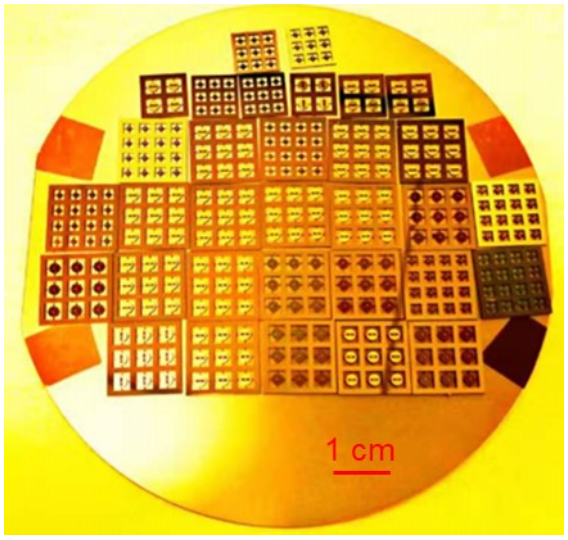

Figure 2-16. A processed silicon wafer with various designs of micro bearings

Micro fabrication techniques can be roughly divided into three categories: additive micro fabrication techniques, patterning and subtractive micro fabrication techniques.

2.4.1 Additive Micro Fabrication Methods

Additive Microfabrication is to deposit specific material layers or grow specific layers on the substrates to achieve certain purposes. Some commonly used additive microfabrication techniques are given as follows:

Thermal Oxidation

Thermal oxidation is technique to generate thin oxide layers (usually silicon dioxide) on the silicon substrate, it enables oxidizing agents to diffuse into the substrates and react with the substrates at high temperatures.

Depending on the type of oxidation agents, thermal oxidation techniques can be categorized as dry oxidation (use oxygen as the oxidant) or wet oxidation (use water vapour as the oxidant).

$$Si + O_2 \rightarrow SiO_2$$

$$Si + 2H_2O \rightarrow SiO_2 + 2H_2$$

Dry oxidation is used to grow thin layer of oxide with high density, but the low growth rate makes it impractical to grow thick oxide layers. The oxide growth rate of wet oxidation is high

but the fast oxidation results in more dangling bonds at the silicon interface and the oxide density is also lower. [88, 89]

Chemical Vapor Deposition (CVD)

Chemical vapor deposition is a technique to produce high quality, high performance and solid material thin layers (particularly useful for atomic layer deposition) on the substrates, the coating layers by CVD can be sufficiently uniform. Number of different types of thin films can be coated on the wafer surfaces for different usages. One practical application is that special nitrides and carbides layers deposited by CVD can help to achieve high wear-resistance; another application is that polymerization layers coated by CVD can make the wafer surfaces lubricious and hydrophobic.

Chemical vapor deposition is conducted by exposing the substrates to one or more volatile precursors under vacuum conditions, the volatile precursors will react with and decompose the surfaces of the substrates thereby generating the deposit layers. [90, 91]

Physical Vapor Deposition (PVD)

Corresponding to chemical vapor deposition, physical vapor deposition is another type of technique to create thin film layers and coatings on substrates surfaces under vacuum conditions. It is characterised by a process in which the materials of the thin film layers (coatings) transfers from condensed phase to vapor phase then deposits on the substrate surfaces and turns back to condensed phase again (thin film layers are created this way). Evaporation deposition and sputter deposition are the two most common method of PVD.

For sputter deposition, atoms of the materials to be coated on the substrates are sputtered off from a ‘target’ (normally a large block of the coating materials) by ions or atoms (the source of the ions or atoms which are so called ‘sputtering gas’ is usually an inert gas) bombardment. The sputtered atoms travel and reach the substrates surface then condensed on the substrate surfaces, a thin layer of the coated materials thereby growing on the substrate surface.

For evaporation deposition, the source materials are evaporated under vacuum conditions and the vapor material particles travel directly to the substrate surfaces and grows a thin film deposition layer.

Sputter deposited thin film layers normally have a stronger adhesion on the substrates than the film layers by the evaporation deposition, it is also more suitable to deposit materials with very

high melting points (e.g. chromium, copper, gold, etc.). However, the deposition rate of evaporation is higher than that of sputter deposition. [92]

2.4.2 Patterning Methods

In micro fabrication, distinct features (size of the features are on micrometre or nanometre scales) are required to be patterned on the pre-designed region of the substrates with certain depth (material removed from substrates) or height (material added to the substrates). In addition, different features are often desired to be patterned in different regions in different layers. Patterning technology is what archives these precisely patterned micro features and is what defines micro fabrication. 'Masks' is the tool commonly to define the patterned shape where apertures in the same shape of the desired patterned features are applied. Photolithography and stencil (shadow mask) lithography are the two patterning techniques which are commonly used in micro fabrication. [93, 94]

Photolithography

Photolithography (also known as UV lithography) is the patterning method used in most micro fabrication processes. This technique is able to transfer the designed patterns which are printed on the optical masks to the light-sensitive chemical photoresists which are uniformly spin coated on the substrates by using ultraviolet light. After some special treatments (mainly photoresists chemical developing and wafer cleaning), the region of the substrates surfaces which are precisely in the same shape with the designed patterns will be exposed (previously whole surface is covered with photoresist). The patterned and exposed substrates surfaces are then prepared for following subtractive or additive micro fabrication processes. [93] Figure 2-17 below demonstrates the mask aligning process to achieve patterning on the processed silicon wafer using on the mask aligner.

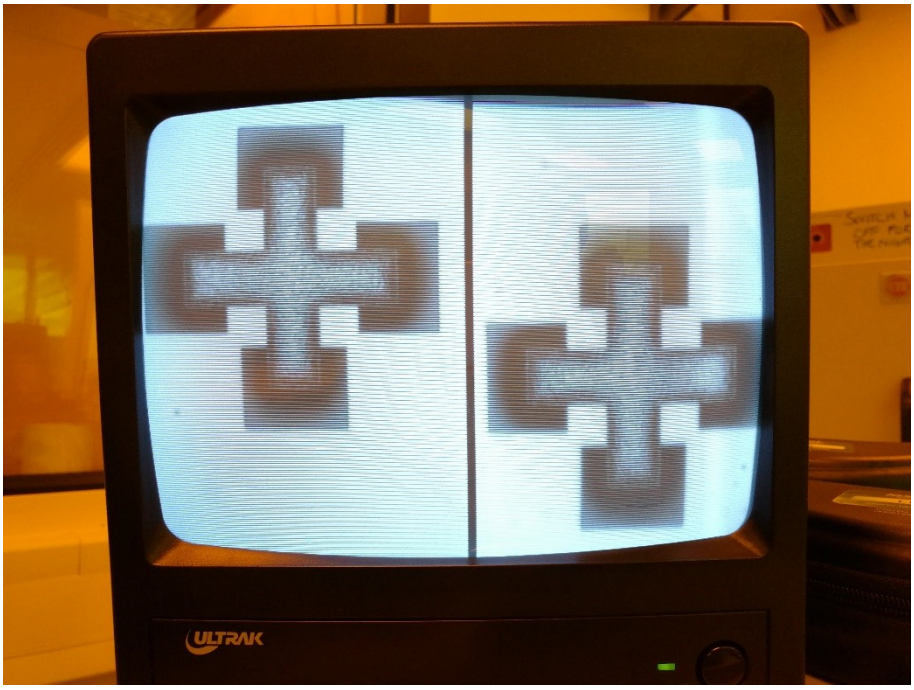

Figure 2-17. Aligning the marks on the masks to the marks on the processed wafer

Stencil lithography

Stencil lithography (also known as shadow mask lithography) is a relatively simple patterning method compared to photolithography. It does not require to apply photoresist, chemical treatment, liquid rinsing and substrates cleaning processes. The designed patterns are completely etched through a thin sheet of metal to construct the shadow masks. The specially made shadow masks will then be placed into intimate contact with the substrate surfaces, additive or subtractive fabrication processes can be conducted in the intended region of the wafer through the patterned apertures of the shadow masks.

However, the resolution of this patterning method might not be as high as of photolithography and the edges and corners of the constructed feature on the substrates are more ragged than those constructed using photolithography. [94]

2.4.3 Subtractive Micro Fabrication Methods

Subtractive microfabrication, or more commonly known as etching, is the process to remove the materials from the selected region (the exposed region which is formed through patterning processes) of the substrates. Etching techniques can be classified into two categories which are dry etching and wet etching.

Dry Etching

In dry etching process (which are also known as plasma etching process), the substrates will be placed in environments where plasma of reactive gases is generated (some commonly used reactive gases are: oxygen, fluorocarbons and sulphur hexafluoride), some portions of the materials in the region where the substrates surfaces are exposed to the surrounding environments (formed through patterning processes) will be removed by the bombardments of ions from the plasma of reactive gases. [95, 96]

Reactive Ion Etching (RIE)

Reactive ion etching is one of the commonly used dry etching technique. The substrates are placed in a vacuum chamber. The chemically reactive plasma of the reactive etchant gases is generated under low pressure by an electromagnetic field. Some portion of the materials in the exposed area of the substrates will be removed by the attacks of the high energy ions. A table of some commonly processed materials and the corresponding etchants are given below. [95]

Table 2-3 Etchant gases and gaseous by-product of different materials [95]

Solid	Etch Gas	Etch Product
Silicon	CF_4,Cl_2, SF_6	SiF_4, $SiCl_4$, $SiCl_2$
SiO_2, SiN_x	CF_4, C_4F_8, CHF_3, SF_6	SiF_4, CO, O_2, N_2, FCN
Al	BCl_3/Cl_2	Al_2Cl_6, $AlCl_3$
Ti, TiN	Cl_2, CF_4	$TiCl_4$, TiF_4
Organic Solids	O_2, O_2/CF_4	CO, CO_2,
GaAs & III-V	Cl_2/Ar, BCl_3	Ga_2Cl_6, $AsCl_3$
Cr	Cl_2/O_2	CrO_2Cl_2

Deep Reactive Ion Etching (DRIE)

In MEMS fabrication, features with deep penetrations, steep walls are required to be constructed. These features cannot be constructed through typical RIE processes since the chemical reactive etching is isotropic whereas anisotropic etching is needed to fabricate these features.

Deep reactive ion etching is the technique that can achieve etching process with very high anisotropy, the angle of the etched walls can reach 90°.

There are two types of etching coexists in the DRIE process. Reactive etching and ion etching. Reactive etching is an isotropic process, but its etching selectivity and etching rate is high whereas ion etching is an anisotropic process (ions only bombard upward facing surfaces do not attack side walls) with low etching selectivity and etching rate. By using a combined reactive and ion etching together with a side wall passivation process, etching with very high anisotropy can be achieved and that is how DRIE functions.

The etching in DRIE process is not conducted continuously but in cycles. Each etching cycle consists of two stages: one standard reactive ion etching process and a sidewall passivation process.

Sidewall deposition and passivation: carbon polymer gases (e.g. C_4F_8) is introduced into the chamber and yields a thin passivation layer which deposits on the substrate surfaces. The passivation layer prevents the substrates materials from being reactive etched.

Standard reactive ion etching process: a standard reactive ion etching with which the anisotropy of the constructed features is not very high.

In a single DRIE cycle, the exposed substrates will be deposited with passivation substances on both upward-facing surfaces and side walls in the sidewall deposition and passivation stage first. Then in the etching stage, the low etching selectivity ions only attacks the passivation substance layer in the upward-facing direction and sputter the layer off. The materials of the substrates at upward-facing surfaces are thus exposed to the reactive etchant and removed. Deep etched side walls can be constructed by applying hundreds of such short (only a few seconds) cycles. [96, 97]

For both RIE and DRIE process, the etching quality and speeds are affected by many parameters including etching cycle time, etching temperature, chamber pressure, RF power and etchant flow rate.

Wet Etching

Corresponding to dry etching. Wet etching is the process to remove the materials of the exposed region of the substrates by immersing the substrates into liquid phase etchants. For example, different acids can be used for the removal of metal materials; buffered hydrofluoric acid can be used for the removal of silicon dioxide. Wet etching is normally isotropic, and it is not suitable for deep etched features. [98]

Chapter 3: Development of the Finite Volume Micro Pocketed Parallel Thrust Bearing Model

As mentioned in the first chapter, a micro pocketed parallel thrust bearing is to be fabricated in this research. To systematically investigate the lubrication behaviours of the micro parallel thrust bearings operating in hydrodynamic lubrication regime, a mass-conservation considering finite volume-based model in polar coordinates is developed. Details of the graphic shape of the modelled micro thrust bearing, fluid mechanics of the modelled micro bearing, boundary condition setups and the discretization of the FVM micro bearing model are reported in this chapter. Two validation cases which are used to confirm that the developed model can describe the bearing behaviours correctly are also shown in this chapter.

3.1 Background Introduction on Hydrodynamic Thrust Bearings and Thrust Bearing Models

Fluid film thrust bearings are components commonly used to support applied axial loads. Lubricant entrained in these bearings becomes pressurised and thereby separates surfaces to achieve low friction and high transmission efficiency. Thrust bearing geometry normally consists of a flat rotating runner and a stator containing several sector-shaped pads surrounding the shaft. The configuration of the stator pads classifies bearings as being either a tilted, Rayleigh step, tapered land thrust bearing, etc. [99-101]

The most important performance parameters for thrust bearings are load carrying capacity, friction coefficient, power loss and lubricant temperature rise. [102-105] Understanding, predicting and improving these has been the subject of much research. Anant Singh et al [106] for instance solved the Reynolds equation using a finite difference method to investigate the optimum parameters of tilting bearings including the ratio between inner and outer radius of the stator pad and the inclination angle under different operating velocities. Thermal effects

were also considered in this study by assuming the lubricant temperature rise due to the frictional heating.

A potential way to optimise thrust bearings is to apply surface texture to the stator pads with appropriate texturing parameters (texture shape, density, texture extent in radial and circumferential directions, texture depth, etc.) in order to increase the load capacity and reduce the frictional torque. [107-111] The benefits have been demonstrated experimentally by Wang et al [112] who characterised the effects of circular dimples on the performance of a SiC parallel thrust bearing under water lubrication. It was shown that of all texture parameters evaluated (dimple diameter, texture density, dimple depth), it is texture density that plays the most important role in determining load capacity, which can be increased to three times greater than that of an untextured bearing. However, when the texture density is higher than 15%, the load capacity of the bearing is reduced. Interestingly, both large dimples and small dimples are equally effective in reducing friction.

More significant improvement in terms of load support and friction reduction may be obtained from partial surface texturing so that the textured region can function as a step bearing. [113-117] For instance, Henry et al. [118] tested the pressure distribution, load support and friction coefficient of a partially textured thrust bearing. Using a rectangular pattern, with a texture extent of 70% pad length and 75% pad width, they showed that, under low applied load, a 56% friction reduction and 32% load support increase could be achieved for a texture density of 56%. However, no benefit from texture was observed for high applied loads. Furthermore, worse performance compared to the smooth surface thrust bearing was found for low texture densities.

Given the vast range of possible texture designs, which may function differently depending on the contact configuration and working conditions [111,119,120], it is valuable to have reliable simulation methodologies and tools [121-132] to provide a better understanding of the underlying lubrication mechanisms of textured interfaces. These in turn can be used, in conjunction with experimental investigations [133-139], to give insights and guidance for the design of components with optimum texturing parameters [7,140].

Most modelling studies into textured thrust bearings are based on solving the Reynolds equation. Factors including liquid compressibility, thermal effects and complex rheology may be considered in the simulation in different ways. Particularly with respect to fluid cavitation, in early studies the so-called half-Sommerfeld and Reynolds (or Swift-Steiber) boundary

conditions for cavitation were extensively applied. However, as already consolidated in the literature, such cavitation boundary conditions do not fully guarantee the mass conservation of the lubricant flow, especially in the presence of textures, thus resulting in inaccuracies and unrealistically large load carrying capacity predictions.[111] In order to improve the accuracy of numerical analysis of lubricated contact in the presence of texture, the JFO (Jakobsson, Floberg and Olsson) mass-conserving boundary conditions, which correctly describe the fluid film rupture and reformation and distinguish the boundary between cavitated and active regions, have been introduced and are widely used. [141-143] Modified versions of the Reynolds equation based either on the switch function (g) or on the p-θ Elrod-Adams model are effectively adopted in many numerical works [121,127,144]. The solution these equations obtained using adequate discretization methods and specific algorithms simultaneously ensure the JFO boundary conditions and hence the mass conservation of the lubricant flow throughout the lubrication domain.

Numerous simulation studies have been conducted based on the Elrod-Adams model or its modified version. [144-146] Zhang et al. [147] used the modified Elrod-Adams algorithm to develop a finite difference solution to study the hydrodynamic lubrication behaviour of thrust bearings with transverse grooves distributed evenly in the circumferential direction. Experiments were also conducted to measure the friction coefficient, cavitation area ratio and minimum film thickness. This demonstrated that when the cavitation pressure is set properly, the performance values for the grooved thrust bearings predicted from the model agree with experimental results.

Meng et al. [148] adapted the governing equation of the modified Elrod-Adams algorithm by applying the Streamline-Upwind-Petrov-Galerkin [149] technique and developed a finite element model. This was used to investigate the effect of different texture shapes on the leakage and load carrying capacity of mechanical seal faces. It was found that the orientation of the surface texture can control the liquid flow within the mechanical seal. Yin Song et al. [150] used a 3D Navier-Stokes model together with the Rayleigh-Plesset equation for cavitation to predict the pressure distribution in a tapered land bearing with no oil grooves. Their predictions were validated by measuring the pressure profile in the bearing using a pressure sensor. The reader is referred to Gropper et al. [111] for a more comprehensive review on textured conformal bearing systems.

It can be concluded that much research has been carried out on textured thrust bearings. However, there are aspects which have been overlooked. Specific topics that require further studies are the role of the cavitated area in determining load support and the effect of boundary conditions at the external and internal boundaries of the bearing on the performance of pocketed parallel thrust bearings. Another important aspect is the effect of dimensional scales on the performance of pocketed parallel bearings especially when they are miniaturised. This is of particular importance when considering bearings for MEMS (micro-electro-mechanical systems) applications. [3,151]

In this chapter, details of the development of the finite volume method based numeric model in cylindrical polar coordinates considering mass conservation which is used to predict the lubrication performance of the micro pocketed parallel thrust bearing are reported. The model developed reported in this chapter are also able to predict the lubrication behaviours of other thrust bearings in different size scales and are particularly useful for the bearings in which cavitation occurs.

3.2 Geometry of the Modelled Micro Pocketed Parallel Thrust Bearings

The thrust bearing studied in this work consists of two circular pads as shown in Figure 3-1. The lower stator pad is textured with recessed pockets and the upper rotor pad is flat. The two pads are aligned parallel with each other. The minimum film thickness h_{min} is defined as the distance between the upper runner and the untextured surface of the lower stator.

The pattern textured on the stator pad is shown in Figure 3-1 (a). It consists of several sector-shaped pockets distributed equally in circumferential direction. The inner radius edges of the pockets are linked by a recessed circular region with a uniform depth that can be varied. As the pocketed bearing is rotationally symmetric and can be viewed as a combination of identical sectors, only one sector of the whole bearing is sufficient for the model development as depicted in Figure 3-2. Detailed parameters of the bearing are listed in Table 3-1. Properties of the lubricants used in the bearing simulation is given in Table 3-2.

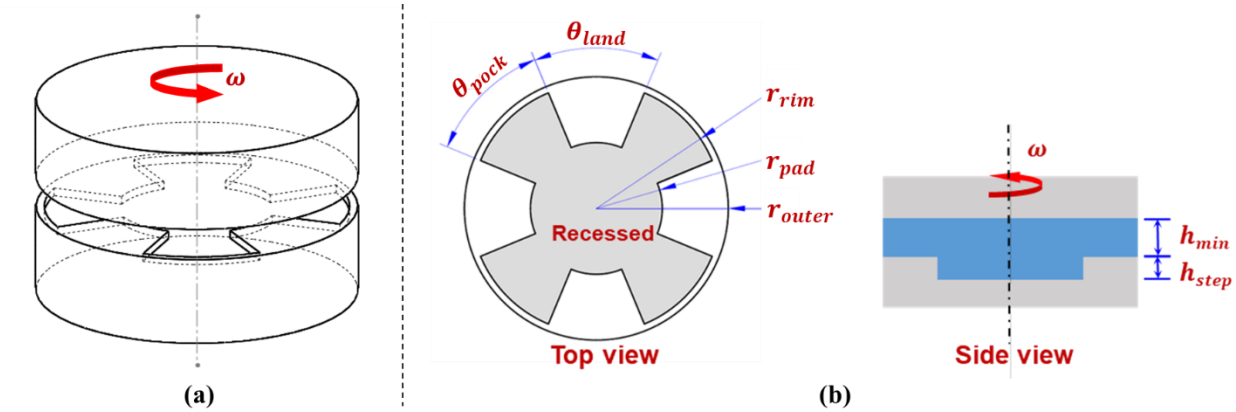

Figure 3-1. (a) Parallel thrust bearing consisting of an evenly recessed pocket pattern on the stator and flat rotor. (b) Shape and pocket parameters.

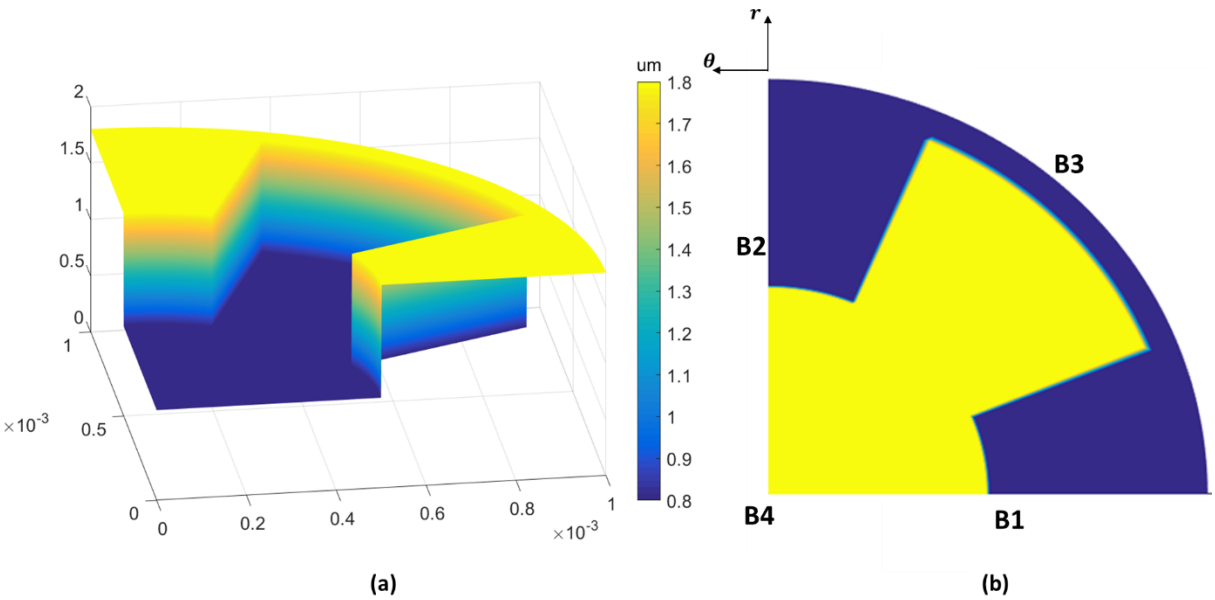

Figure 3-2. Geometry of the bearing showing one sector. (a) 3D view. (b) 2D view showing the boundaries of the one sector domain.

Table 3-1: Parameters of the pocketed bearing varied in the research

Graphic & Operational Parameters	Symbols	Range
Bearing radius	r_{out}	0.1 mm, 1 mm, 10 mm
Rim point radius	r_{rim}	0.095mm, 0.95 mm, 9.5 mm
Central circular region radius	r_{pad}	Depending on TE_r and r_{outer}
Angular width of un-recessed pad region	θ_{land}	$\frac{9\pi}{20}$ to $\frac{\pi}{20}$
Angular width of recessed pocket region	θ_{pock}	$\frac{\pi}{20}$ to $\frac{9\pi}{20}$
Pocket extent in radial direction	TE_r	20% to 80%
Pocket extent in circumferential direction	TE_θ	10% to 90%
Minimum film thickness	h_{min}	-
Pocket depth/ Step height	h_{step}	-
Rotational Speed	ω	733-1571 $rad \cdot s^{-1}$
Lubricant Temperature Outside the Bearing	$Temp_o$	25℃

N. B.

The pocket extents in radial and circumferential directions are the most important parameters of the investigated bearing, the definitions of the two parameters are given below:

$$TE_r = \frac{length\ of\ the\ step}{bearing\ radius} = \frac{r_{rim} - r_{pad}}{r_{out}}$$

$$TE_\theta = \frac{angular\ width\ of\ the\ pocket}{angular\ width\ modelled\ bearing\ region} = \frac{\theta_{pock}}{\theta_{pock} + \theta_{land}}$$

Table 3-2: Properties of the lubricant in the simulation

Lubricant Properties	Symbols	Value
Lubricant Name	–	Hexadecane
Lubricant Density	ρ	0.77 $g \cdot cm^{-3}$
Dynamic viscosity at 25 ℃	η_{25}	3.02 cP
Dynamic viscosity at 30 ℃	η_{30}	2.38 cP
Dynamic viscosity at 40 ℃	η_{40}	1.92 cP
Specific heat	c_p	2000.7 $J \cdot (kg \cdot K)^{-1}$

3.3 Reynolds Equation in Cylindrical Polar Coordinates and Fluid Mechanics of the Modelled Thrust Bearing

The performance of the pocketed parallel thrust bearing is analysed by solving the steady and isothermal Reynolds equation in its normalized form with $p-\theta$ Elrod-Adams mass-conserving cavitation model, which can be written in cylindrical polar coordinates in its dimensionless form as:

$$\frac{\partial}{\partial \bar{r}}\left(\frac{\bar{r}\,\bar{\rho}\,H^3}{12\bar{\eta}}\frac{\partial P}{\partial \bar{r}}\right)+\frac{1}{\bar{r}}\frac{\partial}{\partial \theta}\left(\frac{\bar{\rho}\,H^3}{12\bar{\eta}}\frac{\partial P}{\partial \theta}\right)=\frac{1}{2}\frac{\partial}{\partial \theta}\left(\bar{\rho}\,S\,\bar{\omega}\,\bar{r}\,H\right) \tag{3-1}$$

with complementary conditions for cavitation:

$$\begin{cases} S=1 \ \text{ and } \ P>P_{cav}\,, & \text{(pressure active zone)} \\ 0\le S<1 \ \text{ and } \ P=P_{cav}\,, & \text{(cavitation zone)} \end{cases} \tag{3-2}$$

In the above equations, $\bar{r}$ and θ are the radial and circumferential coordinates, $\bar{\eta}$ and $\bar{\rho}$ the respective dynamic viscosity and density of the lubricant, $H(\bar{r}\,,\theta)$ the lubricant film thickness, $\bar{\omega}$ the rotational speed of the upper running surface, $P(\bar{r}\,,\theta)$ the fluid pressure and $S(\bar{r}\,,\theta)$ the film fraction associated with cavitation. According to the bearing configuration illustrate in Figure 3-2b, the lubricant film thickness can be expressed as:

$$H(\bar{r}\,,\theta)=\begin{cases} H_{min}\,, & \text{(outside the pocket)} \\ H_{min}+H_{step}\,, & \text{(inside the pocket)} \end{cases}, \tag{3-3}$$

where H_{min} is the minimum oil film thickness and H_{step} is the pocket depth. It is important to remark that all variables in the above equations are normalized according to the main bearing parameters (see nomenclature list). The detailed derivation of Eq. (3-1) from Navier-Stokes and mass conservation equations, the normalization process of the bearing model and the mass flow rates in circumferential direction and radial direction within the modelled bearing are summarized in the following sections.

N.B.

Several assumptions are made in the micro thrust bearing model developed in this research. Brief descriptions and explanations of these assumptions are given as follows.

- *The lubricant is Newtonian in the model*

The liquid used in the current model is n-hexadecane, the shear rate at which obvious shear thinning occurs is around $1 \times 10^9\ s^{-1}$. The maximum shear rate (reached when rotational speed is 1500 $rad \cdot s^{-1}$) studied with the presented micro thrust bearing model is below $3 \times 10^7\ s^{-1}$ which is far below the hexadecane shear thinning point. This assumption is also valid for various liquids. However, this assumption is not valid when studying polymeric or high molecular weight liquids [152].

- *The viscosity and density of the lubricant is constant with pressure*

The practical applied load on the micro thrust bearing is very low (below 0.1 N) so the contact pressure within the thrust bearing is low as well (below 5 MPa). Therefore, the effect of pressure on the variation of liquid viscosity and density is almost negligible under such a low contact pressure condition.

- *Bearing surface deformation is negligible in this model*
- *Inertia forces including centrifugal force are negligible in this model*

This assumption is adopted initially because the size of the micro bearing is small, the radius of the bearing is 1 mm. However, this assumption can be dubious when the rotational speed is very high. The effects of centrifugal force are considered but not fully investigated in this research, and it is worthy investigating in the future.

- *The bearing operates in steady state*
- *No slip occurs at the bearing surface-lubricant interfaces*

This assumption is dubious, but the effects of slip is not studied in the current research.

- *Thermal effects are not considered initially*

An isothermal model is developed initially to investigate the micro thrust bearing performance. A simple thermal model is integrated into the initially developed isothermal model by adding a thermal balance loop later in this research (presented in Chapter 4). Thermal effects on the micro thrust bearing performance is discussed by comparing the results from the thermal and isothermal models (presented in Chapter 4).

3.3.1 Derivation of the Mass Flow Rates in Circumferential and Radial Directions

The performance of the pocketed parallel bearing under hydrodynamic lubrication conditions is analyzed by obtaining the pressure and fluid film fraction fields between the surfaces. The

model is developed using finite volume method (a unitary control volume cell with surrounding cells is demonstrated in figure 3-4 (a) in page 54). The model is therefore based on the mass conservation of each control volume and the mass flux passing each boundary needs to be derived.

The mass flux in radial and circumferential directions are obtained from simplified Navier-Stokes equations (Equ (3-4). and Equ (3-5).) for a steady state isothermal incompressible fluid. Fluid compressibility and thermal effects are neglected as the applied load for the thrust bearing is low (below 0.1 N). The momentum in the z direction (axial direction) is not considered as there is no movement or flow applied in this direction.

Radial direction momentum equation

$$\rho\left(u_r\frac{\partial u_r}{\partial r}+\frac{u_\theta}{r}\frac{\partial u_r}{\partial \theta}-\frac{u_\theta u_\theta}{r}\right)=-\frac{\partial p}{\partial r}+\eta\left(-\frac{u_r}{r^2}-\frac{2}{r^2}\frac{\partial u_\theta}{\partial \theta}+\frac{\partial^2 u_r}{\partial z^2}\right) \tag{3-4}$$

Circumferential direction momentum equation

$$\rho\left(u_r\frac{\partial u_\theta}{\partial r}+\frac{u_\theta}{r}\frac{\partial u_\theta}{\partial \theta}+\frac{u_\theta u_r}{r}\right)=-\frac{1}{r}\frac{\partial p}{\partial \theta}+\eta\left(-\frac{u_\theta}{r^2}+\frac{2}{r^2}\frac{\partial u_r}{\partial \theta}+\frac{\partial^2 u_\theta}{\partial z^2}\right) \tag{3-5}$$

Time dependent terms and terms including velocity in axial direction can be ignored as the pocketed thrust bearings operate in steady state and the properties of the lubricant are constant across the film thickness.

The N-S equations can be further simplified by making the flowing assumptions: i) Inertia forces including centrifugal force are negligible compared to viscous force of the thrust bearings studied in this contribution; ii) Thin film assumptions hold, *i.e.* velocity gradients in film thickness direction are much larger than velocity gradients in radial and circumferential directions; iii) The liquid within the bearing is in equilibrium state.

Radial direction:

$$\frac{\partial^2 u_r}{\partial z^2}=\frac{1}{\eta}\frac{\partial p}{\partial r} \tag{3-6}$$

Circumferential direction:

$$\frac{\partial^2 u_\theta}{\partial z^2}=\frac{1}{\eta r}\frac{\partial p}{\partial \theta} \tag{3-7}$$

Mass flow rates in radial and circumferential directions can be derived from Equ (3-6). and Equ (3-7).

Mass flow rates in radial and circumferential directions are given as follows:

$$\dot{m}_\theta = -\frac{\rho h^3}{12\eta r}\frac{\partial p}{\partial \theta} + \frac{1}{2}\rho\omega r h \tag{3-8}$$

$$\dot{m}_r = -\frac{\rho h^3}{12\eta}\frac{\partial p}{\partial r} \tag{3-9}$$

3.3.2 Cavitation Treatment and Mass-Conservation Guarantee of the Model

Cavitation may occur in the pocketed region especially when the pocket depth is high. Mass conservation must be guaranteed in the whole simulated domain and is achieved by incorporating Jakobsson-Floberg-Olsson (JFO) boundary conditions. [141-143] which are applied using a modified Elrod-Adams algorithm proposed by Ausas. [144]

A variable *S*, defined as the ratio between local density and the density at the boundary of film rupture (where cavitation just occurs), is introduced to account for the cavitation and guarantee mass conservation.

$$S = \frac{\rho_l}{\rho_c} \tag{3-10}$$

In the pressure active region, no cavitation exists, so that *S* is constant and equal to one. In this region as the liquid is incompressible (liquid density stays unchanged and equals to the density value ρ_c at the location where cavitation just occurs) whereas pressure varies above cavitation pressure. In the cavitation region, pressure drops to a certain value then cavity occurs and results in a reduction of equivalent density of the liquid (as bubbles are mixed with liquid in this region), and *S* varies between zero and one. Pressure is constant in the cavitation region and is equal to cavitation pressure. We set the cavitation pressure to equal the vapour pressure of the lubricant as the cavitation is assumed to occur when the liquid pressure drops to the vapour pressure so that the vapour phase of the lubricant exists and forms cavities in the liquid.

After incorporating JFO cavitation boundary conditions, the modified mass flow rates in circumferential and radial directions are given by:

$$\dot{m}_\theta = -\frac{\rho_c h^3}{12\eta r}\frac{\partial p}{\partial \theta} + \frac{1}{2}\rho_c S\omega r h \tag{3-11}$$

$$\dot{m}_r = -\frac{\rho_c h^3}{12\eta}\frac{\partial p}{\partial r} \tag{3-12}$$

In the pressurized region

$$\begin{cases} S = 1 & | \ \rho_l = \rho_c \\ p = active\ pressure\ value \end{cases}$$

In the cavitation region

$$\begin{cases} S = \frac{\rho_l}{\rho_c} \ | \ \rho_l < \rho_c \\ p = p_{cav} \end{cases}$$

The variable *S* should also be integrated into the Poiseuille terms of the mass flow rates. However, when the pressure gradient is nonzero, *S* must be equal to one, and when *S* varies between zero and one, the pressure gradient must equal to zero as it is in the cavitation region. Therefore, S can be omitted from the Poiseuille terms. [144]

3.3.3 Nondimensionalization of the Parameters in the Model

Nondimensionalization is conducted for all the parameters involved in the model using the following equations:

- **Normalized Radius: $\bar{r}$**

$$\bar{r} = \frac{r}{r_{outer}}$$

- **Normalized Film thickness: H**

$$H = \frac{h}{h_{min}}$$

- **Normalized Rotational speed: ω**

$$\bar{\omega} = \frac{\omega}{\omega}$$

- **Normalized Dynamic viscosity: $\bar{\eta}$**

$$\bar{\eta} = \frac{\eta}{\eta}$$

- **Normalized Hydrodynamic Pressure: P**

$P = \frac{p}{p_{ref}}$, where $p_{ref} = \frac{\eta \omega {r_{outer}}^2}{{h_{min}}^2}$

- **Normalized Liquid Density: $\bar{\rho}$**

$\bar{\rho} = \frac{\rho}{\rho_{ref}}$, where $\rho_{ref} = \frac{\eta}{\omega {h_{min}}^2}$

3.4 Boundary Conditions

As illustrated in Figure 3-2 (b), four boundaries are defined in the one sector bearing domain: (**B1**) leading edge of the modelled sector; (**B2**) trailing edge of the modelled sector; (**B3**) outer radius edge of the bearing; and (**B4**) central point of the bearing. Applying proper boundary conditions, which correctly represent the actual physical conditions at the four boundaries, is crucial to improve the accuracy of fluid pressure and film fraction predictions. In this sense, the following set of boundary conditions was applied at the four boundaries of the one sector domain:

Boundary Conditions on B1 & B2

As the shape of the pocketed bearing is rotationally symmetric, the pressure distribution should be periodic in the circumferential direction, *i.e.* pressure and film fraction distribution should be the same for any sector of the bearing. Therefore, periodic boundary conditions should be applied at the leading and trailing edges of the modelled sector.

$$P\,|_{\boldsymbol{B1}} = P\,|_{\boldsymbol{B2}} \quad \text{and} \quad \nabla P\,|_{\boldsymbol{B1}} = \nabla P\,|_{\boldsymbol{B2}} \tag{3-13}$$

Boundary Conditions on B3

Lubricant is supplied into the bearing through the outer radius edge of the bearing with a certain supply pressure. Therefore, the boundary condition at this boundary is:

$$P\,|_{\boldsymbol{B3}} = P_{\,supply} \tag{3-14}$$

Boundary Conditions on B4

Boundary B4 is special as physically it is the central point of the bearing. This type of boundary is rarely discussed, since for most thrust bearings there is a circular hole in the center which is open to the outside environment so the pressure in the inner boundary is set to a certain value. However, the boundary condition for the thrust bearings in this research is special as there is no hole located in the central region, which indicates that this region is enclosed and only the outer radius edge of the bearing is open to the surrounding environment.

In order to take into account this peculiar characteristic of the bearing, the radius at B4 was set to a small positive value $R_c = 5 \times 10^{-8}$ m rather than zero to avoid the singularity problem

resulting from a zero-radius value of the central point. This tiny circle is assumed to be isolated in the central region so that the Couette flow can be neglected at this boundary and the bearing operates hydrodynamically in steady state regime. The value of the radius of this artificially placed tiny central circle has been varied and examined during the model development. It shows that the bearing pressure distribution and film distribution results generated by the model would barely vary with the radius of the tiny circle in the centre if the radius value reaches a sufficiently small value. Therefore, bearing performance parameters including load carrying capacity, frictional torque and friction coefficient, etc. would also reach the stable and converged values when sufficiently small radius is taken for the tiny circle in centre (which is B4).Under these conditions no pressure variation occurs inside the circle and no mass flow should be passing in or out of the circle in radial direction. Mathematically, this is equivalent to the condition that the radial pressure gradient along boundary B4 should be zero:

$$\frac{\partial P}{\partial \bar{r}} \mid_{\boldsymbol{B4}} = 0 \tag{3-15}$$

Figure 3-3 below demonstrates the pressure distribution contours of a thrust bearing from the model under same operational conditions, the radius of the tiny circle in the centre are set with different values. It can be seen that the pressure distribution barely changes when the radius of the tiny circle is smaller than 5×10^{-6} m.

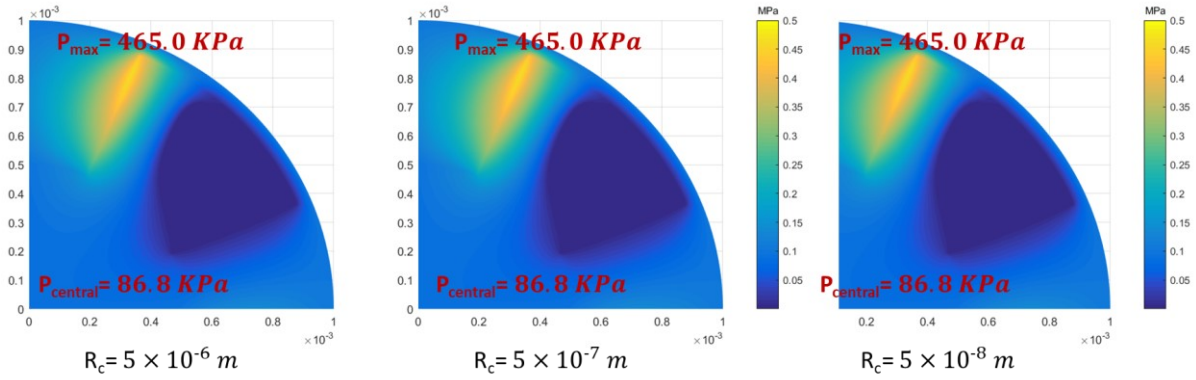

Figure 3-3. Effects of the radius of the artificially placed tiny circle in the centre on the simulation results from the developed model.

3.5 Bearing Performance Parameters

The normalized pressure field, $P(\bar{r}, \theta)$, and the film fraction field, $S(\bar{r}, \theta)$ can be computed from the model and transferred to the original pressure field, $p(r, \theta)$ and film fraction field, $S(r, \theta)$. The bearing performance parameters can then be computed using the following equations.

Load Carrying Capacity

The load carrying capacity (*LCC*) is defined as the net lift hydrodynamic force due to the fluid pressure minus the atmospheric force acting on the pad:

$$LCC = N \cdot \left[\iint p(r,\theta) \cdot r d\theta dr - p_{atm} \cdot A_{pad}\right] \tag{3-16}$$

where, p_{atm} the atmospheric pressure, A_{pad} the area of the thrust bearing and *N* the number of the sectors of the bearing.

Frictional Torque

The frictional torque is defined by integrating the lubricant shear stress over the pad domain. Accordingly,

$$T = N \cdot \left\{ \underbrace{\iint \left(\eta \frac{\omega r}{h} \mathrm{S}\right) r^2 d\theta dr}_{\text{Couette Flow}} + \underbrace{\frac{1}{2} \iint \left(\frac{h}{r}\frac{dp}{d\theta}\right) r^2 d\theta dr}_{\text{Poiseuille Flow}} \right\} \tag{3-17}$$

Note that the film fraction S is included in the calculation of shear stress in the Couette flow term since the gap between the surfaces is not completely filled with liquid lubricant when cavitation occurs (mixture of liquid lubricant and gas/vapour phase).

Friction Coefficient

The friction coefficient, which represents the frictional efficiency of the bearing as a normalized parameter is defined as the ratio between the normalized torque and the normalized hydrodynamic force in rotating systems:

$$\mu = \frac{\bar{T}}{\bar{W}} = \frac{T}{W \cdot r_{out}} \tag{3-18}$$

Where $\bar{T}$ is the normalized frictional torque and $\bar{W}$ is the normalized hydrodynamic force.

3.6 Numerical Solution Setups

3.6.1 Finite Volume Discretization of the Reynolds Equation

The Reynolds equation in cylindrical polar coordinates (Eq. (3-1)) is solved numerically using the finite volume method (FVM), which ensures conservation of mass flow rate in each control volume. Therefore, the net mass flow rate through the boundaries of every control volume equals zero (see Figure 3-4 (b)). Mathematically,

$$\dot{M}_{\theta_{in}} + \dot{M}_{r_{in}} - \dot{M}_{\theta_{out}} - \dot{M}_{r_{out}} = 0 \tag{3-19}$$

where $\dot{M}_r$ and $\dot{M}_\theta$ are the normalized mass flow rates in the radial and circumferential directions, respectively:

$$\dot{M}_\theta = -\frac{\bar{\rho}H^3}{12\bar{\eta}\bar{r}}\frac{\partial P}{\partial \theta} + \frac{1}{2}\bar{\rho}S\bar{\omega}\bar{r}H \tag{3-20}$$

$$\dot{M}_r = -\frac{\bar{\rho}H^3}{12\bar{\eta}}\frac{\partial P}{\partial \bar{r}} \tag{3-21}$$

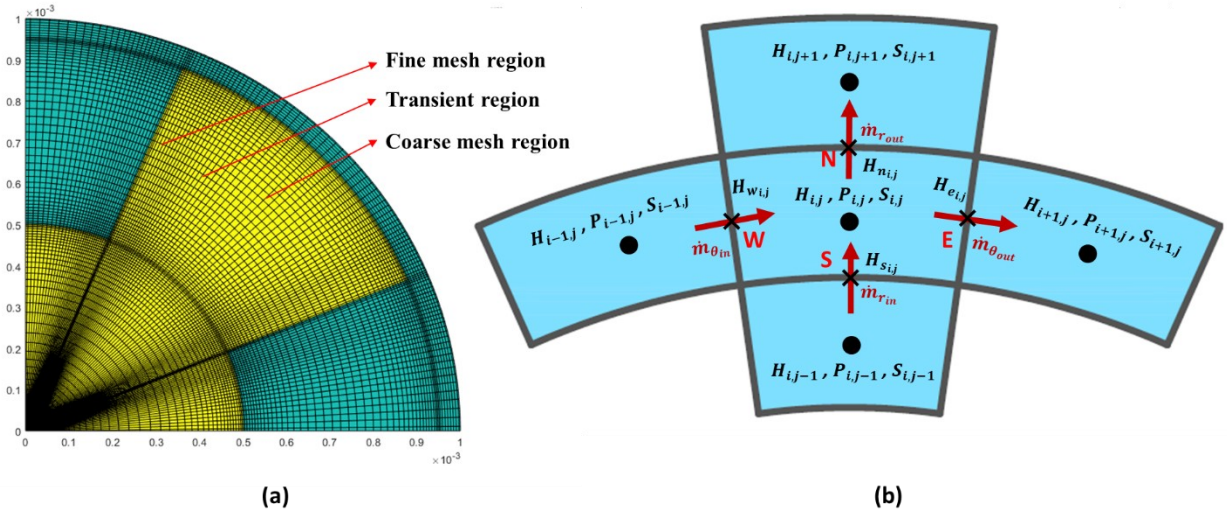

Figure 3-4. (a) Meshed pocketed bearing illustrating the fine, coarse and transient mesh regions; (b). Variables defined for each control volume.

Variables and Parameters of a Single Control Volume

As shown in Figure 3-4 (b), a control volume consists of four boundaries and a nodal point which is located at the centre of the cell. Pressure ($P_{i,j}$), film fraction ($S_{i,j}$) and film thickness ($H_{i,j}$) are defined in the central nodal point of the control volume. Film thickness is also

required to be defined at the boundaries of the cell ($H_{w_{i,j}}, H_{e_{i,j}}, H_{s_{i,j}}, H_{n_{i,j}}$) as it is necessary to compute the inward and outward mass flows through the control volume boundaries. The film thickness values at the boundaries are calculated by linear approximations of the film thickness from the two neighbouring central nodal points. For instance, the east side boundary film thickness ($H_{e_{i,j}}$) is computed as follows:

$$H_{e_{i,j}} = \frac{\theta_{e_{i,j}} - \theta_{i,j}}{\theta_{i+1,j} - \theta_{i,j}} H_{i+1,j} + \frac{\theta_{i+1,j} - \theta_{e_{i,j}}}{\theta_{i+1,j} - \theta_{i,j}} H_{i,j} \tag{3-22}$$

A similar process is used to compute the film thickness values and other variables at the other boundaries. This setup approximates the film discontinuity as a very steep slope. (when the mesh is fine enough, this approximation can be ignored)

Mass Flow Rates in Discrete Form

After discretization, the mass flow rates passing through the boundaries of a given control volume can be obtained by substituting the discrete variables into Eq. (3-23) to Eq. (3-26). Accordingly,

$$\dot{M}_{\theta_{in}} = \dot{M}_w = \bar{\rho}\left[-\frac{{H_{w_{i,j}}}^3}{12\bar{\eta}\bar{r}_{i,j}}\left(\frac{P_{i,j}-P_{i-1,j}}{\theta_{i,j}-\theta_{i-1,j}}\right) + \frac{(\bar{\omega})}{2}\bar{r}_{i-1,j}H_{w_{i,j}}S_{i-1,j}\right]\cdot\left(\bar{r}_{n_{i,j}} - \bar{r}_{s_{i,j}}\right) \tag{3-23}$$

$$\dot{M}_{\theta_{out}} = \dot{M}_e = \bar{\rho}\left[-\frac{{H_{e_{i,j}}}^3}{12\bar{\eta}\bar{r}_{i,j}}\left(\frac{P_{i+1,j}-P_{i,j}}{\theta_{i+1,j}-\theta_{i,j}}\right) + \frac{(\bar{\omega})}{2}\bar{r}_{i,j}H_{e_{i,j}}S_{i,j}\right]\cdot\left(\bar{r}_{n_{i,j}} - \bar{r}_{s_{i,j}}\right) \tag{3-24}$$

$$\dot{M}_{r_{in}} = \dot{M}_s = \bar{\rho}\left[-\frac{{H_{s_{i,j}}}^3}{12\bar{\eta}}\left(\frac{P_{i,j}-P_{i,j-1}}{R_{i,j}-R_{i,j-1}}\right)\right]\cdot\bar{r}_{s_{i,j}}\left(\theta_{e_{i,j}} - \theta_{w_{i,j}}\right) \tag{3-25}$$

$$\dot{M}_{r_{out}} = \dot{M}_n = \bar{\rho}\left[-\frac{{H_{n_{i,j}}}^3}{12\bar{\eta}}\left(\frac{P_{i,j+1}-P_{i,j}}{R_{i,j+1}-R_{i,j}}\right)\right]\cdot\bar{r}_{n_{i,j}}\left(\theta_{e_{i,j}} - \theta_{w_{i,j}}\right) \tag{3-26}$$

In the above equations, the pressure gradient in the Poiseuille terms are computed using central differencing approximation. The Couette mass flow passing through the boundaries of the cells are using the values from upstream nodal points (up-wind scheme). Finally, by substituting Eq. (3-23) to Eq. (3-26) into Eq. (3-19), the discrete form of the Reynolds equation for each control volume can be written in the compact form as:

$$a_{i,j}P_{i,j} + \sum_{nb}(a_{nb}P_{nb}) = b_{i,j}\Theta_{i,j} + \sum_{nb}(b_{nb}\Theta_{nb}) + B_{i,j} \tag{3-27}$$

where the subscript '*nb*' denotes the neighbour cells around the control volume (i,j).

3.6.2 Mesh Setup and Film Discontinuities

The simulated domain is divided into numbers of control volume cells and an unequal mesh setup is adopted to achieve a good compromise between computation accuracy and speed. As demonstrated in Figure 3-4 (b), the mesh is generated by placing grid lines, which are the boundary faces of the control volumes, in radial and circumferential directions. An important issue is that there must be grid lines corresponding to the film discontinuities and boundaries of the whole simulated region. The simulated domain is divided into three types of meshed regions according to the interval value of the control volumes in radial and circumferential directions: fine mesh region, coarse mesh region and mesh size transition region. The fine mesh is implemented in the area around the film discontinuities as abrupt pressure variation might occur. Coarse mesh is implemented in regions far from the film discontinuities to reduce computation time. The mesh interval within each fine or coarse mesh region is uniform. [152, 153] Computation inaccuracy or even computation error might occur if the coarse and fine regions are linked directly. Therefore, transition regions where the control volume size gradually varies are implemented between fine mesh regions and coarse mesh regions. The unequal mesh set up of the simulated region can be viewed clearly in Figure 3-4 (a).

3.6.3 Iterative Solution of the Discrete Reynolds Equation

The discrete form of governing equation (Eq. (3-27)) corresponds to a linear system of equations that can be solved for both pressure ($P_{i,j}$) and film fraction ($S_{i,j}$) using the complementary conditions for cavitation. In the cavitation regions, the film fraction can be computed using the discrete equation with the pressure being set to P_{cav}. In the active region, the pressure value can be computed using the same discrete equation with the film fraction being set to one. A Gauss-Seidel iterative process with successive relaxation (SOR) is used to obtain the converged solution for the pressure and film fraction for all nodal points [151]. Accordingly, the values of pressure and film fraction for the nodal point (i,j) in the k-th SOR iteration are computed as:

$$P_{i,j}{}^{k} = \omega_p \cdot P_{i,j}{}^{k} + \left(1 - \omega_p\right) \cdot P_{i,j}{}^{k-1} \tag{3-28}$$

$$S_{i,j}{}^{k} = \omega_s \cdot S_{i,j}{}^{k} + (1 - \omega_s) \cdot S_{i,j}{}^{k-1} \tag{3-29}$$

The convergence of the solver is checked by considering the local error criterion:

$$\varepsilon_{conv} = \max\left(\frac{|{P_{i,j}}^{k} - {P_{i,j}}^{k-1}|}{|{P_{i,j}}^{k}|}, \frac{|{S_{i,j}}^{k} - {S_{i,j}}^{k-1}|}{|{S_{i,j}}^{k}|}\right) < \varepsilon_{tol} \mid (i \in [1, NT], j \in [1, NR]) \qquad (3\text{-}30)$$

Further details about the algorithm used for the pressure-film fraction solver can be found in Refs. [127,144,151]

The algorithm of the developed model is demonstrated in figure 3-5 and the algorithm of the pressure and film fraction fields solver are shown in figure 3-6.

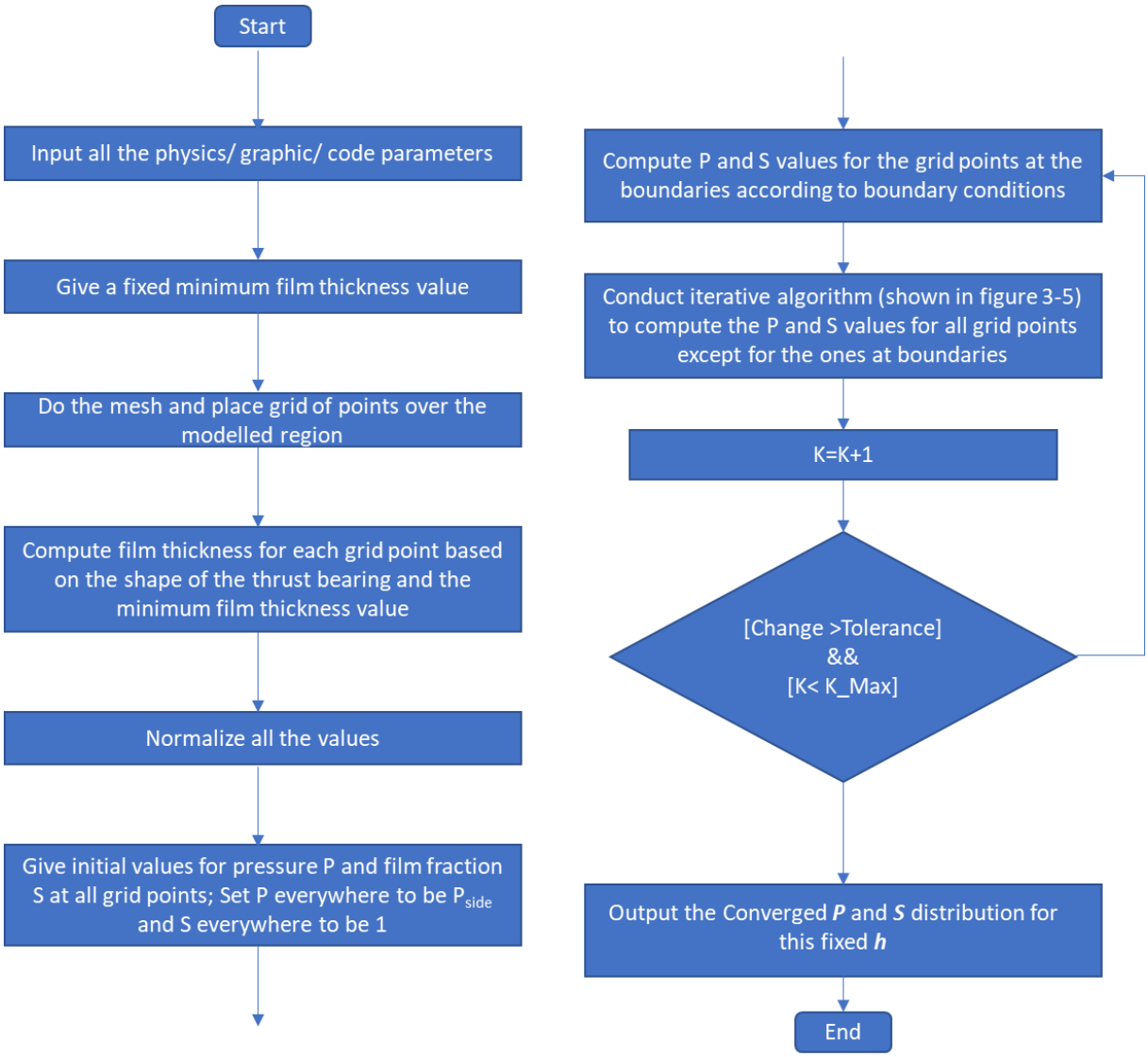

Figure 3-5. Algorithm of the FVM bearing model

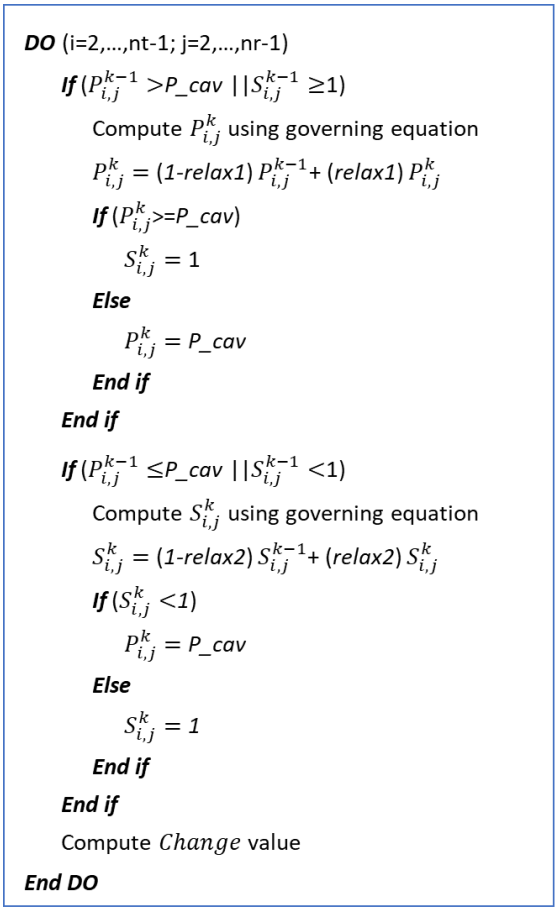

Figure 3-6. Algorithm of the pressure and film fraction fields solver

3.7 Model Validation

The model is validated by reproducing the pressure distribution results of a pivoted thrust bearing with plain contact surface and textured surfaces which are generated by published CFD models.

The results produced from model developed in this research agree well with those generated by CFD codes which were published previously. The film profile of the pivot bearing with plain surfaces and the pressure distributions from the previous publication and current contribution are displayed in figure 3-7. The film profile of the pivot bearing with textured surfaces and the pressure distributions from the previous publication and current contribution are displayed in figure 3-8. Detailed parameters of the validation case are given in table 3-3. [153,154]

Table 3-3. Detailed parameters of the pivot bearing used in validation [153,154]

Graphic & Operational Parameters	Value	Graphic & Operational Parameters	Value
Angular width of single pad: θ_{pad}	$\frac{5\pi}{18}$	Pivot pitch angel: α_r	$0.4\ rad$
Outer pad radius: R_o	$114.3\ mm$	Pivot roll angel: α_θ	$-0.185\ rad$
Inner pad radius: R_i	$57.15\ mm$	Texture extent in circumferential direction: TE_θ	70%
Pivot position coordinates: (θ_p, R_p)	$(\frac{5\pi}{18}, 85.725\ mm)$	Texture extent in radial direction: TE_r	70%
Rotational speed: ω	$314.16\ rad \cdot s^{-1}$	Texture density in circumferential direction: TE_θ	63.25%
Lubricant density: ρ	$855\ Kg \cdot m^{-3}$	Texture density in radial direction: TD_r	63.25%
Viscosity at 40°C: ν_{40}	42.65 cSt	Texture depth: H_t	$15\ \mu m$
Viscosity at 100°C: ν_{100}	6.50 cSt	Is pocket at bearing inlet open?	Yes
Lubricant temperature set in study: T	70°C		
Film Thickness at pivot point: H_p	$50\ \mu m$		

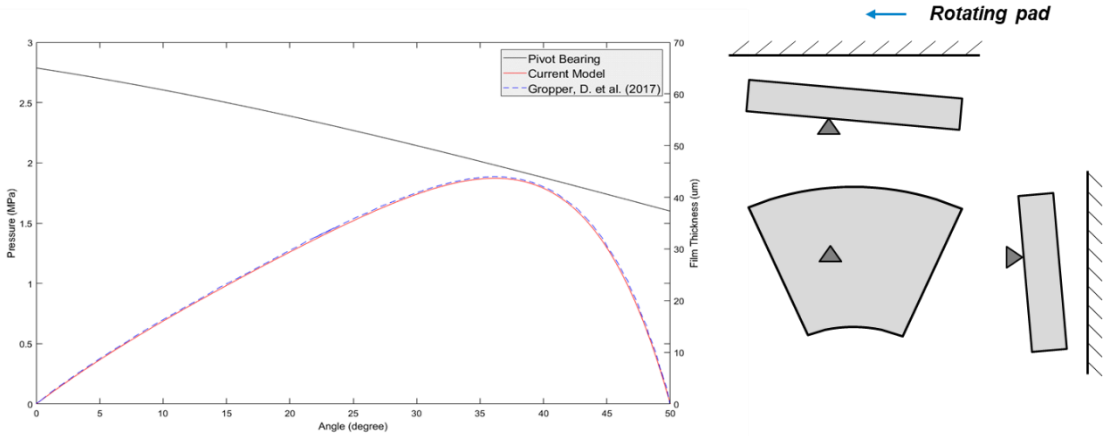

Figure 3-7. Validation 1: reproduce circumferential direction pressure distribution of the pivoted bearing with plain surface (at r = 85.725 mm, i.e. midradius) [153,154]

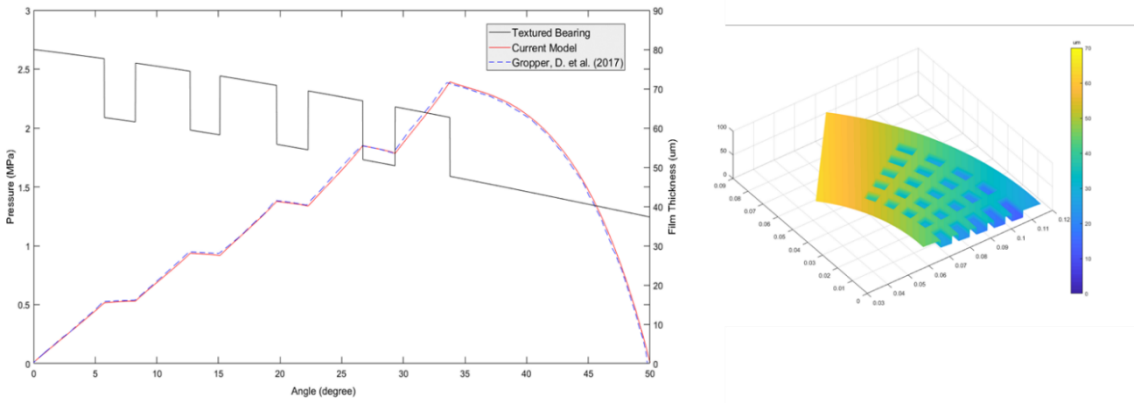

Figure 3-8. Validation 2: reproduce circumferential direction pressure distribution of the pivoted bearing with textured surface (at r = 85.725 mm, i.e. midradius) [153,154]

Chapter 4: Simulation Results of the Micro Pocketed Parallel Thrust Bearing

In this chapter, effects from factors including bearing size, bearing designs and bearing operation conditions on the performance of the micro pocketed parallel thrust bearings are investigated by using the mass-conservation considered FVM model. The simulation results are classified and reported in this chapter.

First, the effect of scaling is considered with geometries varied from metre/centimetre down to millimetre/micrometre in order to understand differences in lubrication mechanism between macro-scale bearings and those in micro-electro-mechanical systems (MEMS) devices. Then, effects of operation conditions including the minimum film thickness and the rotational speed on the micro pocketed parallel thrust bearing performance are systematically studied. Optimization work is conducted by varying the geometric parameters of the sector pockets to achieve high load capacity and low friction coefficient.

The simulated results show that cavitation would occur in the micro pocketed parallel thrust bearings and affects the bearing pressure distribution and film thickness distribution significantly. Simulated results indicate that the performance of this type of bearing is dependent on the interplay between the magnitude of the load support in the high-pressure region and the size of the negative pressure cavitated region.

4.1 Overview of the Simulation Results

Various sets of simulations have been conducted to systematically investigate the lubrication behaviours of a pocketed parallel thrust bearing and its performance (including load carrying capacity, frictional torque, friction coefficient, etc.) as a function of different parameters. Results showing how the bearing can be optimised under different conditions have also been obtained.

Figure 4-1 shows how the simulation results are divided into three sections. The first set of results shows how the performances of bearings with the same pocket pattern vary with overall

bearing size. The second set shows how the performance of a relatively small scale (1mm-radius) bearing is affected by operational conditions and pocket shape. The third set shows how the optimum design of the bearing performs under different operating conditions.

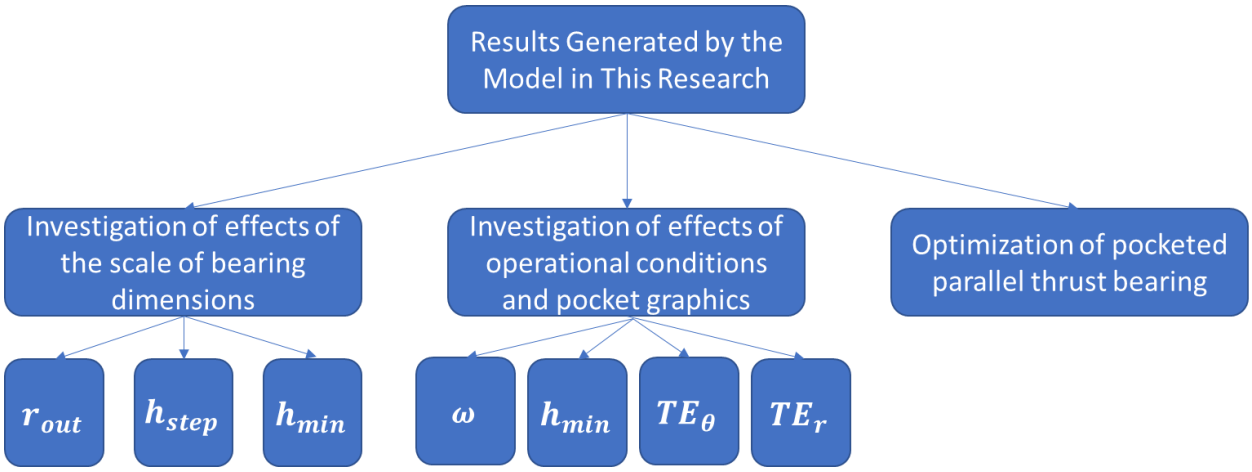

Figure 4-1. Classification of the results in this chapter

To show the results clearly, graphic shape of the simulated micro pocketed parallel thrust bearing which would also be fabricated and tested in this research is shown in Figure 4-2. Detailed graphic parameters of the bearing which are varied in the simulation investigation are given in Table 4-1 below. Properties of the lubricant used in the simulation (hexadecane) is shown in Table 4-2 below.

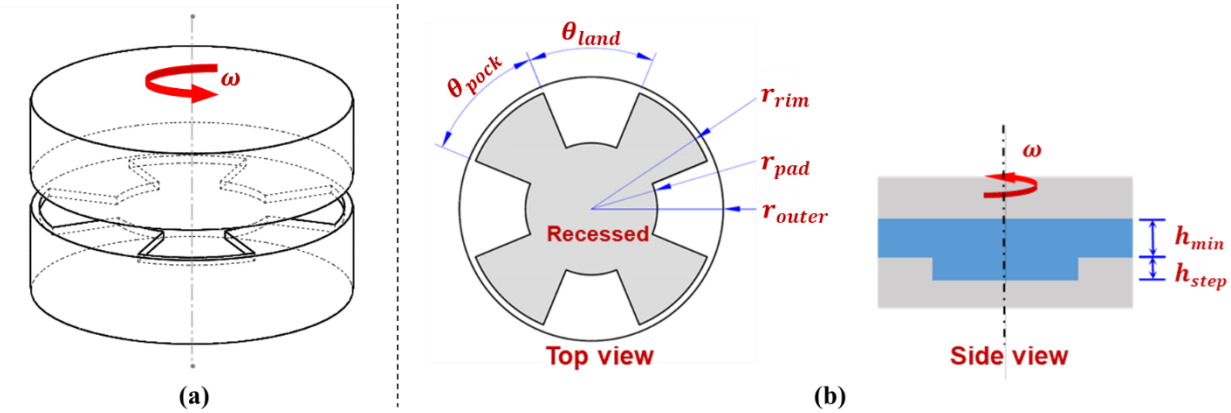

Figure 4-2. Graphic shape of the simulated micro pocketed parallel thrust bearing

Table 4-1. Parameters of the pocketed bearing varied in the research

Graphic & Operational Parameters	Symbols	Range
Bearing radius	r_{out}	0.1 mm, 1 mm, 10 mm
Rim point radius	r_{rim}	0.095mm, 0.95 mm, 9.5 mm
Central circular region radius	r_{pad}	Depending on TE_r and r_{outer}
Angular width of un-recessed pad region	θ_{land}	$\frac{9\pi}{20}$ to $\frac{\pi}{20}$
Angular width of recessed pocket region	θ_{pock}	$\frac{\pi}{20}$ to $\frac{9\pi}{20}$
Pocket extent in radial direction	TE_r	20% to 80%
Pocket extent in circumferential direction	TE_θ	10% to 90%
Minimum film thickness	h_{min}	-
Pocket depth/ Step height	h_{step}	-
Rotational Speed	ω	733-1571 $rad \cdot s^{-1}$
Lubricant Temperature Outside the Bearing	$Temp_o$	25℃

N. B.

The definitions of two important graphic parameters of the bearing, pocket extent in radial and circumferential directions are given below:

$$TE_r = \frac{length\ of\ the\ step}{bearing\ radius} = \frac{r_{rim} - r_{pad}}{r_{out}}$$

$$TE_\theta = \frac{angular\ width\ of\ the\ pocket}{angular\ width\ modelled\ bearing\ region} = \frac{\theta_{pock}}{\theta_{pock} + \theta_{land}}$$

Table 4-2. Properties of the lubricant used in the simulation

Lubricant Properties	Symbols	Value
Lubricant Name	–	Hexadecane
Lubricant Density	ρ	0.77 $g \cdot cm^{-3}$
Dynamic viscosity at 25 ℃	η_{25}	3.02 cp
Dynamic viscosity at 30 ℃	η_{30}	2.38 cp
Dynamic viscosity at 40 ℃	η_{40}	1.92 cp
Specific heat	c_p	2000.7 $J \cdot (kg \cdot K)^{-1}$

4.2 Performance of Pocketed Parallel Thrust Bearing at Different Scales

Here we investigate the influence of bearing size scaling on the performance of a parallel thrust bearing with uniformly shaped pocket pattern (*i.e.* same *TR*% and *Tθ*% ratios). The bearing

outside diameter, pocket depth and minimum film thickness are scaled in different ways. The simulation cases in the scaling investigation can be divided into three groups. The characteristics of each group are described in the following sections, and the detailed information for each simulation case is summarized in Table 4-3.

Table 4-3. Parameters of simulation cases for scale effect investigation

Case No.	r_{out}/ mm	h_{min}/ um	h_{step}/ um	TE_θ	TE_r	$\omega/\ rad \cdot s^{-1}$
1	1	0.4	1	50%	50%	942.5
2	10	4	10	50%	50%	942.5
3	10	0.4	1	50%	50%	942.5
4	0.1	0.4	1	50%	50%	942.5
5	1	0.4	1	50%	50%	2827.4
6	10	4	10	50%	50%	2827.4
7	1	0.4	0.5	50%	50%	942.5
8	1	0.4	1.5	50%	50%	942.5
9	1	0.4	2	50%	50%	942.5

In addition to the performance parameters including max pressure p_{max}, generated hydrodynamic force W, friction coefficient μ and frictional torque T, special attention is also paid to the normalized performance parameters (normalized hydrodynamic force $\overline{W}$ and normalized frictional torque $\overline{T}$) to compare bearing performances at different scales properly.

$$\overline{W} = W \frac{1}{\eta\omega} \frac{\left(\frac{h_{min}}{r_{outer}}\right)^2}{{r_{outer}}^2} \tag{4-1}$$

$$\overline{T} = T \frac{1}{\eta\omega} \frac{\left(\frac{h_{min}}{r_{outer}}\right)}{{r_{outer}}^3} \tag{4-2}$$

$$P = p \frac{1}{\eta\omega} \left(\frac{h_{min}}{r_{outer}}\right)^2 \tag{4-3}$$

4.2.1. Scaling Bearing Radius, Depth of the Recessed Pocket Pattern and Minimum Film Thickness Simultaneously

The first set of comparisons (cases 1 and 2 in Appendix Table 2) shows what happens when the bearing radius, the pocket geometry and the minimum film thickness are all scaled by a factor of 10 whereas the pocket shape stays unchanged (same TE_θ% and TE_r%). As all bearing dimensions are scaled by the same ratio, the ratio between minimum film thickness and pocket

depth (δ) of the two bearings stays the same. Similarly, the ratio between minimum film thickness and bearing radius (γ) and the ratio between the pocket depth and the bearing radius (ε) of the two bearings remain unchanged.

According to the simulation results, the normalized hydrodynamic force values for the two bearings are equal (1.76×10^{-2}). The normalized frictional torque and friction coefficient of the two bearings also have the same value ($\bar{T}$: 1.04, μ: 3.56×10^{-2}). It can therefore be concluded that when all the bearing dimensions are scaled, and the key ratios of the geometric parameters (TE_θ%, TE_r%, γ, δ, ε) stay constant, the normalized bearing performance does not change. Also, the hydrodynamic force generated by the 1-mm-radius bearing is $\frac{1}{100}$ of the force generated by the 10-mm-radius bearing (0.331N to 33.1N) whereas the frictional torque of the 1-mm-radius bearing is $\frac{1}{1000}$ of that of the 10-mm-radius bearing (7.86 μNm to 7860 μNm). It can be further concluded from the simulation results together with equations (3-1) and (3-1) that when the dimensions of all the bearing geometric features are scaled up linearly, the load carrying capacity increases quadratically and the frictional torque increases cubically. Detailed performance values of the two bearings studied in this group can be found in Table 4-4.

Table 4-4. Performance of bearings in different dimension scales (all dimensions scaled in same ratio, ω = 942.5 $rad \cdot s^{-1}$)

Case No.	ω / $rad \cdot s^{-1}$	h_min/ μm	h_step/ μm	$\frac{h\_min}{h\_step}$ / (δ)	r_out/ mm	$\frac{h\_min}{r\_out}$ / (γ)	p_max/ KPa	p_central/ KPa	W_h/ N	W_a/ N	W_n/ N	LCC/ mN	$\overline{W\_h}$	$\overline{W\_n}$	T/ μNm	$\bar{T}$	f_coeff / (μ)
1	942.5	0.4	1	0.4	1	4.00E-04	662.93	67.47	3.31E-01	3.14E-01	1.73E-02	1.73E+01	1.76E-02	9.18E-04	7.86E+00	1.04E+00	0.0356
2	942.5	4	10	0.4	10	4.00E-04	662.93	67.47	3.31E+01	3.14E+01	1.73E+00	1.73E+03	1.76E-02	9.18E-04	7.86E+03	1.04E+00	0.0356

Variables	Meaning	Variables	Meaning
W_h	Hydrodynamic force	TE	Pocket extent in circumferential direction
W_a	Atmospheric force	RE	Pocket extent in radial direction
W_n	Net supporting force	$\overline{W\_h}$	Normalized hydrodynamic force
LCC	Load carrying capacity in unit of gram	$\overline{W\_n}$	Normalized net supporting force
T	Frictional torque	$\bar{T}$	Normalized frictional torque
f_coeff	Friction coefficient		

The pressure distribution and film thickness distribution of the two bearings in this comparison are uniform and can be found in Figure 4-3.

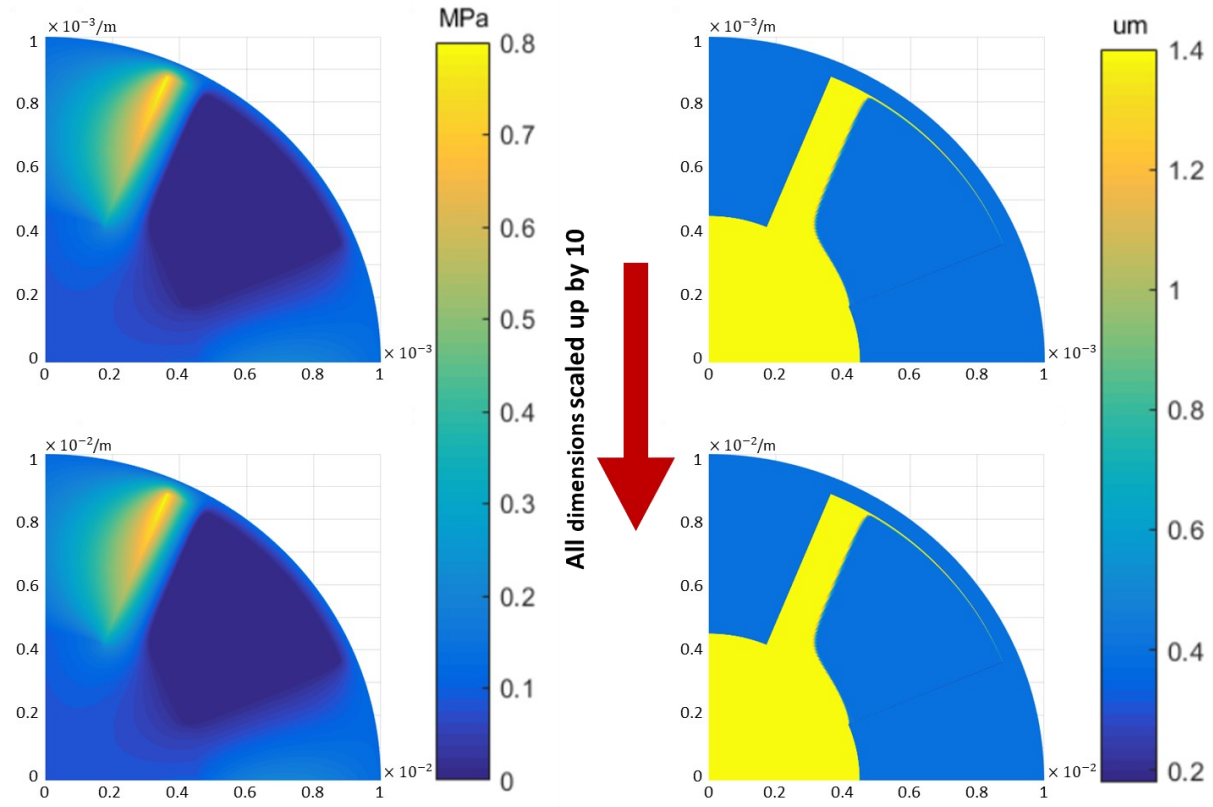

Figure 4-3. Pressure distribution and Film thickness distribution of the bearings in different size scales (all dimensions scaled in same ratio, ω=942.5 $rad \cdot s^{-1}$)

A comparison was also made between two bearings with the same geometry (cases 5 and 6) at higher rotational speed (2827.4 $rad \cdot s^{-1}$). Similar conclusions were obtained, as shown by the simulation results in Table 4-5 and Figure 4-4.

Table 4-5. Performance of bearings in different dimension scales (all dimensions scaled in same ratio, ω = 2827.4 $rad \cdot s^{-1}$)

Case No.	ω / $rad \cdot s^{-1}$	h_min/ μm	h_step/ μm	$\frac{h\_min}{h\_step}$ / (δ)	r_out/ mm	$\frac{h\_min}{r\_out}$ / (γ)	p_max/ KPa	p_central/ KPa	W_h/ N	W_a/ N	W_n/ N	LCC/ mN	$\overline{W\_h}$	$\overline{W\_n}$	T/ μNm	$\overline{T}$	f_coeff / (μ)
5	2827.4	0.4	1	0.4	1	4.00E-04	904.20	54.53	3.45E-01	3.14E-01	3.04E-02	3.04E+01	6.09E-03	5.37E-04	2.26E+01	9.99E-01	0.0984
6	2827.4	4	10	0.4	10	4.00E-04	904.20	54.53	3.45E+01	3.14E+01	3.04E+00	3.04E+03	6.09E-03	5.37E-04	2.26E+04	9.99E-01	0.0984

Variables	Meaning	Variables	Meaning
W_h	Hydrodynamic force	TE	Pocket extent in circumferential direction
W_a	Atmospheric force	RE	Pocket extent in radial direction
W_n	Net supporting force	$\overline{W\_h}$	Normalized hydrodynamic force
LCC	Load carrying capacity in unit of gram	$\overline{W\_n}$	Normalized net supporting force
T	Frictional torque	$\overline{T}$	Normalized frictional torque
f_coeff	Friction coefficient		

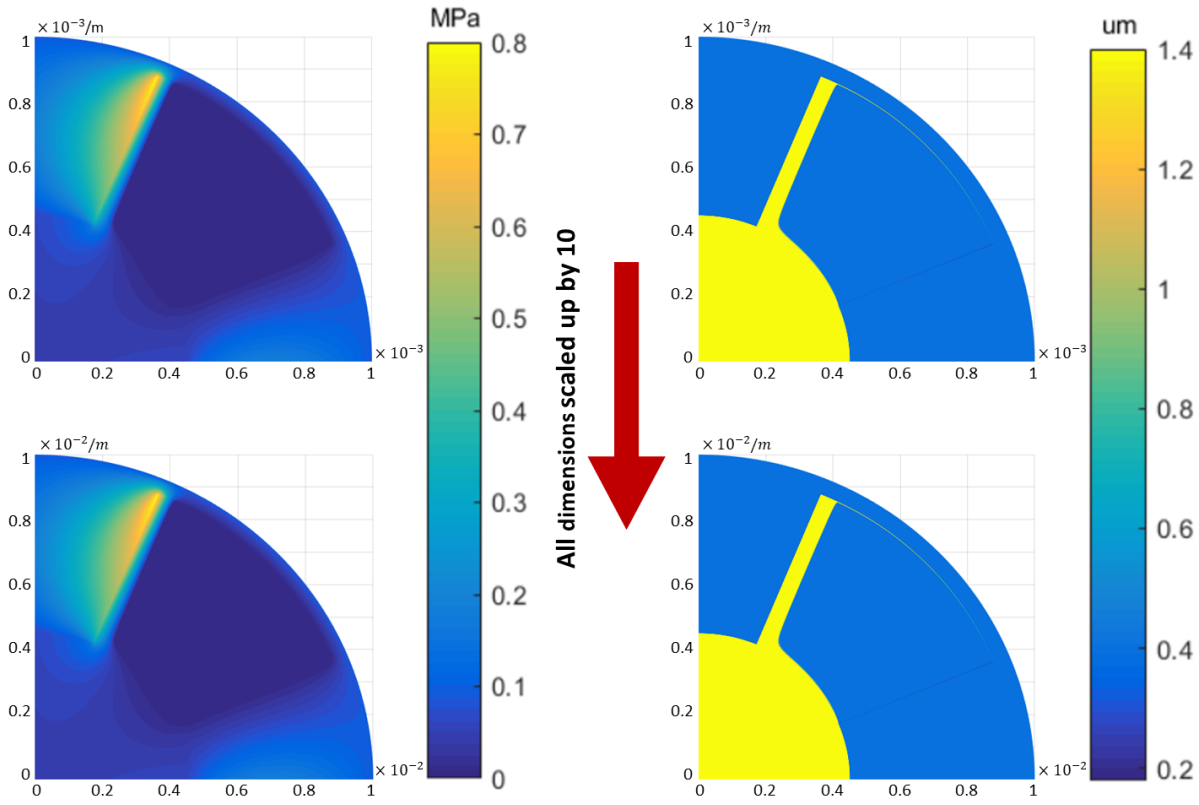

Figure 4-4. Pressure distribution and Film thickness distribution contours of the bearings in different size scales (all dimensions scaled in same ratio, ω = 2827.4 $rad \cdot s^{-1}$)

4.2.2. Scaling Bearing Radius while Fixing Pocket Depth and Minimum Film Thickness

The second set of comparisons (cases 1, 3 and 4 in Table 4-3 shows what happens when only the bearing radius is scaled up by a factor of 10 or 100 (case 4: $r_{out} = 0.1\ mm$, case 1: $r_{out} = 1\ mm$, case 3: $r_{out} = 10\ mm$). All other features including textured pocket pattern (TE_θ% and TE_r%), the depth of the pocket (h_{step}) and the minimum film thickness (h_{min}) of all the bearings in this group are kept constant.

Pressure distribution and film thickness distribution contours of the 0.1-mm, 1-mm and 10-mm bearings are shown in Figure 4-5. It can be seen that the film thickness distribution varies drastically when only the bearing radius is scaled up. No cavitation occurs within the 0.1-mm-radius bearing. However, when the bearing radius is scaled up to 1 mm, cavitation occurs in the downstream region of the trailing step of the pocket and the full film reforms at the upstream region close to the leading step of the pocket. The cavitation region is a combination of cavity and liquid. In this case, δ (ratio of h_{min} over h_{step}) is kept constant whereas γ (ratio of h_{min} over R_{out}) and ε (ratio of h_{step} over R_{out}) are reduced to 1/10 of the previous values. When the

bearing radius is further scaled up by 10 times to 10 mm, the cavitation region expands and almost covers the whole pocket region. The pressure distribution also varies drastically when only the radius of the bearing is scaled up. The maximum pressure generated by the 0.1 mm-radius bearing in case 4 is 115.7 kPa. This increases to 662.93 kPa for the 1 mm-radius bearing in case 1, and to 1859.2 kPa for the 10 mm-radius bearing in case 3. However, the maximum normalized pressure P_{max} of the bearings investigated in this group decreases when the radius is scaled up. The P_{max} of 0.1 mm bearing is 6.14×10^{-1}, the P_{max} drops to 3.52×10^{-2} when the bearing radius is scaled up to 1 mm and to 9.86×10^{-4} when the bearing radius is scaled up to 10 mm.

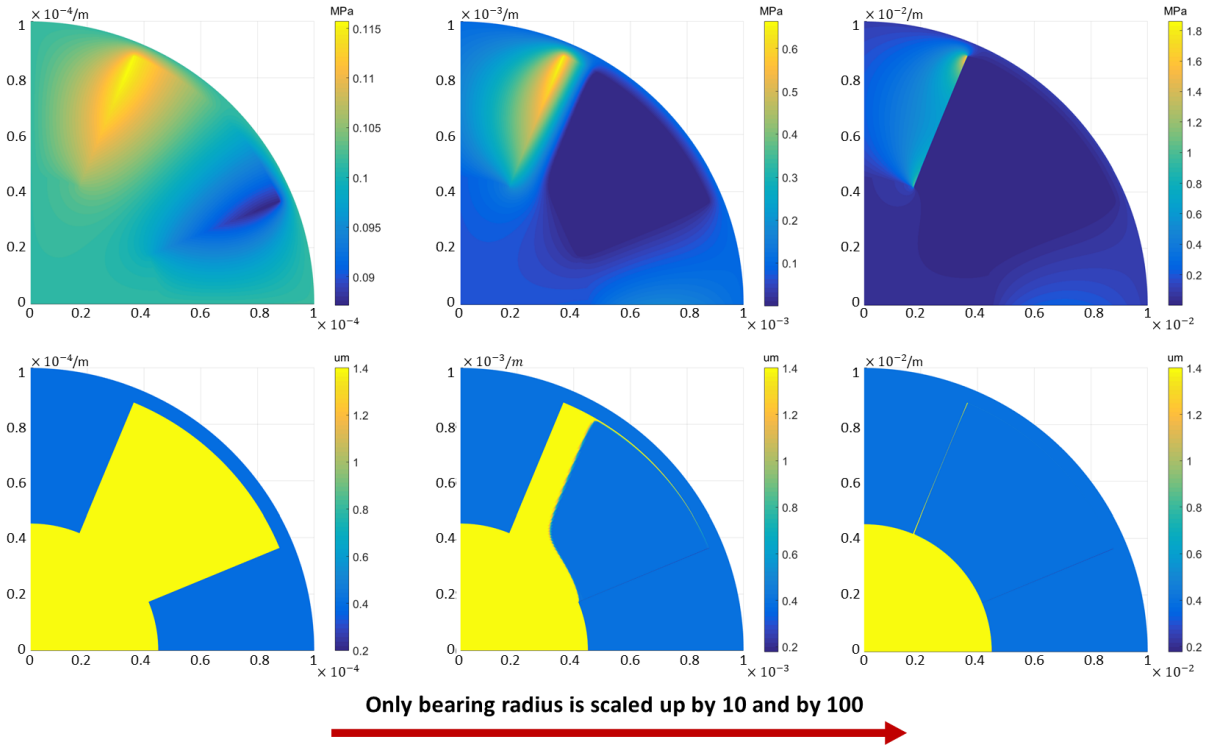

Figure 4-5. Pressure distributions and Film thickness distributions for bearings at different size scales (only bearing radius is scaled)

The correlation between the normalized hydrodynamic force and the ratio γ (ratio of h_{min} over R_{out}) obtained by scaling up the just bearing radius is shown in Figure 4-6 (a). When the bearing radius is scaled up by 10 times, the normalized hydrodynamic force is increased almost by 100 times. This indicates that the load support efficiency for this parallel pocketed bearing increases when the bearing is scaled down, which suggests that it is a suitable configuration for micro to millimetre scale components. For example, a 1 mm-radius pocketed parallel bearing can bear load above 2 grams whereas the mass of the bearing itself is just around 9 micro grams.

As displayed in Figure 4-6 (b), the normalized frictional torque rises slightly from 0.97 to 1.30 when the bearing radius is scaled down from 10 mm to 0.1 mm. The friction coefficient, however, declines sharply from 0.34 to 0.0046 when only the bearing radius is scaled down as the normalized load capacity increases drastically. That indicates the transmission efficiency is also improved when this type of bearing is miniaturised.

It can be concluded from that when only the bearing radius is scaled and the other geometric feature parameters are fixed, the pressure distribution and film thickness distribution changes dramatically. Therefore, the normalized bearing performance varies and the performance (normalized load carrying capacity and transmission efficiency) is better when this type of bearing is used in micro scales.

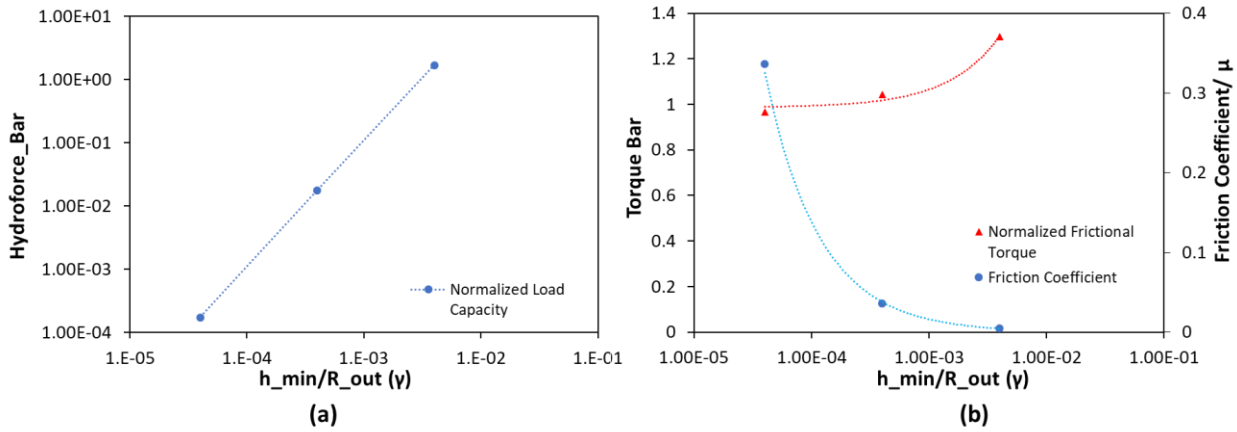

Figure 4-6. Correlations between (a) normalized hydrodynamic force and $\frac{h\_min}{R\_out}$ (γ) and (b) frictional properties and $\frac{h\_min}{R\_out}$ (γ). Only bearing radius is scaled

More detailed simulation results from this section be found in Table 4-6.

Table 4-6: Performance of bearings in different dimension scales: scale only r_out, fix h_min and h_step, ω = 942.5 $rad \cdot s^{-1}$)

Case No.	ω / $rad \cdot s^{-1}$	h_min/ μm	h_step/ μm	$\frac{h\_min}{h\_step}$ / (δ)	r_out/ mm	$\frac{h\_min}{r\_out}$ / (γ)	p_max/ KPa	p_central/ KPa	W_h/ N	W_a/ N	W_n/ N	LCC/ mN	$\overline{W\_h}$	$\overline{W\_n}$	T/ μNm	$\bar{T}$	f_coeff / (μ)
4	942.5	0.4	1	0.4	0.1	4.00E-03	115.70	101.29	3.19E-03	3.14E-03	4.42E-05	4.42E-02	1.69E+00	2.35E-02	9.79E-04	1.30E+00	0.0046
1	942.5	0.4	1	0.4	1	4.00E-04	662.93	67.47	3.31E-01	3.14E-01	1.73E-02	1.73E+01	1.76E-02	9.18E-04	7.86E+00	1.04E+00	0.0356
3	942.5	0.4	1	0.4	10	4.00E-05	1859.15	33.84	3.25E+01	3.14E+01	1.11E+00	1.11E+03	1.73E-04	5.90E-06	7.29E+04	9.67E-01	0.3363

Variables	Meaning	Variables	Meaning
W_h	Hydrodynamic force	TE	Pocket extent in circumferential direction
W_a	Atmospheric force	RE	Pocket extent in radial direction
W_n	Net supporting force	$\overline{W\_h}$	Normalized hydrodynamic force
LCC	Load carrying capacity in unit of gram	$\overline{W\_n}$	Normalized net supporting force
T	Frictional torque	$\bar{T}$	Normalized frictional torque
f_coeff	Friction coefficient		

4.2.3. Scaling Pocket Depth and Fixing Bearing Radius and Minimum Film Thickness

The third set of comparisons (cases 1, 7, 8 and 9 in Appendix Table 2) shows how the performance of the bearing varies when only the pocket depth is gradually scaled up with a fixed interval (0.5 μm) from 0.5 μm to 2 μm. The pocket pattern, minimum film thickness and bearing radius are kept constant (TE_θ% = 50%, TE_r% = 50%, h_{min} = 1 μm, R_{out} = 1 mm).

The pressure distributions and film thickness distributions for different pocket depths are illustrated in Figure 4-7, showing that the cavitation region shrinks towards the trailing step of the bearing when the pocket depth is increased from 0.5 μm to 2 μm. Correspondingly, the pressure active region expands when the pocket depth is increased from 0.5 μm to 2 μm. However, the maximum hydrodynamic pressure drops when the pocket depth increases, (the maximum pressure generated by the 0.5 μm-pocket depth bearing is 770.73 kPa whereas that of the 2 μm-pocket depth bearing is 485.43 kPa). The ratio between the minimum film thickness and pocket depth, δ, decreases from 0.8 to 0.2 when the pocket depth is increases from 0.5 μm to 2 μm.

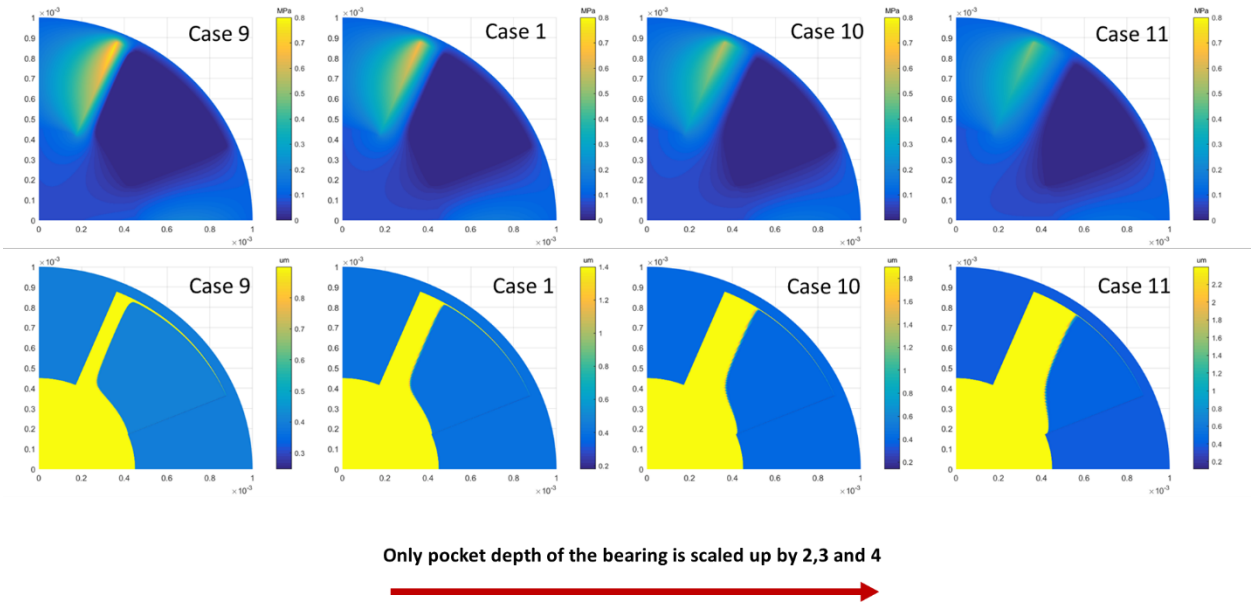

Figure 4-7. Pressure distributions and Film thickness distributions for bearings with different pocket depths

The correlation between the normalized hydrodynamic force and the ratio of minimum film thickness to pocket depth (δ) obtained by varying the pocket depth and fixing all other geometric parameters is shown in Figure 4-8 (a). Here, the normalized hydrodynamic force increases with increasing δ, which indicates that the load capacity increases when the pocket depth is reduced (Figure 4-8 (b)). The normalized frictional torque increases with increasing δ. However, the friction coefficient first decreases and reaches minimum value when δ = 0.4 and almost levels out when δ is increased to 0.8.

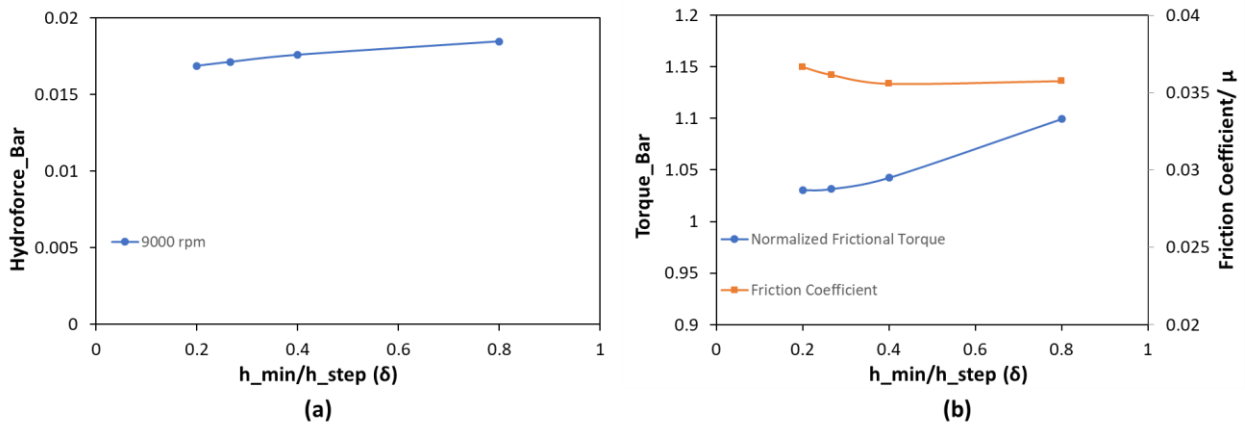

Figure 4-8. Correlations between (a) normalized hydrodynamic force and $\frac{h\_min}{h\_step}$ (δ) and (b) normalised frictional torque and $\frac{h\_min}{h\_step}$ (δ). (Only pocket depth is scaled)

4.2.4. Summary of Bearing Feature Size Scaling Investigation

It can be concluded from the results in this section that:

1. When all the geometric parameters of the pocketed parallel bearing are scaled simultaneously, the normalized bearing performance (including normalized load carrying capacity, normalized frictional torque and friction coefficient) remain unchanged. The film thickness distribution and the pressure distribution are uniform at all studied scales.
2. When only bearing radius is scaled while pocket depth and shape are fixed, the film thickness distribution and pressure distribution vary drastically. The normalized load capacity increases by 2 orders when the radius of the bearing is scaled down by 1 order, which indicates that parallel pocketed thrust bearing is more efficient in load capacity when this type of bearing is miniaturized. The friction coefficient and normalized frictional torque also decreases when only the bearing radius is scaled down. These characteristics make pocketed parallel thrust bearing an appropriate option to bear load and achieve high transmission efficiency in MEMS applications.
3. The maximum hydrodynamic pressure decreases when only the pocket depth is scaled up but the area of pressure active region where positive load capacity is generated expands. For the bearings studied, an increase in pocket depth results in a decrease of load carrying capacity.

4.3 Effects of Operational Parameters and Shape of the Recessed Pocket on Bearing Performance

The results in the following sections systematically characterise the effects of operational conditions (minimum film thickness and rotational speed) and geometric parameters (pocket extent in radial and circumferential directions) on bearing performance, is the latter being assessed in terms of load capacity, frictional torque and friction coefficient. To demonstrate a clear correlation between each parameter and bearing performance, the numeric tests are conducted by varying each of the parameters individually and fixing other parameters.

4.3.1. Effects of Minimum Film Thickness

A range of minimum film thickness values from 80 to 2000 nm are studied, which represents all normal bearing operating conditions. Speeds are varied from 733.0 $rad \cdot s^{-1}$ to 1570.8 $rad \cdot s^{-1}$, which covers all practical operational speeds for bearings used in MEMS. The shape and depth of the textured pattern in this group of bearings is fixed (texture extent in θ direction, TE_θ, is 50%; texture extent in r direction, TE_r, is 50%).

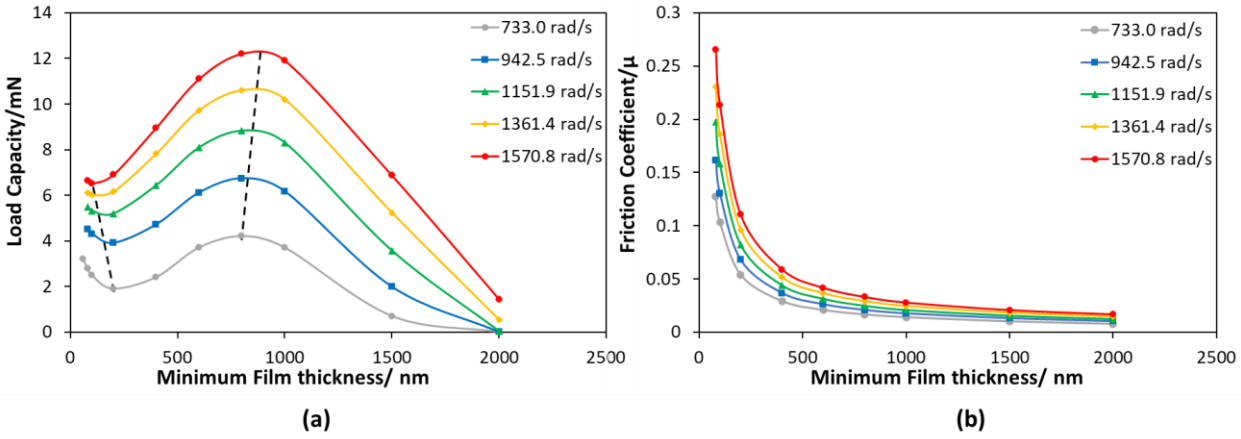

Figure 4-9. Variations of (a) load carrying capacity and (b) friction coefficient of pocketed bearing with minimum film thickness at different speeds (50% TE_θ, 50% TE_r)

Load Carrying Capacity

The relationships between load carrying capacity and minimum film thickness are shown in Figure 4-9 (a). It is well known that parallel flat surfaces should not be capable of any load support. However, as Figure 4-9 (a) shows, circular thrust bearings can generate load support when textured pockets are added. The 1-mm radius thrust bearing can support load above 9.8 mN which is typical in MEMS devices.

For all of the curves in Figure 4-9 (a), the load support tends to zero when the minimum film thickness is higher than 2000 nm. For all simulated speeds, the load support increases when the film thickness drops from 2000 nm to 900 nm, which is a normal behaviour for a hydrodynamic bearing. For most hydrodynamic bearings, the load carrying capacity increases monotonically with decreasing minimum film thickness. However, the correlation between load carrying capacity and minimum film thickness of these pocketed bearings appears anomalous when the film thickness is further decreased below 900 nm. Take the curve at 1570.8 $rad \cdot s^{-1}$ as an example. Here, the load support of the bearing falls from 12.34 mN to

6.52 mN when the film thickness is reduced from 900 to 100 nm. If the film thickness is further decreased below 100 nm, the load carrying capacity will rise again.

The trends of the load carrying capacity vs. minimum film thickness curves are the same for all speeds, *i.e.* load carrying capacity first rises with decreasing film thickness, then declines and rises again when the film is very thin (below 100 nm). However, the width of the region where the load support is positively correlated with film thickness varies with speed. Moreover, the two dashed lines (one crosses all max LCC points and the other crosses all min LCC points of all the curves) show that the width of the region increases with speeds. The turning points of the 1570.8 $rad \cdot s^{-1}$ curve are at 900 nm and 100 nm, whereas the turning points of the 733.0 $rad \cdot s^{-1}$ curve are at 800 nm and 200 nm.

This abnormal correlation with minimum film thickness is related to the cavitation that occurs during the pocketed bearing operation and will be discussed in detail in the pressure and film thickness distribution results part of this section.

Frictional Torque and Friction Coefficient

The correlations between friction coefficient and minimum film thickness are presented in Figure 4-9 (b). The friction coefficient of the pocketed bearing (50%TE_θ, 50%TE_r) decreases with increasing minimum film thickness for all simulated speeds, which is similar to most hydrodynamic bearings as both Couette and Poiseuille shear stresses reduce as the minimum film thickness increases. Take the curve of 942.5 $rad \cdot s^{-1}$ curve as example: the friction coefficient exceeds 0.16 when the bearing operates at 100 nm minimum film thickness whereas it is below 0.013 when the film thickness is increased to 2000 nm.

$$\tau_c = \eta \frac{\omega r}{h} S \tag{4-4}$$

$$\tau_p = \frac{1}{2} \frac{h}{r} \frac{dp}{d\theta} S \tag{4-5}$$

The trends of the friction coefficient vs. film thickness curves of all speeds are almost the same and show a similar trend to curve: $y = \frac{constant}{h}$. This indicates that the friction is dominated by the shear stress from Couette flow. This is validated by plotting the frictional torque components, i.e. Couette frictional torque (Figure 4-10. (a)) and Poiseuille frictional torque (Figure 4-10. (b)), versus minimum film thickness separately and comparing them against each other. The trend of the frictional torque curves is similar to that of the frictional coefficient

curves and the Poiseuille contribution is smaller than the Couette. For example, the Couette frictional torque of the bearing operating at 942.5 $rad \cdot s^{-1}$ and 100 nm minimum film thickness is 34 μNm whereas the Poiseuille contribution is 0.44 μNm. This is because the maximum pressure of the bearing is below 1 MPa and the pressure gradient is very low.

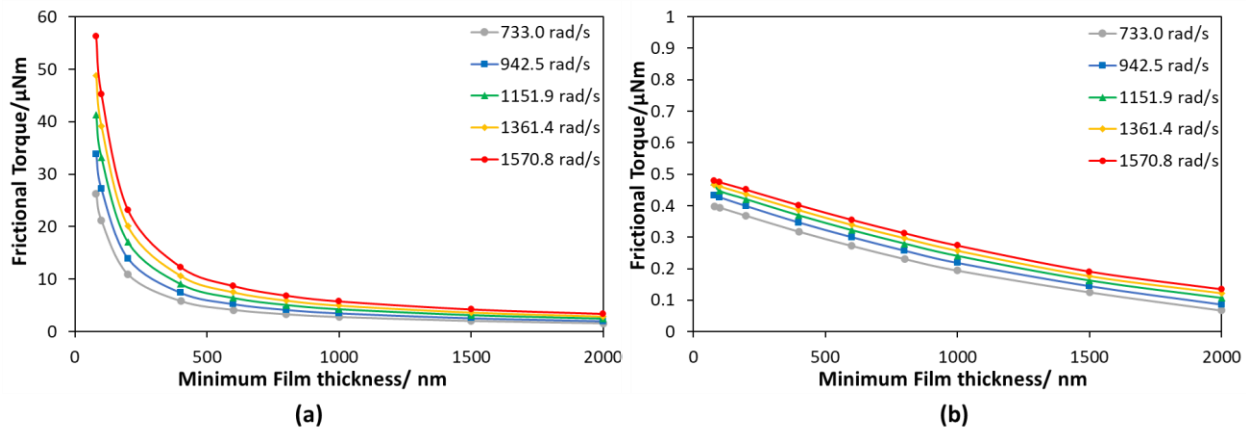

Figure 4-10. Variations with minimum film thickness of (a) Couette frictional torque and (b) Poiseuille frictional torque for pocketed bearing at different speeds (50% TE_θ, 50% TE_r)

Pressure Distribution and Film Thickness Distribution Contours

A series of film thickness distribution and pressure distribution contours for a bearing (50%TE_θ, 50%TE_r) operating at a fixed rotational speed (942.5 $rad \cdot s^{-1}$) and different minimum film thickness are presented in Figures 4-11 (a) and 4-11 (b) respectively. When the minimum film thickness is 2000 nm, cavitation does not occur, and fluid fills the entire bearing area. This shows that cavitation will not occur if the film is sufficiently thick.

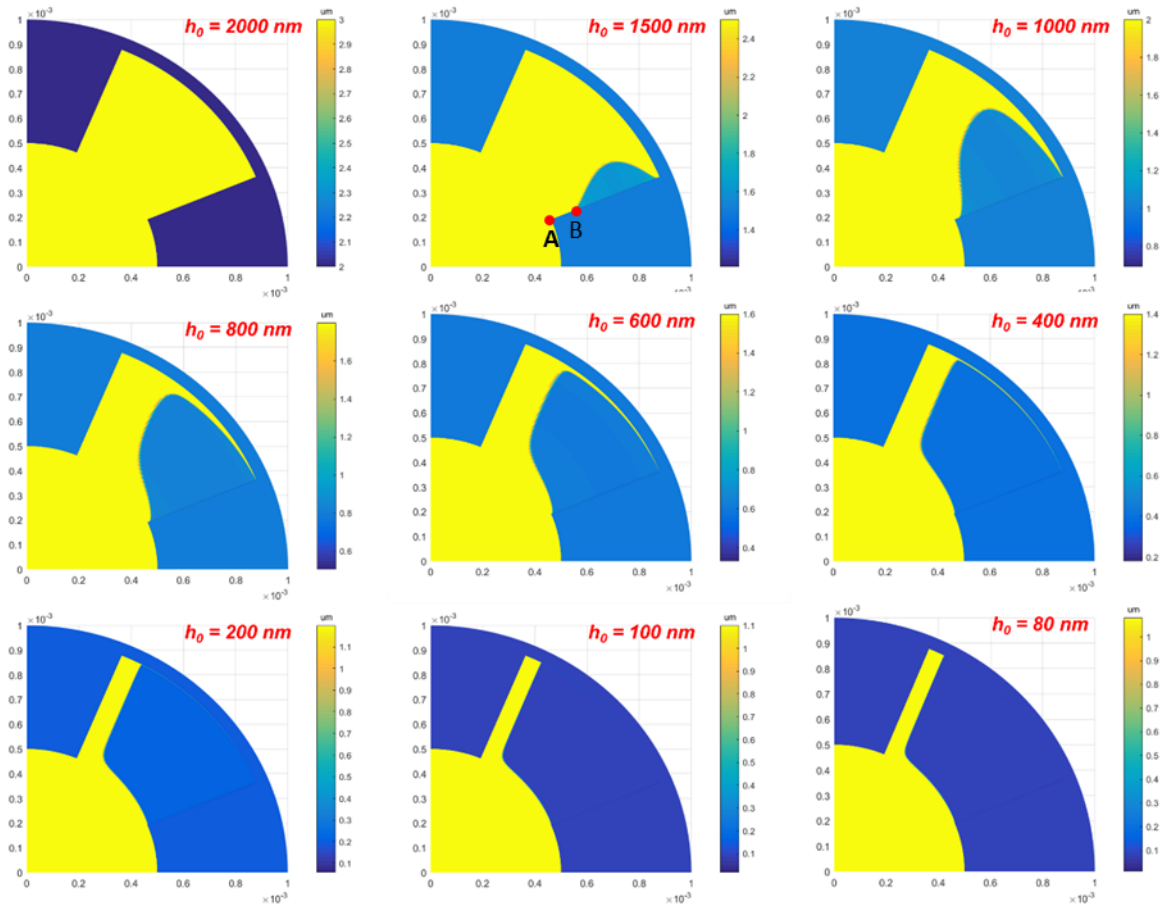

Figure 4-11 (a). Film thickness distribution of pocketed bearing at different minimum film thicknesses (942.5 $rad \cdot s^{-1}$, 50% TE_θ, 50% TE_r)

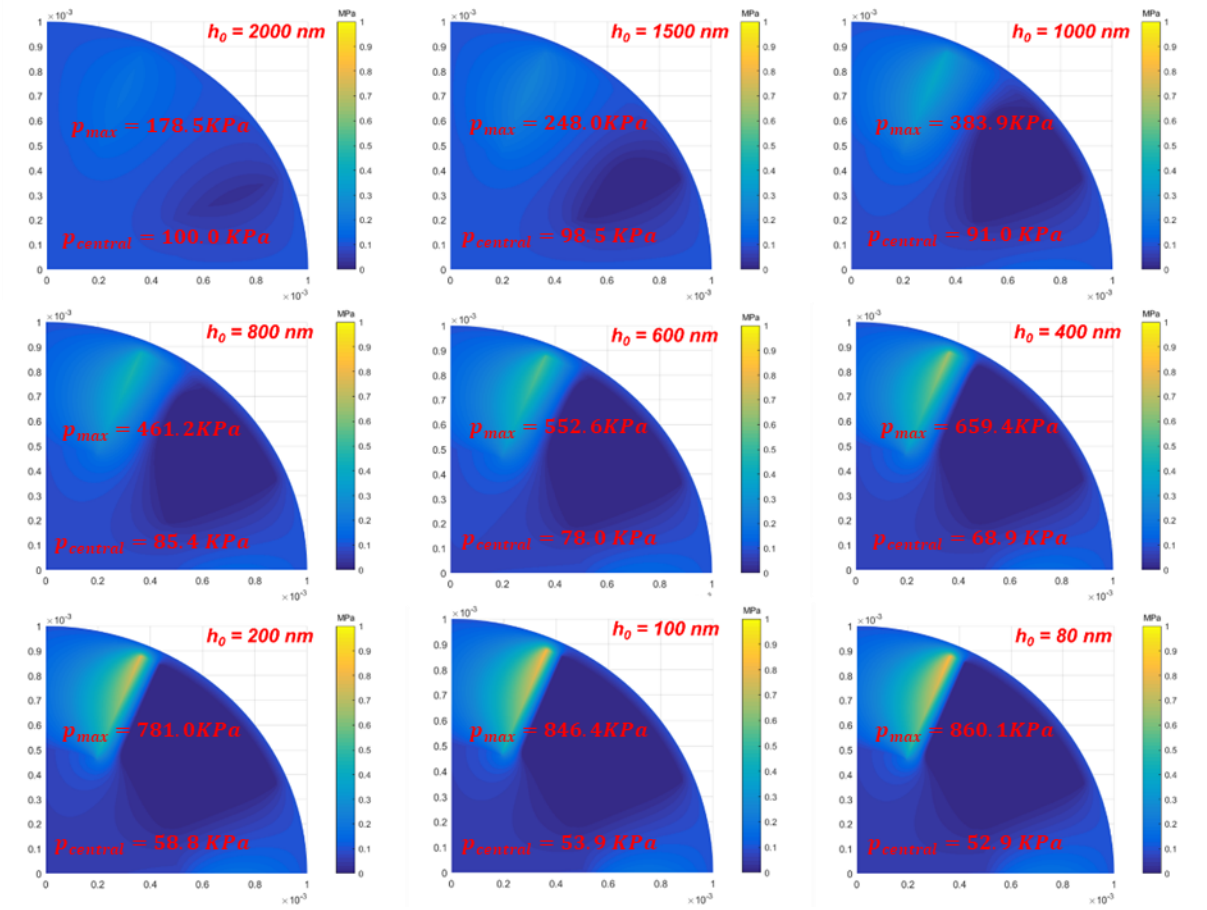

Figure 4-11 (b). Pressure distribution of pocketed bearing at different minimum film thickness (942.5 $rad \cdot s^{-1}$, 50% TE$_\theta$, 50% TE$_r$)

As the minimum film thickness is reduced to 1500 nm, cavitation occurs along the trailing edge of the pocketed region, where the gap between the surfaces is filled with the mixture of gaseous cavity and liquid. It can be concluded that cavitation occurs exactly in the location where there is a divergence of the bearing surfaces and the cavity expands downstream. Furthermore, the starting point of the cavitation area in the radial direction is not the initial point of the step (marked A in the figure) but a point located at a larger radius of the step (marked B) where that speed is slightly higher. This indicates that cavitation occurs only when the fluid flow speed reaches a threshold value. The cavity size in the circumferential direction becomes larger as the radius increases. However, the location of maximum cavity size in the radial direction is not at the end point of the step where the speed is a maximum. The cavity size increases and then decreases along the trailing step, and there is no cavitation in the area around the end point of the step. This phenomenon results from two conflicting effects. On one hand, higher speed boosts cavity development so cavity size first increases with rising radius. On the other hand, the circumferential region where the radius is greatest (flow speed higher) is also closer to the

outer edge of the bearing where fluid is supplied and the pressure at the edge is equal to 1.015e5 Pa (which is higher than the 1 Pa cavitation pressure), so that the supplied inward flow assists film reformation in radial direction and reduce the cavity size along the step inwards.

Similar film thickness distributions can be found when the film thickness is reduced from 1500 to 1000 nm, but here the cavitated area expands both in the circumferential and radial directions and covers almost half of the recessed region so that the film reformation boundary is pushed towards the leading step of the bearing. This indicates that the cavitated area increases and expands along the fluid flow direction as the minimum film thickness is decreased.

The cavitation area expands steadily in both circumferential and radial directions as the film thickness is reduced from 1000 to 200 nm. When the bearing operates at 200 nm, the neighbouring downstream region of the whole trailing step is cavitated and $\frac{8}{9}$ of the whole recessed channel area is cavitated so that the film reformation boundary is close to the leading step. There is almost no increase in the cavitation area when the film thickness is further decreased from 200 nm to 80 nm.

For all the film thickness values, the cavitation area does not expand to the central flat area of the bearing as there is no diverging gap in this area.

A series of pressure distribution contours are also obtained from the same operating conditions and displayed in figure 4-11 (b). When the film thickness is 2000 nm, the maximum pressure is 180 kPa, and the load supporting pressure is generated around the leading step of the bearing. Even though cavitation does not occur in this case, a low-pressure area ($p << p_{atm}$) still forms around the diverging step of the bearing. A clear pressure gradient can be observed in both directions in the area where r>r_{pad} (the area where the steps are located). In the area where the radius is slightly lower than r_{pad}, a clear pressure gradient is only observed in the radial direction. In the area close to the central point, there is no evidence of a pressure gradient. This is because the bearing surfaces within the area where r<r_{pad} are totally flat and parallel to each other, so no supporting pressure is generated (inertia and thermal effect neglected) and the pressure in the central area is almost equal to the boundary pressure at the outer edge.

When the film thickness is reduced from 2000 to 1500 nm, cavitation occurs as discussed in the film fraction results section and the bearing separates into two regions: a pressurized region where supporting liquid pressure varies and a cavitation region where the liquid pressure stays constant (equal to cavitation pressure: 1 Pa). The cavitation area is larger than the low-pressure

area seen at 2000 nm film thickness, but the pressure in the pressurized area is larger than in the 2000 nm case. This agrees with fluid mechanics that when the film thickness is reduced the cavitation area expands and the generated pressure around the converging step rises.

When the film thickness is reduced from 1500 to 800 nm, the cavitation area gradually increases, and the maximum pressure increases from 250 to 480 kPa. When the film thickness is reduced further from 800 to 200 nm, the cavitation region is still expanding rapidly, which results in the drastic shrinking of the pressurized area (only a ninth of the area where r> r_{pad} is pressurized) and the maximum pressure increases from 480 to 790 kPa.

The size of the pressurized region and cavitation region remain almost unchanged when the film thickness further reduces from 200 to 80 nm. The maximum pressure, however, keeps increasing from 790 to 860 kPa.

As mentioned in the load carrying capacity section, the correlation between the load support and film thickness is abnormal, since the load support increases and then decreases before finally increasing again when the film thickness is continuously reduced from 2000 to 80 nm. This correlation is different from most other hydrodynamic bearings where the load capacity decreases monotonically with increasing film thickness. This abnormal variation in load support with minimum film thickness is a result of two well-known aspects of fluid behaviour, which in this case oppose each other. These two effects can be observed from the pressure distribution in the circumferential direction which is displayed in Figure 4-12. On one hand, the cavitation area, where the pressure has a constant low value, expands with decreasing film thickness. Consequently, the area where hydro pressure higher than the atmospheric pressure is reduced. In addition to this, when the film thickness is decreased, the expansion of the low-pressure cavitation area also results in the reduction of the pressure in the central flat region, (Figure 4-11 (b), where the pressure in the central flat region is reduced from 100 kPa to 52 kPa). These two effects induced by the film thickness reduction can undermine the load carrying capacity of the bearing. On the other hand, the maximum pressure generated along the diverging step rises with decreasing film thickness; this can be seen in Figure 4-11 (b) where the pressure over the un-recessed pad area is increased when the film thickness is reduced. This can also be observed from figure 4-12, where the pressure distributed from $\theta = 0$ to $\theta = \frac{\pi}{4}$ and the pressure distributed from $\theta = \frac{3\pi}{4}$to $\theta = \frac{\pi}{2}$ increase when the film thickness is decreased. This results in an increase in load support in the un-recessed area of the bearing.

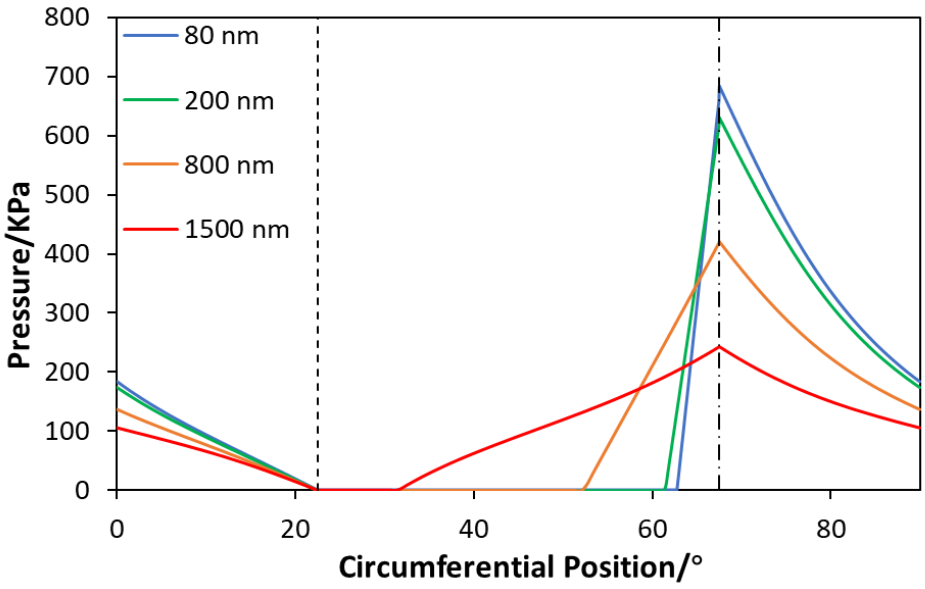

Figure 4-12. Pressure distribution in circumferential direction at mid-radius for different minimum film thicknesses

Summary of Effects of Minimum Film Thickness on Micro Bearing Performance

A decrease in film thickness simultaneously results in *i*) a reduction in load supporting area and a reduction of pressure in the central pad area due to the expansion of the cavitated area, and *ii*) an increase in pressure and load support in the un-recessed pad area. The overall load carrying capacity of the bearing therefore changes with film thickness depending on which of these opposing effects is stronger. For example, when the film thickness of a 50%TE_θ, 50%TE_r bearing, operating at 942.5 $rad \cdot s^{-1}$, is decreased from 2000 to 800 nm, the generated pressure around the converging step increases rapidly. Even though the cavity size also increases in this range, there is no drastic change of the pressure in the central region (from 100 to 90 kPa). Therefore, the increase of load support from pressure rise is larger than the reduction due to cavitation expansion and bearing load capacity therefore increases with decreasing film thickness. Conversely, when the film thickness is decreased from 800 to 200 nm, the generated pressure around the converging step still increases. However, the cavity size also increases rapidly and the pressure in the central region falls significantly (from 90 to 58 kPa). Therefore, the increase in load carrying capacity due to pressure rise is smaller than the reduction of load carrying capacity from cavity expansion so that bearing load capacity decreases with decreasing film thickness. When the film thickness is decreased from 200 to 80 nm, the generated pressure around the converging step still increases. Here, the cavity size remains almost unchanged and the pressure in the central region falls only slightly (from 58 to 53 kPa).

Therefore, the increase in load carrying capacity from pressure rise is larger than the reduction of load carrying capacity from cavitation expansion so that bearing load capacity increases with decreasing film thickness again.

The correlation between the two opposing effects on the load carrying capacity from film thickness reduction does not depend on film thickness alone; it is also affected by rotational speed. Effects from cavitation are stronger at higher rotational speed, therefore the film thickness where load support reaches minimum value for the 1570.8 $rad \cdot s^{-1}$ case is higher than for the 733.0 $rad \cdot s^{-1}$ case. Moreover, the film thickness where load support begins to rise with decreasing film thickness at 1570.8 $rad \cdot s^{-1}$ is lower than at 733.0 $rad \cdot s^{-1}$.

4.3.2. Effect of Rotational Speed

Effects of rotational speed on bearing performance are demonstrated in this section. The investigated rotational speed ranges from 733.0 $rad \cdot s^{-1}$ to 1570.8 $rad \cdot s^{-1}$, which is a typical speed range over which micro bearings operate in the hydrodynamic regime. The correlation between rotational speed and thrust bearing performance is also studied at different minimum film thickness values. For this, the shape and the depth of the textured pattern of the bearing are fixed (texture extent in θ direction, TE_θ, is 50%; texture extent in r direction, TE_r, is 50%).

Load Support

The correlations between load support and rotational speed under different minimum film thickness are displayed in Figure 4-13. For all film thickness values greater than 2000 nm, load support increases with rotational speed in accordance with hydrodynamic theory. When the bearing operates at 2000 nm film thickness, no load support is generated for rotational speeds below 1151.9 $rad \cdot s^{-1}$.

A notable feature of Figure 4-13 is that the load support vs. rotational speed curves obtained at different film thickness have different behaviours in terms of curvature. For the curve obtained at 2000 nm, the gradient increases with rotational speed (*i.e* the curve is concave). For the 1500 nm curve, the gradient still increases with rotational speed but the rate at which the gradient increases is smaller than that of the 2000 nm curve, so the curve tends to a straight line. The curve becomes convex when the film thickness is decreased to 1000 nm, which indicates the gradient decreases with rotational speed. Moreover, the load support vs. rotational speed curve

becomes increasingly convex when the minimum film thickness is further reduced from 1000 to 80 nm. This phenomenon is also related to the cavitation in the bearing and will be explained in detail with the pressure and film thickness distribution results.

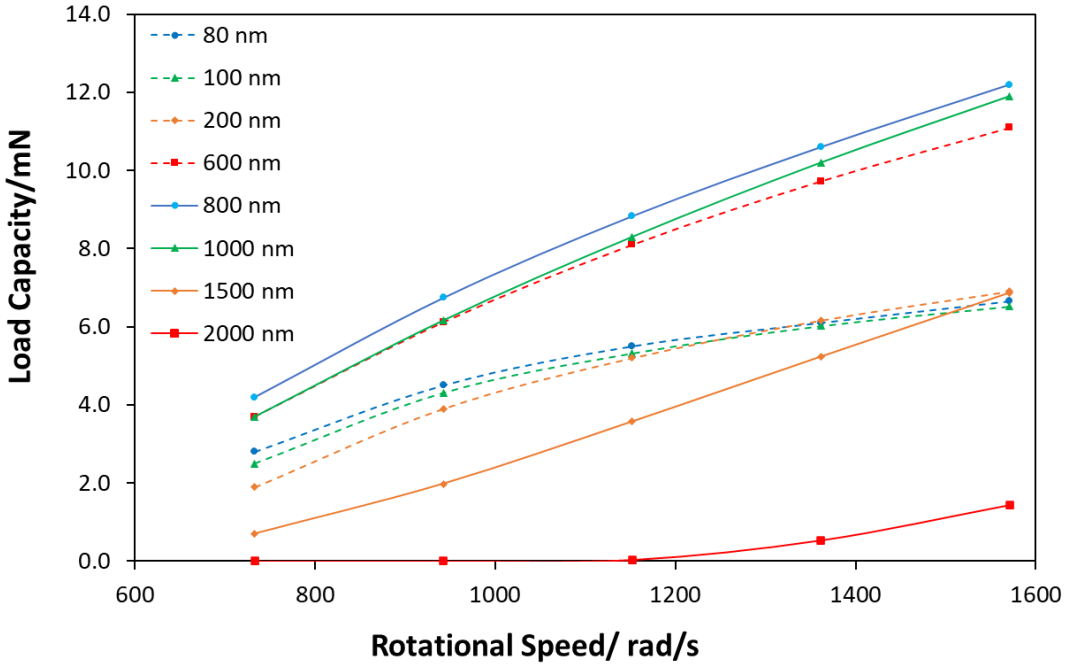

Figure 4-13. Load carrying capacity of pocketed bearing vs. rotational speed for different film thickness (50% TE_θ, 50% TE_r)

Pressure Distribution and Film Thickness Distribution

Effects of rotational speed on the film thickness distribution, pressure distribution and cavitation development for a bearing with fixed geometric design (50%TE_θ, 50%TE_r) are demonstrated in this section.

It can be seen from Figure 4-14 (a) that, when the film is thick (1500 nm), cavitation occurs for all investigated speeds and the cavity expands with increasing rotational speed. Similar to the case of decreasing film thickness, the cavity expands both in radial and circumferential directions, but the expansion speed in the circumferential direction is much greater than in the radial direction. Comparing the film thickness and pressure distribution results for a series of different rotational speeds (Figure 4-14) to those of a series of different film thicknesses (Figure 4-11), it can be noticed that the latter has the greatest effect for the parameter ranges investigated. The pressure generated around the leading step rises with increasing rotational speed, which agrees with hydrodynamic theory.

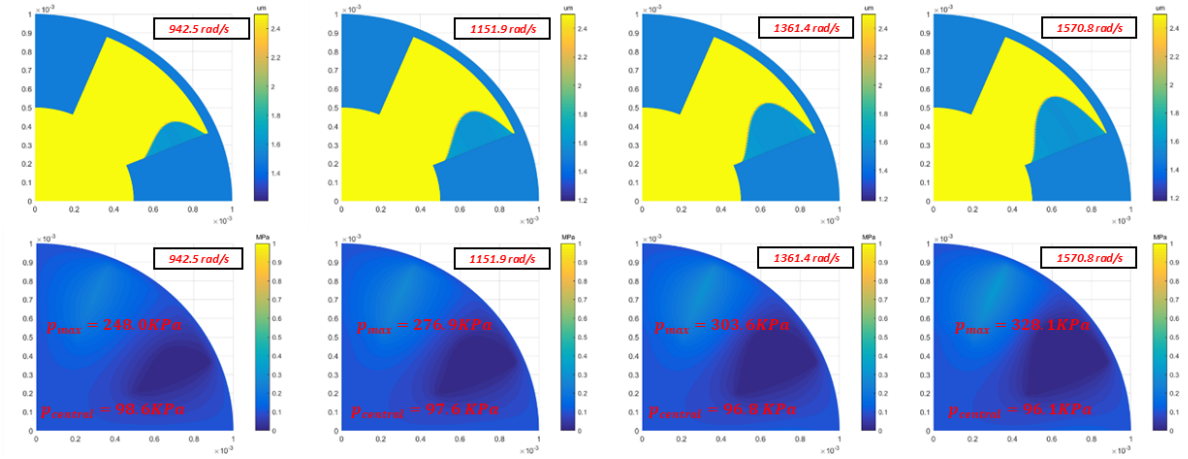

Figure 4-14 (a). Film thickness and pressure distribution of pocketed bearing at different rotational speeds (1500 nm, 50% TE_θ, 50% TE_r)

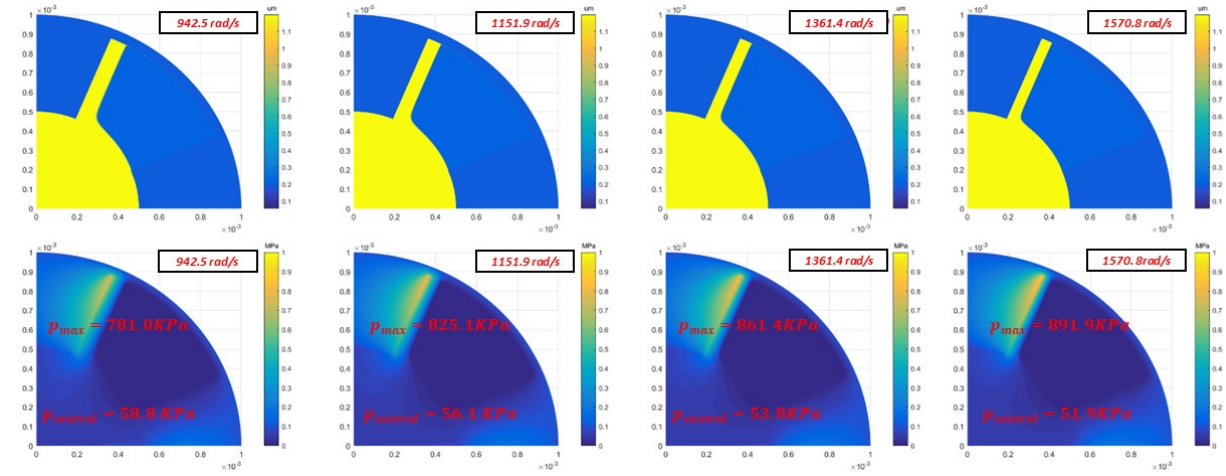

Figure 4-14 (b). Film thickness and pressure distribution of pocketed bearing at different rotational speeds (200 nm, 50% TE_θ, 50% TE_r)

Comparing Figures 4-14 (a) and 4-14 (b), it is evident that the effect of rotational speed on the cavity size is different when the bearing operates at different film thicknesses. When the film is thin and most area of the pocketed region is covered by the cavity, an increase in rotational speed has little effect on the cavity expansion. This is exemplified by Figure 4-15, which shows that when the film thickness 200 nm (figure 4-15 b), the cavitation region only expands by 3° in circumferential direction when rotational speed is increased from 942.5 $rad \cdot s^{-1}$ to 1570.8 $rad \cdot s^{-1}$. Conversely, when the film thickness is 1500 nm (figure 4-15 a), the cavitation region expands by 12° when the film thickness is increased from 942.5 $rad \cdot s^{-1}$ to 1570.8 $rad \cdot s^{-1}$.

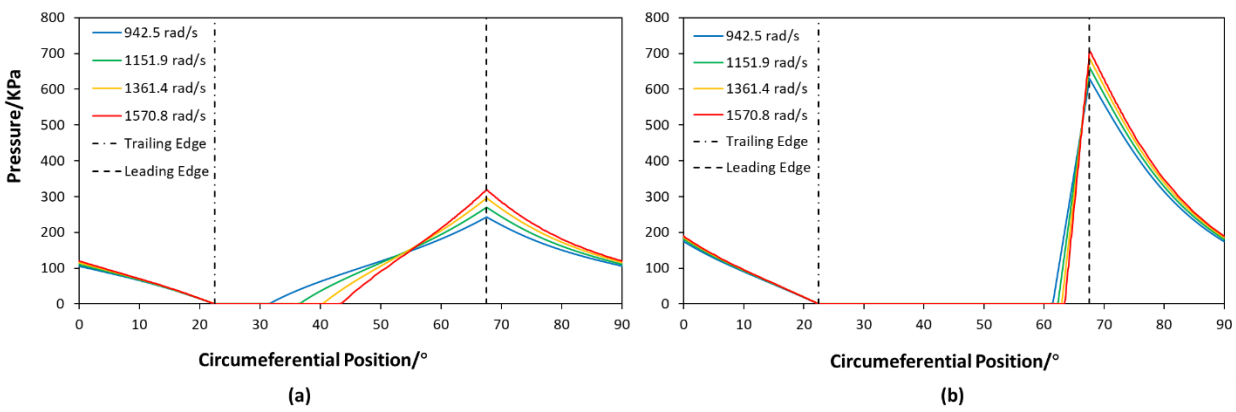

Figure 4-15. Pressure distribution in circumferential direction at mid-radius for different rotational speeds and for (a) 1500 nm film thickness (50% TE_θ, 50% TE_r) and (b) 200 nm film thickness (50% TE_θ, 50% TE_r)

Load support increases monotonically with rotational speed, in contrast to its fluctuating behaviour as a function of film thickness. This indicates that, as the rotational speed is increased, the load support increase from the pressure rise overwhelms the load support reduction due to cavity expansion and the pressure reduction in the central region. It can be seen from the pressure distribution in Figure 4-14 that, when the rotational speed rises from 733.0 to 1570.8 $rad \cdot s^{-1}$, the pressure in the central flat region falls by just 2.5 kPa for 1500 nm and by 7 kPa for 200 nm. This pressure reduction (and hence load support reduction) is much smaller compared to the reduction caused by decreasing film thickness, which explains why the load support increasing factors outweigh the load support decreasing factors as rotational speed increases. As the area of pressurized region shrinks, the increase of the pressure generated around the leading step results in an increasingly smaller load support increase when the film thickness is reduced from 1500 to 200 nm. In addition, the load support in the central flat pad reduces more rapidly for 200 nm as the pressure reduces faster. Therefore, the rate at which load support increases with rotational speed reduces with decreasing film thickness, which is observed in the load carrying capacity vs. rotational speed curves.

4.3.3. Effect of Pocket Extent in Circumferential Direction

Results showing the effects of varying pocket extent in the circumferential direction are shown in this section. The circumferential pocket extents studied range from 20% to 90% with a fine interpolation between neighbouring data points, which enables an accurate optimum circumferential pocket extent to be obtained in terms of load carrying capacity and friction

coefficient (frictional torque) and also aids the analysis of the mechanism relating θ-direction pocket extent to bearing performance. The investigation is conducted under fixed rotational speed (942.5 $rad \cdot s^{-1}$) while the minimum film thickness is systematically varied from 400 to 2000 nm. This is done since minimum film thickness has a much stronger effect on pressure build-up and cavitation and hence determines bearing performance (as demonstrated in the previous two sections). The pocket depth and radial extent are also fixed to distinguish the effects of circumferential pocket extent (h_{step}=1 μm, TE_r=50%).

Load Carrying Capacity

The correlation between load carrying capacity and pocket size in the circumferential direction (TE_θ) under different minimum film thickness is shown in Figure 4-16 (a). For all minimum film thickness values investigated, the variation of load support with TE_θ has a single maximum, falling away at low and high values of TE_θ. An optimum circumferential pocket extent exists for all minimum film thickness values. Load carrying capacity is also significantly affected by TE_θ. When film thickness is equal to 400 nm, load support of bearings with TE_θ below 40% or above 90% is negative, which indicates that the generated hydrodynamic force is smaller than the force applied by the atmospheric pressure on the bearing surface. The bearing surfaces will not separate for these cases (which agrees with the phenomena observed from some researches that badly designed surface texture undermines the smooth-surface hydrodynamic bearings). In contrast, a bearing with 70% TE_θ can support a load of 19.6 millinewton (which is large for a 2-mm diameter thrust bearing) when the minimum film thickness is 400 nm. Another phenomenon illustrated in Figure 4-16 (a) is that the load support improvement achieved by optimizing TE_θ increases as the film becomes thinner.

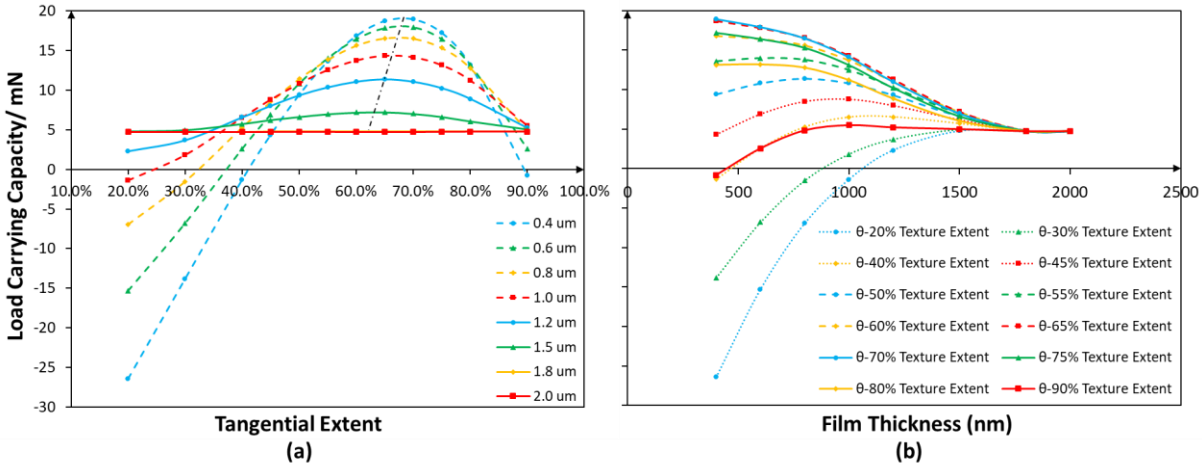

Figure 4-16. (a) Load carrying capacity of pocketed bearing vs. circumferential extent of pocket for different minimum film thicknesses (50% TEr, 942.5 $rad \cdot s^{-1}$); (b) Load carrying capacity of pocketed bearing vs. minimum film thickness for different circumferential extent values (50% TEr, 942.5 $rad \cdot s^{-1}$)

It can also be observed from Figure 4-16 (a) that the optimum TE_θ is negatively correlated with minimum film thickness. The optimum TE_θ gradually rises from 62% to 68% when the film thickness is reduced from 1500 to 400 nm. Even though the optimum TE_θ varies under different minimum film thicknesses, the range within which the optimum varies is small and any TE_θ with this range can achieve good load support for all film thicknesses.

Curves showing the correlation between load support and minimum film thickness for pockets with different TE_θ values are shown in Figure 4-16 (b). The load carrying capacity and h_{min} curves distinguish between different TE_θ. For the bearings with TE_θ near to the optimum value (TE_θ from 60% to 75%), the load support increases monotonically with decreasing film thickness whereas for bearings with TE_θ below 40% or above 80%, the load support decreases monotonically with reducing film thickness. This can also be explained by the simultaneous pressure build-up and cavity expansion theory described in previous sections.

Frictional Torque and Friction Coefficient

The correlation between friction coefficient (μ) and pocket extent in the circumferential direction (TE_θ) is shown in Figure 4-17 (a). The friction coefficient decreases with increasing TE_θ for all film thickness cases. The frictional torque versus TE_θ curve for the 0.4 μm minimum film thickness case in Figure 4-17 (b) shows Poiseuille and Couette terms plotted against TE_θ. The Couette friction torque decreases rapidly with TE_θ whereas the Poiseuille friction torque

increases with TE_θ. As the circumferential pocket extent is increased, the region with larger film thickness (i.e. the pocketed region) expands, which result in a decrease of shear stress and hence Couette friction. The pressure gradient upstream of the converging step, however, increases with larger TE_θ and therefore the Poiseuille friction also increases. As shown in Figure 4-17 (b), Couette friction is much larger than Poiseuille friction and consequently the total frictional torque decreases with increasing TE_θ.

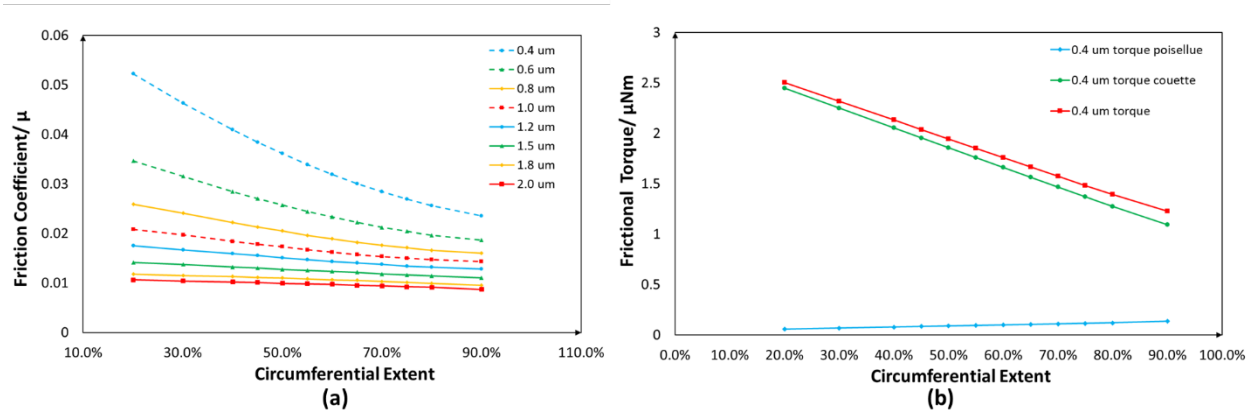

Figure 4-17. (a) Friction coefficient of pocketed bearing vs. circumferential extent of pocket for different film thicknesses (50% TEr, 942.5 $rad \cdot s^{-1}$); (b) frictional torque of pocketed bearing vs. circumferential extent of pocket (50% TEr, 942.5 $rad \cdot s^{-1}$)

Pressure Distribution and Film Thickness Distribution

The effects of circumferential pocket extent (TE_θ) on the film thickness distribution and pressure distribution are displayed in Figure 4-18 (942.5 $rad \cdot s^{-1}$ ω, 400 nm h_{min}). Cavitation occurs in all bearing configurations and the angular width of the cavity increases with circumferential pocket extent (Figure 4-18 (a)). However, the angular width of the film reformation region (the region between the locus of film reformation and the leading step of the pocket) also expands with TE_θ. Pressure distributions for different TE_θ are displayed in Figure 4-18 (b). Corresponding to the film thickness distributions, the low-pressure cavitation region expands with increasing circumferential pocket extent. The maximum pressure generated at the leading edge of the pocket increases with TE_θ. For example, the maximum pressure generated by the bearing with 20% TE_θ is 426 kPa whereas the maximum pressure generated by the bearing with 90% TE_θ is increased to 1005 kPa. The pressure in the pressure active region rises when circumferential pocket extent increases, and the pressure in the central flat region also rises with increasing TE_θ. When TE_θ is 20%, the pressure in the central flat

region is 64 kPa, and this is increased to 83 kPa when the circumferential direction pocket extent is increased to 90%. In the previous minimum film thickness and rotational speed investigations, the central flat region pressure drops as the cavitation region grows, which contrasts with the phenomenon observed when TE_θ is increased. This is because the pressure in the central flat region is determined by the surrounding pressure in the pocket region and this increases significantly (faster than the increase caused by reducing minimum film thickness or increasing rotational speed) in the pressure active region around the leading step of the pocket. Therefore, the pressure in the central flat region increases when the pocket extent in circumferential direction is increased.

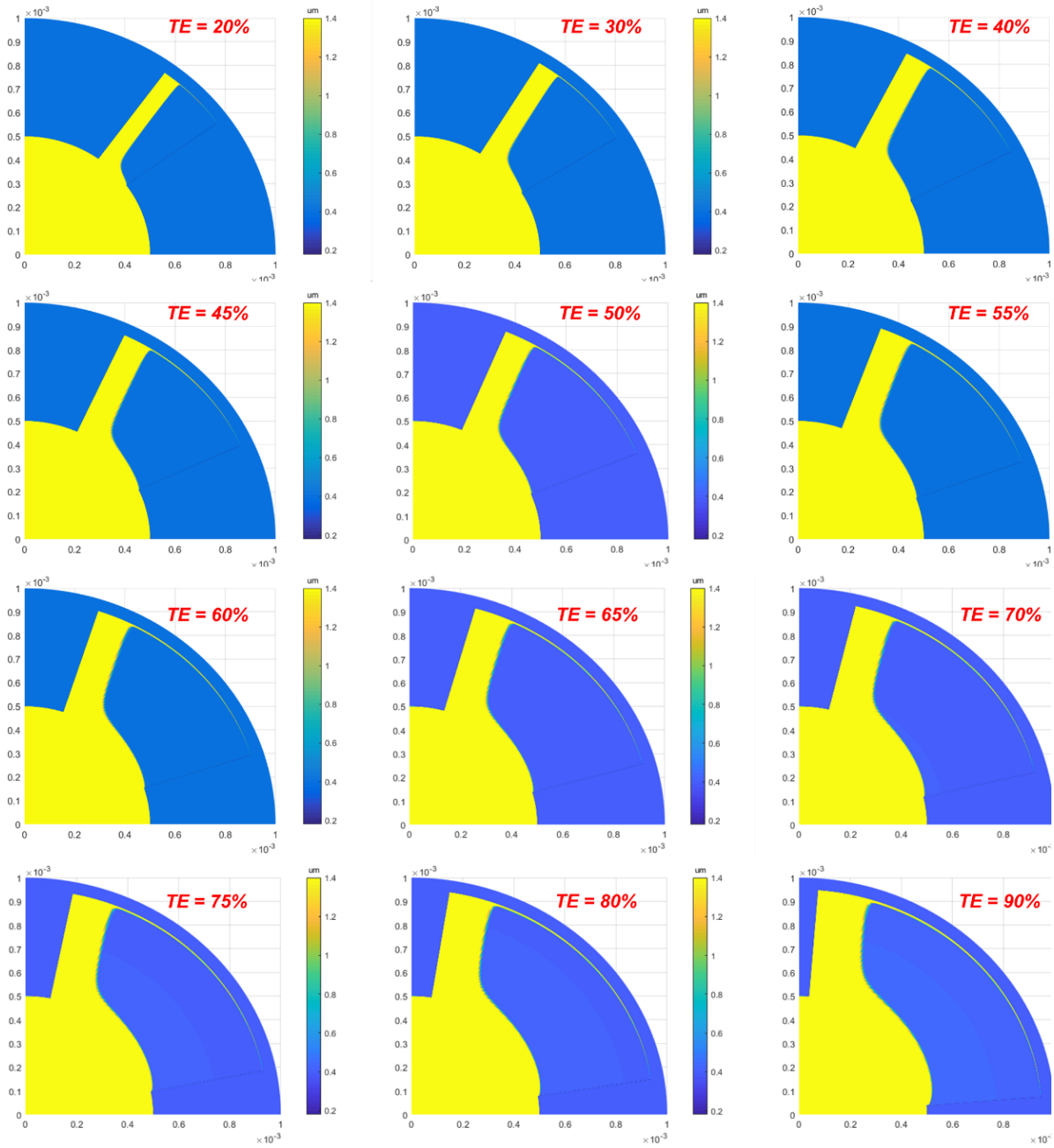

Figure 4-18 (a) Film thickness distribution of pocketed bearing at different TE_θ (400 nm, 942.5 $rad \cdot s^{-1}$, 50% TE_r)

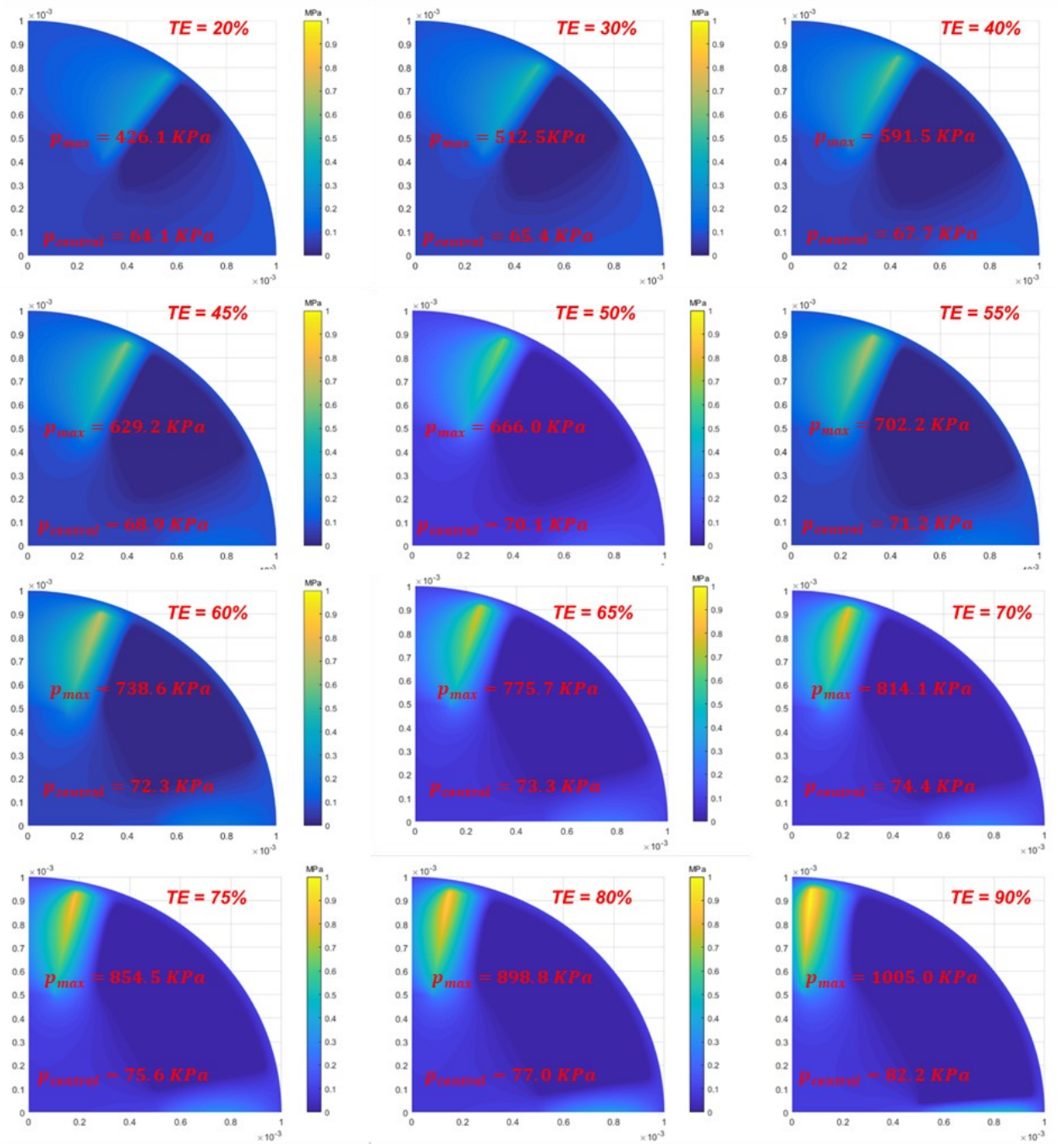

Figure 4-18 (b). Pressure distribution of pocketed bearing at different TE_θ (400 nm, 942.5 $rad \cdot s^{-1}$, 50% TE_r)

Mechanism of Load Support Variation with TE_θ

The mechanism underlying the variation in load support as a function of circumferential pocket extent is analysed in this section. As described above, several effects occur simultaneously when the circumferential pocket extent increases:

1. The low-pressure cavitation region expands. Correspondingly, the pressure active region

where positive load support is generated shrinks, which acts to reduce load support.

2. The average pressure in the pressure active region increases steeply, which acts to increase load support.

3. The pressure in the central flat region increases, which acts to the increase of load support.

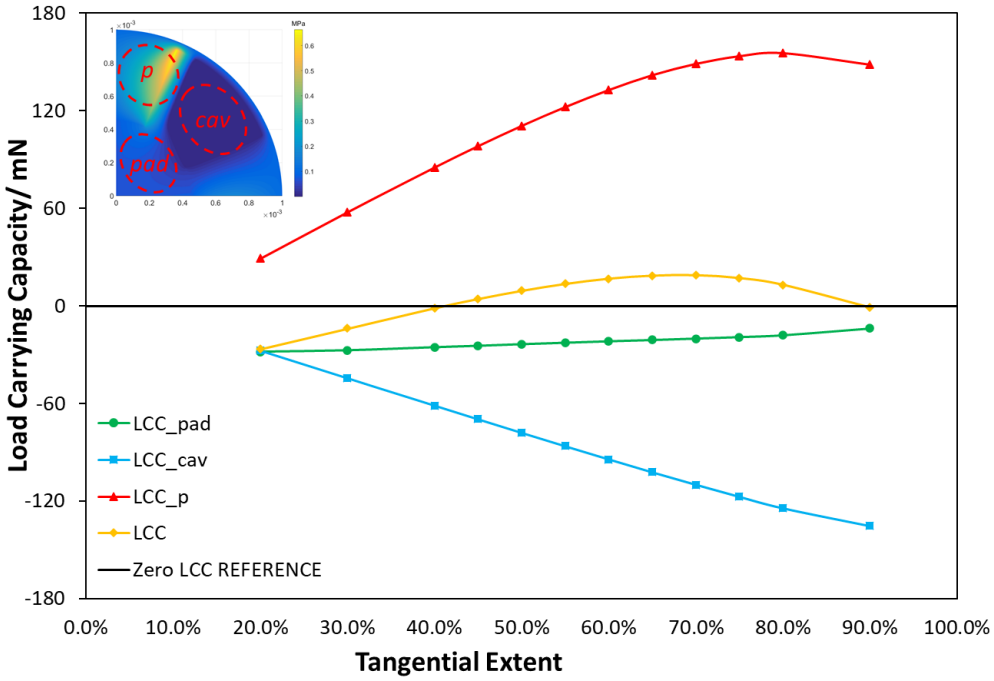

Figure 4-19. Variations with TE_θ of total load carrying capacity and contributions from central pad, cavitation region and pressure active region (400 nm, 942.5 $rad \cdot s^{-1}$, 50% TE_r)

As demonstrated in Figure 4-19, the total load capacity has three contributions: the load supported by the central flat region (LCC_pad), the load supported by the pressure active region (LCC_p) and load supported by the cavitation region (LCC_cav). The load supported by the pressure active region (LCC_p) increases monotonically with circumferential pocket extent for TE_θ values in the range 20% to 80%; this trend is dominated bythe average pressure in the active region which increases with rising TE_θ. However, the gradient of the LCC_p curve gradually decreases due to contraction of the pressure active region. LCC_p passes through a maximum when TE_θ ~ 80%, then decreases with any further increase in TE_θ >80%. In this region, even though the pressure in the active region still increases, the area of this region is too small and still decreasing so that the overall load capacity decreases. The load supported

by cavitation region is negative as the pressure in the cavitation region is constant and lower than the atmospheric pressure. The area of this region of constant low pressure increases with increasing TE_θ and this results in continually decreasing load support. As demonstrated in Figure 18 (b), the pressure in the central flat region keeps increasing with rising TE_θ, and consequently the load supported by the central flat region increases with increasing TE_θ.

The total load support first increases with TE_θ as the contribution from the pressure active region and central flat region outweigh the load support decrease from cavity expansion. As the load support in the pressure active region rises increasingly slowly while the load support in the cavitation region falls at almost a constant rate, the load support increase equals the load support decrease in the cavitation region when TE_θ is 68%. Therefore, the total load support peaks when TE_θ is 68% and then decreases as TE_θ is further increased.

4.3.4. Effect of Pocket Extent in Radial Direction

This section investigates the effect on bearing performance of varying the radial pocket extent (TE_r) from 20% to 80% with minimum film thickness values from 400 nm to 2000 nm under a fixed rotational speed (942.5 $rad \cdot s^{-1}$). The pocket step height and circumferential pocket extent also remain unchanged (h_{step}=1 μm, TE_θ=50%).

Load Carrying Capacity

Curves showing load carrying capacity as a function radial pocket extent (TE_r) for different minimum film thicknesses are shown in Figure 4-20. For all minimum film thicknesses less than 2 μm, the load capacity increases monotonically with increasing radial pocket extent. The gradients of the load capacity versus curves are small in the range where TE_r rises from 20% to 30%. The gradients of the curves jump to high values when TE_r is increased from 30% to 40% and then gradually decrease as TE_r is further increased from 40% to 90%. Comparing Figures 4-16 and 4-20 it can be seen that a much larger load capacity improvement can be achieved by increasing TE_r than by setting TE_θ to the optimum value. For example, as the radial pocket extent increases from 50% to 90%, the load capacity of the 0.4 μm bearing curve increases from 18.6 mN to 44.1 mN. Similar to the phenomenon observed in TE_θ optimization, the load support improvement achieved by increasing TE_r is lager when minimum film thickness is lower.

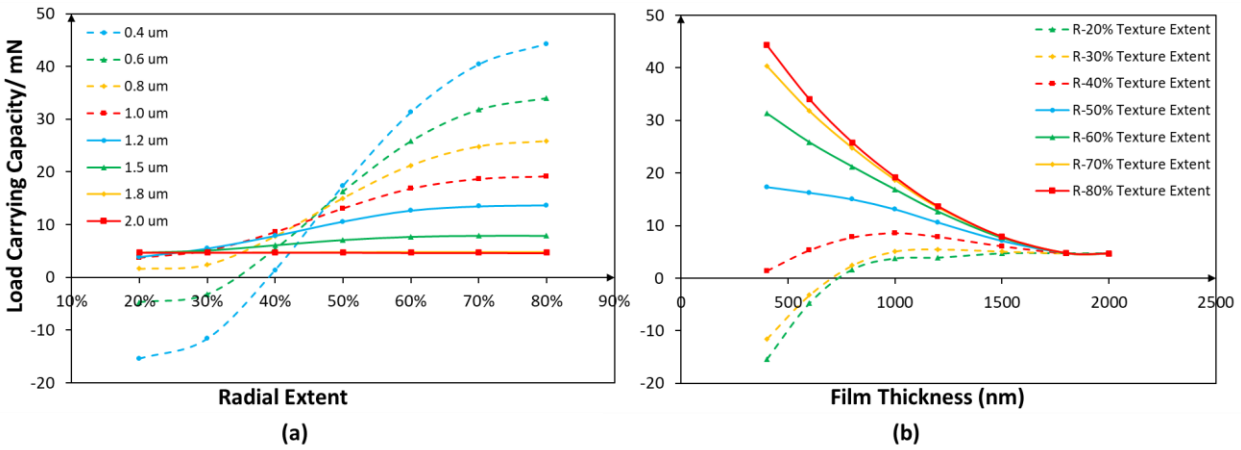

Figure 4-20. (a) Load carrying capacity of pocketed bearing vs. radial extent of pocket (50% TE$_\theta$, 942.5 $rad \cdot s^{-1}$); (b) Load carrying capacity of pocketed bearing vs. minimum film thickness (50% TE$_\theta$, 942.5 $rad \cdot s^{-1}$)

Load capacity versus minimum film thickness curves for different TE_r values are demonstrated in Figure 4-20 (b). When the radial pocket extent is less than 40%, the load capacity decreases as the film thickness is reduced. This indicates that, for pockets with small extent in radial direction, the load capacity loss due to cavity expansion overweighs the load capacity increase due to pressure increase in the active region when minimum film thickness is reduced. The load capacity for the pocketed parallel bearing with 50% TE_r first rises when minimum film thickness is reduced from 2000 to 1000 nm then decreases as film thickness is further reduced. This phenomenon has been explained in the previous film thickness variation section. When radial pocket extent is greater than 50%, the load capacity keeps increasing with decreasing minimum film thickness and the slope of the curves increases with increasing TE_r. This indicates that, for large values of radial pocket extent, the load capacity loss resulting from cavity expansion is outweighed by the load capacity gain from pressure increase in the active region as film thickness is reduced.

Frictional Torque and Friction Coefficient

The variations in total frictional torque, Couette friction and Poiseuille friction as a function of radial pocket extent at fixed operational conditions (942.5 $rad \cdot s^{-1}$, 400 nm) are displayed in figure 4-21 (a). Here, the total frictional torque increases slightly with TE_r (*e.g.* when the pocket extent is 20%, the frictional torque is 1.7 μNm and this rises to 2 μNm when the radial pocket extent reaches 90%). Both the Couette and Poiseuille friction increase with increasing radial pocket extent. As the radial extent increases, the area with thicker film ($h = h_{min} + h_{step}$)

shrinks. Correspondingly, the thin film region increases causing an increase in shear rate Therefore, Couette frictional torque increases with increasing radial pocket extent. When TE_r increases, the length of the leading edge of the pocket where hydrodynamic pressure is generated increases and causes the expansion of the high pressure region. Therefore, the Poiseuille friction torque increases with rising TE_r. The rate at which the frictional torque rises with TE_r gradually reduces towards zero when TE_r approaches 100%. This is because the pocket expands towards the inner part of the bearing where the radius is smaller. Therefore, the rate at which the area of the high pressure region increases with TE_r becomes smaller as TE_r approaches 100%.

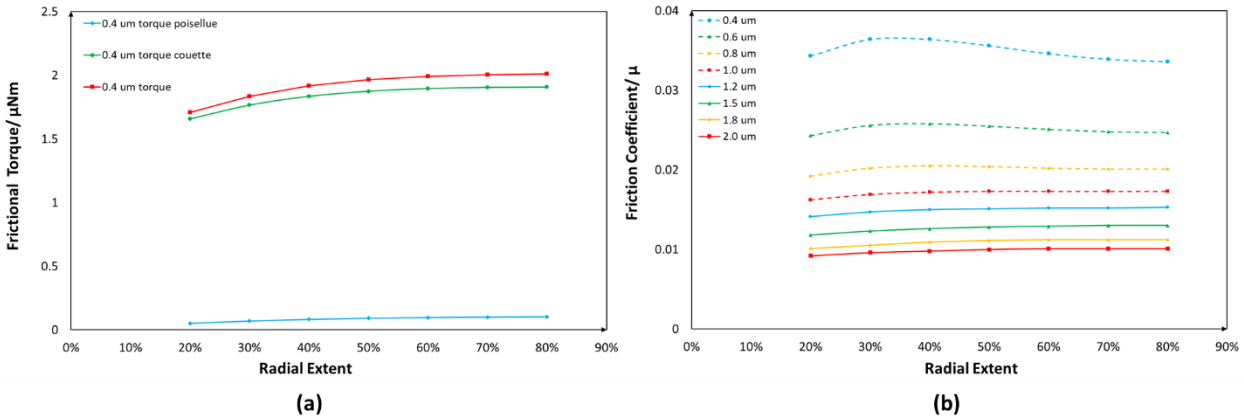

Figure 4-21. (a) frictional torque of pocketed bearing vs. radial extent of pocket (50% TE$_\theta$, 942.5 $rad \cdot s^{-1}$); (b) Friction coefficient of pocketed bearing vs. radial extent of pocket for different film thicknesses (50% TE$_\theta$, 942.5 $rad \cdot s^{-1}$)

Curves of friction coefficient versus TE_r are displayed in figure 4-21 (b). For all minimum film thickness values below 1000 nm, the friction coefficient increases slightly when TE_r is increased from 20% to 30%. This is because the frictional torque rises rapidly whereas the load support increases slowly in this range. As TE_r rises from 30% to 70%, the load capacity increases rapidly whereas the frictional torque increases more slowly, and consequently the friction coefficient decreases with TE_r. When TE_r is further increased, both the load capacity and frictional torque become stable so that the friction coefficient versus TE_r curves levels out when TE_r is greater than 70%.

Pressure Distribution and Film Thickness Distribution

Film thickness distribution and pressure distribution contours obtained under fixed operational

conditions (50% TE_r, 942.5 $rad \cdot s^{-1}$ ω, 400 nm h_{min}) for bearings with a series of different radial pocket extent values are shown in Figures 4-22 (a) and (b).

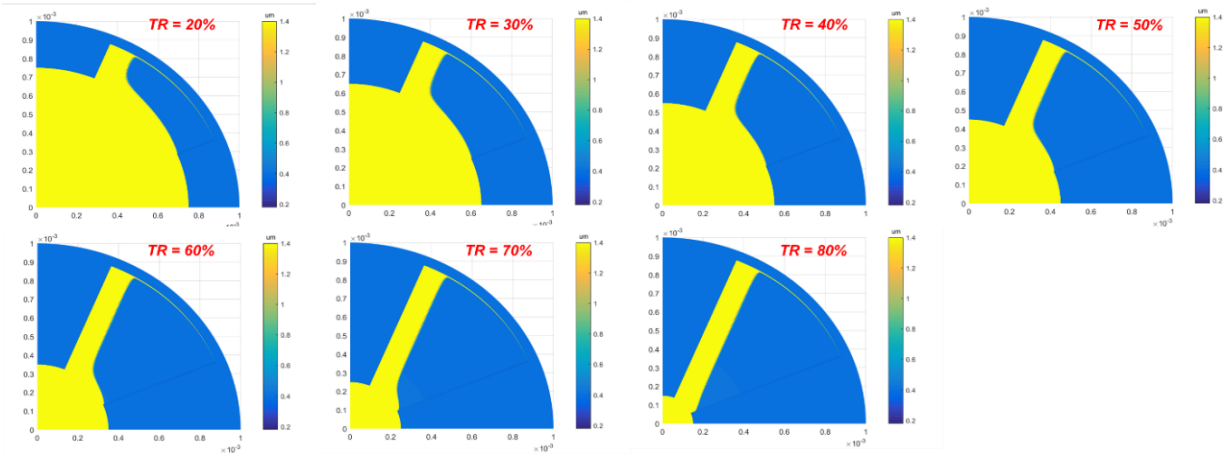

Figure 4-22 (a). Film thickness distribution of pocketed bearing at different TE_r values (400 nm, 942.5 $rad \cdot s^{-1}$, 50% TE_θ)

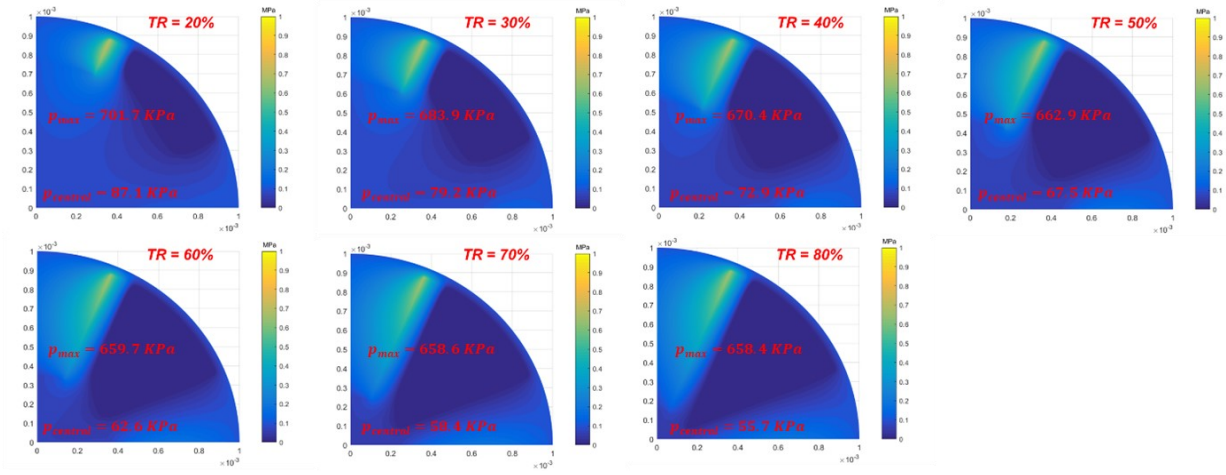

Figure 4-22 (b). Pressure distribution of pocketed bearing at different TE_r values (400 nm, 942.5 $rad \cdot s^{-1}$, 50% TE_θ)

Figure 4-22 (a) shows that cavitation occurs for all TE_r values, and the area of the cavity enlarges in the radial direction with increasing radial pocket extent. In the radial extent range from 20% to 70%, cavitation starts to occur when liquid initially passes the diverging step. It can also be seen for the bearing with 80% TE_r that cavitation does not occur in areas where the radius is smaller than a threshold value, not even in the trailing step of the pocket. This is because, when the pocket extent is increased to 80%, the radius at the inner end of the pocket's leading step is very small (r = 0.15 mm) and therefore liquid speed is low so that cavitation is

less favourable or does not occur at all. Also, as the pocket is gradually extended towards the centre, the angular width of the pressurised region becomes larger whereas the angular width of the cavity becomes smaller. This indicates that, when TE_r is increased, the increase in pressurised area is larger than the expansion of the cavity. For all TE_r values, cavitation does not occur in the central flat region where liquid experiences no divergence.

The low-pressure cavity expands in radial direction with increasing radial pocket extent as a result of the increase in length of the trailing step. The pressure active region also expands with increasing radial pocket extent as the length of leading step is extended. The maximum pressure generated around the leading step is relatively constant with TE_r, (*e.g.* the maximum pressure generated by 20% TE_r is 700 kPa and this declines only slightly to 660 kPa when the radial extent is increased to 80%). The pressure in the central region decreases from 87 kPa when TE_r is 20% to 56 kPa when TE_r is increased to 80%. The pressure reduction in the central flat region results from the inwards expansion of the cavitation region. However, the area of the central flat region where the pressure is below ambient also decreases as the pocket is extended inwards.

Mechanism of Load Support Variation with TE_r

The mechanism underlying the variation in load capacity as a function of radial pocket extent is analysed in this section. Similar to the case when circumferential pocket extent is varied, several effects occur simultaneously:

1. The low-pressure cavitation region expands. As the pressure in this region is much lower than ambient, this acts to decrease load support.
2. The pressure active region also expands with increasing TE_r, which can result in an increase in load support. In addition, the angular width of the pressurised region increases whereas the angular width of the cavity decreases as the pocket is extended towards the bearing centre, which indicates that the area expansion rate of the pressurised region is greater than that of the cavitation region.
3. The pressure in the central flat region decreases when TE_r is increased. The area of the central flat region also decreases when TE_r is increased.

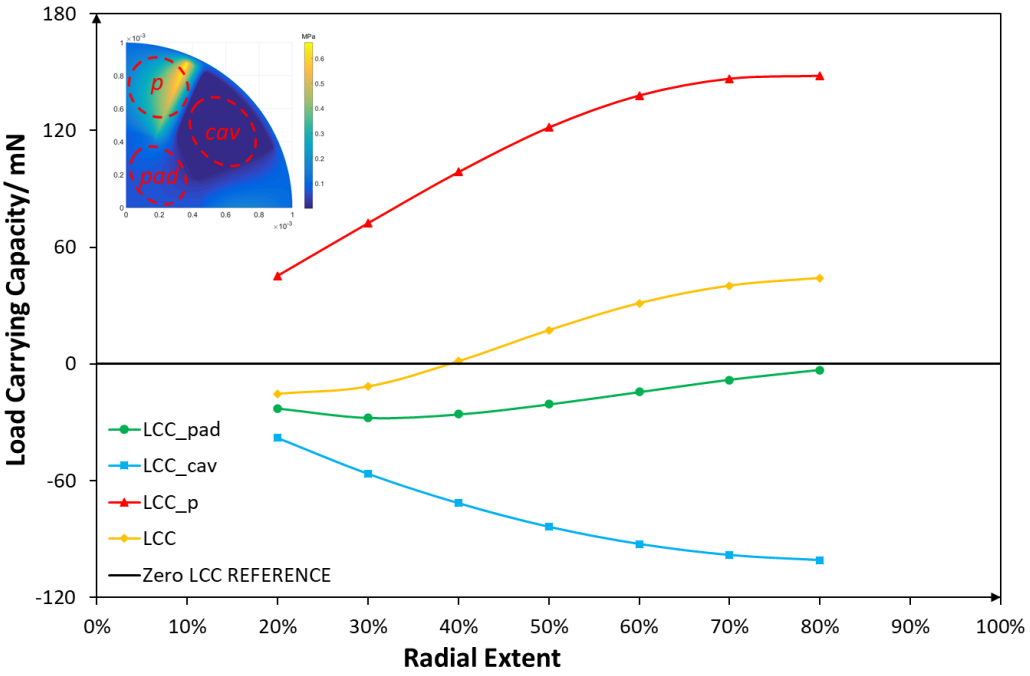

Figure 4-23. Variations with TE_r of total load carrying capacity and contributions from central pad, cavitation region and pressure active region (400 nm, 942.5 $rad \cdot s^{-1}$, 50% TE_θ)

Figure 4-23 shows the total load capacity, LCC, divided into three parts: LCC_p, LCC_cav and LCC_pad. This shows that the load supported by the pressure active region (LCC_p) keeps increasing with TE_r, which agrees with the effect described in bullet point no. 2 of the previous paragraph. The rate at which the LCC_p increases with ascending radial extent approaches zero when TE_r reaches 90%. It indicates that increasingly smaller increase of LCC_p is achieved when pocket radial extent gets gradually larger. That is resulted from an increasingly smaller rate at which the area of the pressure active region expands.

As the pressure in the cavity is constant and lower than ambient, the load support from this region is negative. The area of the cavitation region increases with TE_r and this results in an increasingly negative contribution to load support.

Figure 4-23 shows that the load supported by the central flat region is also negative as the pressure here is also below ambient. Moreover, the negative LCC_pad declines when TE_r is increases from 20% to 30%. This results from the pressure reduction in this region. Conversely, LCC_pad increases with TE_r above 30%, as a result of the area of the central flat pad region decreasing rapidly when the pocket extent in radial direction is extended beyond 30%.

The total load support increases monotonically with TE_r as the contribution from the pressurised region outweighs the negative contribution due to cavity expansion. When TE_r reaches 30% and keeps increasing, the load capacity in the central flat pad region also increases with TE_r and the pressurised region expands faster than the cavitation region. Therefore, the load capacity increase due to the pressure active region and central flat pad region outweighs the load capacity decrease from the cavitation region for the whole TE_r range. It is reasonable to predict that higher load capacity can always be achieved using pockets with larger TE_r.

4.4 Geometric Optimization of the Micro Pocketed Parallel Thrust Bearing

In terms of load support, it can be concluded that there is an optimum value of circumferential pocket extent (between 62% and 68% depending on the minimum film thickness) whereas load support keeps increasing with increasing radial pocket extent (at least for all investigated minimum film thickness values). Friction coefficient (*i.e.* transmission efficiency), improves with increasing radial extent, and only fluctuates slightly when the radial pocket extent is varied. However, these conclusions are approximate since they are arrived at by fixing the pocket extent in one direction while varying it in the other. This approach can be improved by varying the pocket extent in both directions simultaneously to obtain the optimum pocket shape for the pocketed parallel thrust bearing under different operating conditions. To achieve this, the pocket extent in the radial direction was varied from 20% to 80% while the pocket extent in the circumferential direction was varied from 20% to 90%. Fine interpolation between data points were used to precisely obtain the optimum pocket shape and resulting friction and load support performance values. The results are shown in Figure 4-24.

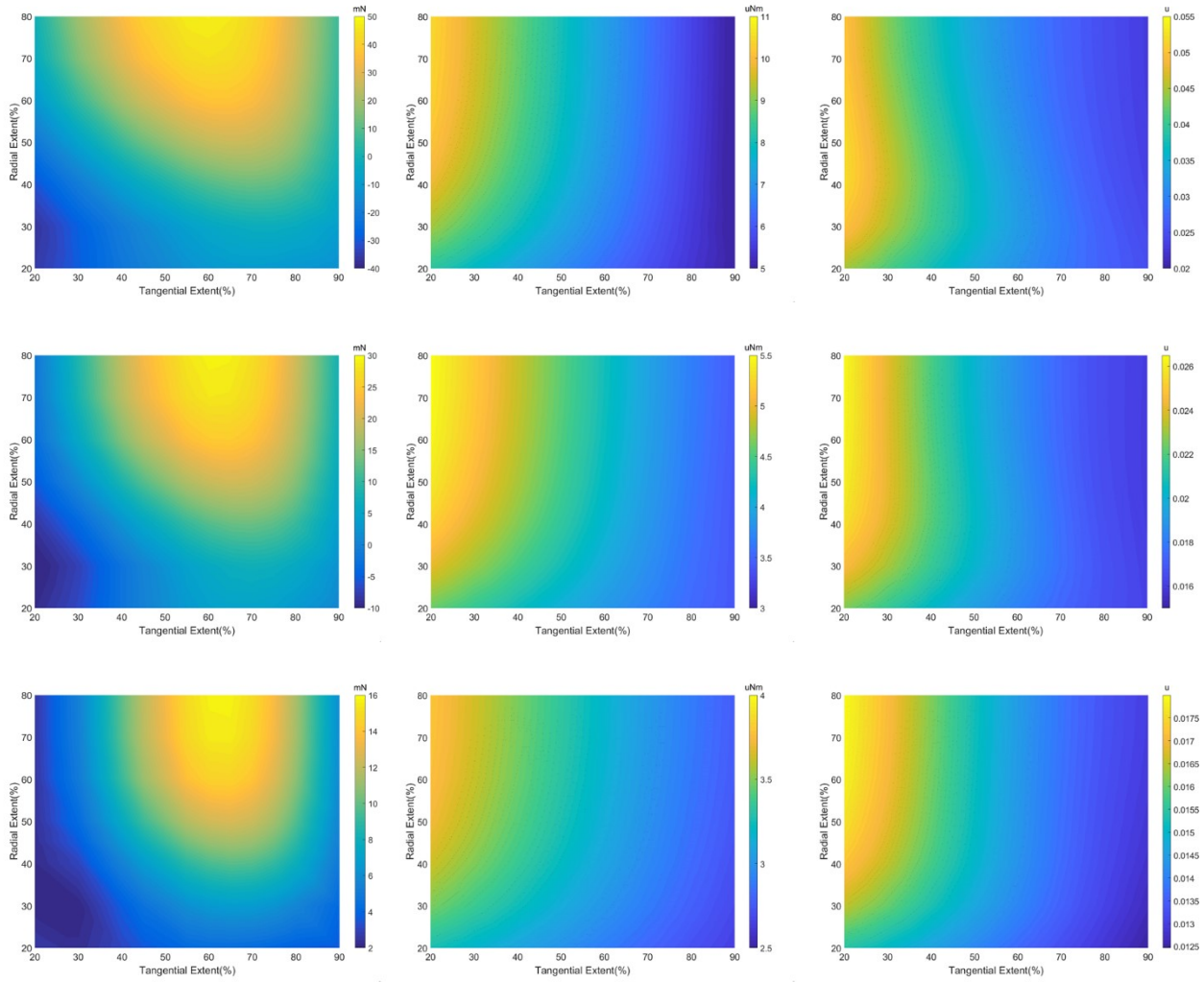

Figure 4-24. Load carrying capacity (left), frictional torque (centre) and friction coefficient (right) of the pocketed parallel thrust bearing against circumferential and radial pocket extent at film thicknesses of 400 nm (top), 800 nm (middle), and 1200 nm (bottom)

Load Carrying Capacity

Figure 4-24 shows that, for all minimum film thicknesss (loading conditions), the load support is positively correlated with radial pocket extent for all values of circumferential pocket extent.

Load capacity increases with circumferential extent (TE_θ) first and peaks at an optimum value before reducing as TE_θ is further increased. This trend holds for all values of radial extent (TE_r) and all minim film thicknesses. The optimum TE_θ value is not only affected by the operating condition (minimum film thickness), which has been discussed in the previous section but also varies with different TE_r values. When the minimum film thickness is 400 nm, the optimum TE_θ is 60% for a bearing with 80% TE_r and the load support reaches 47.53 mN. However, it is

obvious from the load carrying capacity map that the optimum TE_θ increases with decreasing radial pocket extent in direction. When TE_r equals 20%, the optimum TE_θ reaches 75%. A similar trend can be observed when minimum film thickness is increased to 800 and 1200 nm.

When the minimum film thickness is increased to 1200 nm, the optimum TE_θ and TE_r combination is 80% TE_r and 65% TE_θ (15.7 mN LCC is achieved), which is slightly different from the value when minimum film thickness is 400 nm (80% TE_r and 60% TE_θ). However, the pocketed parallel thrust bearing with 80% TE_r and 60% TE_θ can still achieve good LCC performance under this operational condition (15.58 mN LCC is achieved).

It can be concluded that for pocketed parallel thrust bearings, the largest load carrying capacity can be achieved by manufacturing pockets with a large radial pocket extent combined with a circumferential pocket extent of around 65%.

Frictional Torque and Friction Coefficient

Figure 4-24 shows that, for all minimum film thickness, the frictional torque decreases with increasing circumferential pocket extent whereas it increases with increasing radial pocket extent. As discussed above, the total frictional torque results mainly from the Couette flow friction whereas the Poiseuille friction accounts for only a small percentage. Therefore, the frictional torque reduces when the area of the region with high film thickness is increased (*i.e.* pocket size is increased) and this can be achieved by increasing TE_θ or reducing TE_r.

Figure 4-24 also show that friction coefficients are negatively correlated with circumferential pocket extent whereas it fluctuates slightly with radial pocket extent. The pocket shape giving lowest friction coefficient is: $TE_\theta = 90\%$, $TE_r = 80\%$ (*i.e.* the maximum values of pocket extent in both directions). The minimum friction coefficient for this optimised shape varies from 0.0231 to 0.0160 to 0.0130 as the film thickness is varied from 400 to 800 to 1200 nm. However, the load capacity ($TE_\theta = 90\%$ and $TE_r = 80\%$) is greatly reduced compared to that of the $TE_\theta = 65\%$ and $TE_r = 80\%$ bearing. The friction coefficients for the bearing with optimum load support ($TE_\theta = 65\%$ and $TE_r = 80\%$) are 0.0271, 0.0179 and 0.0141 for film thickness values of 400, 800 and 1200 nm, which constitutes increases above the optimum friction values of 17.3%, 11.9% and 8.5% respectively. Therefore, the friction coefficient of the bearing shape giving maximum load support is only slightly higher than the friction optimised shape.

Optimization Guide of the Pocketed Parallel Thrust Bearing

For this type of pocketed parallel thrust bearing, large load carrying capacity can be achieved by designing radial pocket extent to be high (80% or higher) and the circumferential pocket extent to be around 65%. Minimized friction coefficient can be achieved by manufacturing the bearing with larger pocket extent in both radial and circumferential directions but the load carrying capacity efficiency would be unacceptably low. On the other hand, the friction coefficient of the bearing generating the maximum load carrying capacity is only slightly higher than the minimum value. Therefore, the pocket with high TE_r value and TE_θ to be around 65% can be considered optimum in terms maximum load carrying capacity and acceptably low friction coefficient.

4.5 Thermal Effect Investigation

All the simulated bearing performance results demonstrated in the previous sections of this chapter are generated by the iso-thermal model in which the thermal effect is neglected. The thermal effect on the bearing performance is neglected initially as the temperature increase of the lubricant within the micro thrust bearing are assumed to be low. That assumption is made based on the fact that the size of the simulated bearing and the applied load on the bearing are both tiny. However, this assumption might not be appropriate for all cases as the rotational speeds of the micro thrust bearing in the simulation are quite high (higher than 730 $rad \cdot s^{-1}$). Therefore, the heat generated from the high sliding speed shearing might still be high enough to cause large increase of lubricant temperature. The temperature rise will lead to reduction of the lubricant viscosity thereby affecting the performance of the micro thrust bearing (including load carrying capacity and frictional torque, etc.).

A relatively simple thermal model with which the approximated effective temperature of the lubricant ($Temp_{eff}$) and the maximum lubricant temperature rise ($\delta Temp_{max}$) can be computed is integrated into the current micro thrust bearing model. [153] Results from this method is approximate and are not able to show temperature distribution over the thrust bearing. A more precise thermal model with which temperature distribution can be generated will be built in the future (after this research).

4.5.1. Temperature Computation Model

After obtaining the converged pressure distribution ($P_{i,j}$) and film fraction distribution ($S_{i,j}$), the frictional torque of the bearing, *T*, and the power loss caused by the frictional torque, *PL*, can be calculated. The power lead to the heat generation within the thrust bearing. Some amount of (γ) the generated heat is removed by the convection through the lubricant flow, which results in the temperature rise of the lubricant within the micro thrust bearing. The effective temperature of the lubricant can be then calculated with Eq. (4-6) below.

$$Temp_{eff}^{k} = Temp_{in} + \gamma \frac{PL}{c_p \dot{M}_{in}} \tag{4-6}$$

$Temp_{eff}^{k}$ is the effective temperature of the lubricant from k^{th} temperature computation iteration. $Temp_{in}$ is the lubricant temperature at the inlet where the lubricant is entrained into the bearing - in this simulation, it is equal to 25 ℃.

γ is the amount of heat transferred away by lubricant flow convection, some literatures show that the amount of heat transferred away by lubricant flow convection usually ranges from 50% to nearly 100% [155]. The γ value is assumed to be 70% in this research, this assumption value could be dubious but it lies in the reasonable range and the results can still roughly show how the bearing performance is affected by the thermal effects.

c_p is the specific heat of the lubricant (hexadecane), which has been given in Table 4-2 of this chapter. $\dot{M}_{in}$ is the mass flow rate entrained into the thrust bearing.

The lubricant flow is automatically entrained into the thrust bearing through the outer boundary of the thrust bearing, B3. Along the outer boundary of the thrust bearing, at the parts where the radial direction pressure gradient is negative, the lubricant will be sucked into the bearing by the negative liquid pressure gradient.

$$\dot{M}_{in} = \int_0^{2\pi} \left[-\frac{\rho h^3}{12\eta} \cdot \left(\frac{\partial p}{\partial r} \right) \cdot r_{out} \right] \cdot d\theta \tag{4-7}$$

Integral only conducted in parts where $\frac{\partial p}{\partial r}$ is negative.

The viscosity of the lubricant is determined by the effective temperature:

$$log\, log(v + 0.7) = b - c\, log(Temp_{eff}) \tag{4-8}$$

The variation of the lubricant viscosity will in turn affect the pressure and film thickness

distribution of the thrust bearing. With the converged $P_{i,j}$ and $S_{i,j}$ computed from $(k+1)^{th}$ iteration, $Temp_{eff}^{k+1}$ can be computed. The thermal computation loop is conducted for several loops until the effective temperature reach converged status.

4.5.2. Results Showing the Thermal Effects on the Micro Thrust Bearing Performance

The thermal effects on the micro thrust bearing performance are investigated by comparing simulation results obtained from the iso-thermal numeric model and the simulation results obtained from the thermal effected-integrated numeric model. Detailed graphic parameters of the simulated bearing and its operational conditions are given in Table 4-7 below.

Table 4-7. Graphic parameters of the micro bearing and operation conditions in the thermal effect investigation

Graphic & Operational Parameters	Symbols	Value
Lubricant used in simulation	–	Hexadecane
Simulated bearing number of pads	N_p	4
Pocket extent in radial direction	TE_r	50%
Pocket extent in circumferential direction	TE_θ	50%
Minimum film thickness	h_{min}	400 nm/ 800 nm/ 120 nm
Pocket depth/ Step height	h_{step}	1 μm
Rotational Speed	ω	942.5 $rad \cdot s^{-1}$
Lubricant Temperature Outside the Bearing	$Temp_o$	25°C

Temperature Rise

There is no temperature increase in the results from the iso-thermal simulation model – *i.e.* the temperature of the lubricant within the micro bearing is equal to the temperature of the lubricant outside the bearing (25 ℃). However, results from the thermal-effect considering model shows that, when the bearing operates at 942.5 $rad \cdot s^{-1}$ speed with 400 nm-thick minimum film thickness, the effective temperature of the lubricant entrained in the bearing climbs up by around 52 ℃ from 25 ℃ to 77 ℃. For the case that the bearing operates with 800 nm-thick minimum film thickness, the increase of the effective temperature is approximately 13 ℃, from 25 ℃ to 38 ℃. When the minimum film thickness is increased to 1200 nm, the lubricant temperature within the thrust bearing ascends from 25 ℃ to 29 ℃.

The increase of the lubricant effective temperature decreases drastically with increasing minimum film thickness. This is because when the minimum film thickness increases, the shear

stress of the entrained lubricant becomes smaller as the shear rate is reduced, which results in less generated heat from the thrust bearing. In addition, it is indicated from equation (27) that the flow rate at which the lubricant is entrained into the thrust bearing increases with ascending minimum film thickness. Therefore, more heat can be taken away from the bearing by the lubricant convection when the minimum film thickness is larger hence resulting in lower temperature rise.

Thermal Effects on the Bearing Pressure Distribution and Film Thickness Distribution

Film thickness distribution contours of the micro thrust bearing operating at 942.5 $rad \cdot s^{-1}$ rotational speed with different minimum film thickness values obtained from iso-thermal model are demonstrated in figure 4-25 (a). The film thickness distribution contours of the micro thrust bearing operating at the same conditions obtained from thermal effect-considered model are illustrated in figure 4-25 (b). The temperature rise results in the reduction of the dynamic viscosity of the lubricant thereby affecting the film thickness distribution of the micro thrust bearing. It can be seen from figure 4-25 that, after considering the thermal effect, the predicted cavity size becomes smaller. That is because when all other operation conditions are fixed, the cavity size shrinks with decreasing liquid viscosity.

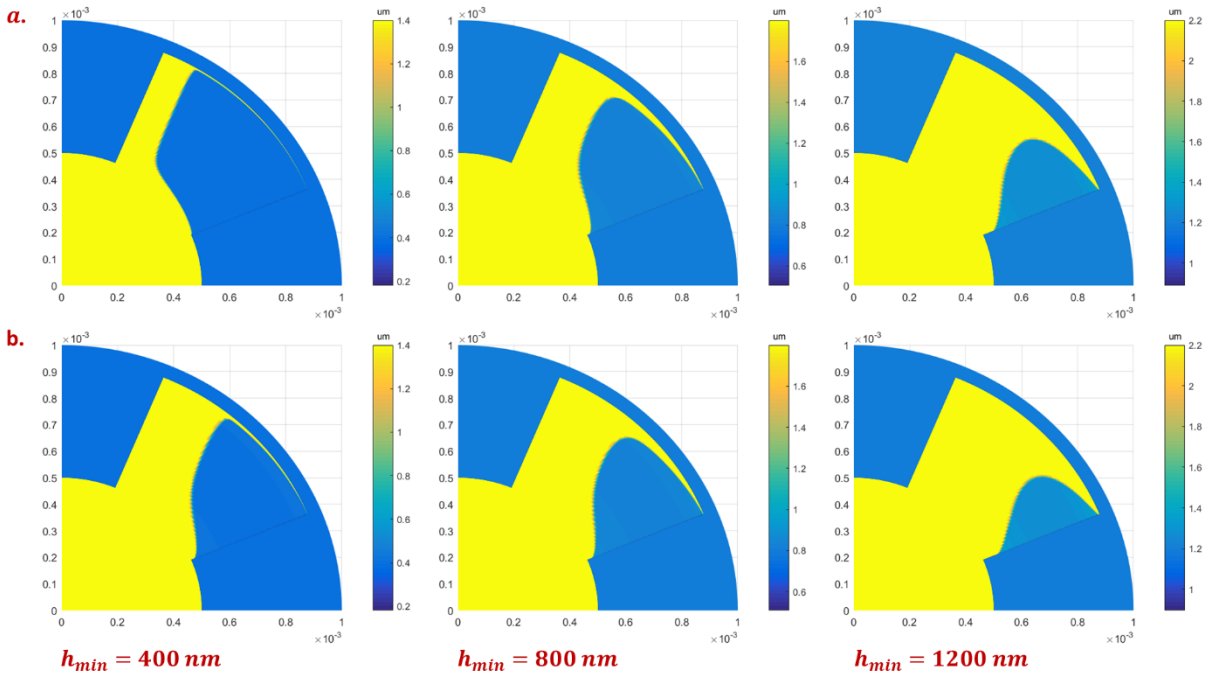

Figure 4-25. (a) Film thickness distribution of the thrust bearing obtained from iso-thermal model; (b) Film thickness distributions of the thrust bearing obtained from thermal effect integrated model

Pressure distribution contours of the thrust bearing operating at 942.5 $rad \cdot s^{-1}$ rotational speed with different minimum film thickness values obtained from iso-thermal model are demonstrated in figure 4-26 (a). The pressure distribution contours of the micro thrust bearing operating at the same conditions obtained from thermal effect-considered model are illustrated in figure 4-26 (b). Comparing figure 4-26 (a) and figure 4-26 (b) it can be seen that the predicted maximum pressure generated around the leading step of the thrust bearing decreases after considering thermal effect. That is caused by the reductions in the liquid lubricant after considering the liquid temperature climb-up. The pressure in the central flat area increases for all simulated cases, which is resulted from the shrink of the cavitation area.

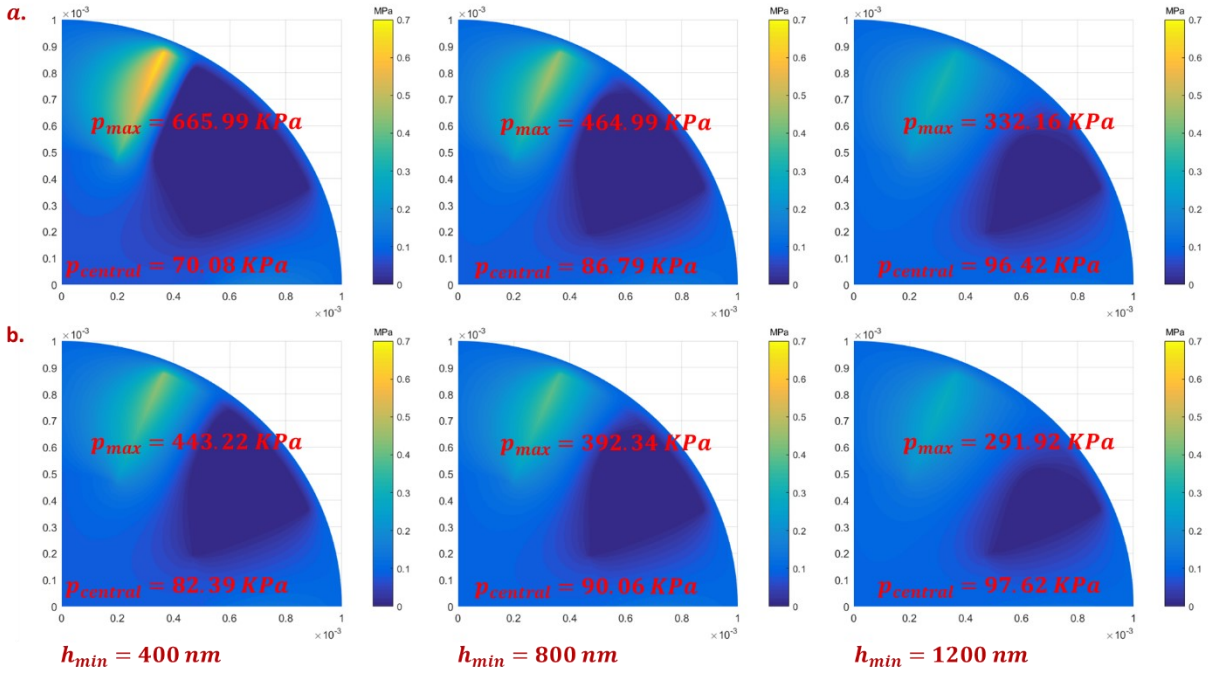

Figure 4-26. (a) Pressure distribution contours of the thrust bearing obtained from the iso-thermal model; (b) Pressure distribution contours of the thrust bearing obtained from the thermal effect integrated model

Thermal Effects on the Bearing Load Carrying Capacity and Frictional Torque

An increase in lubricant temperature would lead to the reduction of the load carrying capacity as the viscosity of the lubricant descends with increasing lubricant temperature. Reduction of the liquid lubricant would also result in the reduction of the frictional torque as both the Couette shear stress and the Poiseuille shear stress decreases with declining liquid viscosity.

The thermal effect on the bearing performance becomes increasingly smaller when the

minimum film thickness ascends as the increase of the lubricant effective temperature drops sharply when the minimum film thickness is increased.

4.6 Conclusions

This research has presented a mass-conserving, finite volume model and the use of this model to investigate the performance of pocketed parallel thrust bearings operating in the steady state hydrodynamic lubrication regime. Cavitation is properly treated with JFO boundary conditions so that cavities exist when the lubricant pressure drops to the vapour pressure. The effect of the dimensional scales of the bearing geometry, operational conditions (rotational speed and minimum film thickness) and pocket shape (circumferential and radial extent) on performance (pressure distribution, film thickness distribution, load carrying capacity and frictional torque) have been studied. Optimization of pocket geometry to achieve high load capacity and transmission efficiency under different operational conditions has also been achieved.

The key findings are:

- **Normalized bearing performance is determined by the key ratios representing bearing geometry ($TE_\theta, TE_r, \delta, \gamma, \varepsilon$).** When all dimensions are scaled simultaneously, all the normalized performance values including pressure distribution, film thickness distribution, load carrying capacity and friction coefficient remain unchanged. The actual load capacity increases quadratically and the frictional torque increases cubically with the bearing size.
- **The pocketed parallel thrust bearing is suitable for small scale applications (MEMS).** This is because the transmission efficiency and normalized load capacity increase significantly when the bearing radius is reduced to μm-mm scales (while keeping pocket shape constant).
- **Lubrication behaviors (cavitation development and pressure generation) are strongly affected by operating conditions (minimum film thickness and rotational speed).** Low film thickness and high rotational speed act to increase the pressure within the active region; however, this is counteracted by a simultaneous contraction of this region accompanied by an expansion of the cavitation region.

- **The dependence of load support on operational conditions is largely affected by the cavitation development.** As cavitation expands, due to an increase in speed or decrease in film thickness, two antagonistic effects occur simultaneously: i) cavitation area increase which acts to decrease load support and ii) pressure increase in the active region which acts to increase load support. The overall load support behavior is therefore determined by which effect outweighs the other.

- **Pocket extent in radial and circumferential directions also affect the load carrying capacity and transmission efficiency by determining cavitation development and pressure generation.** Large circumferential pocket extent expands the cavitation region and increases the pressure in the active region. Large radial pocket extent expands both the pressure active and cavitation region.

- **High load support and relatively low friction coefficient can be achieved by designing the bearing with a circumferential pocket extent of 65% and radial pocket extent of 80%.** Load capacity increases monotonically with radial pocket extent; however, it increases and then decreases as the circumferential pocket extent is increased (with max value at $TE_\theta = 65\%$). Friction coefficient decreases with higher TE_θ and fluctuates slightly with TE_r.

- **Effective temperature rise of the entrained lubricant can be higher than 50 °C when the minimum film thickness of the thrust bearing is lower than 400 nm but it declines drastically to lower than 5 °C when the minimum film thickness is increased to 1200 nm.** The load carrying capacity, frictional torque, maximum generated hydrodynamic pressure and the cavitation area decrease, which is caused by the thermal effect. The thermal effect can be severe for the cases in which the minimum film thickness is low because of the high shear (more heat is generated) and the low income lubricant flow rate (less heat is taken away by the convection); whereas the thermal effect becomes negligible when the minimum film thickness is higher than 1200 nm because of the low shear rate (less heat is generated) and the high entrained lubricant flow rate (more heat is taken away by the convection).

Chapter 5: Experimental Methodology

Fabrication process of the 500 μm-radius micro pocketed parallel thrust bearings is developed in this research. The micro pocketed parallel thrust bearings are manufactured with micro fabrication techniques and tested on a specially designed MEMS tribometer. Following the lab tests of the bearing performance, the micro bearings are then installed on the prototype energy harvesting turbine together with ruby journal bearings.

This chapter can be divided into two parts. In the first part the detailed fabrication processes for the micro thrust bearing are reported. Introduction of the operation mechanism and calibration procedures of the MEMS tribometer on which Stribeck curves of the micro thrust bearings can be obtained are presented in the second part.

5.1 Fabrication Processes of the Micro Thrust Bearing

As mentioned in the literature review chapter, micro fabrication techniques have many unique advantages including high fabrication accuracy, ability to construct micro and complicated features and ability to manufacture parts with different designs simultaneously. Therefore, micro fabrication techniques are selected as the methods to manufacture the micro thrust bearing in this research.

Detailed procedures and parameters of the fabrication processes of the micro thrust bearings are presented in this section. As stated, micro fabrication process enables bearings with different graphics to be manufactured simultaneously from one single wafer. Figure 5-1 below demonstrates the overview of the distribution of all the thrust bearings on a single wafer which are fabricated simultaneously.

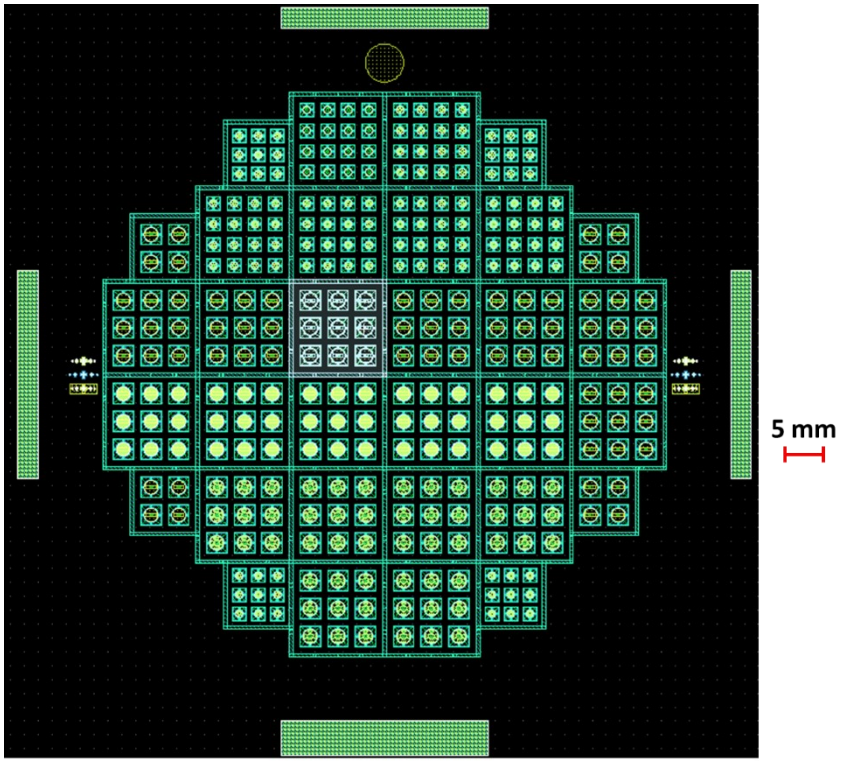

Figure 5-1. Distribution of All the Micro Thrust Bearings on a Single Wafer

5.1.1 Graphics of All the Fabricated Micro Thrust Bearings and the Masks with Different Features for the Bearing Fabrication

As introduced before, one of the most important principles of micro fabrication is that the graphic features of the fabricated parts are accomplished layer by layer. The graphic features of all the fabricated micro bearing parts are demonstrated in this section. Brief introduction of fabrication process for all the graphic features are also given in this section.

Five layers of fabrication processes in total are conducted to complete the manufacture for all the thrust bearing parts within a single wafer, which are:

Layer 1: Shallow etching process 1 on the front side of the wafer;

Layer 2: Shallow etching process 2 on the front side of the wafer;

Layer 3: Deep etching process 1 on the front side of the wafer;

Layer 4: Metal deposition process on the back side of the wafer;

Layer 5: Deep etching process 2 on the back side of the wafer.

Graphic Features of All Types of Bearings and How the Features Are Fabricated

i. 1-mm Diameter Patterned Thrust Bearing Stator Pad

Graphic features of the 1-mm diameter thrust bearing stator pad with three different patterns are demonstrated in figure 5-2.

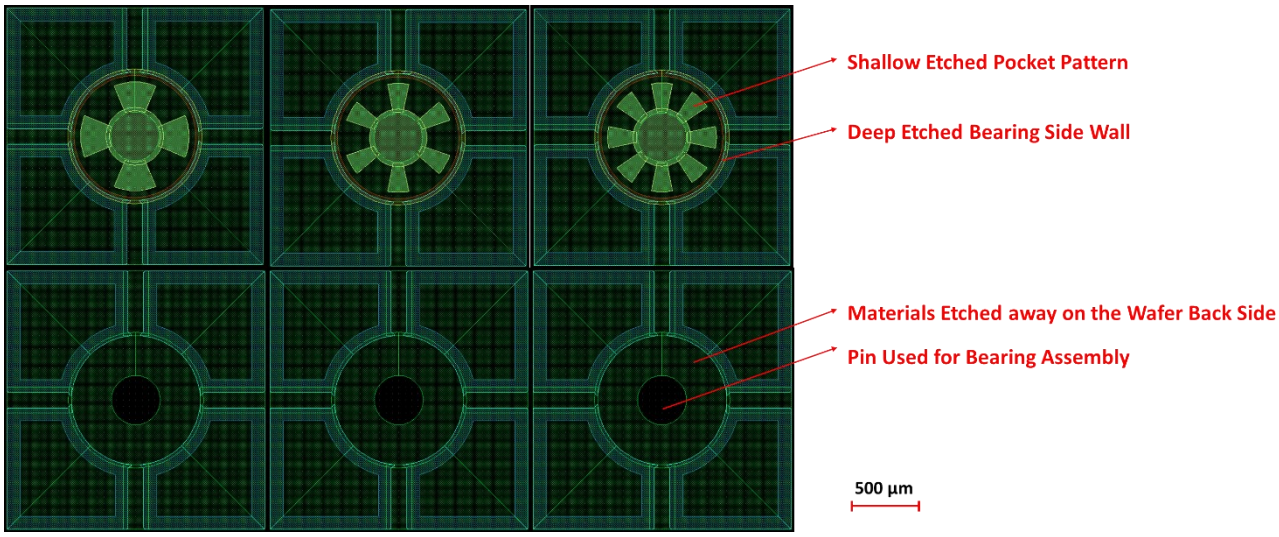

Figure 5-2. Graphic Features of 1-mm Diameter Bearing Stator Pads

It can be seen from figure 5-2 that, for the 1-mm diameter thrust bearing stator pad, pocket patterns with low depth are etched on the front surface (which is the surface in contact with the rotor pad surface), this feature is completed through layer 2 process.

The side walls of the stator pads are fabricated by deep etching through layer 3 process.

A circular pin which is used for bearing assembly is fabricated by etching away all the materials surrounding this circular pin. This is conducted through layer 5 process.

ii. 2-mm Diameter Patterned Thrust Bearing Stator pad

Graphic features of the 2-mm diameter thrust bearing stator pad with three different patterns are demonstrated in figure 5-3.

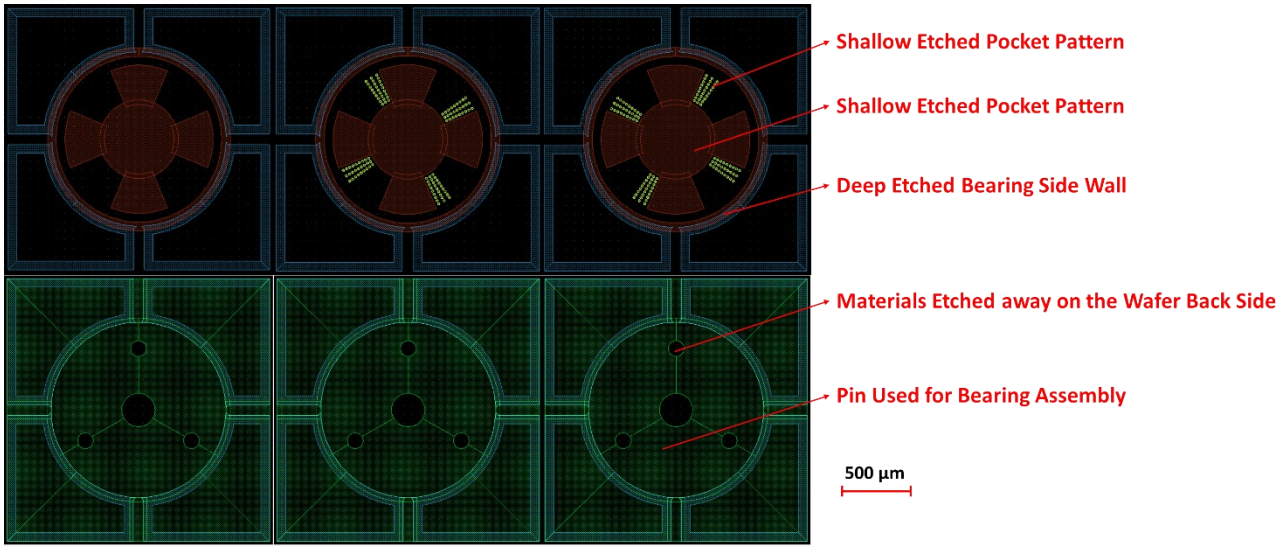

Figure 5-3. Graphic Features of 2-mm Diameter Bearing Stator Pads

It can be seen from figure 5-3 that, for the 2-mm diameter thrust bearing stator pad, micro dimples with 25 µm diameter are firstly etched on the front surface with designed etching depth, this is conducted through layer 1 process. Then the pocket patterns are etched on the front surface with another designed etching depth, which is completed through layer 2 process.

The side walls of the stator pads are fabricated by deep etching through layer 3 process.

Four circular pins which are used for bearing assembly are fabricated by etching away all the materials surrounding the circular pins. This is conducted through layer 5 process.

iii. 2-mm diameter flat thrust bearing rotor pad

Graphic features of the 2-mm diameter thrust bearing rotor pad with smooth contact surface is demonstrated in figure 5-4.

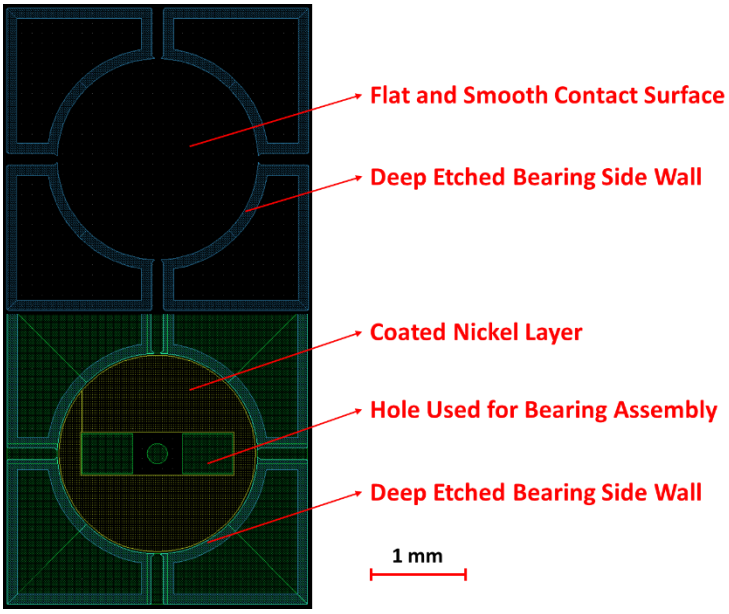

Figure 5-4. Graphic Features of 2-mm Diameter Bearing Rotor Pads

It can be seen from figure 5-4 that, for the 2-mm diameter thrust bearing rotor pad, the contact surface is the unprocessed flat and smooth wafer surface.

The side walls of the stator pads are fabricated by deep etching through layer 3 process.

A thin nickel layer is coated on the back side of the rotor pad, which is used to hold the rotor pad on a magnetic ring when installing the rotor pad on the micro turbine or on the test rig. This is accomplished through layer 4 process.

There are two square holes and one circular hole on the back side of the rotor pad which is conducted by deep etching in the layer 5 process.

5.1.2 Alignment Marks

Alignment marks on the masks for each layer fabrication process are used to guarantee the features fabricated through different layers of processes can be aligned correctly together. Figure 5-5 below demonstrates all the alignment marks for the bearing fabrication.

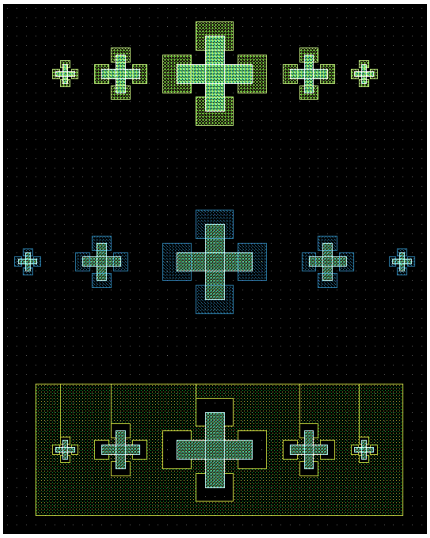

Figure 5-5. Alignment Marks for the Micro Bearing Fabrication

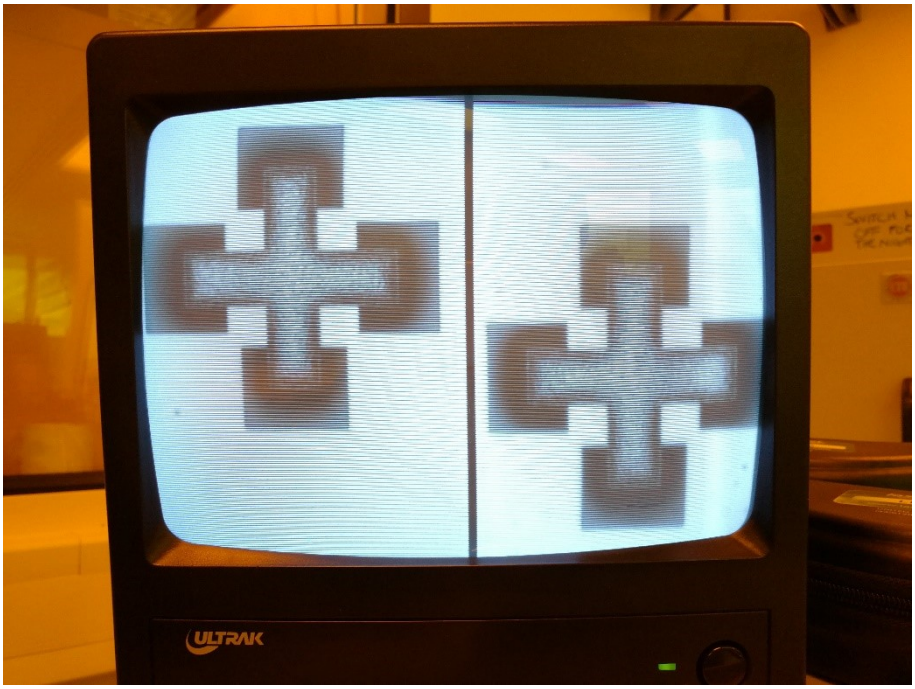

Figure 5-6. Aligning the Marks on the Masks to the Marks on the Processed Wafer

5.1.3 Fabrication Procedures of the Micro Thrust Bearings

Detailed procedures of the micro fabrication processes for the micro thrust bearings are given below in chronological order.

Silicon Wafer Used for Bearing Fabrication

All the micro thrust bearing pads are produced from a BSOI silicon wafer. As demonstrated in figure 5-7, the silicon wafer consists of three layers which are: a 380 μm-thick handle layer, a

300 µm-thick device layer and a 1 µm-thick silicon dioxide layer buried inside, between the device layer and handle layer.

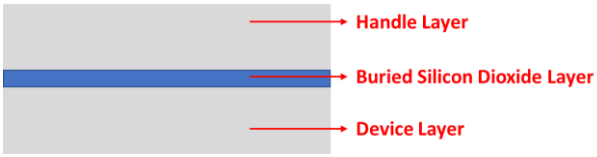

Figure 5-7. Silicon Wafer Used for Fabrication

Both sides of the silicon wafer are polished, the surface roughness for both sides, R_a, is lower than 2 nm.

The features on the front side of the bearing pads (side which is in contact) are fabricated on the handle layer of the wafer whereas the features on the back side of the bearing pads are fabricated on the device layer of the wafer. Therefore, the fabrication process of the silicon bearing pads are conducted firstly on the handle layer then on the device layer of the wafer. The thin buried silicon dioxide layer between the handle layer and the device layer are used to prevent the processing conduct on one side of the wafer from affecting the other side of the wafer.

Other detailed Technical parameters of the wafer are listed in table 5-1 below.

Table 5-1. Technical Parameters of the Silicon Wafer

Technical Parameter	Value
Handle Layer Thickness	380 µm
Device Layer Thickness	300 µm
Buried Silicon Dioxide Layer Thickness	1 µm
Surface Roughness of Handle Layer Side	$R_a < 2$ nm
Surface Roughness of Handle Layer Side	$R_a < 2$ nm
Resistivity	1 KΩ·m^{-1}to 2 KΩ·m^{-1}
Doping Type	P type, Boron using as the dopant
Silicon Wafer Orientation	<1 0 0>
Silicon Wafer	100 mm

Handle Layer Fabrication Processes

As mentioned, the etched patterns of the bearing pads and the side walls of the bearing pads are fabricated on the handle layer of the wafer, which is completed through layer 1, layer 2 and layer 3 fabrication processes.

i. Layer 1 Fabrication Process: Shallow Etching Process of the Micro Dimples on the Bearing Stator Pads

In this layer of fabrication process, the shallow micro dimples are etched on the contact surface of the bearing stator pads.

a. Using compressed air to blow both sides of the wafer to blow away any possible dusts on the wafer surfaces.

b. Growing 100 nm-thick silicon dioxide layer over the wafer surfaces to provide additional protect for the photoresist covered area of the handle and device layer surfaces during etching processes. This is conducted in the oxidation furnace.

- Oxidation Temperature: 1100 ℃
- Temperature ramp up rate: 20 ℃·min^{-1}
- Oxidation temperature dwelling time: 20 min
- Oxygen flow supply rate: 1 L·min^{-1}

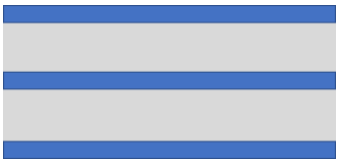

c. Measure the grown silicon dioxide layer thickness by using ellipsometer.

d. Clean the wafer surfaces using oxygen plasma, this is conducted in the Plasma System 80.

- Plasma gas supply rate: 60 sccm O2 and 2 sccm O2
- Plasma cleaning temperature: 20 ℃
- Plasma cleaning ambient pressure: 50 mTorr
- Plasma power: 200 W
- Cleaning time: 10 min

e. Shallow etching step 1: photoresist spin coating. In this step, the photoresist is spin coated over the handle layer surface of the wafer, a baking process is conducted after the spin coating process to harden the photoresist. That is to prevent possible deformation of the photoresist in the fabrication processes afterwards.

- Photoresist: AZ9260
- Spinning conditions: first, 500 (rpm·min-1) ·sec-1 acceleration/ 500 rpm·min-1 terminate speed/ 10 sec dwell time; then, 2000 (rpm·min-1) ·sec-1 acceleration/ 5000 rpm·min-1 terminate speed/ 40 sec dwell time;
- Baking photoresist on the hot plate after spin coating: 100 ℃ for 2 min.

f. Shallow etching step 2: photolithography of the photoresist to form the patterned mask for etching process afterwards. Three procedures are conducted in chronological order in this step which are: UV light exposing, photoresist mask developing and residual photoresist descum.

- UV light exposing. In this procedure, designed mask for layer 1 fabrication process is placed over the wafer on the mask aligner. The mask lefts the pattern area which will be shallowly etched later exposed to the UV light and covers all other area of the photoresist covered wafer. UV light power density for the exposure: 6.32 mW ·cm-2; exposing time: 80 sec.

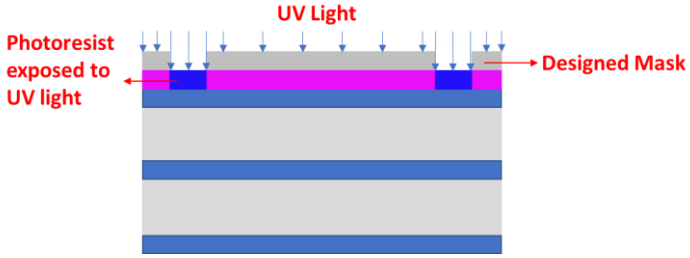

- Photoresist mask developing. In this step, the wafer is rinsed into developer liquid, the photoresist which has been exposed to the UV light will get released from the wafer and dissolve in the developer liquid whereas the photoresist which has not

been exposed to the UV light will not be affected by the developer liquid. The patterns on the designed mask are then formed on the photoresist. The developer liquid consisting of 20 ml AZ400K developer and 80 ml DI water. The temperature of the developing liquid is 26 ℃. The time for the photoresist mask developing is 4 min 5 sec.

- Photoresist descum. After photoresist developing procedure, some residual photoresist still exists. That tiny portion of residual photoresist needs to be totally cleared. This is achieved by low power oxygen plasma cleaning. The conditions of the plasma cleaning are given as follows:

  Plasma gas supply rate: 60 sccm O_2 and 2 sccm O_2. Plasma cleaning temperature: 20 ℃. Plasma cleaning ambient pressure: 30 mTorr. Plasma power: 100 W. Cleaning time: 3 min.

g. Shallow etching step 3: Silicon dioxide layer etching. Reactive ion etching (RIE) is used to remove the silicon dioxide protecting layer at open area of the photoresist mask. The etching gas is CHF_3. The etching process is not conducted continuously as the surface temperature might become too hot, hence affecting the etching rate. A Cooling procedure is conducted between two etching procedures to cool down the surface temperature. Detailed parameters of the silicon dioxide etching step are given as follows:

- Etching procedure. Etching gas supply rate: 25 sccm CHF_3, 25 sccm Ar and 2 sccm O2. Etching temperature: 10 ℃. Etching ambient pressure: 30 mTorr. Plasma power: 200 W. Etching time: 2 min.

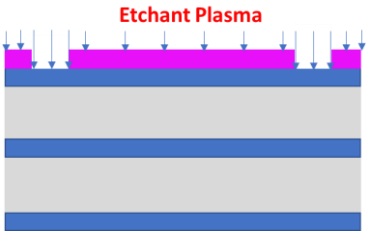

- Cooling procedure. Cold inert gas flow is used to cool down the hot wafer surface after etching. Cooling gas supply rate: 2 sccm O_2 and 50 sccm Ar. Cooling temperature: 10 ℃. Cooling ambient pressure: 50 mTorr. Cooling time: 10 min.

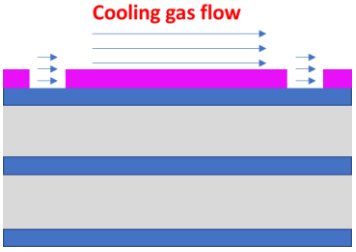

- One etching procedure and one cooling procedure consists one etching loop. After testing, 40 nm-thick silicon dioxides can be etched away. Therefore, 3 etching loops are required to completely etch the 100 nm-thick silicon dioxide layer.

h. Shallow etching step 4: Shallow Silicon etching to form the patterns on the bearing pads surfaces. Reactive ion etching (RIE) is used to etch the pattern to 1 μm depth. The etching gas is SF_6. The Si etching process is not conducted continuously neither as the surface temperature will also become hot, hence affecting the etching rate. A Cooling procedure is conducted between two etching procedures to cool down the surface temperature. Detailed parameters of the Si etching step are given as follows:

- Etching procedure. Etching gas supply rate: 30 sccm SF_6 and 10 sccm O_2. Etching temperature: 20 ℃. Etching ambient pressure: 30 mTorr. Plasma power: 200 W. Etching time: 55 sec.

- Cooling procedure. Cold inert gas flow is used to cool down the hot wafer surface after etching. Cooling gas supply rate: 2 sccm O_2 and 50 sccm Ar. Cooling temperature: 10 ℃. Cooling ambient pressure: 50 mTorr. Cooling time: 10 min.

- One etching procedure and one cooling procedure consists one etching loop. After testing, 500 nm-thick silicon can be etched away. Therefore, 2 etching loops are required to completely etch the 1 μm-thick pattern.

i. Shallow etching step 5: Post processing of RIE process for the shallow patterns. After the shallow pattern etching, the photoresist has to be stripped off for the following fabrication processes. Photoresist stripping consists of three procedures, the first procedure is to rinse the wafer into organic solvents, the second procedure is to rinse the wafer into chemical liquids the final procedure is the residual photoresist descum.

- Organic solvents rinsing. The photoresist can get dissolved in the organic solvent, the solvent used here is acetone. The wafer is rinsed into acetone for 24 hours, most of the photoresist can be stripped off in this procedure.

- Chemical liquid rinsing. Some photoresist is still left on the wafer soft after solvent rinsing as the photoresist is strongly baked on the surface. 1165 is selected as the chemical liquid to react with the left photoresist. The wafer is rinsed into 100 ml 1165 with the liquid to be heated up to 70 ℃. This rinsing procedure takes 90 min.

- Photoresist descum. After chemical liquid rinsing, tiny portion of residual photoresist might still exist. That is totally cleaned by oxygen plasma cleaning. The conditions of the plasma cleaning are given as follows:

  Plasma gas supply rate: 60 sccm O_2 and 2 sccm O_2. Plasma cleaning temperature: 20 ℃. Plasma cleaning ambient pressure: 100 mTorr. Plasma power: 250 W. Cleaning time: 10 min.

ii. Layer 2 Fabrication Process: Shallow etching process of the pocket patterns on the bearing stator pads

In this layer of fabrication process, the shallow pocket patterns are etched on the contact surface of the bearing stator pads.

Fabrication ***step d*** to ***step i*** of ***layer 1 fabrication process*** are repeated here to complete the layer 2 fabrication. However, one additional step is required to conduct before photoresist spin coating (***step e***). That is to place the wafer into a sealed pot which is filled with HMDS molecules (in gas state) for 6 min before conducting photoresist spin coating.

HMDS stands for hexamethyldisilazane, the molecular formula for HMDS is $[(CH_3)_3Si]_2NH$. It is used as the adhesion promoter for the photoresist. As micro dimples are etched on the wafer surface in layer 1 fabrication process. Direct Spin coating the photoresist on the wafer will lead to the formation of micro gas bubbles around the etched micro dimples. That could be solved by strengthening the adhesion between the photoresist and the wafer surface.

iii. Layer 3 Fabrication Process: Deep reactive ion etching process of the side walls of the bearing pads

In this layer of fabrication process, the side walls of all the bearing pads are constructed by deep reactive ion etching. The silicon handle layer has to be completely etched through to the buried 1 μm-thick silicon dioxide layer to form the bearing pads side wall.

Fabrication ***step d*** to fabrication ***step g*** are repeated before conducting the deep reactive ion etching step.

Deep reactive ion etching step. Operation mechanism of deep reactive ion etching has been introduced in detail in the previous section. Steep side walls are constructed through the anisotropic deep etching.

As mentioned before, the etching is not continuously conducted during DRIE process, the etching process and the passivation process are conducted alternatively during DRIE.

Technical details of deep reactive ion etching are given as follows. For one etching process and passivation process loop, the passivation process is firstly conducted for 8 sec, the etching process is then conducted for 3 sec. The total DRIE process lasts for 165 min.

To make sure the exposed area of the handle layer has been thoroughly etched to the buried silicon dioxide layer, the wafer has to be checked under microscope. The smooth blue silicon dioxide layer should be observed if the handle layer has been thoroughly etched.

After deep reactive ion etching of handle layer is cleared, ***step i*** of layer 1 fabrication process is repeated here to strip off the photoresist and thoroughly clean both sides of the wafer. The processing of the handle layer side is completed after finishing this step, the device layer is then conducted.

Device Layer Fabrication Processes

As mentioned, features including the thin nickel layer and the deep holes used for bearing installation on the back side of the rotor pads together with the pins which is also used for installation on the back side of the stator pads are fabricated on the device layer of the wafer. That is completed through layer 4 and layer 5 fabrication processes.

iv. Layer 4 Fabrication Process: Nickel deposition on the back side of the thrust bearing rotor pads

In this layer of fabrication process, a 10 μm-thick nickel layer is coated on the back side of the thrust bearing rotor pads. The nickel layer is coated on the rotor pads using electroplating. However, seed layer consisting of cropper and copper layers has to be sputter coated on the silicon wafer surface before nickel electroplating. The metal seed layer functions as an electrode in the electroplating process, the nickel layer grows on the metal seed layer surface.

a. Completely remove the 100 nm-thick silicon dioxide layer which is previously grown on the device layer surface of the wafer. This is also conducted using reactive ion etching method. ***Step g*** of layer 1 fabrication process is repeated here to complete silicon dioxide removing.

b. Nickel layer electroplating step 1: seed layer deposition. In this step, chromium is first deposited on the wafer device layer surface, the copper layer which is used as the electrode in the nickel electroplating process is then deposited on the chromium layer. Both layers are deposited on the wafer device layer by sputter coating.

- Chromium sputter coating. This is conducted in the sputter coater, the sputter coating power is 400 W, the coating time is 4 min.
- Copper sputter coating. The sputter coating power is 400 W, the coating time is 10 min.
- After seed layer deposition, procedures in ***step i*** of layer 1 fabrication process are conducted to strip off the photoresist and thoroughly clean the device layer surface of the wafer.

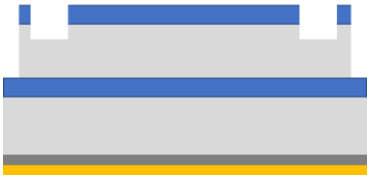

c. Nickle layer electroplating step 2: photoresist spin coating. This spin coating step are required to be conducted immediately after copper deposition as oxidation of copper will form very quickly when the copper is exposed in air. Therefore, the copper has to be covered with photoresist to prevent copper oxidation.

- Photoresist: AZ9260
- Spinning conditions: first, 500 (rpm·min^{-1}) ·sec^{-1} acceleration/ 500 rpm·min^{-1} terminate speed/ 10 sec dwell time; then, 2000 (rpm·min^{-1}) ·sec^{-1} acceleration/ 5000 rpm·min^{-1} terminate speed/ 40 sec dwell time;

- Baking photoresist on the hot plate after spin coating: 100 ℃ for 2 min.

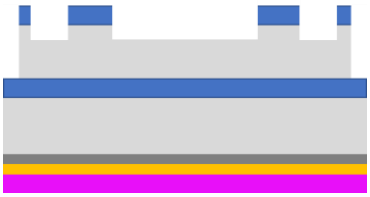

d. Nickel layer electroplating step 3: photolithography of the photoresist to form the patterned mask for nickel electroplating process afterwards.

- UV light exposing. In this procedure, designed mask for layer 3 fabrication process is placed over the wafer on the mask aligner. The mask lefts the pattern area which will be deposited with nickel layer later exposed to the UV light and covers all other area of the photoresist covered wafer. Mask alignment has to be conducted to make sure the features which are to be fabricated from the wafer device layer are accurately aligned with the features which have been fabricated from the wafer handle layer. Infrared radiation is used to here to view the alignment marks which are etched on the handle layer side.

  UV light power density for the exposure: 6.32 mW ·cm^{-2}; exposing time: 80 sec.

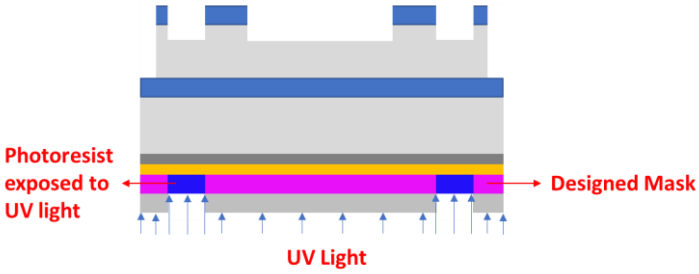

- Photoresist mask developing.

  The developer liquid consisting of 20 ml AZ400K developer and 80 ml DI water. The temperature of the developing liquid is 26 ℃. The time for the photoresist mask developing is 4 min 5 sec.

- Photoresist descum.

  Plasma gas supply rate: 60 sccm O_2 and 2 sccm O_2. Plasma cleaning temperature: 20 °C. Plasma cleaning ambient pressure: 30 mTorr. Plasma power: 100 W. Cleaning time: 3 min.

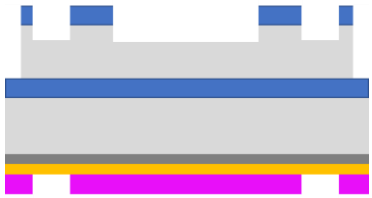

e. Nickel layer electroplating step 4: deposit nickel layer on the exposed seed layer. In this step, nickel is electroplated on the pre-deposited seed layer surface. In this process, copper layer is connected to a nickel plate, they are then rinsed into electrolyte together. Electric current is applied to force the nickel cations dissolved in the electrolyte form a coherent nickel coating layer on the copper layer surface (which functions as the electrode in the electroplating process). Before electroplating process, dioxides of copper formed on the copper layer surface are required to be removed, otherwise, the electroplating circuit would be open.

   - Dioxides of copper removement. This is conducted by rinsing the wafer into 100 ml 10% sulfuric acid for 10 sec.
   - The current applied in the electroplating process is 50 mA, the electroplating process is 52 min to grow a 10 μm-thick nickel layer over the copper seed layer.
   - photoresist stripping and wafer cleaning. ***step i*** of layer 1 fabrication process is repeated here to strip off the photoresist and thoroughly clean both sides of the wafer.

f. Nickle layer electroplating step 5: Removing unwanted copper and chromium. Before the final deep etching of the silicon wafer device layer, the unwanted copper and

chromium layers are quired to be cleared off the silicon wafer surface. Otherwise, the silicon deep etching will be prevented.

- Rinse the wafer into the copper selective etchant for 20 sec
- Rinse the wafer into the chromium selective etchant for 40 sec

v. Layer 5 Fabrication Process: Deep reactive ion etching process of the pins on the stator pads and the holes on the rotor pads

In this layer of fabrication process, the pins on the stator pads and the holes on the rotor pads are constructed by deep reactive ion etching on the silicon wafer device layer. The silicon device layer has to be completely etched through to the buried 1 µm-thick silicon dioxide layer.

Fabrication ***step d*** to fabrication ***step g*** are repeated before conducting the deep reactive ion etching step.

Within each DRIE loop, the passivation process lasts for 8 sec, the etching process lasts for 3 sec. The total time for the DRIE process for the device layer thorough etching is 131 min.

vi. Finalization of the Micro Fabrication Processes

step i of layer 1 fabrication process is conducted here to strip off the photoresist and thoroughly clean both sides of the wafer. The processing of the device layer side is completed after this step.

To finalize the fabrication process, silicon dioxide left on the handle layer surface are required to be removed as silicon dioxide is very hydrophilic and it might result in severe adhesion when the bearing pads are loaded in contact. The excessive buried silicon dioxide layer should also be removed, and it can be easily broken and blown away by compressed air.

5.2 Introduction of the MEMS Tribometer

The fabricated micro pocketed parallel thrust bearings with 500 μm radius are tested on a MEMS tribometer which is designed to mimic the bearing operation conditions in MEMS devices (tiny applied load but high rotational speed). This device is capable of accurately measuring the low frictional torque (in the scale of micro Newton meter) of the millimetre scale MEMS bearings under different load and rotational speed. The operation mechanism of the MEMS tribometer and calibration procedures of this rig are given in this section.

5.2.1 Operation Mechanism of the MEMS Tribometer

Figure 5-8 below demonstrates the MEMS tribometer with key components labelled. In the following sections, brief explanations for the mechanism of the key functions of this MEMS tribometer are given in the following paragraphs. Details of the tribometer development can be found in this reference [156]

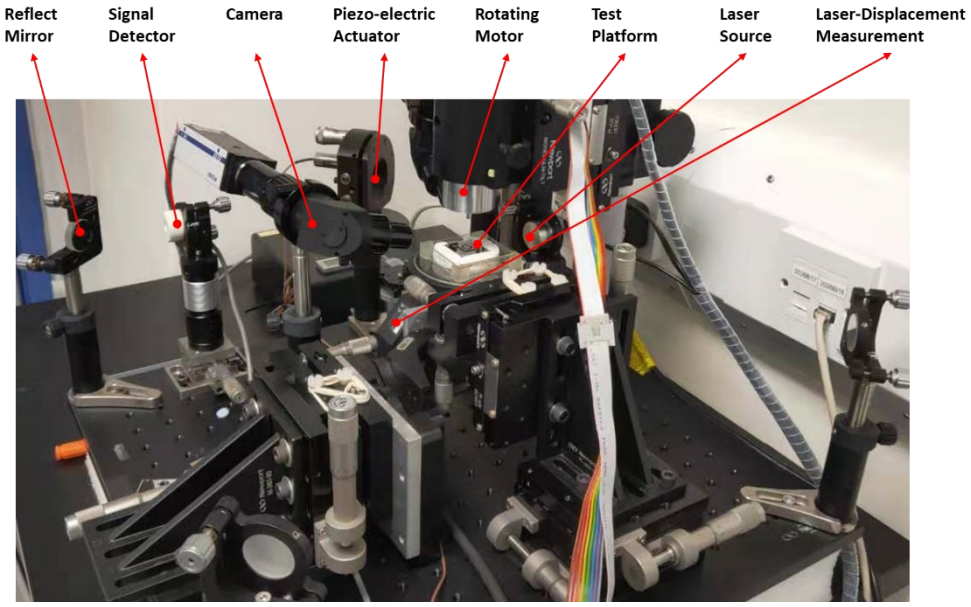

Figure 5-8. MEMS Tribometer with Key Components Labelled

Installation of the MEMS Bearing Samples and Self-Alignment Mechanism

As reported previously in this chapter, both the stator pad and the rotor pad of the MEMS thrust bearing are fabricated from silicon wafers with deep reactive ion etching techniques (DRIE). Figure 5-9 displays both sides of the 1-mm diameter thrust bearing stator pad. The stator pad is installed at the centre of the test platform by fitting the 0.38 mm-diameter central pin at the back side of the stator into the 0.39 mm-diameter hole located at the centre of the test platform. The stator bearing pad is rigidly fixed on the test platform by using transparent extra thin super glue, which is displayed in figure 5-10.

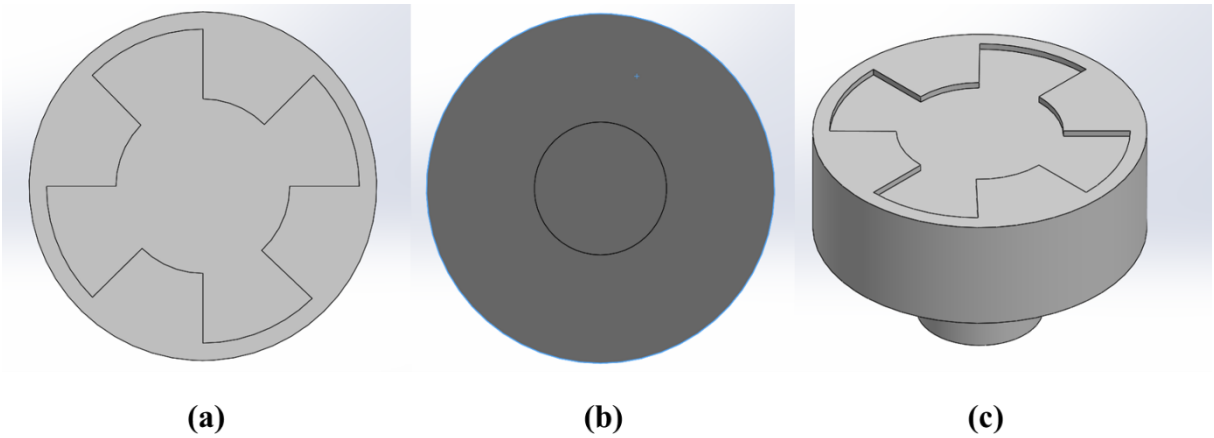

Figure 5-9. (a) Front Side of the Bearing Stator Pad (b) Back Side of the Stator Pad

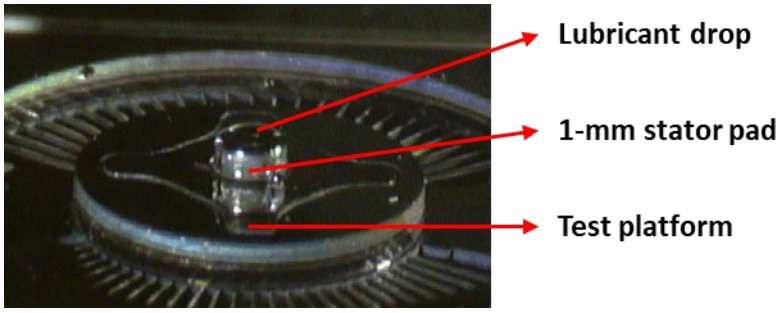

Figure 5-10. 1-mm Diameter Bearing Stator Pad Installed and Fixed on Test Platform

Figure 5-11 shows both the front and back side of the rotor pad of the thrust bearing. The contact surface of the rotor pad is flat and smooth. On the back side of the bearing rotor pad, two square holes that are symmetrically located about the centre axis of the rotor pad and one 0.2 mm-diameter circular hole located at the centre of the rotor pad. The backside of the rotor pad of the MEMS thrust bearing is uniformly coated with a 100 nm-thick nickel layer with which the rotor pad can be held by magnets.

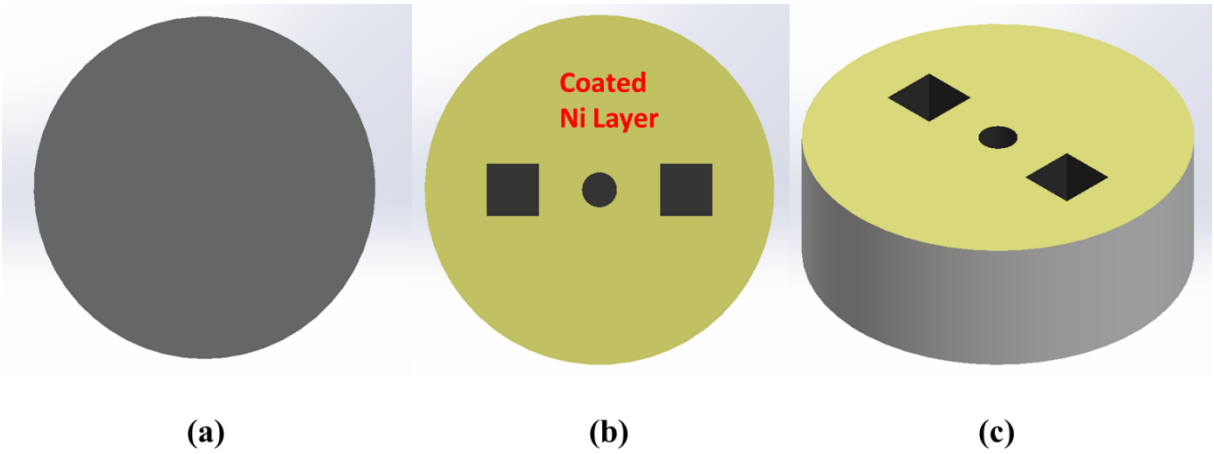

Figure 5-11. (a) Front Side of the Bearing Rotor Pad (b) Back Side of the Rotor Pad

The rotor pad of the thrust bearing is installed on the rotating shaft (shaft is directly attached to a high-speed step motor) as shown in figure 5-12 below. As shown in the cross-section view of the rotating shaft-rotor pad assembly displayed in figure 5-12, there are two square pins at the end surface of the shaft which are fitted into the corresponding pin holes on the backside of the bearing rotor pad and are used to drive the rotor pad to rotate in the same axis with the rotating shaft. A hollow cylinder-shaped magnet is fitted to the rotating shaft which is used to hold the downward facing rotor pad in position (from dropping).

A 0.3 mm-diameter ruby sphere is fixed in the tapered hole which is located at the centre of the rotating shaft end surface. When the rotor pad is installed onto the rotating shaft, the 0.2 mm-diameter circular hole at the backside of the pad will sit on the 0.3 mm-diameter ruby sphere. Considering the sphere is larger than the circular hole of the rotor pad and the surface of the ruby sphere is smooth and slippery, the rotor pad of the thrust bearing can swing freely about the sphere (which is at the centre of the rotating shaft) hence overcoming the possible misalignment when the rotor pad is loaded on the stator pad of the thrust bearing. Figure 5-13 demonstrates the rotor pad and the stator pad of the MEMS thrust bearing before and after loading, in this figure, 2 mm-diameter stator pad is used for clearer demonstration of the self-aligning mechanism of the thrust bearing. Figure 5-14 shows how the 2 mm-diameter rotor pad is loaded onto the 1 mm-diameter stator pad.

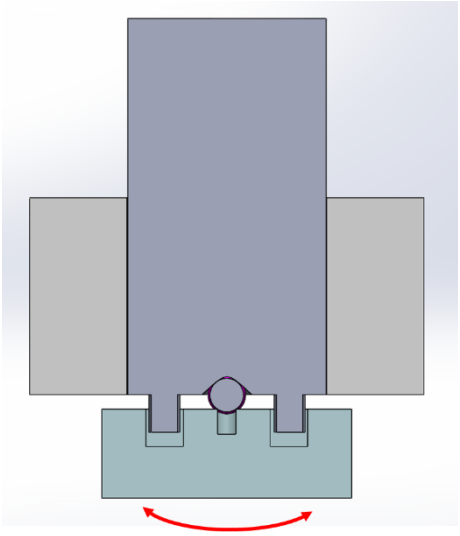

Figure 5-12. Cross-section View of the Rotating Shaft and Rotor Pad Assembly

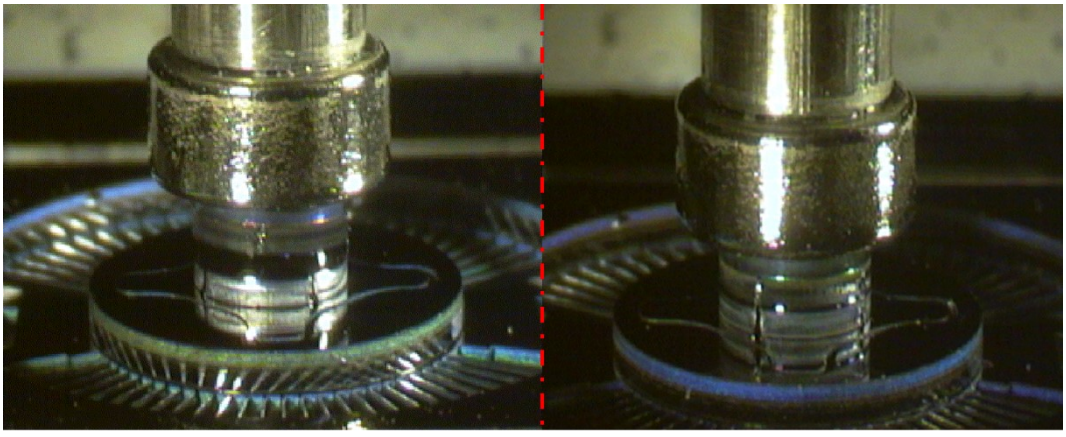

(a) **(b)**

Figure 5-13. (a) Thrust Bearing before Loading; (b) Thrust Bearing after Loading

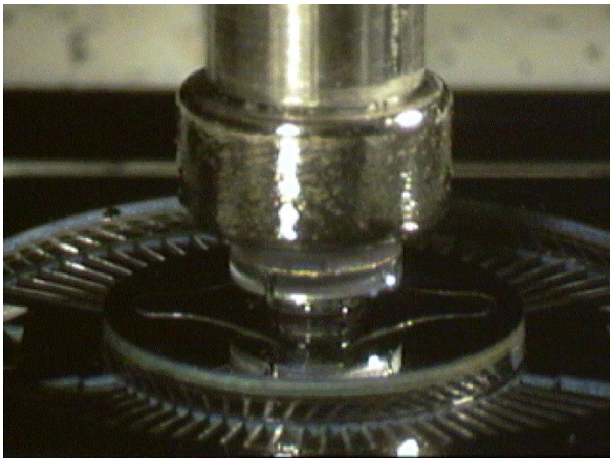

Figure 5-14. Thrust Bearing Consisting of 1-mm Stator and 2-mm Rotor after Loading

Test Platform, Applied Load Control

As mentioned before, a specially designed platform is installed on the MEMS tribometer to conduct the tests. The stator pad of the tested bearing is installed and fixed on the centre of the platform. Figure 5-15 below clearly demonstrates both sides of the test platform.

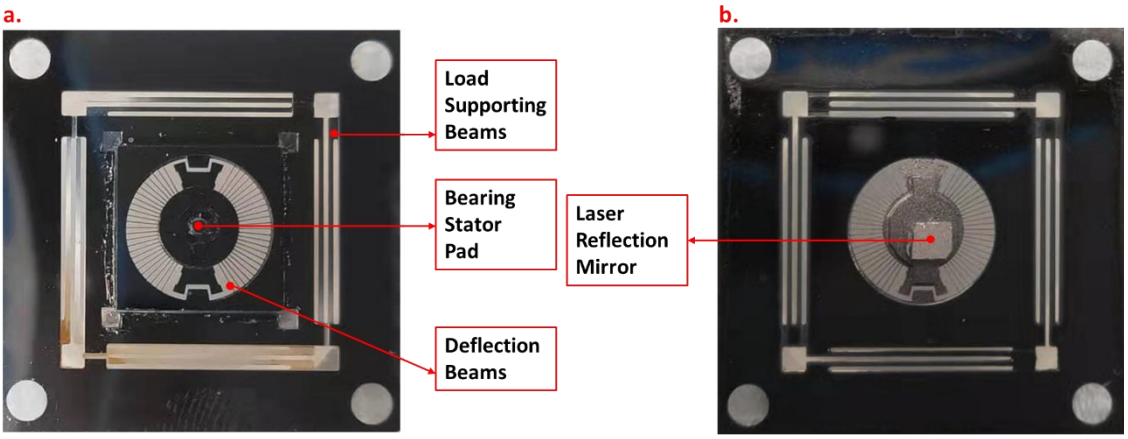

Figure 5-15. (a) Front Side of the Test Platform (b) Back Side of the Test Platform

As demonstrated in figure 5-15, there are four load supporting beams which is used to support the load applied on the thrust bearing. When the rotor pad of the thrust bearing is loaded onto the stator pad of the thrust bearing which is installed on the test platform, the load supporting beams of the platform will deform elastically hence resulting a vertical displacement of the centre of the test platform (where the thrust bearing is installed) in the same direction of the load applied on the thrust bearing. The correlation between the applied load and the displacement at the platform centre is described in equation (5-1):

$$W = K_{stiff} \cdot \delta_v \tag{5-1}$$

where W is the load applied on the thrust bearing, δ_v is the vertical displacement and K_{stiff} is the elastic stiffness of the load supporting beams.

The displacement of the centre of the platform which is caused by the applied load on the MEMS thrust bearing can be measured by the reflecting mirror attached beneath the stator pad (shown in figure 5-15 (b)) together with the laser displacement measurement device installed below the test platform (shown in figure 5-8). Conversely, the load applied on the thrust bearing can be controlled by varying the displacement of the test platform centre. A simplified diagram showing the mechanism of load control of this MEMS tribometer is given in figure 5-16 below.

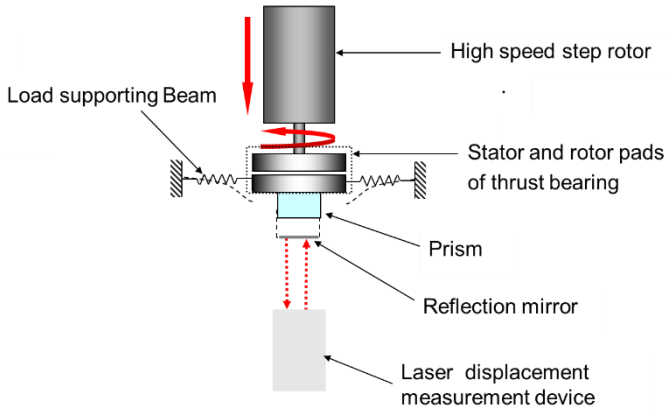

Figure 5-16. Mechanism of Load Control of the Tribometer

Frictional Torque Measurement

When the thrust bearing is tested in this tribometer, the stator pad of the thrust bearing is fixed on the platform, the rotor pad is loaded into contact with the stator pad of the thrust bearing. The rotor pad of the thrust bearing is driven by a DC step motor (the DC step motor is able operate in the speed range from 1 $rad \cdot s^{-1}$ to 2100 $rad \cdot s^{-1}$, the rotating speed is monitored via an attached encoder) and rotates against the stator pad resulting in a frictional torque which is applied to the deflection beams of the test platform.

As displaced in figure 5-15, the deflection beams of the test platform can deform elastically when frictional torque is applied hence leading to a rotational displacement of the central part of the test platform. The correlation between the frictional torque from the thrust bearing and rotational displacement of the central part of test platform is described in equation (5-2).

$$T = k_{rotate} \cdot \delta_r \tag{5-2}$$

where, T is the frictional torque from the thrust bearing, k_{rotate} is the rotational stiffness of the deflection beams and δ_r is the resulting rotational displacement of the central part of the platform.

Since the rotational displacement, δ_r, is tiny, an optical lever is used to exaggerate δ_r, which is displayed in figure 5-17 below. It can be seen from figure 5-17 that a prism is attached to the test platform beneath the stator pad of the thrust bearing. Laser signal from the laser source is shot towards the prism in the direction that is adjacent to one-right angle side of the prism. The laser signal is then reflected to the reflection mirror which is controlled by a piezoelectric actuator. The laser signal finally shot to the signal detector before being reflected by four fixed reflection mirrors. Therefore, the small rotational displacement of the central part of the platform resulted from frictional torque can result in a large movement of the signal in the place of the signal detector, δ_s.

$$\delta_s = L \cdot \delta_r \tag{5-3}$$

where, L is the length of the optical path.

In the test, a close control loop is built between the piezoelectric actuator and the signal detector. The piezo voltage applied on the piezoelectric actuator is adjusted according to the rotational displacement of the prism (attached to the central part of the platform) to drive the controlled reflection mirror to guarantee the laser signal always shot directly to the centre of the signal detector. The correlation between the piezo voltage, V, and the signal movement in the place of the signal detector is described with equation (5-4)

$$V = K'_{detector} \cdot \delta_s \tag{5-4}$$

Therefore, the correlation between the piezo voltage and the rotational displacement of the central part of the platform is:

$$V = K'_{detector} \cdot L \cdot \delta_r = K_{detector} \cdot \delta_r \tag{5-5}$$

Another calibration is required to link the torque applied on the platform and the piezo voltage of actuator.

$$T = K_{torque} \cdot V \tag{5-6}$$

Therefore, the correlation between the frictional torque and the rotational displacement of the central part of the platform can be derived:

$$T = K_{torque} \cdot K_{detector} \cdot \delta_r \tag{5-7}$$

In each test, the correlation between the piezo voltage and the rotational displacement of the central part of the platform might change as each component of the MEMS tribometer might be moved slightly. Therefore, this correlation must be built before each test:

$$V = K_{\ variable} \cdot \delta_r \tag{5-8}$$

In each test, the direct result we measured is the piezo voltage of the actuator. Therefore, the measured frictional torque is calculated with equation (5-9):

$$\boldsymbol{T} = \frac{K_{torque} \cdot K_{\ detector}}{K_{\ variable}} \cdot \boldsymbol{V} \tag{5-9}$$

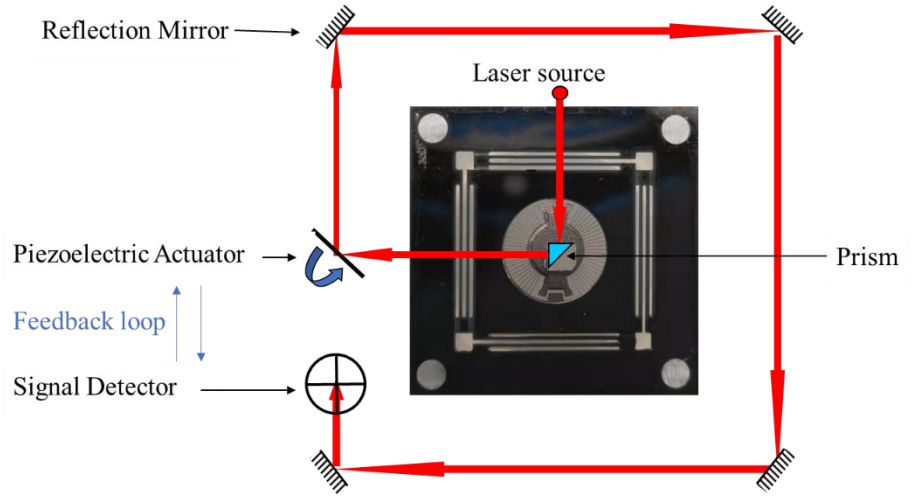

Figure 5-17. Mechanism of Frictional Torque Measurement of MEMS Tribometer

5.2.2 Calibration of the MEMS Tribometer

As described in the previous section, several calibrations are required to obtain the calibration constants which are necessary to control the applied load and measure the frictional torque: K_{stiff}, K_{torque}, $K_{\ detector}$ and $K_{\ variable}$.

Alignment of the Stator and Rotor Pad of the Thrust Bearing

The stator pad and rotor pad of the thrust bearing must be appropriately aligned with each other so that the centre axis of the stator pad and the centre axis of the rotor pad (which is also the rotating axis of the rotor pad) should be collinear. This is achieved by two cameras the shooting directions of which are adjacent to each other.

The axis of the stator and rotor pad of the thrust bearing should also be in the same direction of the loading direction to avoid any tilting of the thrust bearing (that significantly affects the

results). That is achieved by adjusting the test platform to be horizontal and the rotor shaft to be vertical. Gradienter is initially considered to be used for the platform and rotor shaft adjustment. But that is hard to achieve as the accuracy is not enough.

The problem is solved by using a slippery smooth sphere. The sphere is placed on the platform and the end surface of the motor. The position adjustments of the platform and motor shaft are complete once the sphere stays stably.

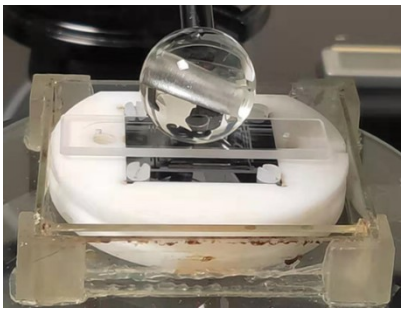

Figure 5-18. Orientation Adjustment of the Test Platform

Figure 5-19. Orientation Adjustment of the Motor

Load Control Calibration

The correlation between the applied load and the vertical displacement is described with equation (5-1). The K_{stiff} is obtained by placing several known weights on the centre of the platform (1g, 2g, 3g, 5g, 6g, 7g and 10g) and recording the vertical displacements of the test platform. The load calibration curve of the test platform is displayed in figure 5-20 below.

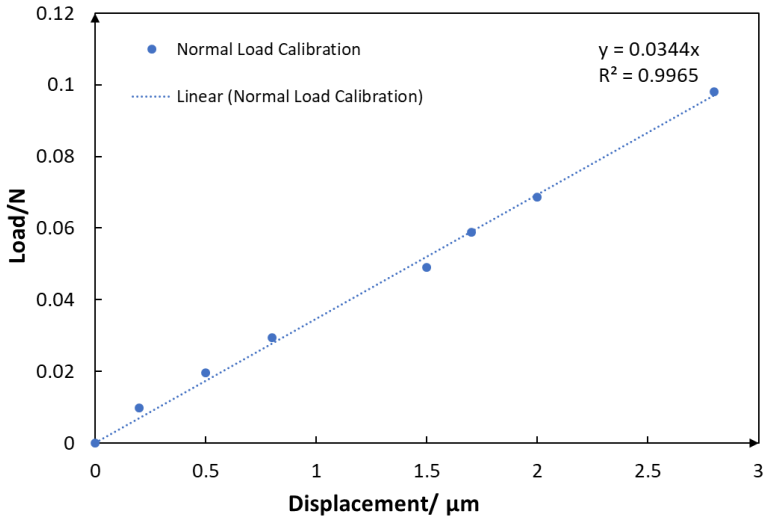

Figure 5-20. Load Calibration Curve of the Test Platform

After calibration, K_{stiff} is 0.344 N/μm.

Detector and Variable Calibrations

These calibrations are to obtain $K_{detector}$ and $K_{variable}$. The calibration process for these two calibration constants obtainment is the same. That calibration is achieved by manually move the detector and record the piezo voltage values for every 5 μm movement of the detector position. The detector calibration curve of the test platform is displayed in figure 5-21.

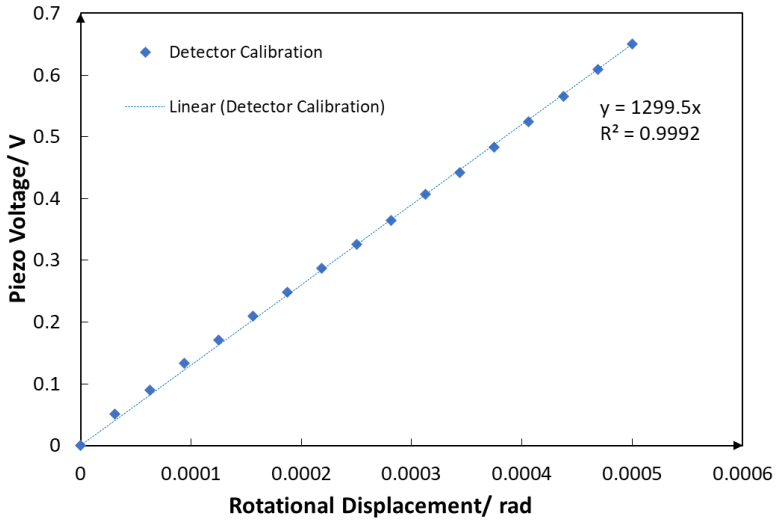

Figure 5-21. Detector Calibration Curve of the Test Platform

After calibration, $K_{detector}$ is 1299.5 V· rad^{-1}.

Torque calibration

The correlation between the frictional torque and the piezo voltage is described with equation (5-6). A specially designed tool on the platform which allows controlled torque (through a torque meter) to be applied on the test platform. K_{torque} is obtained by recoding the applied torque values read from the torque meter and corresponding piezo voltage values.

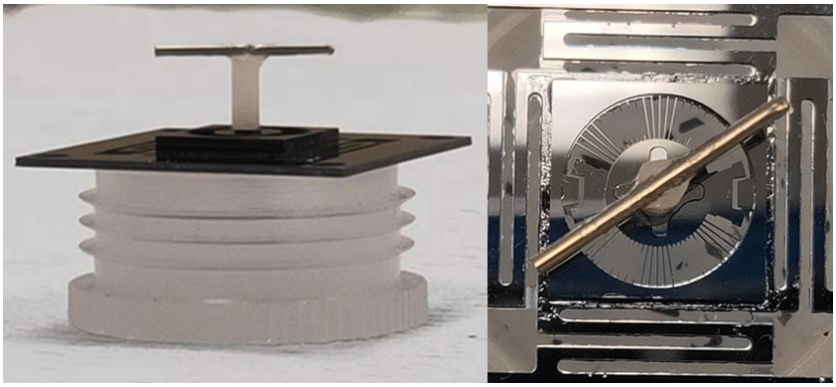

Figure 5-22. Test Platform with Torque Calibration Tool Installed

The torque calibration curve of the test plat form is displayed in figure 5-23.

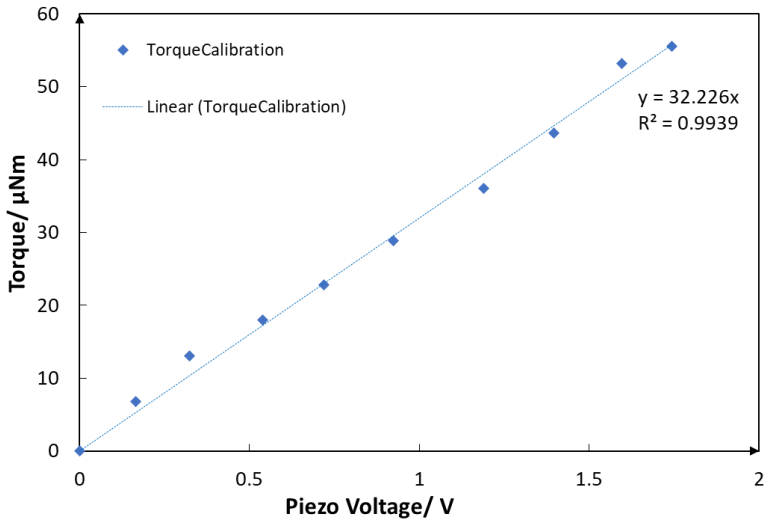

Figure 5-23. Torque Calibration Curve of the of the Test Platform

After calibration, K_{torque} is 32.23 µNm· V^{-1}.

By substituting the obtained K_{torque}, $K_{detector}$ and $K_{variable}$ into equation (5-9), correlation can be then established between the frictional torque which is the data we want and the actually measured piezo voltage of the mirror which is driven by the piezo-actuator.

Chapter 6: Performance of Micro Thrust Bearings Tested on MEMS Tribometer

Results demonstrating the performance of a micro pocketed parallel thrust bearing are presented in this chapter. The diameter of the micro thrust bearing is 1 mm and the pocket pattern which is designed to generate hydrodynamic pressure within the entrained lubricant is accurately etched on the stator pad to 1 μm. The micro bearing is tested on a specially designed MEMS tribometer which is able to control the applied load and rotational speed and characterize the frictional torque and friction coefficient of the micro bearing. The load applied on the micro bearing in the tests is equal to the force which will be supported by the micro thrust bearing when it is installed and functions on the practical MEMS device (a mems energy harvesting turbine in this research) and the bearing rotational speed in the testes ranges from 1 $rad \cdot s^{-1}$ *to 680* $rad \cdot s^{-1}$*, which covers all lubrication regimes. Effect of the lubricant viscosity and additives on the bearing performance are investigated and discussed in this chapter.*

6.1. Brief Introduction of Liquid Thrust Bearings and the Bearing Lubrication Regimes

Liquid thrust bearings are machine elements which are applied to support the load acted along the axial direction of the shaft of the rotating part, liquid phase lubricants are selected and used to lubricate this type of bearing. Fluid thrust bearings are characterized with the pressurized thin layer of fluid film which separates the stator pad surface and rotor pad surface of the thrust bearings from direct contact hence allows very low friction coefficient, low wear rate and vibration for this type of bearing. [4]

One of the most important performance values of the thrust bearing is the friction coefficient. However, the friction coefficient of the bearing might be determined by different factors as the liquid thrust bearings might operate in different lubrication regimes. The lubrication regime of the bearing under certain conditions is mainly determined by the applied load, rotational speed

and viscosity of the lubricant and can be judged by the so called (λ) value which is the ratio between the fluid film thickness and the surface roughness of the bearing. [157]

Boundary Lubrication Regime

When the rotational speed of the thrust bearing is very low or the applied load is too heavy, the fluid film is too thin to separate the thrust bearing surfaces. In this lubrication regime, majority of the total applied load (over 90%) is supported by the peaks of the surface, the asperities of the bearing surfaces directly are in direct contact and shear against each other when the two surfaces moves relatively. A majority of high friction coefficient and wear rate problems are caused in this lubrication regime and they are largely affected by the roughness of the bearing surfaces and shear strength of the asperities of the bearing surfaces (i.e. properties of the bearing materials).

Mixed Lubrication Regime

As rotational speed increases, the lubrication regime transfers from boundary lubrication regime to mixed lubrication regime. In this lubrication regime, thicker lubrication film is generated among the contact asperities of the bearing surfaces, the extent of asperity contact is reduced, and the load is partly supported by the lubricant film and partly supported by the direct surface contact. Friction coefficient and wear rate declines fast with increasing rotational speed in this case as lubricant film becomes increasingly thicker.

Hydrodynamic Lubrication Regime (Full film lubrication regime)

When the rotational speed and the viscosity of the lubricant are sufficiently high, the fluid film would be higher than the surface roughness of the thrust bearings. Therefore, the bearing surfaces are completely separated by the lubricant. The friction coefficient of the bearing in this lubrication regime can be very low and almost determined by the properties of the liquid lubricant alone (viscosity, density, specific heat, etc.). The friction coefficient in this regime is computed based on the pressure distribution of the thrust bearing which is described by the Reynold's equation:

$$\frac{\partial}{\partial x}\left(\frac{h^3}{12\eta}\frac{\partial p}{\partial x}\right)+\frac{\partial}{\partial y}\left(\frac{h^3}{12\eta}\frac{\partial p}{\partial y}\right)=\frac{(u_t+u_b)}{2}\frac{\partial h}{\partial x}+\frac{\partial h}{\partial t} \tag{6-1}$$

where, h is the fluid film thickness, η is the dynamic viscosity of the liquid, u_t and u_b are the speeds of the top and bottom surfaces of the thrust bearing respectively.

Figure 6-1 below presents the friction coefficient versus the speed curve of a typical thrust bearing which is the so-called stribeck curve.

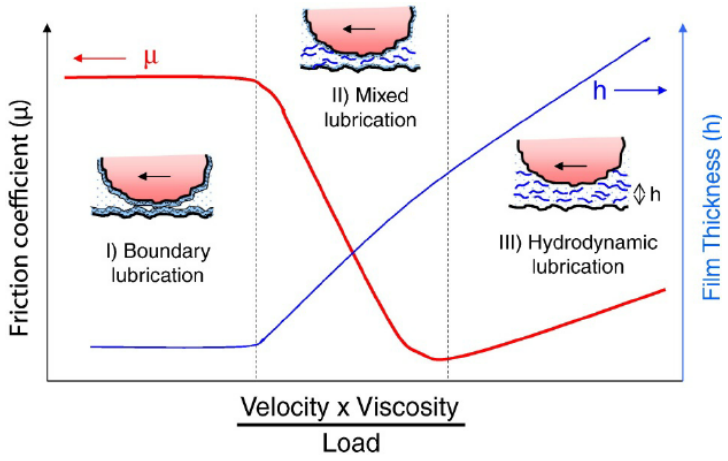

Figure 6-1. Typical Stribeck Curve of Liquid Thrust Bearing [157]

The work conducted in this chapter investigates the friction behaviours of the 1 mm-diameter micro liquid thrust bearing and how the friction behaviours are affected by the viscosity of applied liquid and the selected friction modifier. The tests presented in this chapter are conducted in a wide speed range of the thrust bearing, the rotational speed of the micro thrust bearing is increased from 1 $rad \cdot s^{-1}$ to above 680 $rad \cdot s^{-1}$ for each test, which ensures that all the lubrication regimes the micro thrust bearing might experience are investigated. All the results shown in this chapter are obtained from tests conducted on the MEMS tribometer which has been introduced in Chapter 5 of the thesis.

6.2. Detailed Information on the Test Setup

The experiments conducted in this chapter are aimed to investigate the friction behaviours of a 1-mm diameter pocketed parallel thrust bearing over a speed range which covers all lubrication regimes. Effects of the lubricant viscosity and effects from a friction modifier on the 1-mm bearing performance are also studied.

In this section, detailed information on the test setup including test conditions, parameters of the tested thrust bearing, properties of the tested lubricants and properties of the tested friction modifier.

Test Conditions

- **Temperature**

  This series of tests are all conducted in room temperature: 25 ℃.

- **Applied Load**

  Applied load for all the tests conducted in this series of investigation is 39.2 mN. That is equal to the load that the MEMS thrust bearing supports in practical applications.

- **Rotational Speed**

  In this series of tests, the speed ranges from 1.0 $rad \cdot s^{-1}$ to 680.7 $rad \cdot s^{-1}$. Therefore, the performance of the 1-mm diameter MEMS thrust bearing in all lubrication regimes (boundary regime/ mixed regime/ hydrodynamic regime) can be investigated.

- **Ambient Pressure**

  This series of tests are all conducted under atmosphere pressure which is 1.01×10^5 Pa.

Parameters of Tested Thrust Bearing

The graphics of the rotor pad, stator pad and the side view of the thrust bearing in operation are demonstrated in figure 6-2, figure 6-3 and figure 6-4 respectively.

- **Thrust Bearing Rotor Pad**

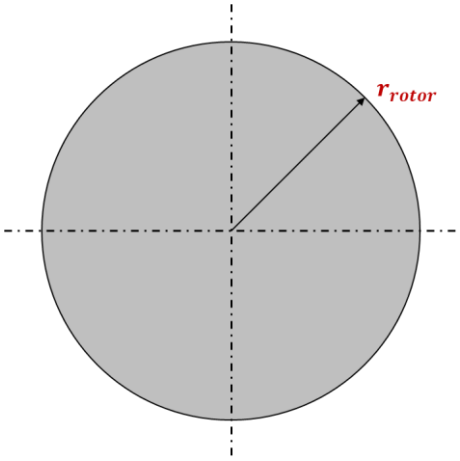

Figure 6-2: Graphics of the Rotor Pad of the Thrust Bearing

The material of the rotor pad of the thrust bearing is silicon. The surface of the rotor pad is flat and smooth, the surface roughness is: $R_a = 5$ nm. The diameter of the rotor pad, r_{rotor} is 1 mm.

- **Thrust Bearing Stator Pad**

  The material of the stator pad of the thrust bearing is also silicon. The surface of the stator pad is etched with a pocket pattern using deep reactive ion etching technique. The surface

roughness of the land region (the region where etching is not conducted) is also: $R_a = 5$ nm, the surface roughness of the etched pocket region is $R_a = 7$ nm.

The diameter of the stator pad, r_{stator} is 0.5 mm, the inner radius of the etched pocket, r_{inner} is 0.25 mm, the rim radius of the etched pocket, r_{rim} is 0.475 mm. The angular width of the etched pocket, θ_{pocket} is $\frac{\pi}{2}$, the angular width of the land region, θ_{land} is also $\frac{\pi}{2}$. The depth of the etched pocket, h_{pocket} is 1 μm.

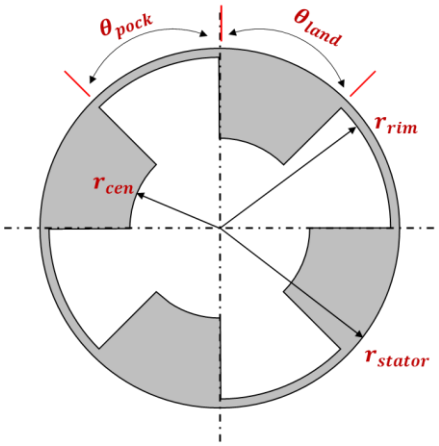

Figure 6-3: Graphics of the Stator Pad of the Thrust Bearing

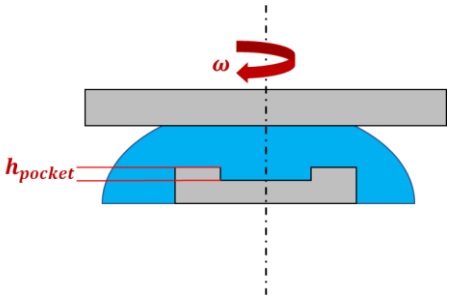

Figure 6-4: Side View of Thrust Bearing in Operation

Properties of Tested Lubricants

Detailed properties of the tested base lubricants are listed in table 6-1 below.

Table 6-1: Properties of Tested Base Lubricants at 25 °C

Lubricant	Dynamic Viscosity (cP)	Density (g·cm^{-3})	Surface Tension (N/cm)
DI Water	0.89	1.00	72
Hexadecane	3.02	0.77	27
Squalane	28.0	0.81	32

As demonstrated in figure 6-4, the supply of the lubricant for the MEMS thrust bearing in this series of test is achieved by delivering a drop of lubricants on the stator pad of the bearing, the added lubricant should be sufficient to cover the whole stator pad of the bearing. The meniscus effect helps to sustain the added lubricant in place.

Properties of Tested Friction Modifier

The friction modifier selected for the investigation of this research is octadecylamine ($C_{18}H_{39}N$). It consists of an 18-carbon straight chain and an amine group at the end of the carbon chain. The molecular weight of this additive is 269.5 $g \cdot mol^{-1}$. The chemical structure of it is demonstrated in figure 6-5.

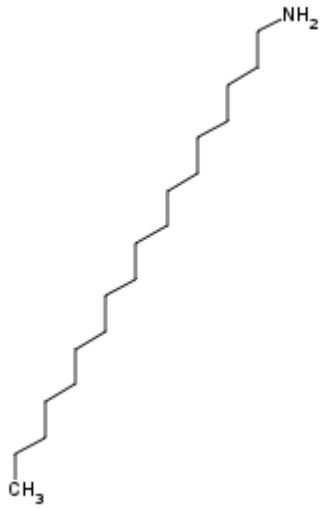

Figure 6-5. Chemical Structure of Octadecylamine

The amine group of the ODA molecule enables the molecule with straight chain to attach to the silicon surfaces and form a slippery thin film which helps friction reduction in boundary lubrication regime and mixed lubrication regime.

6.3. Results and Discussion

6.3.1. Repeatability of the MEMS Tribometer Tests

Good repeatability is shown in the friction coefficient versus rotational speed curves from the MEMS tribometer tests. Figure 6-6 shows the three repeated friction coefficient versus rotational speed curves under same conditions (applied load: 39.2 mN, speed range: 1.0

$rad \cdot s^{-1}$ to 680.7 $rad \cdot s^{-1}$, lubricants: pure hexadecane). It can be seen that the repeated curves approximately coincide.

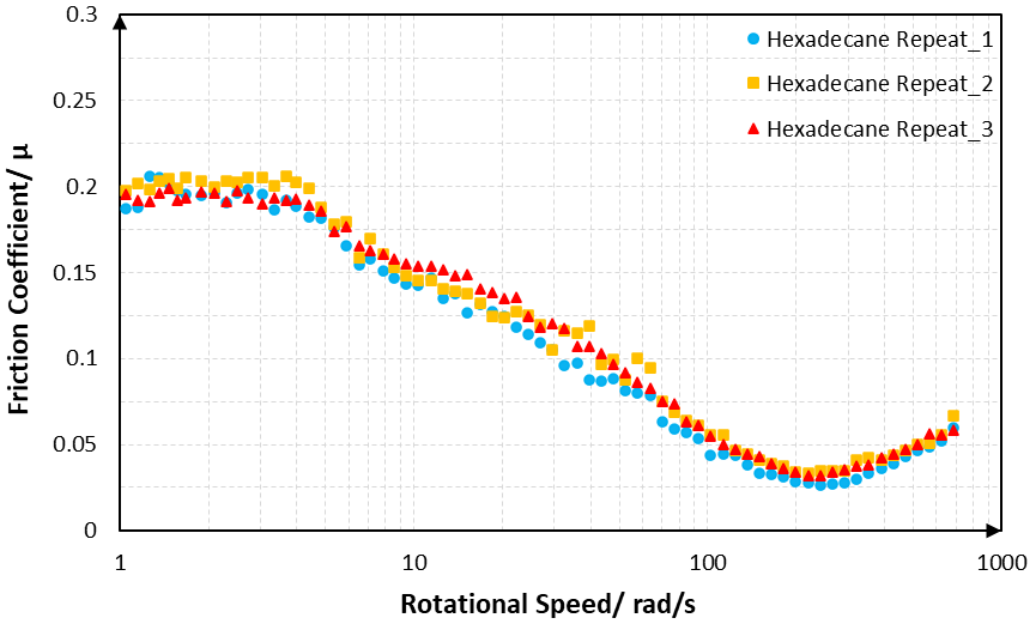

Figure 6-6. Curves Showing the Repeatability of the MEMS Tribometer Tests

6.3.2. Performance of the 1-mm Diameter MEMS Thrust Bearing Lubricated with Different Liquids

MEMS tribometer tests are conducted to investigate the performance of the 1-mm diameter micro thrust bearing when it is lubricated with different liquid lubricants (DI water, hexadecane and squalane). As demonstrated in table 6-1, the three tested liquids are very different in viscosity value which is one of the most important properties determining the liquid lubrication behaviours in macro scale. At 25 ℃ temperature and atmospheric pressure, the viscosity of hexadecane is more than three times as high as that of DI water whereas the viscosity of squalane is more than nine times as high as that of hexadecane. It can also be noticed from table 6-1 that the tested liquids are different in terms of surface tension value. Surface tension is often ignored in the analysis of macro scale liquid lubrication behaviours. However, surface tension of the liquid might affect the performance of the micro thrust bearings as the meniscus force is no longer neglectable in microscale devices. Hexadecane and squalane have roughly the same surface tension value at 25 ℃ temperature whereas the surface tension of DI water is more than twice as high as that of hexadecane or squalane.

The friction coefficient versus rotational speed curves of the 1-mm diameter thrust bearing under different liquids lubrication are demonstrated in figure 6-7 below. It can be seen that all curves of different lubricants displayed in figure 6-7 are in the shape of a typical Stribeck curve. That is, the friction coefficient slightly fluctuates around a certain value at low rotational speed range (boundary lubrication regime), then the friction coefficient declines with increasing rotational speed (mixed lubrication regime) and rises again when the rotational speed is further increased from a threshold value (hydrodynamic lubrication regime).

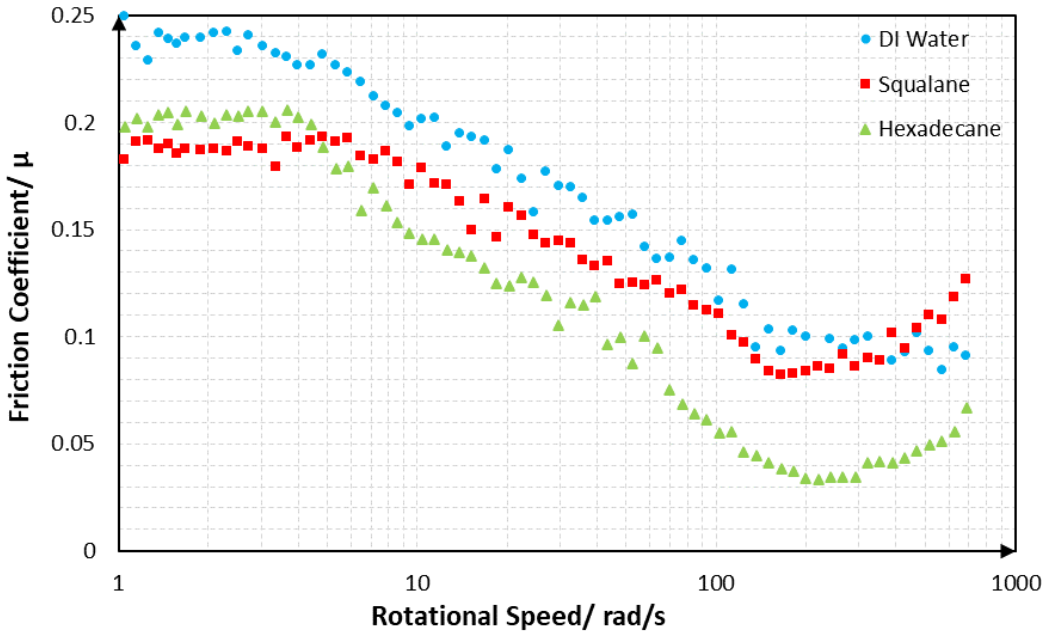

Figure 6-7. Friction Coefficient versus Rotational Speed Curves of the MEMS Thrust Bearing Lubricated by Different Liquids

It can be seen from figure 6-7 that, when the MEMS thrust bearing is lubricated with the thickest oil of this series of tests, squalene (28.0 cP at 25 ℃), the friction coefficient of the bearing at rotational speed lower than 4 $rad \cdot s^{-1}$ fluctuates around 0.19, the lubrication regime in this case is boundary lubrication regime. When the rotational speed is increased from 5 4 $rad \cdot s^{-1}$ above, the thrust bearing lubricated with squalane enters mixed lubrication regime and the friction coefficient declines. When the rotational speed is increased to around 157 $rad \cdot s^{-1}$, the friction coefficient reaches the bottom value at about 0.08. The surfaces of the thrust bearing are just separated by the formed lubrication film at this speed. The friction coefficient ascends with rising rotational speed when the speed is higher than 157 $rad \cdot s^{-1}$ as the shear stress increases with rotational speed in hydrodynamic lubrication regime. When the speed reaches 680 $rad \cdot s^{-1}$, the friction coefficient reaches the peak value at 0.13.

When the MEMS thrust bearing is lubricated with hexadecane (3.02 cP at 25 ℃), the friction coefficient when the rotational speed ranges from 1 $rad \cdot s^{-1}$ to 4 $rad \cdot s^{-1}$ fluctuates around 0.21. When the rotational speed is increased from 4 $rad \cdot s^{-1}$to 220 $rad \cdot s^{-1}$, the friction coefficient descends from 0.21 to 0.03. The friction coefficient rises when the rotational speed is further increased from 220 $rad \cdot s^{-1}$ and reaches about 0.07 at 680 $rad \cdot s^{-1}$.

When the 1-mm diameter MEMS thrust bearing is lubricated with DI water (0.89 cP at 25 ℃), the friction coefficient at low speed is range varies around 0.24, the friction coefficient keeps decreasing with increasing rotational speed. When the speed is higher than 210 $rad \cdot s^{-1}$, the friction coefficient curve is very noisy.

Compared to the Stribeck curves of the macro scale thrust bearings, there are several phenomena which need to be noticed in the Stribeck curves of the micro thrust bearings obtained in this research.

The first phenomenon is that when the rotational speed is low and the bearing operates in boundary lubrication regime, the boundary friction coefficients of the MEMS thrust bearings lubricated with liquids of different viscosities are equal to different constant values rather than a fixed constant value. It can be summarized from figure 6-7 that the boundary friction coefficient for the 1-mm MEMS bearing increases with decreasing lubricant viscosity. It is reasonable to hypothesize that the interaction between the liquid molecules and the bearing surfaces plays an important role in determining the frictional torque of the micro thrust bearing when it operates at low speed boundary lubrication regime. Additional drag force (possibly from meniscus force or Van der Walls force) or considerable load support is the possible factor resulted from the liquid molecules and micro bearing surfaces interactions that affects the value of the constant boundary lubrication friction coefficient. However, this hypothesis needs to be further investigated in future work by testing a group of liquids (more than three) with almost the same viscosity value but very different surface tension values and by testing another group of liquids (more than three) with almost the same surface tension value but very different viscosity values.

Another strange phenomenon is that, in mixed lubrication regime, the friction coefficient of hexadecane is lower than that of squalane. That could be accounted by the hypothesis that the friction resulted from lubricant shearing accounts for a large proportion of the total friction for small scale bearings. Therefore, the total frictional torque in mixed lubrication regime for small scale bearings is also largely affected by the viscosity of the lubricant, especially when the

viscosity of the comparing lubricants greatly differs (viscosity of suqalane is more than 8 times higher than that of hexadecane). The shear stress of squalane is much larger compared to that of hexadecane.

One phenomenon observed in Stribeck curves of the 1-mm diameter bearing that obeys the lubrication theory of large-scale bearings is that the bearing reaches full film lubrication at lower speed when lubricated with liquid of higher viscosity.

The third special phenomenon is that, the friction coefficient of MEMS thrust bearing when lubricated by DI water is higher than that of the cases when the bearing is lubricated by the other two lubricants almost in the whole speed range. However, the viscosity of the water is much lower than that of hexadecane and squalane. A possible hypothesis explaining this anomaly water molecules have strong polarity and tend to form concave meniscus on the deep reactive ion etched side walls of the MEMS thrust bearing pads which are very hydrophilic. Therefore, the MEMS thrust bearing lubricated by DI water suffers severe adhesion which leads to a high friction coefficient value.

6.3.3. Effect of Friction Modifier on the Performance of the 1-mm Diameter MEMS Thrust Bearing

Figure 6-8 below demonstrate the friction coefficient versus rotational speed curves of the 1-mm diameter thrust bearing lubricated by pure hexadecane and by octadecyl-amine added hexadecane. The weight concentration of the added octadecyl-amine is 0.1%. Therefore, the viscosity, density and specific heat of the bulk lubricant is not affected.

It can be seen from figure 6-8 that, the friction modifier used in the MEMS thrust bearing functions in the same way of the friction modifier function in macro scale bearing lubrication. When 0.1%wt of octadecyl-amine is added in the hexadecane and used as the lubricant if the MEMS thrust bearing, the friction coefficient in the mixed lubrication regime is reduced from around 0.21 to approximately 0.07. In mixed lubrication regime, the octadecyl-amine is still efficient in friction reduction, but the effect gradually vanishes when the rotational speed increases. When the rotational speed is increased to 220 $rad \cdot s^{-1}$ and the lubrication regime of the MEMS thrust bearing reaches hydrodynamic regime (surfaces of the bearing totally separated by the lubricant film), the stribeck curve of pure hexadecane coincides with the stribeck curve of the 0.1%wt octadecyl-amine added hexadecane.

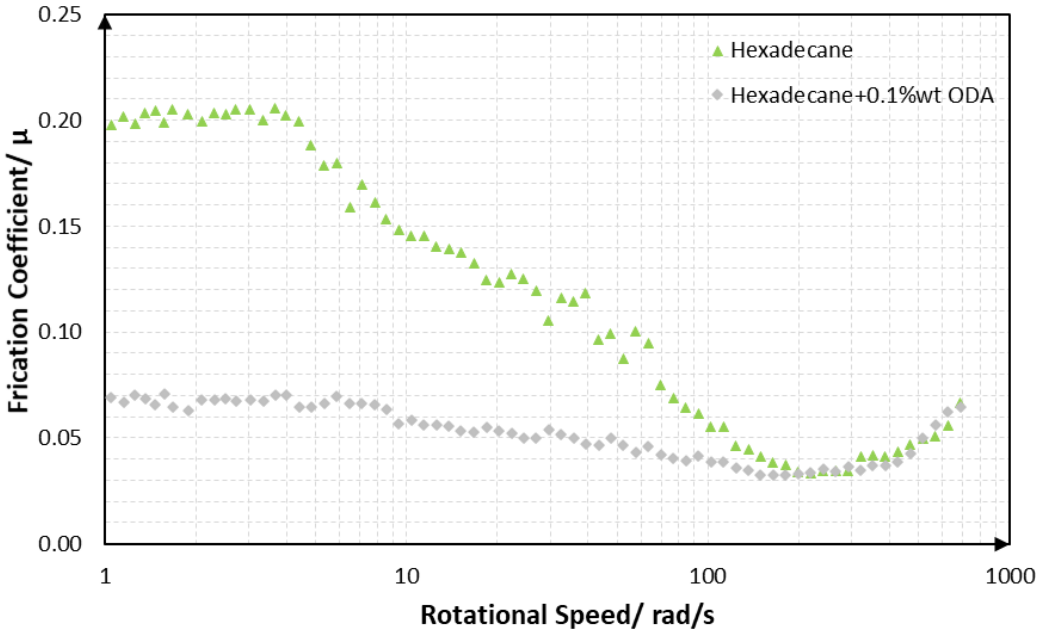

Figure 6-8. Friction Coefficient versus Rotational Speed Curves of the MEMS Thrust Bearing Lubricated by Pure Hexadecane and ODA added Hexadecane

The correlation between the power loss of the MEMS thrust bearing and the rotational speed under optimized lubrication (0.1%ODA added Hexadecane) and 39.2 mN applied load (which is equal to the gravity of 4-gram mass, a typical load value for MEMS devices) is demonstrated in figure 6-9 below.

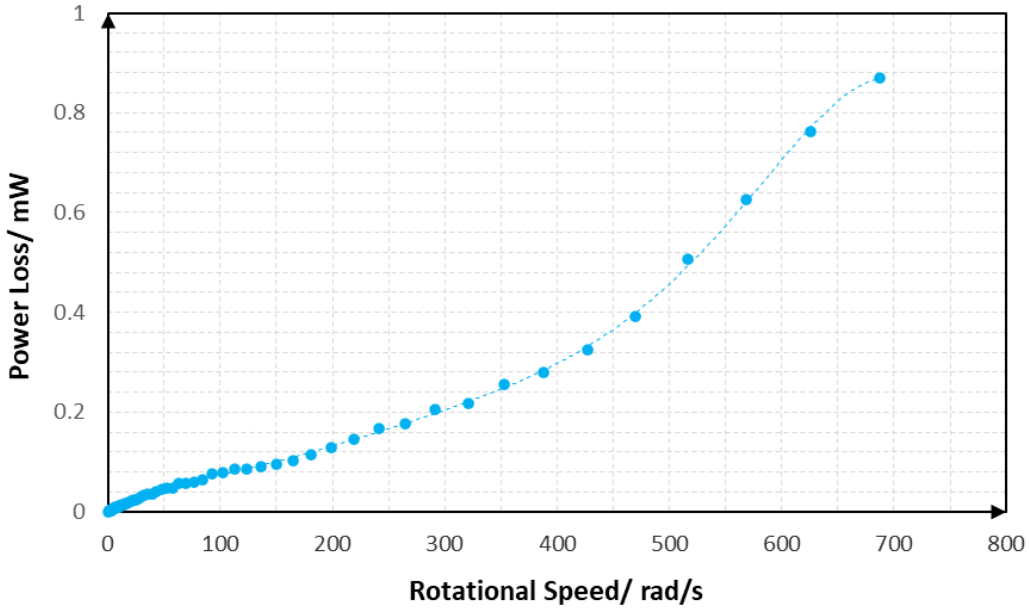

Figure 6-9. Power Loss versus Rotational Speed Curves of the MEMS Thrust Bearing Lubricated by 0.1%wt ODA added Hexadecane

It can be seen that when the rotational speed is increased to 50 $rad \cdot s^{-1}$, the power loss of the MEMS thrust bearing developed in this research is slightly smaller than 0.05 mW (50 μW); when the bearing operates at 210 $rad \cdot s^{-1}$ rotational speed, the power consumed in the bearing is around 0.15 mW; when the speed reaches 420 $rad \cdot s^{-1}$, the power loss ascends to 0.32 mW. The low power loss at high rotational speed makes the MEMS thrust bearing developed in this research suitable for MEMS devices with high sliding contacts, e.g. micro flow energy harvesters.

6.4. Conclusions

A series of experiments are conducted in this chapter to investigate the friction behaviours of the 1-mm diameter pocketed parallel thrust bearing developed in research over a speed range which covers all lubrication regimes.

It can be concluded from the results in this chapter that, the lubrication behaviours of the 1-mm diameter thrust bearing still follows some of the lubrication theories of macro scale liquid hydrodynamic bearings. When the rotational speed is increased from 1.0 $rad \cdot s^{-1}$ to 680.7 $rad \cdot s^{-1}$, the lubrication regime of the 1-mm diameter thrust bearing also transfers from boundary lubrication to mixed lubrication finally to full film hydrodynamic lubrication regime.

However, some phenomena arise possibly due to the tiny size of the MEMS bearing: *(i)*. friction coefficient of the MEMS thrust bearing in boundary lubrication regime is also affected by the lubricant viscosity, it declines with increasing lubricant viscosity; *(ii)*. friction resulted from liquid shearing in mixed lubrication regime accounts for larger percentage of the total friction, so the friction coefficient in mixed lubrication regime is not necessarily negatively correlated with lubricant viscosity; *(iii)*. when the MEMS bearing is lubricated with DI water, severe meniscus adhesion resulted from the strong polarity of the water molecules and hydrophilic bearing pad side walls leads to high friction coefficient in the whole speed range.

For MEMS thrust bearings, friction modifier is still efficient in friction reduction in boundary lubrication and mixed lubrication regimes. The effect of the friction modifier vanishes when the bearing operates in full film regime. When lubricated 0.1%wt ODA added hexadecane, the power loss of the 1-mm diameter pocketed parallel thrust bearing developed in this research is low in both low and high rotational speeds. Therefore, it is suitable to be used in MEMS devices with high sliding contacts.

Chapter 7: Performance of the Micro Bearings Installed on the Micro Energy Harvesting Turbine

In this chapter, results demonstrating how the micro parallel thrust bearings with three different recessed patterns perform when they are installed and operate on a centimetre scale micro energy harvesting turbine are reported. The performance is assessed by conducting turbine spin-down tests. The correlations between the total frictional torque and turbine operating speed under different conditions can be derived through the spin-down curves which are obtained from the spin-down tests. Lubricants with different viscosities are supplied to the bearings operating in the micro turbine and the performance of these lubricants incorporating with the micro bearings are examined. A surface active additive is also added to the bearings and tested to investigate the feasibility of further reducing frictional torque through lubricant optimisation and quantify the friction reduction caused Previously, commercial V bearings were used in the contacts of this micro turbine, comparison between the performance of the previously used V bearings and the thrust bearings fabricated in this project is also presented in this chapter.

7.1. Introduction of Micro Energy Harvesting Turbine Tests

7.1.1. Introduction of Flow-driven Energy Harvesting Turbine and Its Miniaturization

Flow-driven energy harvesting turbines are devices that are able to extract the energy from air (liquid) flows and convert the extracted fluid flow power (which is the mechanical power in the rotor shaft of the turbine) to electric power (typically, a three phase electricity generator is implemented in the energy harvesting turbine). They are useful devices to provide power to many types of wireless sensors and actuators located in pipes and ducts (*e.g.* air conditioning systems and remote gas pipelines). [6]

The electrical power supplied by this type of energy harvester located at a free steam can be calculated with the following equation (7-1):

$$P_{out} = \left(\frac{1}{2}\rho A {U_{flow}}^3\right) \cdot C_m \cdot C_e \tag{7-1}$$

where P_{out} is the electrical power delivered out to the applied load, ρ is the density of the stream fluid, A is the area of the cross section which the stream flows through, U_{flow} is the speed of the flow, $C_m$is the efficiency coefficient with which the harvester converts the stream flow power to the mechanical power of the harvester and C_e is the efficiency coefficient with which the harvester converts the mechanical power extracted from flow to the electrical power supplied to the applied load.

For flow-driven energy harvesters, C_m has a limited maximum theoretical value, $\frac{16}{27}$ which is so called Betz limit [158]. Large scale flow-driven energy harvesters can extract larger fraction of power from fluid flow with C_m approaching the Betz limit value. However, miniaturization of the energy harvester could lead to drastic reduction of C_m value, that is largely caused by high viscous losses at low Reynold's numbers. A simple down-scaling analysis for a rotating energy harvesting turbine is given in the following paragraph.

Value of C_m can be computed with equation (7-2) below,

$$C_m = \frac{P_{shaft}}{P_{flow}} = \frac{P_{shaft}}{(\pi\rho {U_{flow}}^3 D^2/8)} = f\left\{J, Re, \frac{\varepsilon}{D}\right\} \tag{7-2}$$

where, P_{shaft} is the turbine shaft power before loss in rotor contacts, D is the diameter of the turbine rotor, J is the tip speed ratio, *i.e.* the ratio of the rotor blade tip to flow speed, Re is the rotational Reynold's number, $\frac{\varepsilon}{D}$ is the relative blade surface roughness (ε is the surface roughness of the rotor blade). It can be seen from equation (7-2) that coefficient C_m is a function of J, Re and $\frac{\varepsilon}{D}$, decrease of Re or increase of $\frac{\varepsilon}{D}$ results in decrease of coefficient C_m. Computation equations for J and Re are given below:

$$J = \frac{\omega D}{2U_{flow}} \tag{7-3}$$

$$Re = \frac{\omega D^2}{4\nu} \tag{7-4}$$

In practice, the surface roughness ε of the blade is dependent on the fabrication methods and not necessarily correlated with the turbine size. Therefore, the relative blade surface roughness normally rises when the turbine is scaled down.

In practical operation, the tip speed ratio J is kept constant for a fixed flow speed, *i.e.* ωD is kept constant. Therefore, the rotational Reynolds number Re is proportional to the turbine rotor diameter D and decreases when the turbine is scaled down.

Both of the above two factors result in an unavoidable decrease of the coefficient C_mThe C_m value drops to around 0.1 when the turbine is scaled down to the order of 0.1 m. [159] Therefore, it is crucial to achieve a high coefficient C_e, (ratio between the output electrical power P_{out} to the turbine rotor shaft before power loss in rotor contacts P_{shaft}) to guarantee the overall energy harvesting efficiency coefficient, $C_m \cdot C_e$, at a reasonable value (~1% to 10%). Some part of the power will be dissipated in the rotor contacts and some part of the power will be dissipated in the resistance of the electric generator before the shaft power is finally delivered out to the applied load. Therefore, the coefficient C_e can be computed using equation (7-5) below.

$$C_e = C_r \cdot C_b \tag{7-5}$$

where, C_r is the electricity generator efficiency coefficient and C_b is the rotating contacts efficiency coefficient.

For miniaturized devices, the power loss in the rotating contacts can be very high and the wear at the contacts after long periods of operation further increases the power dissipated in the small rotating contacts. The power lost in the micro sliding contacts, $P_{contacts}$ can be computed with equation (7-6).

$$P_{contacts} = T_{contacts} \cdot \omega \tag{7-6}$$

where, $T_{contacts}$ is the frictional torque in the small contacts.

The aim of the tests shown in this chapter is to quantify the frictional torque and the power loss of the micro bearings designed and fabricated in this research when they are installed and operate on the micro energy harvesting turbine, and to find the optimum bearing and lubricants combination with which highest bearing efficiency is achieved.

7.1.2. Key Information of the Micro Turbine Used in the Tests

This section outlines the practical aspects of micro turbine test setup. The miniaturized flow-driven energy harvesting turbine used in the testes is a centimetre scale shrouded wind turbine. The outside radius of the turbine is only 16 mm hence the area of the cross section, A is only 8 mm^2. This MEMS turbine can be easily fitted into a 1 ft diameter duct and only negligible

influence will be caused to the stream flow passing the duct as it only covers 1% of the cross-section area of the duct. The outside radius of the rotor of the turbine is 10 mm. Figure 7-1(a) below displays the assembled miniature turbine next to a one-pound coin. Figure 7-1 (b) demonstrates the cross section of the assembled turbine.

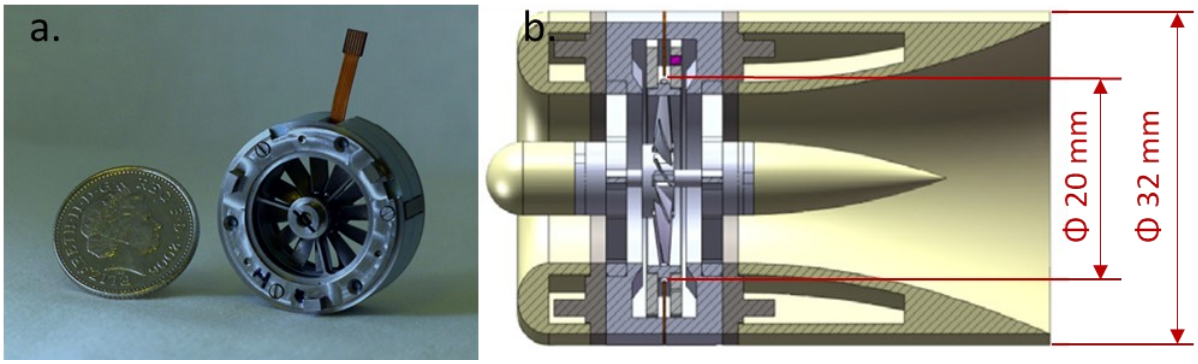

Figure 7-1. (a) Assembled Miniature Turbine and Size Comparison to a Coin; (b) Schematic of the Cross Section of the Turbine [6]

The miniature wind turbine can efficiently operate at air flow with flow speed ranging from 3 ms^{-1} to 8 ms^{-1} and output electric power ranging from 80 μW to 3.5 mW. The electrical power is generated by a three phase AFPM generator built within the micro turbine [6]. The magnetic rings of the generator consists of 16 pairs (16 pole pairs) of 2-mm diameter, 1-mm long NdFeB (neodymium–iron–boron) permanent magnets, the small cylindrical magnets are placed and glued into two machined aluminium formers. The assembled two magnetic rings are tightly fitted (attached) to the rim of the 3D printed rotor facing each other in parallel and will rotate when the rotor is driven by the air flow. The coils of the electric generator which is the stator are installed as a four layer flexible PCB (flexible printed circuit board). The stator coil PCB is placed between the two magnetic rings which are attached to the turbine rotor. Figure 7-2 (a) below demonstrates the turbine rotor with one of the magnetic rings attached to the rotor rim; figure 7-2 (b) displays the stator coil PCB; schematics showing how the generator stator and rotor are placed together on the turbine are illustrated in figure 7-2 (c).

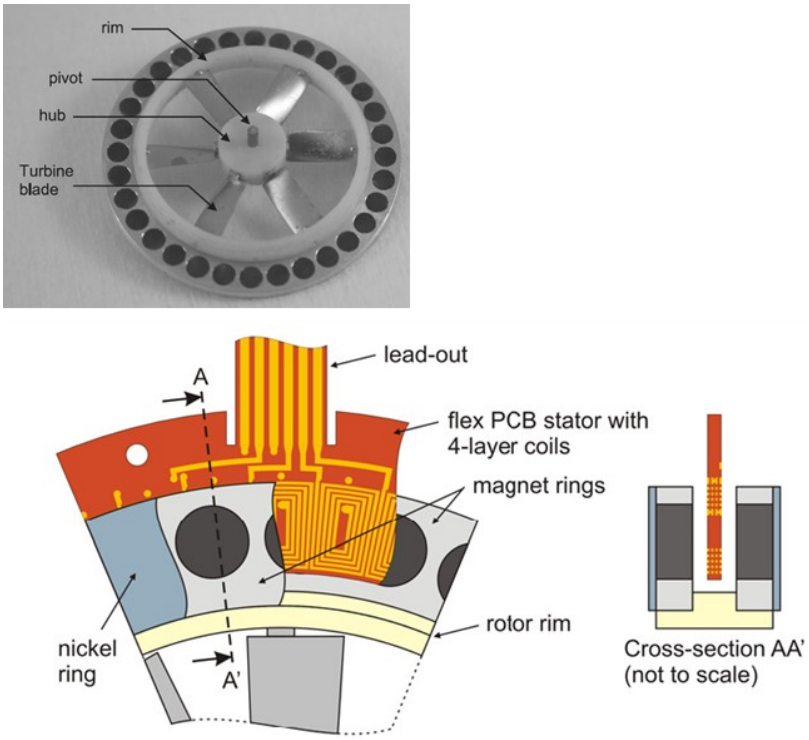

Figure 7-2. (a) Turbine Rotor with Assembled Magnet Ring; (b) Stator Coil Printed Circuit Board (PCB); (c) Cross-section View of the Rotor and Stator Arrangement [6]

An exploded view of all the parts of the miniature turbine are given in figure 7-3.

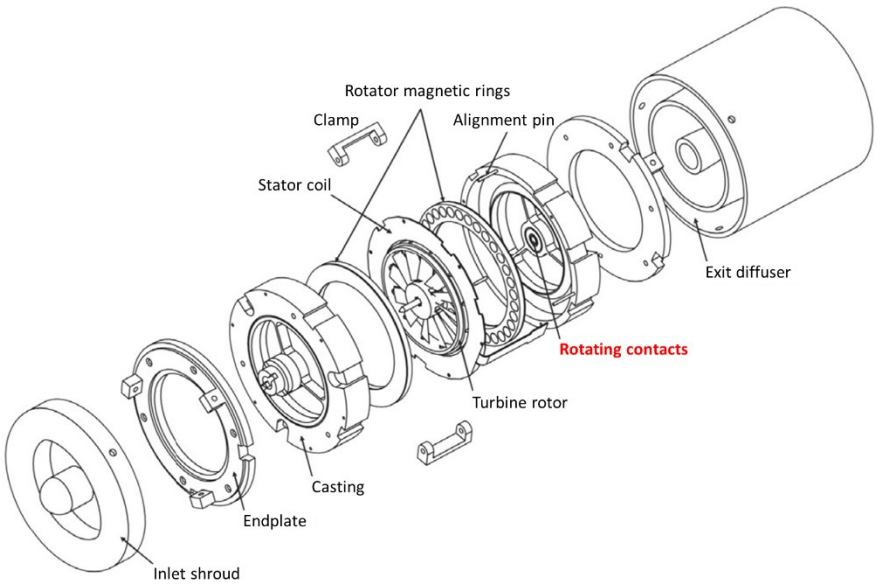

Figure 7-3. Exploded View of All the Parts of the Micro Energy Harvester [6]

7.2. Introduction of the Micro Bearing Assembly and Tests Setup

7.2.1. Micro Bearings Installed on the Miniature Turbine

As demonstrated in figure 7-3, there are two contacts where the two ends of the rotor shaft rotate against. Loading in both axial direction (e.g. wind thrust force) and radial direction (e.g. centrifugal force generated from the rotor imbalance) are generated when the turbine operates and results in frictional torque which dissipates extracted energy. The micro bearings designed and fabricated in this project are to be installed on these two contacts to support load in both axial and radial directions and achieve low frictional torque when the turbine is rotating thereby achieving low bearing power loss and low start-up speed which is the minimum speed of the air flow to enable the rotation of the turbine.

In each contact, there is one journal bearing which supports the radial load and one thrust bearing which supports the axial load. Details of the two types of bearings installed on the turbine are given in the following section. The bearings operate with the speed ranging from 100 rpm to 6000 rpm (10.5 $rad \cdot s^{-1}$ to 628.3 $rad \cdot s^{-1}$) as this is the speed range with which the generator can output electric power efficiently. The correlations between generator output power and rotor rotational speed are demonstrated in figure 7-4 below.

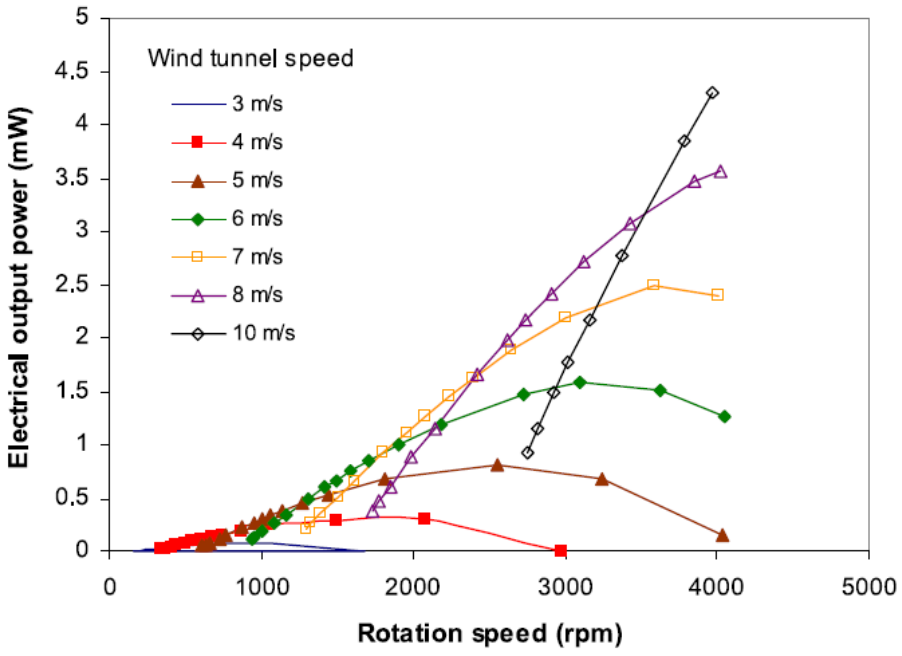

Figure 7-4. Correlations between Output Power and Rotational Speed of the Micro Energy Harvesting Turbine at Different Wind Speeds [6]

7.2.2. Assembly of the Micro Journal and Thrust Bearings

Assembly of the Turbine Rotor, Shaft and the Bearings

The turbine device itself had been designed in previous research, however it ran on unlubricated V bearings. In this section, details of the installed hydrodynamic bearings are explained.

Figure 7-5 below demonstrates clearly how the turbine rotor, turbine shaft and the bearings at the two ends of the turbine shaft are assembled together (note: the bearing housings were manufactured as part of this project, while the turbine rotor was pre-existing).

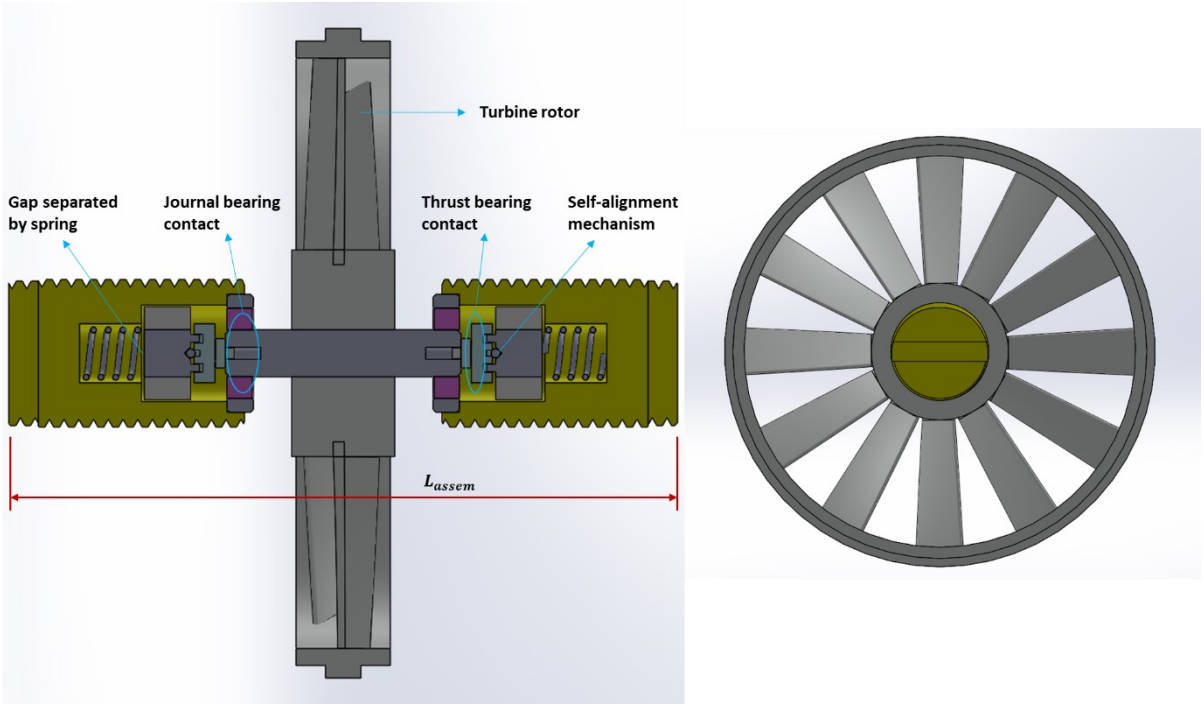

Figure 7-5. Assembly of the Micro Bearings and the Micro Turbine Rotor

The turbine shaft is inserted into the central hole of the turbine rotor. The turbine rotor should be located at the midpoint of the turbine shaft to make sure the weight of the rotor is equally supported by the journal bearings at two shaft ends. The turbine shaft and turbine rotor are tightly fitted with each other, so that no relative sliding or rotating happens at this contact.

Bearing housing, within which the stator pad of the thrust baring and the sleeves of the journal bearing are assembled, is installed by screwing it into the threaded hole in the centre of the casting. Lock nuts are used to ensure no axial movements of the bearing housings occur when the turbine operates especially at high speeds.

The distance between the end surfaces of the two bearing housings (L_{assem} in figure 7-5) can be adjusted using the thread to ensure that the rotor pads of the micro thrust bearings attached

to the end surfaces of the rotor shaft are just in contact and properly aligned with the two stator pads of the thrust bearings which are installed inside the bearing housings. The shaft is inserted into and aligned properly with the sleeve of the journal bearings and functions as the journal of the journal bearing.

The distance between the end surfaces of the two bearing housings at which the micro thrust bearing rotor pads contact and properly aligned with the micro thrust bearing stator pads without any applied force in axial direction can be measured before installing the bearings to the micro turbine. As demonstrated in figure 7-6, the two assembled bearing housings and the shaft inserted rotor are aligned together on a specially designed platform, the distance between the two bearing housings L_{pre} can then be accurately measured with a calliper (measuring accuracy: <0.02 mm).

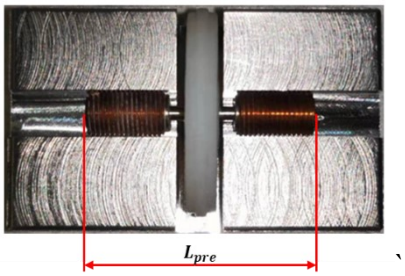

Figure 7-6. Length of the Bearing-Rotor Assembly in Axial Direction

When installing the shaft inserted turbine rotor and the assembled bearing housings on the turbine, L_{assem} can be adjusted to be equal to L_{pre} to achieve proper alignments of the journal and thrust bearings without any load applied in axial direction. L_{assem} can also be adjusted to be smaller than L_{pre} as there is a small gap (L_{gap}) in each of the assembled bearing housings which are separated by a low stiffness compression spring (shown in figure 7-5). When L_{assem} is adjusted to the value smaller than L_{pre}, the spring will be compressed and pre-load (W_{pre}) in axial direction will be applied on the two micro thrust bearings.

$$W_{pre} = k_{spring} \cdot \left(L_{pre} - L_{assem}\right) \tag{7-7}$$

The preserved small gap also guarantees the stator and rotor surfaces of the micro thrust bearings can be separated by the lubricant film when the turbine operates.

Rotor Shaft and Micro Thrust Bearing Rotor Pads

The assembly of turbine rotor, rotor shaft and the rotor pads of two thrust bearings is demonstrated in figure 7-7 below.

The turbine rotor is formed by using high resolution 3D printing process (resolution is around 2 μm), the material is polylactic acid.

The rotor shaft is fabricated using micro machining, the material is tool steel. The length of the shaft is 8 mm, the diameter of the shaft is 1.585 mm. The surface roughness of the cylindrical surface of the shaft is (Ra = 20 nm). Two 0.4 mm- diameter cylindrical hole is drilled in the centres of the two end surfaces of the shaft which is used for the instalment of the stator pads of micro thrust bearings.

The radius of the micro fabricated stator pads of the bearing is 500 μm, the roughness of the pad surface is below 7 nm. A cylindrical pin of 0.39 mm diameter, 0.38 mm length is fabricated at the centre of the back side of the stator pads, which is used for the assembly of rotor shaft and stator pad.

As stated in the previous section, the turbine rotor is tightly fitted with the shaft and located at the midpoint of the rotor shaft. The 0.39 mm diameter pin of the stator pad is installed to the 0.40 mm diameter hole at the end surface of the turbine shaft. The pad is sited and fixed on the end surfaces of the turbine shaft by extra thin super glue.

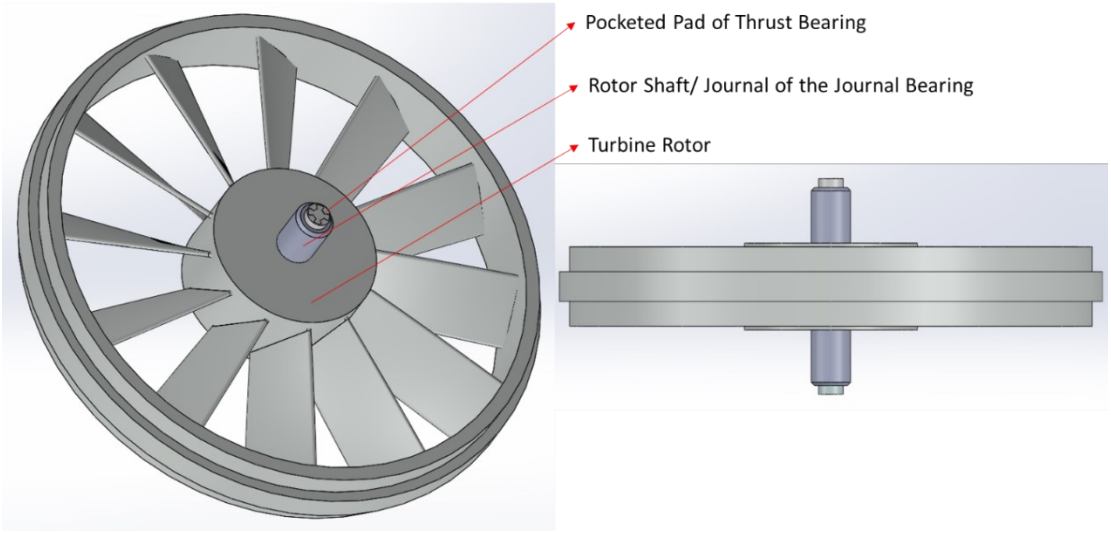

Figure 7-7. Assembly of the Turbine Rotor, Rotor Shaft and the Patterned Rotating Pads of the Micro Thrust Bearing

Assembled Bearing Housing

The bearing housing is the part which is installed and fixed on the casing of the turbine, it contains the sleeve of the shaft bearing, the flat stator pad of the thrust bearing and other parts assisting the operation of the micro thrust and journal bearings.

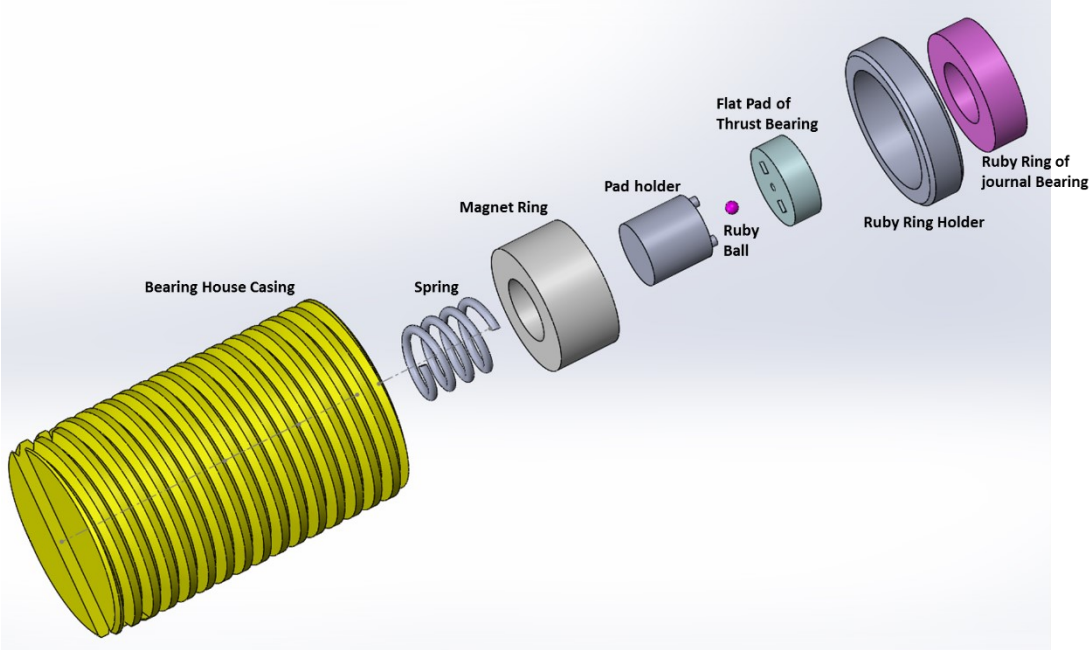

Figure 7-8. Exploded View of the Bearing Housing Assembly

An exploded view of the bearing Cage assembly is shown in figure 7-8 above. The consisting parts of the bearing housing, which were designed and manufactured are listed below:

- Brass copper **bearing housing cage**. It is used to contain all the parts of bearing housing assembly. The thread of the casing is M5×0.5.
- Stainless steel (stainless 302 ASTM A313) **compression spring**. It is used to ensure the micro thrust bearing pads can be aligned together and operate appropriately and it controls the pre-axial direction load on the thrust bearings. The elastic stiffness of the spring is 0.59 N/mm, the maximum applied load is 1.58 N.
- **Magnetic ring** is used to provide magnetic force to the flat stator pad of the micro thrust bearing and hold the stator pad.
- The stainless steel **pad holder** is used to install the stator pad; there are to square pins which are inserted to the holes on the backside of the stator pad and stops the stator pad from rotating.

- A 0.3 mm-diameter **ruby sphere** is glued on the fitting taper hole on the **pad holder**, this could be viewed clearer from the cross section view of the assembled bearing housing which is displayed in figure 7-9. This the key part for the self-alignment setup for the micro thrust bearing. There is a 0.2 mm-diameter hole in the centre of the back side of the stator pad of the thrust bearing which will be sited on the 0.3 mm-diameter ruby sphere. Since the diameter of the ruby ball is larger than the hole on the stator pad, the stator pad can swing freely around the ruby ball to correct any misalignment between the stator and rotor surfaces of the thrust bearing. The stator pad of the thrust bearing is always in full contact with the rotor pad of the thrust bearing.
- The **stator pad** of the thrust bearing which sits on the stator **pad holder** is made from silicon by micro fabrication methods. The radius of the pad is only 1000 μm, the surface roughness Ra of the pad is below 5 nm. A thin nickel layer is uniformly coated on the back side of the bearing enables the stator pad to be held on the pad holder by the magnetic ring.
- The **sleeve of the journal bearing** is a 1.605 mm-diameter **ruby ring bearing**, the width of the bearing is 0.9 mm.
- The **ruby ring** bearing is tightly fitted with the **ruby ring holder**, the ruby ring bearing together with the ruby ring holder is fitted to a 0.5 mm-depth stepped bore and glued on the step surface of the stepped bore.

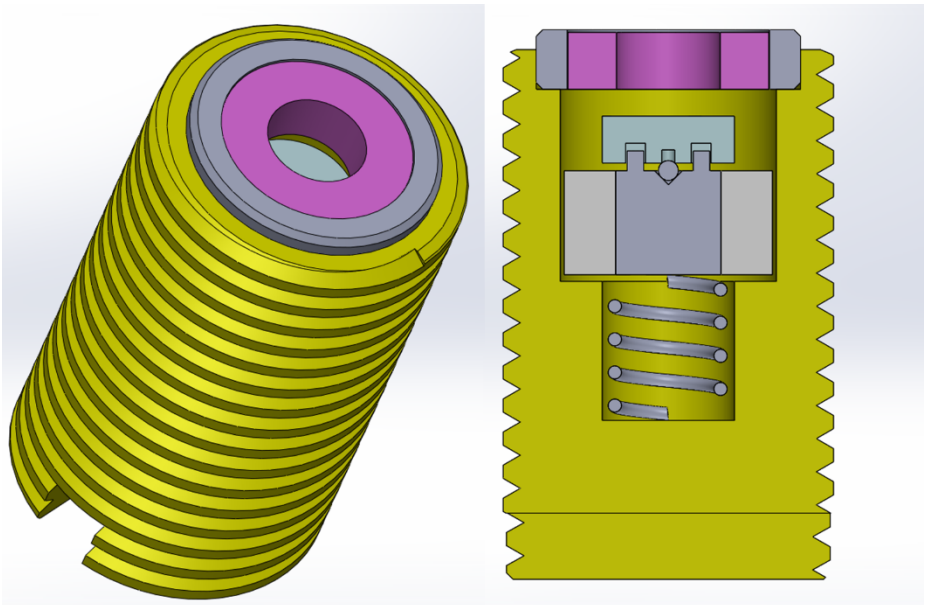

Figure 7-9. Cross-section View of the Assembled Bearing Housing

As shown in figure 7-9. The bearing housing also functions as a chamber for lubricant storage, the lubricant can be added to the bearing housing through the hole of the ruby ring. The chamber will be fulfilled with lubricants and the capillary meniscus helps to stop the lubricant flowing away. Both the ruby ring and stator pad is fully immersed to the lubricants, which ensures sufficient lubricant is supplied for thrust and journal bearing lubrication.

7.2.3. Spin-Down Tests Setup and Tests Process

Introduction on the Spin-Down

The correlation between the frictional torque from both journal and thrust bearings and the rotational speed and the correlation between the power loss from the bearings and the rotational speed is obtained through spin-down tests.

In spin-down tests, the miniature energy harvesting turbine is placed in a vacuum chamber and driven up to a high rotational speed, then the turbine is cut off from the circuit and freely spins down until the rotational speed reaches zero. Rotational speed versus spin-down time curves are obtained directly from the spin-down tests. Turbine rotor angular acceleration ($\dot{\omega}_r$) versus the rotational speed curves can be obtained by differentiating the rotational speed versus spin-down time curves:

$$\dot{\omega}_r = \frac{d\omega}{dt} \tag{7-8}$$

The frictional torque (T_b) versus speed curves and power loss (P_b) versus speed curves can also be obtained:

$$T_b = I_r \cdot \dot{\omega}_r \tag{7-9}$$

$$P_b = T_b \cdot \omega_r \tag{7-10}$$

When the tests are conducted in vacuum chamber, all the torque that reduces the rotational speed is from the bearings. I_r is the moment of inertia of the whole rotor (turbine rotor, rotor shaft, magnetic rings and the rotor pads of the thrust bearing) around the rotating axis of the turbine shaft:

$$I_r = I_{rotor} + I_{shaft} + 2 \times I_{magnets} + 2 \times I_{pads} \tag{10}$$

Spin-Down Tests Setup

Figure 7-10 below demonstrates the setup of the spin-down tests. The generator implemented in the energy harvesting turbine is connected to the circuit, and a drive voltage is supplied and

drive the generator as a synchronous motor to the maximum speed from which the spin-down starts. The drive voltage is then cut off, the turbine functions as a generator again and outputs a generated voltage, but the circuit is open now. The open-circuit voltage generated by the turbine over spin down time can be recorded to LabVIEW, and the rotational speed of the turbine can be computed using the frequency of the generated voltage:

$$\omega_r = \frac{2\times\pi\times f_v}{N_p} \tag{7-11}$$

where, f_v is the recorded voltage frequency and N_p is the number of pole pairs installed on the generator.

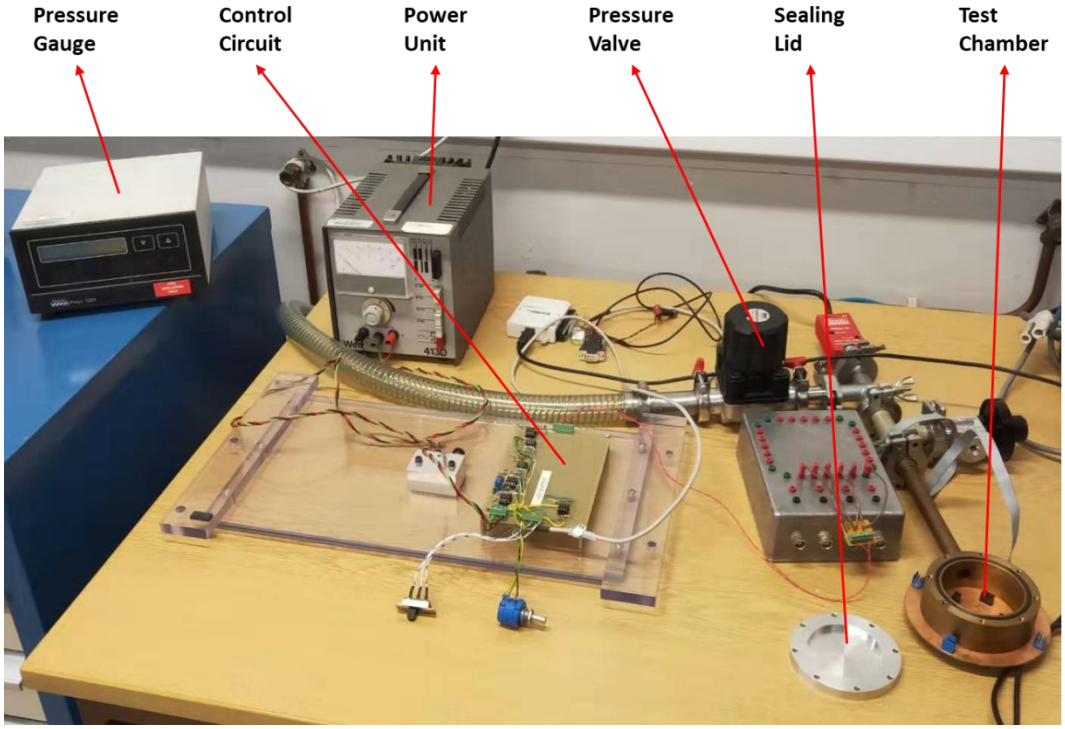

Figure 7-10. Spin-down Test Setup

The spin-down tests can be conducted both in a vacuum chamber where the pressure can be reduced below 0.3 mbar and conducted in atmosphere. The turbine can both be placed horizontally and vertically in spin down tests so that the bearing performance under different loading conditions can be obtained.

Four operating conditions can be applied for the spin-down tests which are:

- Horizontal direction test in vacuum chamber. Under this condition, the turbine is placed with its rotating axis to be placed horizontally, the turbine operates in the vacuum chamber with pressure lower than 0.3 mbar.
- Horizontal direction test in atmosphere. Under this condition, the turbine is placed with its rotating axis to be placed horizontally, the turbine operates in the atmosphere.
- Vertical direction test in Vacuum Chamber. Under this condition, the turbine is placed with its rotating axis to be placed vertically, the turbine operates in the vacuum chamber with pressure lower than 0.3 mbar.
- Vertical direction test in atmosphere. Under this condition, the turbine is placed with its rotating axis to be placed vertically, the turbine operates in the atmosphere.

The horizontal or vertical direction placement of the turbine can be guaranteed using a bubble level in all the tests presented in this chapter.

7.3. Detailed Information of Tested Micro Bearings and Tested Lubricants

7.3.1. Parameters of the Tested Micro Journal Bearing

Two micro journal bearings are installed on the micro energy harvesting turbine to support the load in radial direction of the two sliding contacts. The journal bearing consist of the turbine shaft and a ruby ring. Detailed parameters of the micro journal bearing are given as follows.

Turbine Shaft

The diameter of the shaft is 1.585 mm, the roughness of the shaft surface is below 30 nm (Ra). The shaft is made from stainless steel.

Ruby Ring

The diameter of the ruby ring is 1.605 mm, the roughness of the ruby ring (inner) surface is below 50 nm (Ra). The width of the ruby ring is 0.9 mm, which means the width of the journal bearing is 0.9 mm. [160]

7.3.2. Parameters of the Tested Micro Thrust Bearing

The micro pocketed parallel thrust bearing which has been instigated both numerically and experimentally in the previous chapters is installed on the micro turbine to bear the axial

direction load of the sliding contact. Detailed parameters of the micro journal bearing are given as follows.

Rotor Pad Parameters

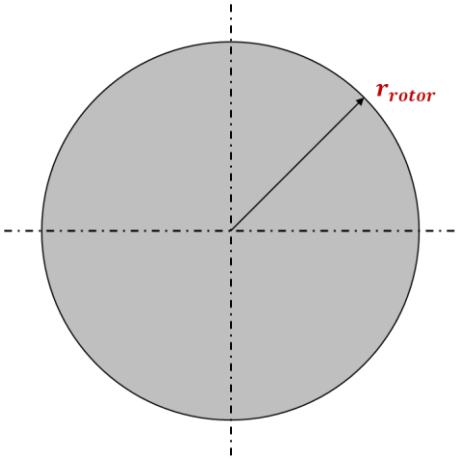

Figure 7-11: Graphics of the Rotor Pad of the Micro Thrust Bearing

The material of the rotor pad of the thrust bearing is silicon. The surface of the rotor pad is flat and smooth, the surface roughness is: $R_a = 5$ nm. The diameter of the rotor pad, r_{rotor} is 1 mm.

Stator Pad Parameters

The material of the stator pad of the thrust bearing is also silicon. The surface of the stator pad is etched with a pocket pattern using deep reactive ion etching technique. The surface roughness of the land region (the region where etching is not conducted) is also: $R_a = 5$ nm, the surface roughness of the etched pocket region is $R_a = 7$ nm.

The diameter of the stator pad, r_{stator} is 0.5 mm, the inner radius of the etched pocket, r_{inner} is 0.25 mm, the rim radius of the etched pocket, r_{rim} is 0.475 mm.

In the turbine tests, we tested three stator pads with different pocket patterns: Pattern A, Pattern B and Pattern C. The different stator pads distinguish from each other with the number of pads.

For the Pattern A, the bearing can be divided into 4 pad regions, for each pad region, the angular width of the etched pocket, θ_{pocket} is $\frac{\pi}{4}$, the angular width of the land region, θ_{land} is also $\frac{\pi}{4}$. The depth of the etched pocket, h_{pocket} is 1 μm.

For the Pattern B, the bearing can be divided into 6 pad regions, for each pad region, the angular width of the etched pocket, θ_{pocket} is $\frac{\pi}{6}$, the angular width of the land region, θ_{land} is also $\frac{\pi}{6}$. The depth of the etched pocket, h_{pocket} is 1 μm.

For the Pattern C, the bearing can be divided into 8 pad regions, for each pad region, the angular width of the etched pocket, θ_{pocket} is $\frac{\pi}{8}$, the angular width of the land region, θ_{land} is also $\frac{\pi}{8}$. The depth of the etched pocket, h_{pocket} is 1 μm.

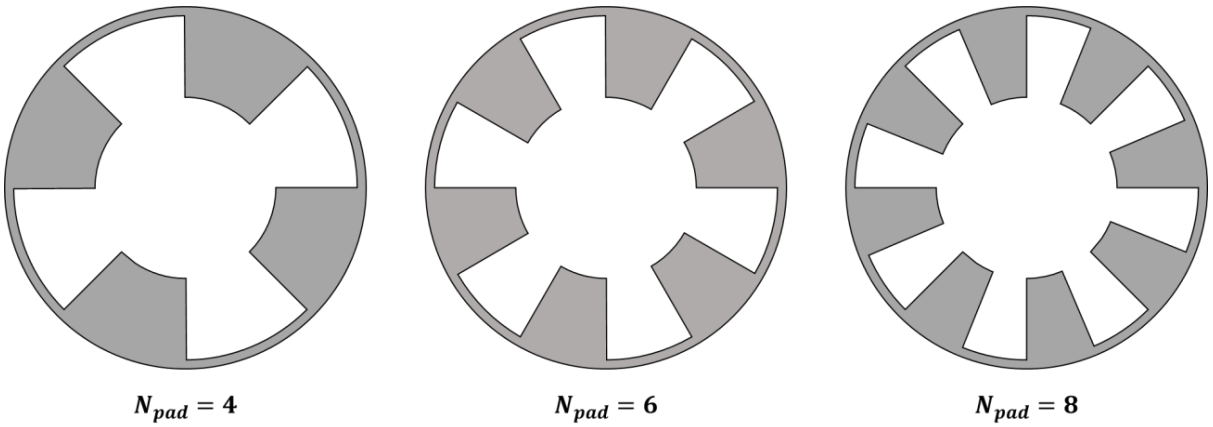

Figure 7-12: Graphics of the Stator Pads of the Micro Thrust Bearings with Different Recessed Patterns

7.3.3. Properties of Tested Lubricants

Detailed properties of the tested base lubricants are listed table 7-1 below.

Table 7-1: Properties of Tested Base Lubricants.

Lubricant	Dynamic Viscosity at 25 °C (cP)	Density at 25 °C (g·cm^{-3})
DI Water	0.89	1.00
Hexadecane	3.02	0.77
Squalane	28.0	0.81

7.3.4. Test Conditions

Detailed test conditions of this series of tests are given as follows.

Temperature

This series of tests are all conducted in room temperature: 25 ℃.

Ambient Pressure

This series of tests are conducted either under atmosphere pressure which is 1.01×10^5 Pa or conducted in the vacuum chamber, the pressure within the vacuum chamber is 30 Pa.

Rotational Speed

In this series of tests, the speed ranges from 1 $rad\cdot s^{-1}$ to 680 $rad\cdot s^{-1}$. Therefore, the performance of the micro bearings in all lubrication regimes (boundary regime/ mixed regime/ hydrodynamic regime) can be investigated.

Applied Load

There is no preload applied in on the micro bearings. When the turbine is in static state, the only load applied on the micro bearings is the gravity of the rotor which is 3.92×10^{-2} N.

7.4. Spin-Down Test Results of Micro Bearings Operating in the Turbine

7.4.1. Repeatability of the Turbine Spin-Down Tests

All the spin-down tests conducted in this research to obtain the frictional torque versus rotational speed curves are repeated at least 3 times for each group of the tests. Good repeatability of the obtained frictional torque versus rotational speed curves is shown in all groups of tests. Figure 7-13 shows all the repeated curves for one test group: thrust bearings with Pattern A on the stator pad lubricated by pure squalene.

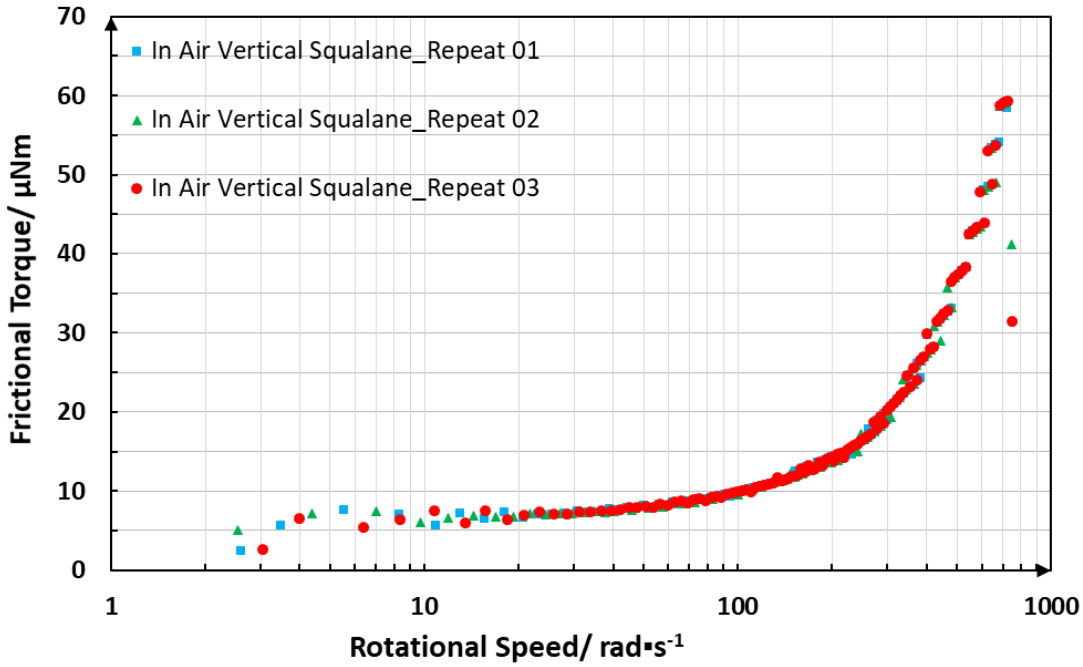

Figure 7-13. Curves Showing the Repeatability of the Spin-down Tests

7.4.2. Bearing Operates in Different Conditions

As introduced in the spin-down test setup section, the turbine spin-down tests are conducted in four different conditions which are:

- Condition HA: Turbine placed horizontally in atmosphere;
- Condition HV: Turbine placed horizontally in the vacuum chamber;
- Condition VA: Turbine placed vertically in atmosphere;
- Condition VV: Turbine placed vertically in the vacuum chamber.

There are several loads applied on the micro thrust bearing and micro journal from different factors which lowers the rotational speed of the turbine including:

- Weight of the rotor ($\boldsymbol{W_r}$);
- Centrifugal force in radial direction from the rotation of the imbalance of the rotor ($\boldsymbol{W_c}$);
- Thrust force in axial direction from the windage force ($\boldsymbol{W_t}$);
- Resistance torque directly from the windage on the turbine blade ($\boldsymbol{T_w}$);

The loading conditions of the micro thrust bearing and micro journal bearing vary under different spin-down test conditions. Comparisons of the correlations between frictional torque and rotational speed under different conditions are conducted to investigate the effects from different factors on the overall frictional torque and power loss from thrust and journal bearings.

The thrust bearing used in this group of investigation is recessed with Pattern A, the lubricant used is pure squalene.

Comparisons of Turbine Performance Operating in Atmosphere and in Vacuum

When the turbine spin-down tests are conducted in the vacuum chamber, the frictional torque decelerating the turbine is almost purely generated from the micro bearings. However, when the turbine spin-down tests are conducted in the atmosphere, additional frictional torque decelerating the turbine, which is caused by windage, is introduced. The windage is caused mainly by two factors: *(i).* the resistance directly from the relative movement between the rotor blades and the air which slows the rotational speed of the rotor; *(ii)* A thrust force in the axial direction which is generated when the rotor moves relative to the air (as there is an angle between the shaft axis and the rotor blade, when rotor moves relative to the air, an axial direction component force is generated from the resistance) can cause additional load on the thrust bearing hence additional decelerating frictional torque from thrust bearing.

In this section, the effects from windage on the frictional torque when the turbine operates in different orientations are analysed.

Figure 7-14 below demonstrates the frictional torque versus rotational speed curves when the turbine shaft is aligned in the horizontal direction. One of the curves is obtained when the turbine operates in atmosphere whereas the other is when the turbine operates in a vacuum chamber.

It can be seen that when the turbine is tested horizontally in the vacuum chamber ($P_{chamber} = 0.3\ mbar$), the frictional torque when the rotational speed is close to zero (6.8 μNm), andthe frictional torque increases with rotor rotational speed in the whole speed range. The curve is best fitted by a polynomial equation with order higher than 2. When the rotor speed is 200 rad·s^{-1}, the frictional torque is 11.3 μNm; when the rotational speed reaches 400 rad·s^{-1}, the frictional torque is increased to 21.5 μNm; when the rotational speed is increased to 600 rad·s^{-1}, the frictional torque rises to 36.9 μNm.

For the curve obtained from spin-down test in atmosphere ($P_{atm} = 1000\ mbar$), the starting frictional torque is 7.0 μNm. The frictional torque also increases with rotational speed in the whole speed range, when the rotational speed reaches 600 rad·s^{-1}, the frictional torque is increased to 47.7 μNm. The in air frictional torque versus rotational speed curve is also best fitted by a polynomial equation with order higher than 2.

The in-air frictional torque versus rotational speed curve almost coincides with the vacuum frictional torque versus rotational speed curve when the rotational speed is below 60 rad·s^{-1}. At 60 rad·s^{-1}, the frictional torque from vacuum chamber test is 7.2 μNm whereas the frictional torque from in air test is 8.1 μNm. The two curves diverge from each other when the rotational speed is increased to 100 rad·s^{-1}, and the gap between the two curves gradually widens with increasing rotational speed.

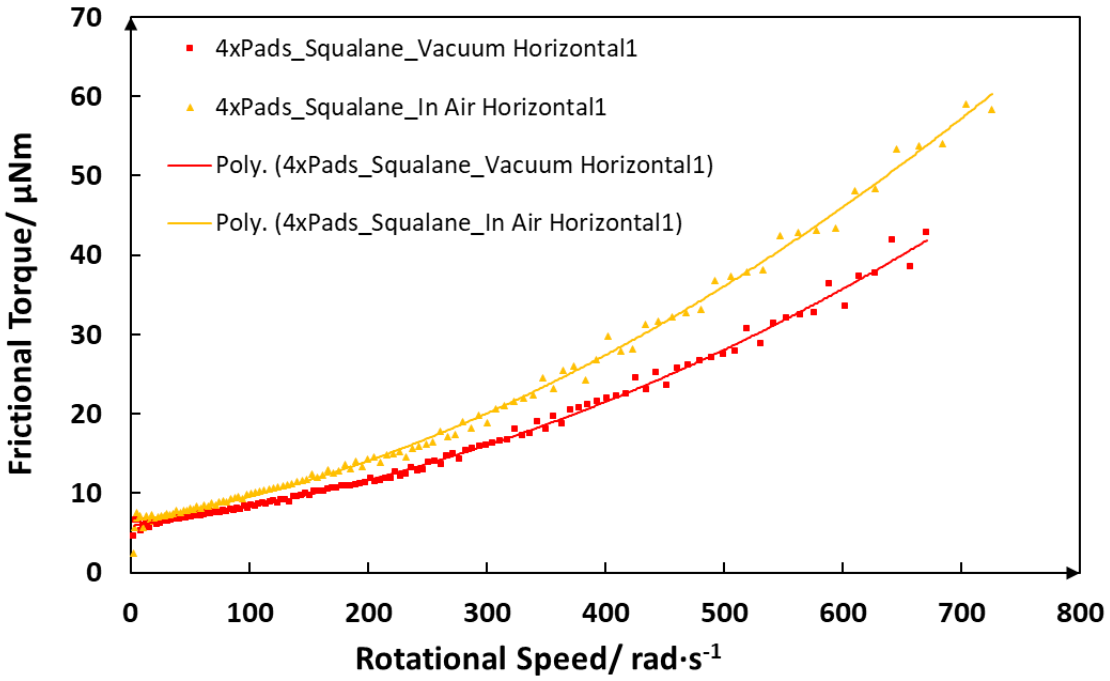

Figure 7-14. Frictional Torque Curves of Thrust Bearing with Pattern A and Journal Bearing Lubricated with Pure Squalene, Turbine Placed Horizontally

When the turbine spins down in the horizontal direction, one component of the load applied on the journal bearing is the constant weight of the rotor ($\boldsymbol{W_r = constant}$); another component of the load applied on the journal bearing is the centrifugal force resulted from the rotation of the imbalance of the rotor which is proportional to the square of the rotational speed ($\boldsymbol{W_c \propto \omega^2}$). Therefore, the load applied on the journal bearing ($\boldsymbol{W_s}$) is the resultant force of $\boldsymbol{W_r}$ **and** $\boldsymbol{W_c}$.

The force analysis diagram of the journal bearing when the turbine operates in the horizontal direction is shown in figure 7-15 below. The rotor is rotating around the axis of the rotor shaft *O*. The centre of the balance of the rotor *O'* is away from the shaft axis and also rotates around the shaft axis *O*. The gravity force of the rotor W_r is constant and the force direction is fixed in vertical direction. The centrifugal force increases quadratically with rotational speed and the

direction of the force is not fixed but rotates around the shaft axis *O*. Therefore, the load applied on journal bearing is dynamic and increases with rotational speed.

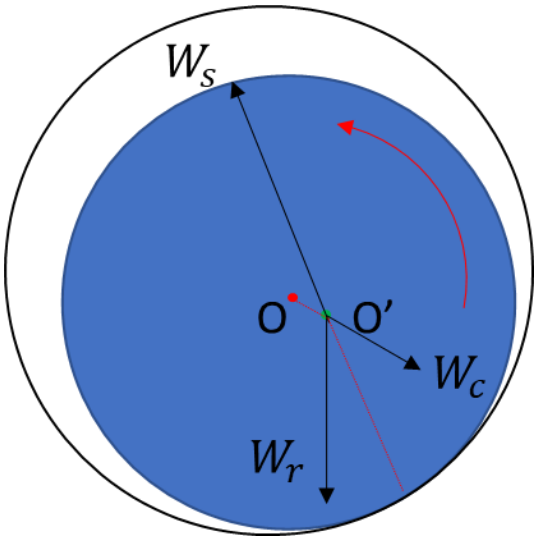

Figure 7-15. Force Analysis Diagram of the Micro Journal Bearing when the Micro Turbine is Placed Horizontally

When the bearing operates in the horizontal direction and placed in the vacuum chamber (the pressure in the vacuum chamber is 0.3 mbar), the load applied on the thrust bearing is negligible. The gravity force and centrifugal force analysed in the previous paragraph are the only loads and they are all applied on the micro journal bearing. When the turbine is placed horizontally and spins down in the vacuum chamber, almost all the measured frictional torque is generated in the journal bearings. As discussed before, the combined total load applied on the journal bearing is dynamic and the centrifugal force component of the total load increases quadratically with rotational speed, which explains the observation that frictional torque increases with rotational speed and the observation that the frictional torque versus rotational speed curve obtained in vacuum horizontal test is best fitted with polynomial equation with order higher than 2.

The applied load on the journal bearing does not change whether the turbine is tested in the vacuum chamber or in the atmosphere as long as the orientation of the turbine is not changed (turbine shaft axis in horizontal direction). Therefore, the correlation between the frictional torque and rotational speed from horizontal spin-down tests conducted in atmosphere is the same with the correlation obtained from vacuum chamber tests. Therefore, the total frictional

torque measured in atmosphere also increases with rotational speed and the best fitted curve is also polynomial and the order is higher than 2.

When the turbine is placed horizontally in atmosphere and spins down, thrust force in the axial direction is generated from windage which is supported by the thrust bearing. That thrust force will generate frictional torque on the micro thrust bearing. In addition, a resistance torque from the relative motion between air and rotor blades also functions as a frictional torque and decelerates the rotational speed of the turbine. However, the frictional torque resulting from windage is dominated by the rotational speed of the rotor and is negligible when the rotational speed is low. This explains the phenomenon that the frictional torque curves obtained from in air test and in vacuum chamber tests almost coincide with each other in low speed range ($\omega < 30\ rad \cdot s^{-1}$). The wind thrust force increases rapidly with rotational speed and result in the drastic increase of frictional torque when rotational speed gets larger. This is the cause of the divergence of two frictional torque versus rotational speed curves.

The correlation between the frictional torque caused by windage and the rotational speed when the turbine operates horizontally can be obtained by subtracting the frictional torque curve measured from vacuum chamber test from the curve measured from in air test. The curve is displayed in figure 7-16 (a) below. It can be seen that when the rotational speed is close to zero, the windage induced frictional torque is below 0.5 μNm and can be ignored. It surges to 13.7 μNm when the rotational speed approaches 700 rad·s^{-1}.

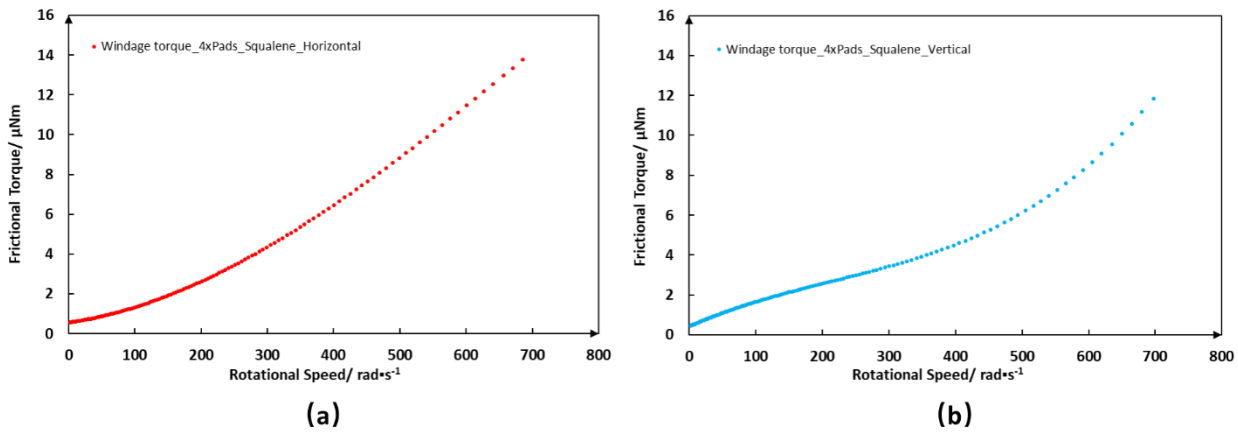

Figure 7-16. (a) Correlation Curve between the Frictional Torque Caused by Windage and the Rotational Speed when the Turbine Operates Horizontally; (b) Correlation Curve between the Frictional Torque Caused by Windage and the Rotational Speed when the Turbine Operates Vertically

Figure 7-17 below also demonstrates two frictional torque versus rotational speed curves obtained from spin-down tests conducted in the vacuum chamber and in atmosphere - both the vacuum chamber and in air tests are conducted by placing the turbine vertically.

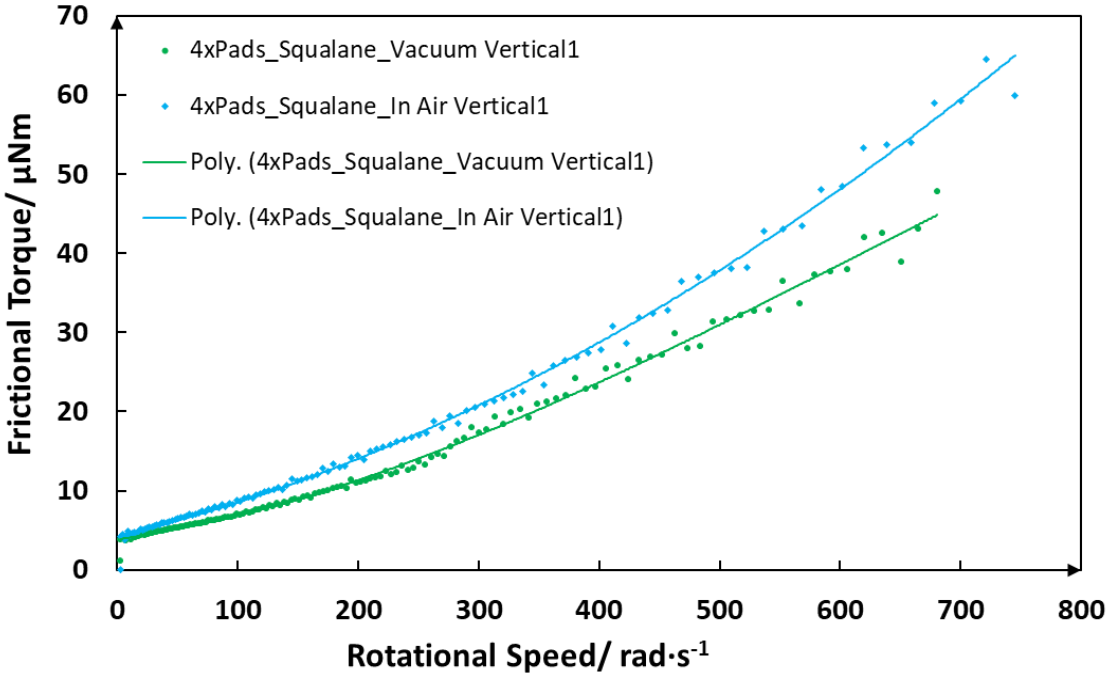

Figure 7-17. Frictional Torque Curves of Thrust Bearing with Pattern A and Journal Bearing Lubricated with Pure Squalene, Turbine Placed Vertically

It can be noticed in the curve obtained from vertical direction vacuum spin-down test that when the rotational speed is close to zero, the frictional torque is 3.75 μNm. The frictional torque ascends quickly with rising rotational speed. When the speed is increased to 200 rad·s^{-1}, the frictional torque rises to 10.92 μNm; when the speed is increased to 400 rad·s^{-1}, the frictional torque reaches 23.14 μNm; when the rotational speed is increased to 600 rad·s^{-1}, the frictional torque surges to 37.95 μNm. The best fitted curve for the results is a polynomial.

As for the curve obtained in the vertical alignment in air, it almost coincides with the curve obtained from vertical direction vacuum spin-down test when the rotational speed is lower than 20 rad·s^{-1}. For the curve obtained from spin-down test in atmosphere, the starting frictional torque is 4.19 μNm; when the speed is increased to 200 rad·s^{-1}, the frictional torque rises to 14.42 μNm; when the speed is increased to 400 rad·s^{-1}, the frictional torque rises to 27.83 μNm; when the speed reaches 600 rad·s^{-1}, the frictional torque ascends drastically to 48.39 μNm. Similar to the result curves from horizontal direction spin-down test, the frictional torque

versus rotational speed curve obtained from vacuum test diverges from the curve obtained from in air test and the gap widens with increasing rotational speed.

When the turbine spins down vertically (turbine rotor axis aligned in vertical direction), the gravity force of the rotor is applied on the thrust bearing in the axial direction of the rotor, and the value of this load is constant. As analysed before, the centrifugal force is applied on the journal bearing in radial direction of the rotor, and this load increases quadratically with increasing rotational speed.

When the vertical direction spin-down test is conducted in the vacuum chamber, the windage is negligible. The only load applied on the thrust bearing is the constant gravity force, and when the rotational speed increases from low to high, the lubrication regime of the thrust bearing immersed fully in lubricant (pure squalene in this case) transfers from boundary lubrication to mixed lubrication to full film hydrodynamic lubrication. The frictional torque from the thrust bearing is therefore expected to descend then ascend when the rotational speed is increased. The only load applied on the journal bearing in this case is the centrifugal force which increases quadratically with rising rotational speed. Therefore, the frictional torque from the journal bearing surges with rising rotational speed. This explains the observation that the total frictional torque increases with rotational speed.

When the vertical direction spin-down test is conducted in atmosphere, the load applied on the journal bearing stay unchanged compared to the case when the test is conducted in the vacuum chamber. As for the load conditions of the thrust bearing; except for the gravity force, an additional thrust force induced by the windage is also applied on the thrust bearing and this thrust force increases drastically with rising rotational speed. Additional frictional torque from the thrust bearing resulted from the windage thrust force leads to the divergence of the two curves.

The correlation between the frictional torque caused by windage and the rotational speed when the turbine operates vertically can also be obtained by subtracting the frictional torque curve measured from vacuum chamber test from the curve measured from in air test. The curve is displayed in figure 7-16 (b) above. It can be seen that when the rotational speed is close to zero, the windage induced frictional torque is below 0.4 μNm. The windage induced frictional increases with rising rotational speed, and when the rotational speed reaches 700 $rad \cdot s^{-1}$, the windage frictional torque is increased to 11.83 μNm.

Comparing figure 7-16 (a) and figure 7-16 (b), it can be noticed that when the rotational speed is below 100 rad·s^{-1}, the windage induced frictional torque when the turbine operates horizontally (at 100 rad·s^{-1}, frictional torque is 1.33 μNm) is slightly lower than the torque when turbine operates vertically (at 100 rad·s^{-1}, frictional torque is 1.33 μNm). When the rotational speed reaches 190 $rad \cdot s^{-1}$, the windage induced frictional torques under two turbine operation orientations are almost equal (horizontal: 2.46 μNm, vertical: 2.44 μNm). At rotational speeds above 300 rad·s^{-1}, the windage on the turbine results in higher frictional torque when the turbine operates horizontally compared to when the turbine operates vertically.

In practice, the energy harvesting turbine operates in an air flow. Based on the analysis in this chapter, the overall frictional torque from the bearings on the turbine can be divided into two parts: *(i)* frictional torque resulted from the gravity force and the centrifugal force applied on the micro bearings; *(ii)* frictional torque from the windage induced thrust force applied on the thrust bearing and the direct resistance torque from the air-rotor blade interface.

Figure 7-18 (a) demonstrates the correlation curves between the two consisting parts of frictional torque and the rotational speed in horizontal operation; Figure 7-18 (b) demonstrates the correlation curves between the two consisting parts of frictional torque and the rotational speed in vertical operation. It can be seen that under both cases, the torque resulting from the windage consists a smaller percentage of the total frictional torque in the complete test speed range, and the overall frictional torque is mainly resulting from the gravity force and the centrifugal force applied on the bearings. When the rotational speed is close to zero, over 90% of the frictional torque is caused by the gravity and the centrifugal force; when the rotational speed is increased to 200 rad·s^{-1}, over 80% of the frictional torque is caused by the gravity and the centrifugal force; when the rotational speed reaches 600 rad·s^{-1}, over 70% of the frictional torque is caused by the gravity and the centrifugal force.

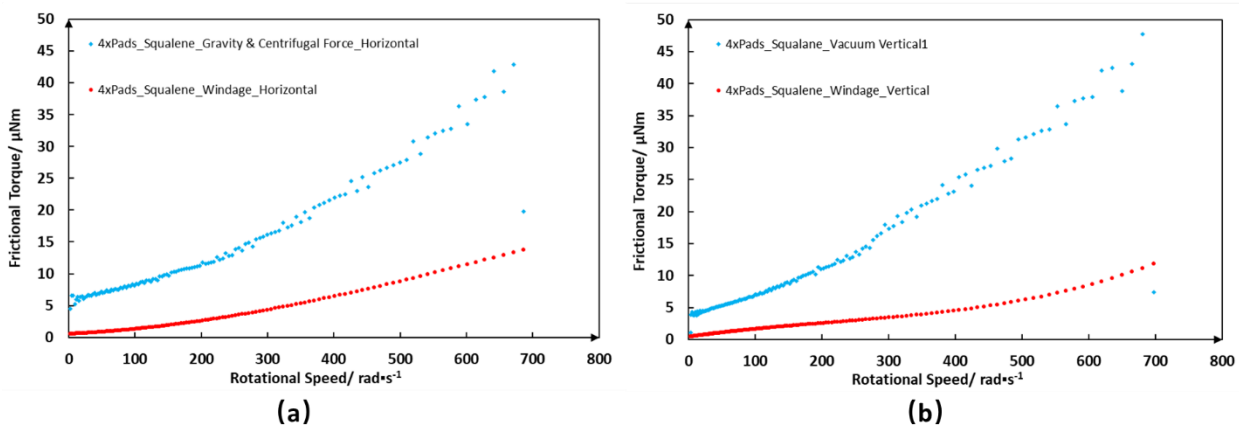

Figure 7-18. (a) Correlation Curves between the Two Consisting Parts of Frictional Torque and the Rotational Speed in Horizontal Operation; (b) Correlation Curves between the Two Consisting Parts of Frictional Torque and the Rotational Speed in Vertical Operation

Comparisons of Turbine Performance Operating in Horizontal and Vertical Directions

Comparisons of the turbine spin-down results obtained from horizontal direction and vertical direction tests are presented in this section. As discussed before, the loading conditions of the turbine bearings are different when the turbine orientation varies. Therefore, the correlation between the frictional torque and the rotational speed also changes with turbine orientation.

Figure 7-19 below demonstrates the frictional torque versus rotational speed curves from horizontal direction test and vertical direction test, with both tests being conducted in the vacuum chamber.

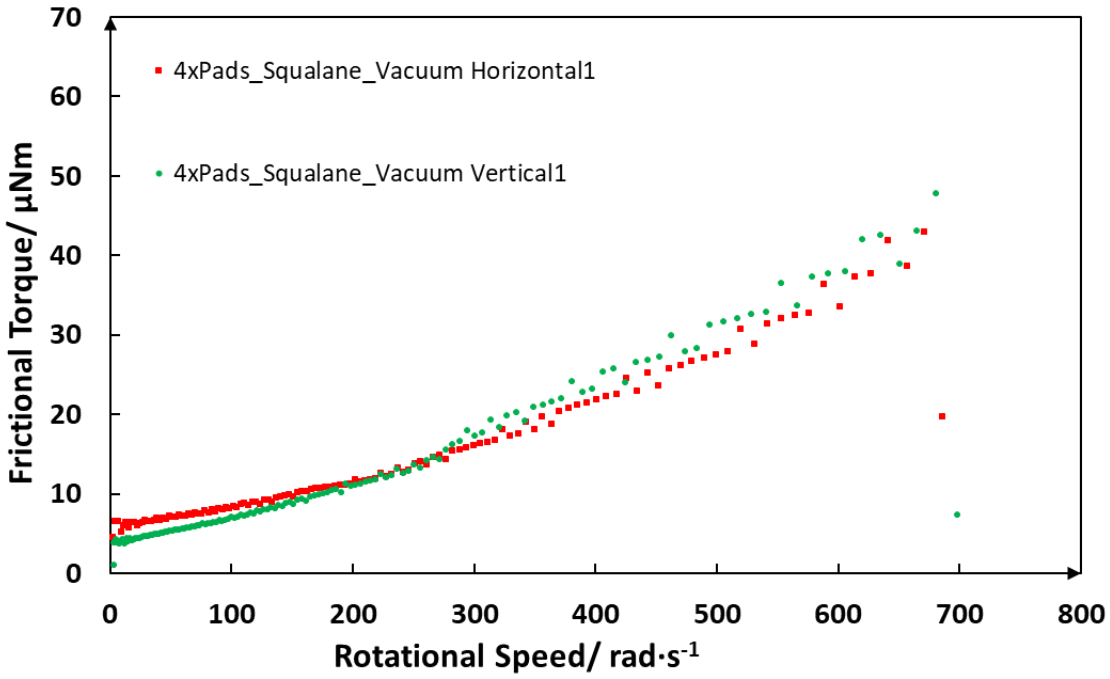

Figure 7-19. Frictional Torque versus Rotational Speed Curves from Horizontal Direction Test and Vertical Direction Test, Both Tests Being Conducted in the Vacuum Chamber (0.3 mbar)

- **Low Speed Range**

It can be seen from figure 7-19 that, when the rotational speed is close to zero, the frictional torque measured in the horizontal test is 6.58 μNm, while the frictional torque measured in vertical test is 3.72 μNm. When the turbine operates in the horizontal direction with low rotational speed (close to zero), the weight of the rotor is supported by the journal bearing (which is the only load applied on journal bearing) and no load is applied on the thrust bearing. The coefficient of the journal bearing at low speed can be computed using the equation 7-12 below,

$$\mu_{jb} = \frac{T_{jb}}{W_r \cdot R_{jb}} \tag{7-12}$$

where μ_{jb} is the friction coefficient of the journal bearing, T_{jb} is the frictional torque from the journal bearing, W_r is the gravity of the rotor and R_{jb} is the radius of the journal bearing.

As stated, the weight of the rotor is 4 gram (gravity: 0.0392 N) and the radius of the journal bearing is 0.8 mm. The calculated friction coefficient of the ruby journal bearing at low rotational speed (boundary lubrication friction coefficient) is 0.21.

Similarly, when the turbine operates in the vertical direction with low rotational speed, the weight of the rotor is supported by the thrust bearing (which is the only load applied on thrust bearing), the load applied on the journal bearing, the centrifugal force, is almost negligible at low rotational speed. The coefficient of the thrust bearing at low rotational speed can also be calculated:

$$\mu_{tb} = \frac{T_{tb}}{W_r \cdot R_{tb}} \tag{7-13}$$

where μ_{tb} is the friction coefficient of the thrust bearing, T_{tb} is the frictional torque from the thrust bearing and $R_{tb}$is the radius of the thrust bearing.

The radius of the thrust bearing is 0.5 mm. The calculated friction coefficient of the thrust bearing at low speed (boundary lubrication friction coefficient) is 0.19.

When the turbine operates in low rotational speed range ($\omega < 20\ rad \cdot s^{-1}$), either the thrust bearing or the journal bearing (depending on the turbine operation orientation) bears all the load in this stage (the gravity of the rotor itself) and operates in boundary lubrication regime. As the boundary friction coefficient of the micro thrust bearing is smaller than that of the journal bearing, in the speed range from 0 $rad \cdot s^{-1}$ to 20 $rad \cdot s^{-1}$ the frictional torque when the turbine operates horizontally is larger than the frictional torque when the turbine operates vertically. That can also be observed clearly from figure 7-19.

- **Medium Speed Range**

It can be seen from figure 7-19 that, when the rotating speed increases from 20 $rad \cdot s^{-1}$ to 100 $rad \cdot s^{-1}$, the frictional torque increases in both horizontal and vertical direction tests. For the vertical operation case, the frictional torque rises from 3.72 μNm to 6.45 μNm when the speed rises from 20 $rad \cdot s^{-1}$ to 100 $rad \cdot s^{-1}$, whereas for the horizontal operation case, the frictional torque goes up from 6.58 μNm to 8.51 μNm.

In this turbine speed range, for the case when the turbine operates in vertical direction, the load applied on the thrust bearing is still the gravity of the rotor, and the load applied on the journal bearing is the centrifugal force from the rotation of the rotor imbalance. For the case when the turbine operates in horizontal direction, no applied load is applied on the thrust bearing, and the dynamic force which is the combined force of the rotor gravity and the centrifugal force is applied on the journal bearing.

The increase of the centrifugal force (centrifugal force increases quadratically with rotational speed) leads to the frictional torque increase for both cases. As the rotational speed is not high in this stage, the gravity load is still the main applied load on the thrust bearing or the journal bearing.

The thrust bearing and the journal bearing operates in the mixed lubrication regime when the turbine rotates in the medium speed range. The friction coefficient of the thrust bearing in mixed lubrication regime is lower than that of the journal bearing in mixed lubrication regime. Therefore, the frictional torque generated in the thrust bearing would be higher than the frictional torque generated in the journal bearing in this speed range when similar load is applied. So, it is clearly shown in figure 7-19 that the frictional torque when the turbine operates horizontally is higher than the frictional torque when the turbine operates vertically in the rotational speed range from $20\ rad \cdot s^{-1}$ to $100\ rad \cdot s^{-1}$.

- **High Speed Range**

It can be seen from figure 7-19 that when the turbine operates with rotating speed higher than $100\ rad \cdot s^{-1}$, the rate with which frictional torque rises with rotational speed for the case turbine operates in vertical direction is higher than that for the case turbine operates in horizontal direction. The frictional torque when the turbine operates horizontally exceeds the frictional torque when the turbine operates vertically at $230\ rad \cdot s^{-1}$ rotational speed. However, that does not necessarily mean the friction coefficient of the thrust bearing (μ_{tb}) is higher than that of the journal bearing (μ_{jb}) when the turbine rotational speed is higher than $230\ rad \cdot s^{-1}$.

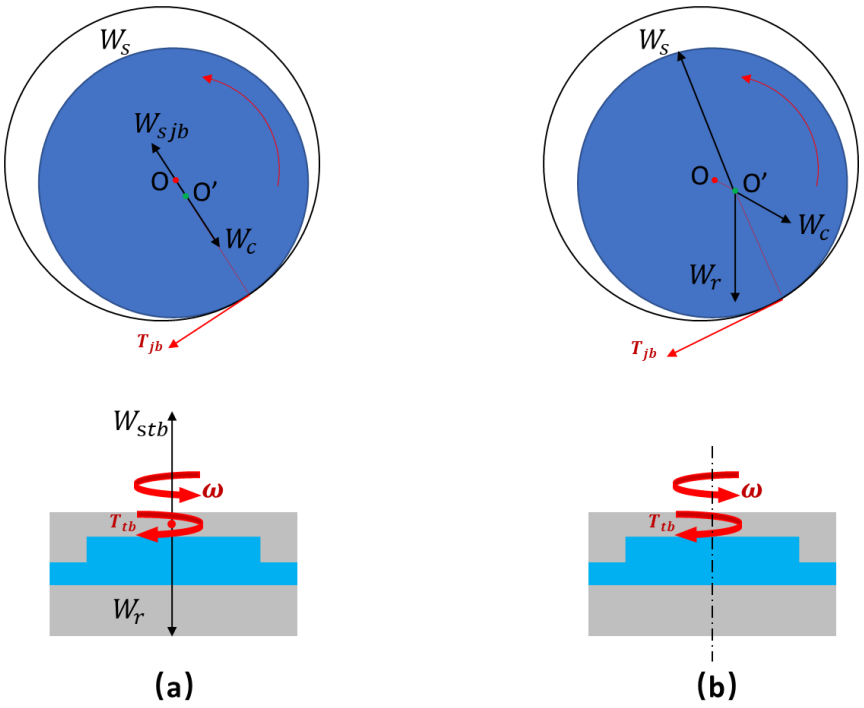

Figure 7-20. (a) Load Analysis of the Thrust Bearing and the Journal Bearing for the Case that the Turbine Operates in Vacuum in Vertical Direction; (b) Load Analysis of the Thrust Bearing and the Journal Bearing for the Case that the Turbine Operates in Vacuum in Horizontal Direction;

Detailed load analysis of the thrust bearing and the journal bearing for the case that the turbine operates in vertical direction is demonstrated in figure 7-20 a. The total frictional torque when the turbine operates vertically, T_v , can be computed with the equations below (equation 7-14 to equation 7-16).

$$T_{tb} = \mu_{tb} \cdot R_{tb} \cdot W_{stb} = \mu_{tb} \cdot R_{tb} \cdot W_r \tag{7-14}$$

$$T_{jb} = \mu_{jb} \cdot R_{jb} \cdot W_{sjb} = \mu_{jb} \cdot R_{jb} \cdot W_c \tag{7-15}$$

$$T_v = T_{tb} + T_{jb} = \mu_{tb} \cdot R_{tb} \cdot W_r + \mu_{jb} \cdot R_{jb} \cdot W_c \tag{7-16}$$

where W_{stb} is the total supporting load from the thrust bearing, when the turbine operates vertically it is equal to the gravity of the rotor W_r; W_{sjb} is the total supporting load from the journal bearing, when the turbine operates vertically it is equal to the centrifugal force of the rotor W_c.

Detailed load analysis of the thrust bearing and the journal bearing for the case that the turbine operates in horizontal direction is displayed in figure 7-20 b. The total frictional torque when

the turbine operates horizontally, T_h , can be computed with the equations below (equation 7-17 to equation 7-19).

$$T_{tb} = \mu_{tb} \cdot R_{tb} \cdot W_{stb} = 0 \tag{7-17}$$

$$T_{jb} = \mu_{jb} \cdot R_{jb} \cdot W_{sjb} \tag{7-18}$$

$$T_h = T_{tb} + T_{jb} = \mu_{jb} \cdot R_{jb} \cdot W_{sjb} \tag{7-19}$$

The total supporting load from the thrust bearing, W_{stb}, is equal to zero when the turbine operates horizontally in the vacuum chamber (no load is applied on the thrust bearing); while the total supporting load from the journal bearing, W_{sjb}, is equal to the combined load of the gravity of the rotor W_r and the centrifugal force of the rotor W_c. In this case, the direction and the module of the gravity W_r is fixed whereas the direction of the centrifugal force W_c rotates around the rotating centre of the rotor, *O*. Therefore, the direction and the module of the total supporting load from the journal bearing W_{sjb}, (which is equal to the combined load of W_c and W_r) also changes continuously as the turbine rotates.

When the turbine operates with a certain rotational speed ω, the supporting force of the journal bearing in its vector form $\overrightarrow{W_{sjb}}$ is given in equation (7-20):

$$\overrightarrow{W_{sjb}} = W_c \cos(\omega t) \cdot \vec{\imath} + [W_c \sin(wt) + W_r]\vec{\jmath} \tag{7-20}$$

where $\vec{\imath}$ is the unite force vector in horizontal direction, $\vec{\jmath}$ is the unite force vector in vertical direction.

The magnitude of the force vector $\overrightarrow{W_{sjb}}$ can be simply derived as shown in equation (7-21):

$$\left|\overrightarrow{W_{sjb}}\right| = \left[{W_c}^2 + {W_r}^2 + 2W_cW_r \sin(wt)\right]^{0.5} \tag{7-21}$$

It can be seen from equation (7-21) that the magnitude of $\overrightarrow{W_{sjb}}$ varies periodically and the average (equivalent) module value of the vector $\overrightarrow{W_{sjb}}$, which is the so defined W_{sjb} can be computed with equation (7-22):

$$W_{sjb} = \left({W_c}^2 + {W_r}^2\right)^{0.5} \tag{22}$$

Therefore, the total frictional torque when the turbine operates horizontally, T_h is:

$$T_h = \mu_{jb} \cdot R_{jb} \cdot W_{sjb} = \mu_{jb} \cdot R_{jb} \cdot \left({W_c}^2 + {W_r}^2\right)^{0.5} \tag{7-23}$$

By comparing the equation of the total frictional torque when turbine operates vertically (equation 7-16) and the equation of the total frictional torque when turbine operates

horizontally (equation 7-23), it can be deduced easily that, when the centrifugal force exceeds a certain value, the T_v is bound to outweigh the T_h .

This is the mechanism behind the observed phenomenon that the vertically measured frictional torque exceeds the horizontally measured frictional torque once the turbine is rotating speed is higher than 230 $rad \cdot s^{-1}$.

Figure 7-21 below demonstrates the frictional torque versus rotational speed curves from horizontal and vertical tests conducted in atmosphere. The trends of these curves are similar to the curves obtained from the vacuum chamber tests, just the frictional torque is higher since an additional windage load is induced when the turbine operates in atmosphere. The total frictional torque when the turbine operates vertically is lower than the total frictional torque when the turbine operates horizontally when the rotational speed is lower than 205 $rad \cdot s^{-1}$. The T_v outweighs T_h once the rotating speed exceeds 205 $rad \cdot s^{-1}$.

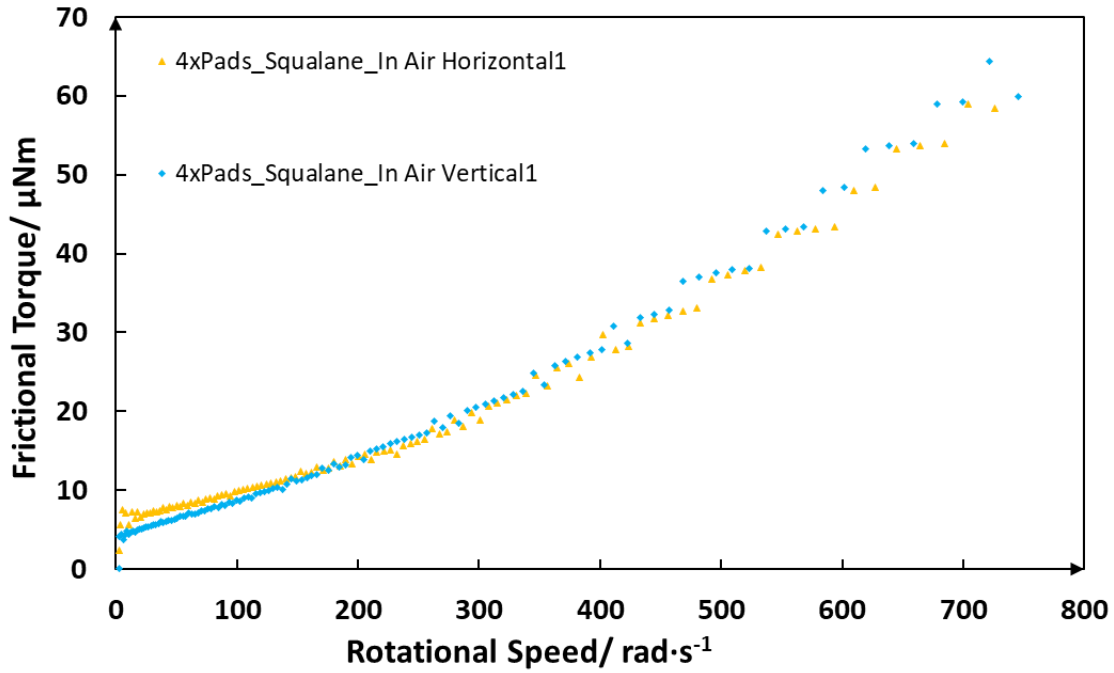

Figure 7-21. Frictional Torque versus Rotational Speed Curves from Horizontal Direction Test and Vertical Direction Test, Both Tests Being Conducted in Atmosphere

7.4.3. Effect of Lubricant Viscosity

In this section, the effect of the lubricant viscosity on the performance of the turbine bearings is investigated.

Three lubricants with different viscosity are tested which are *(i)* water, *(ii)* hexadecane and *(iii)* squalene. All the tests reported in this section are conducted in room temperature which is 25 °C. At this temperature the dynamic viscosity of water is 0.89 cP, the dynamic viscosity of hexadecane is 3.02 cP, the dynamic viscosity of squalene is 28.33 cP. The thrust bearing used in this group of investigation is etched with Pattern A. No extra pre-load is applied on the thrust and journal bearings on the turbine in this group of tests.

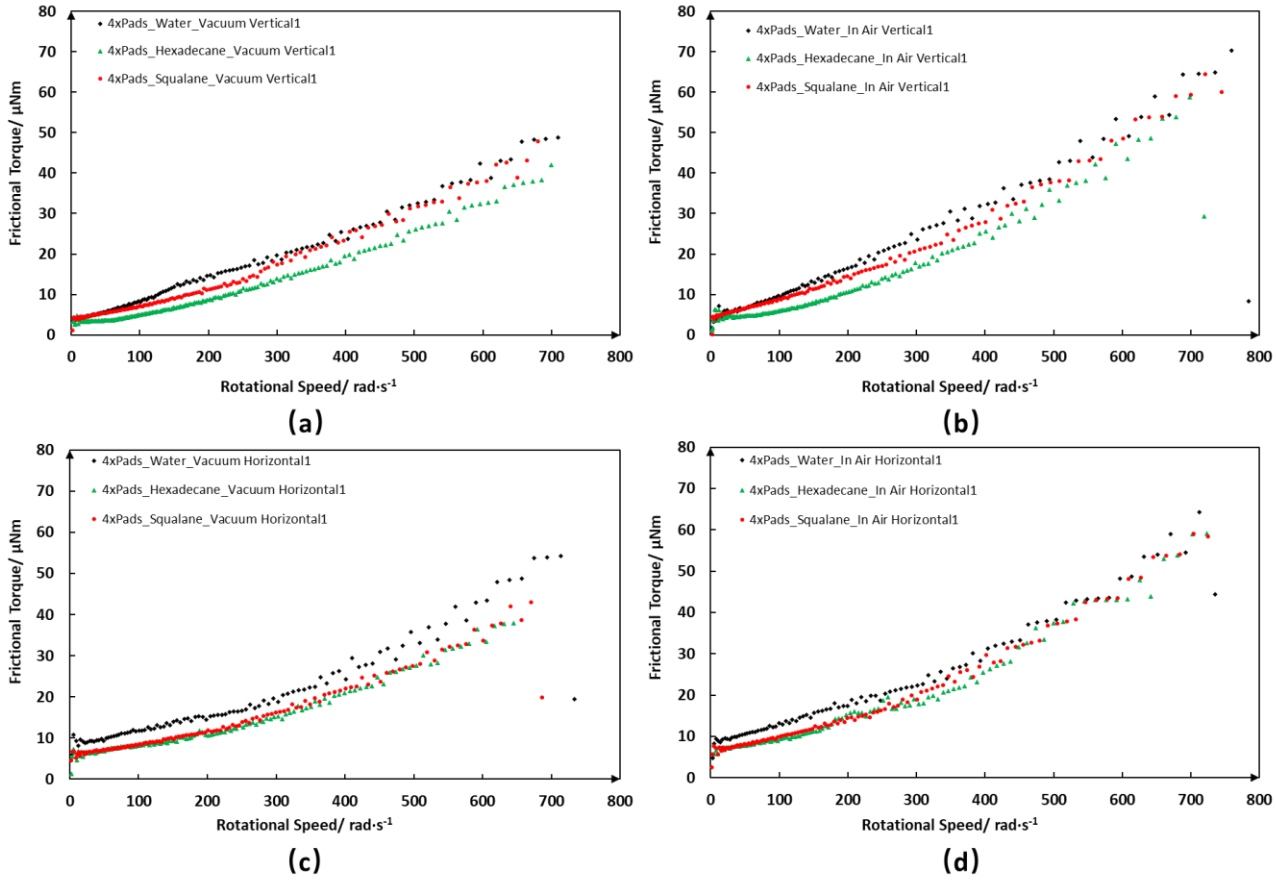

Figure 7-22. Frictional Torque versus Rotational Speed Curves of the Turbine with Micro Bearings Lubricated by Different Viscosity Lubricants Obtained under Four Different Operation Conditions

Figure 7-22 above demonstrates the frictional torque versus rotational speed curves of the turbine lubricated with different viscosity lubricants measured under four different operation conditions:

- Figure 7-22 (a) displayed the curves obtained from **vertical** direction spin down tests conducted in the **vacuum chamber (Top Left)**;

- Figure 7-22 (b) displayed the curves obtained from **vertical** direction spin down tests conducted in the **atmosphere (Top Right)**;
- Figure 7-22 (c) displayed the curves obtained from **horizontal** direction spin down tests conducted in the **vacuum chamber (Bottom Left)**;
- Figure 7-22 (d) displayed the curves obtained from **horizontal** direction spin down tests conducted in the **atmosphere (Bottom Right)**.

It can be seen from figure 7-22 (a) and figure 7-22 (b) that when the turbine rotational speed is close to zero, the total frictional torque is almost equal to the same value, 3.72 μNm, when the bearings are lubricated with lubricants with different viscosities. That is because when the turbine operates vertically with rotational speed close to zero, the only applied load is the gravity of the rotor and it is supported by the thrust bearing. The thrust bearing operates in the boundary lubrication regime in this case (*i.e.* speed close to zero) and its friction coefficient is determined by the thrust bearing surface properties and is independent of the lubricant viscosity hence frictional torque with same the value is generated in this case.

It can also be found from figure 7-22 (a) and figure 7-22 (b) that when the turbine operates vertically and the rotational speed of the bearing is higher than 100 $rad \cdot s^{-1}$, the total frictional torque of the bearings lubricated with hexadecane is lower than that of the bearings lubricated with squalene. That is because the thrust bearing operates in hydrodynamic lubrication regime at high rotational speed, the friction coefficient of the bearing in this case is negatively correlated to the viscosity of the lubricant. The viscosity of hexadecane is much lower than that of squalene, hence the frictional torque of the bearings when lubricated with hexadecane under high rotational speed is lower.

The frictional behaviour of the turbine bearings when the turbine operates horizontally is displayed figure 7-22 (c) and 7-22 (d). It can be seen from figure 7-22 (c) that the frictional torque versus rotational speed curves of the bearings lubricated with hexadecane and squalene almost coincide with each other in whole speed range when the turbine operates horizontally in the vacuum chamber. Under this operational condition, all the applied loads (gravity of the rotor and rotor centrifugal force) are supported by the journal bearing and they are all independent of the lubricant viscosity. That indicates the friction coefficient of the journal bearing stays unchanged when it is lubricated with lubricants with different viscosity in the whole speed range. The reasonable hypothesis for this phenomenon is that the journal bearing currently used in the turbine does not function appropriately and it can only operate in the boundary lubrication regime in which case the friction coefficient is independent of the

viscosity of the lubricant. This hypothesis is highly possible as no lubricant flow supply design is applied to the journal bearing (it is just immersed to the lubricant bath), so the journal bearing is not able to operate properly.

From figure 7-22 (d), when the turbine operates horizontally in atmosphere, the frictional torque curves of the turbine with micro bearings lubricated with hexadecane and squalene also coincide with each other at speed range from 0 to 270 $rad \cdot s^{-1}$. The curves diverge from each other when the rotational speed exceeds 300 $rad \cdot s^{-1}$. The frictional torque of the turbine with bearings lubricated with hexadecane is obviously lower than that of the turbine with bearings lubricated with squalene when the speed is further increased. In this test condition, the frictional torque from the micro journal bearing is almost the same when the bearing is lubricated with different lubricants. However, extra load from windage is applied on the thrust bearing in this case and it increases rapidly with rotational speed. As explained in the previous paragraph, when the thrust bearing operates at high speed and in the hydrodynamic lubrication regime, lower friction coefficient can be achieved using lower viscosity lubricant. Therefore, when the rotational speed is high and the windage load applied on the thrust bearing is comparable to the gravity load and centrifugal force load, and the frictional torque generated from the thrust bearing will be lower if lower lubricant (hexadecane) is used.

Another phenomenon that can be noticed from figure 7-22 is that under all operational conditions, the frictional torque of the turbine with the bearings lubricated with water (which has the lowest viscosity) is always the highest in the whole rotational speed range. That could be attributed to the high evaporation rate of water and is confirmed by the observation that the added water is almost dried after the turbine is tested so insufficient lubricant must have been supplied to the bearings. The starvation of water might cause severe stiction of the bearing surfaces hence resulting in high friction coefficient.

7.4.4. Effect of Friction Modifier

In this section, results showing the effects of the friction modifier additive on the performance of the MEMS bearings that operate on the micro energy harvesting turbine is presented. The friction modifier applied in this series of testes is octadecylamine ($C_{18}H_{39}N$) which consists of an 18-carbon straight chain and an amine group at the end of the carbon chain. The amine group enables the molecules to get attached to the silicon surfaces and form a thin low shear strength film which helps friction reduction of the bearing surfaces in boundary and mixed regime lubrication.

Hexadecane is selected as the base liquid of the lubricant tested in this series of experiments as the lowest frictional torque of the the micro energy harvesting turbine is achieved especially in the high speed range when the bearings are lubricated with this lubricant. 0.1%wt of octadecylamine is added into the hexadecane which enables slippery film form over the bearing surfaces and leaves the bulk viscosity of the lubricant almost equal to that of pure hexadecane (3.02 cp at 25 °C).

This series of tests are conducted under room pressure and temperature (1.01×10^5 Pa, 25 °C). The thrust bearing used here is etched with Pattern A. No extra pre-load is applied on the thrust and journal bearings on the turbine in this group of tests.

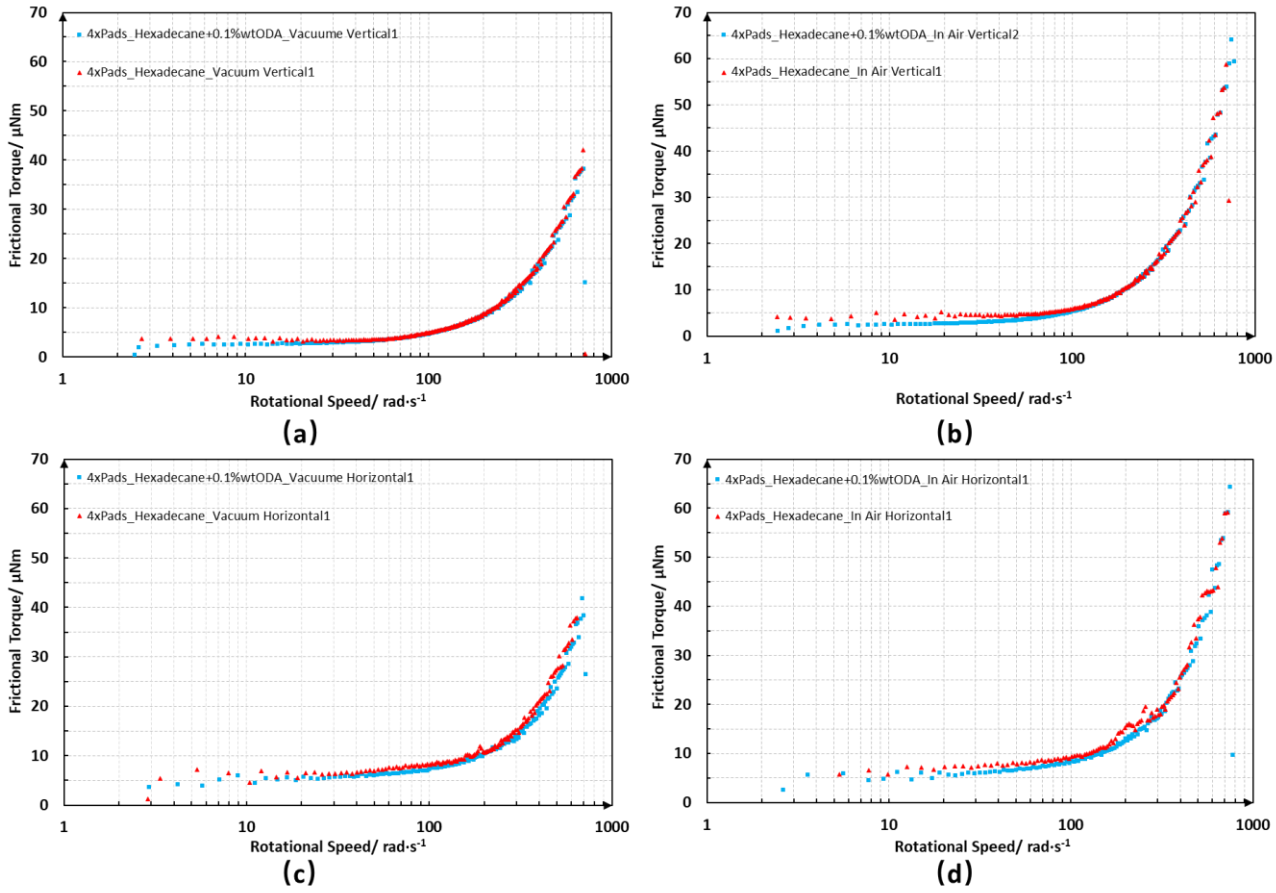

Figure 7-23. Frictional Torque versus Rotational Speed Curves of the Turbine with Micro Bearings Lubricated by Pure Hexadecane and by 0.1%wt ODA Added Hexadecane Obtained under Four Different Operation Conditions

Figure 7-23 above shows the frictional torque versus rotational speed curves of the turbine lubricated with pure hexadecane and hexadecane with octadecylamine which are measured under four different operation conditions:

- Figure 7-23 (a) displayed the curves obtained from **vertical** direction spin down tests conducted in the **vacuum chamber (Top Left)**;
- Figure 7-23 (b) displayed the curves obtained from **vertical** direction spin down tests conducted in the **atmosphere (Top Right)**;
- Figure 7-23 (c) displayed the curves obtained from **horizontal** direction spin down tests conducted in the **vacuum chamber (Bottom Left)**;
- Figure 7-23 (d) displayed the curves obtained from **horizontal** direction spin down tests conducted in the **atmosphere (Bottom Right)**.

It can be seen from figure 7-23 (a) that when the turbine operates vertically in the vacuum with low rotational speed (close to zero), the total frictional torque of the turbine is reduced from 3.72 μNm to 1.91 μNm after adding 0.1%wt of octadecylamine into hexadecane. In this case, the total frictional torque is almost purely resulting from the 1-mm thrust bearing which operates in boundary lubrication regime, and the applied load on the thrust bearing is the gravity of the rotor (W_r). The slippery ODA film which consists of ODA molecules attaching to the silicon surfaces of the thrust bearings archives a 49% frictional torque reduction (power loss reduction) in low speed range. It reduces the boundary friction coefficient of the silicon thrust bearing from 0.19 to 0.098. It can also be observed from figure 7-23 (a) that when the rotational speed of the turbine increases, the friction reduction effect of the added friction modifier gradually vanishes. The friction modifier becomes non-effective on friction reduction when the turbine speed reaches 40 rad·s^{-1} and above because under this condition, the film thickness of the thrust bearing surfaces are separated far enough by the lubrication film and the friction mainly results from the shear of the bulk lubricant film.

Effective frictional torque reduction is even more obvious when the turbine operates vertically in air in the low rotational speed range. As demonstrated in figure 7-23 (b), the rotational speed range within which the octadecylamine is effective in friction reduction is wider when the turbine operates in atmosphere. When the speed reaches 40 rad·s^{-1}, the frictional torque when the bearings are lubricated by pure hexadecane is 4.41 μNm, it is reduced to 3.10 μNm when 0.1%wt of ODA is added, i.e., 29.7% friction reduction is achieved in this case. The ODA losses friction reduction ability when the rotational speed reaches 110 rad·s^{-1} in the case that the turbine operates in air. That threshold speed is higher than that of the case that the turbine operates in the vacuum. This is because the applied load on the thrust bearing in this case is the sum load of gravity of the rotor and the windage thrust force, the thrust bearing transfers from

boundary and mixed lubrication regimes and enters full film lubrication regime at higher rotational speed.

When the turbine operates horizontally in the vacuum chamber, all the load is supported by the micro journal bearing. In this case, octadecylamine is effective in friction reduction in the whole tested speed range, which can be observed from figure 7-23 (c). It can also be then inferred that, the journal bearing functions in the boundary and mixed lubrication regimes in the complete speed range in the experiments and does not enters full film lubrication regime. However, the friction reduction by the friction modifier is limited to a small extent in this case. When the turbine rotational speed is 100 rad·s^{-1}, the frictional torque is reduced from 8.15 μNm to 7.27 μNm (11.1% friction reduction) after 0.1%wt of ODA is added; when the speed is 400 $rad \cdot s^{-1}$, the frictional torque is reduced from 21.02 μNm to 18.58 μNm (11.6% friction reduction). The friction reduction capability of octadecylamine becomes much less effective when the additive functions on the journal bearing than that functions on the silicon bearing. That is because the basic amine group gets attached to the acidic silicon surfaces much easier than it gets attached to the stainless steel or ruby surfaces. Therefore, the slippery boundary lubrication film consisting of ODA molecules forms more stably on the silicon bearing surfaces hence resulting in larger friction reduction percentage.

7.4.5. Effect of Thrust Bearing Patterns

Three thrust bearings with different pocket patterns are assembled on the micro energy harvesting turbine and their performance are assessed by spin-down tests. The graphics of the tested thrust bearings are demonstrated in figure 7-24 below again.

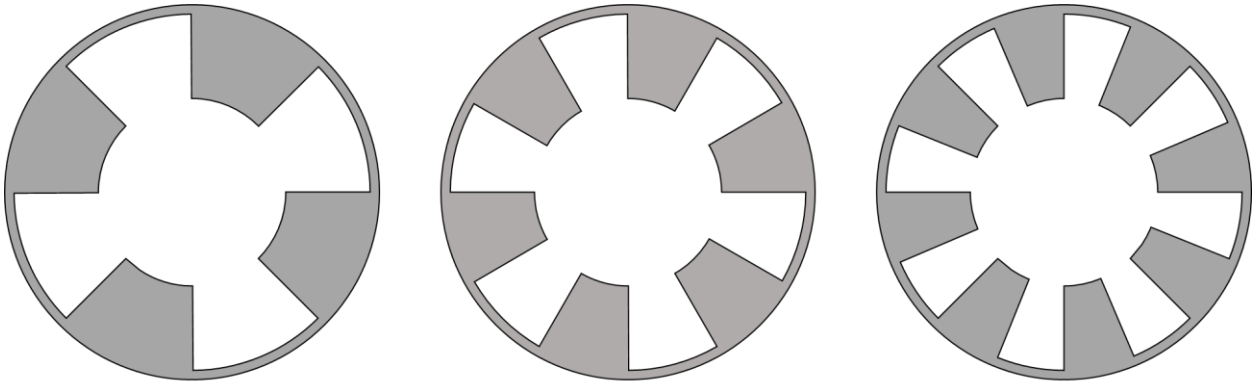

$N_{pad} = 4$ $N_{pad} = 6$ $N_{pad} = 8$

Figure 7-24: Graphics of the Stator Pads of the Micro Thrust Bearings with Different Recessed Patterns

The three thrust bearings distinguish form each other by the number of pads. The thrust bearing *(a)* consists of 4 pad regions, the angular width of each pad is 90°; the thrust bearing (b) consists of 6 pad regions, the angular width of each pad is 60°; the thrust bearing (c) consists of 8 pad regions, the angular width of each pad is 45°. The total angular width of the etched pocket regions for all three thrust bearings is equal to 180°. Correspondingly, the total angular width of the land regions for all three thrust bearings is also equal to 180°.

For the four pads bearing, there are four leading steps (convergence) around which hydrodynamic pressure builds up and there are four trailing steps (divergence) where cavitation develops. For the six pads bearing, there are six leading steps and six trailing steps; for the eight pads bearing, there are eight leading steps and eight trailing steps.

The frictional torque versus rotational speed curves of the micro turbine which is installed with three different thrust bearings (the journal bearing installed on the turbine stays unchanged) and operates vertically in the vacuum chamber and are demonstrated in figure 7-25 (a). The frictional torque versus rotational speed curves of the micro turbine when the turbine operates vertically in the atmosphere are displayed in figure 7-25 (b).

The lubricant used in this series of tests is hexadecane mixed with 0.1%wt of octadecylamine. As the micro journal bearing and the loading conditions on the micro journal bearing remained unchanged in this series of tests, so the variation of the frictional torque versus rotational speed curves are caused by the different performance of the differently patterned micro thrust bearings.

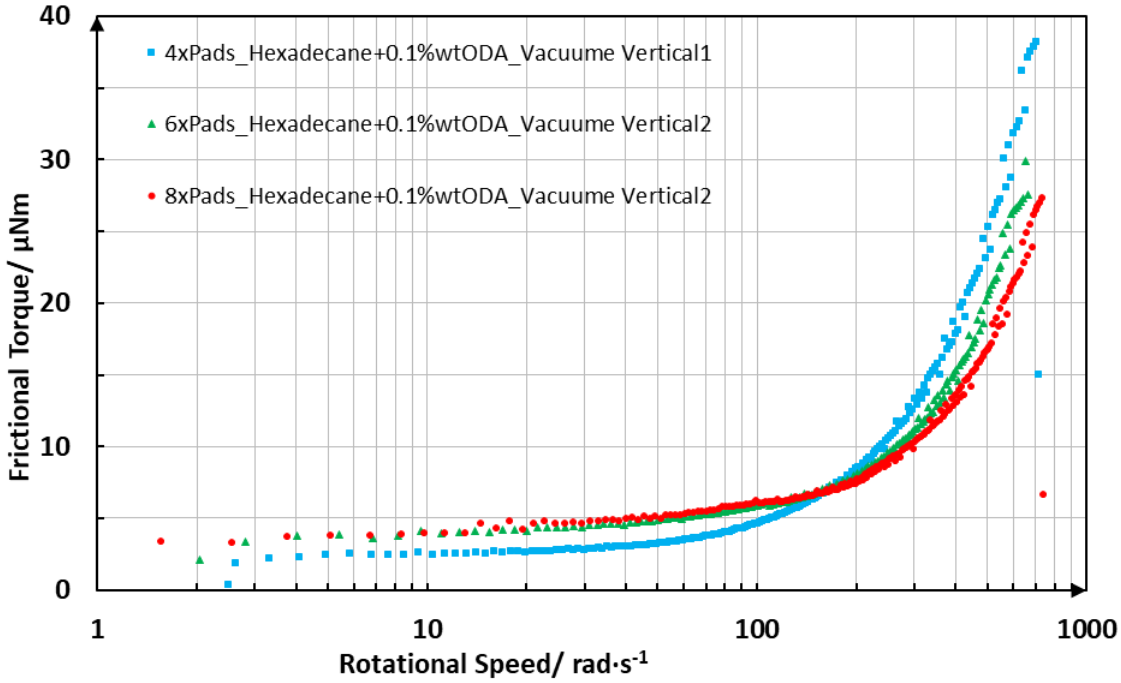

Figure 7-25 (a). Frictional Torque Curves of Turbine Installed with the Same Micro Journal Bearing and Micro Thrust Bearings Recessed with Different Patterns Lubricated by 0.1%wt ODA Added Hexadecane, Turbine Placed Vertically in the Vacuum Chamber

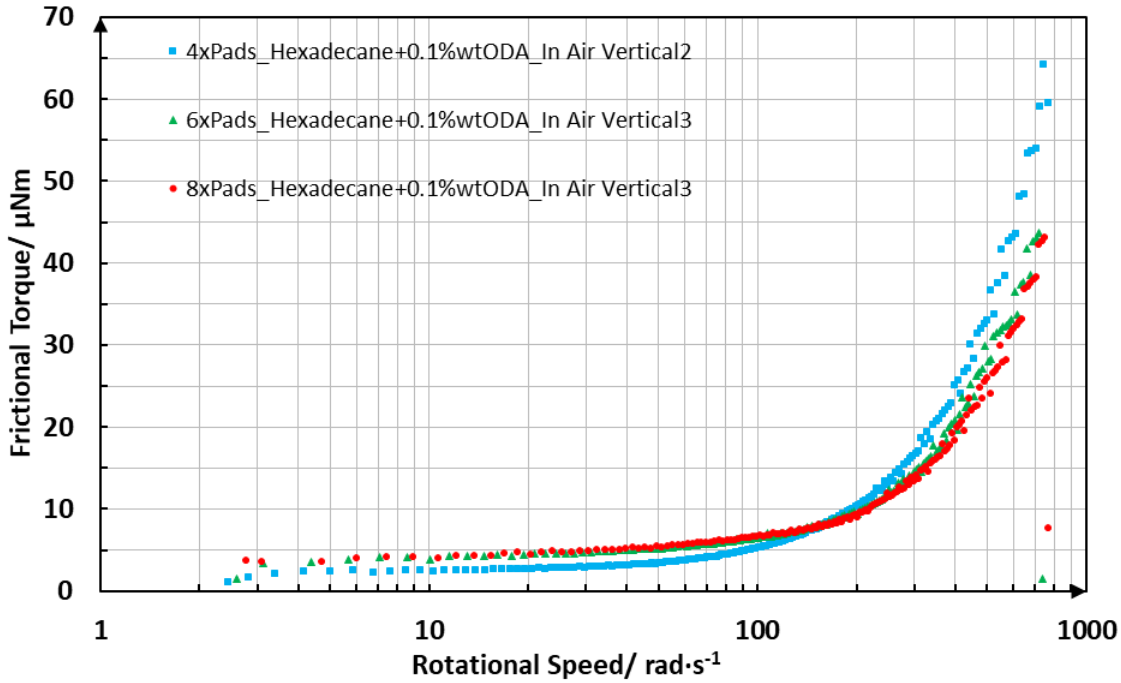

Figure 7-25 (b). Frictional Torque Curves of Turbine Installed with the Same Micro Journal Bearing and Micro Thrust Bearings Recessed with Different Patterns Lubricated by 0.1%wt ODA Added Hexadecane, Turbine Placed Vertically in Air

As demonstrated in figure 7-25 (a), when the speed of the turbine is lower than 40 rad·s^{-1}, larger frictional torque is generated from thrust bearing consisting of more pads. At 20 rad·s^{-1} speed, the frictional torque of the turbine installed with 8 pads thrust bearing is 4.91 μNm, the frictional torque of the 6 pads thrust bearing is 4.09 μNm and the frictional torque of the 4 pads thrust bearing is 2.31 μNm. However, as the rotational speed rises from 40 rad·s^{-1}, the frictional torque versus rotational speed curves of the turbine installed with different thrust bearings gradually diverge and finally intersect with each other. When the turbine rotational speed reaches 400 rad·s^{-1}, smaller frictional torque is generated from thrust bearing consisting of more pads. At 400 rad·s^{-1}, the frictional torque of the turbine installed with 8 pads thrust bearing is 12.89 μNm, the frictional torque of the 6 pads thrust bearing is 14.59 μNm and the frictional torque of the 4 pads thrust bearing is 17.82 μNm.

Similar trend can be observed from the frictional torque versus rotational speed curves of micro turbine installed with different thrust bearings which are obtained from the vertical-in air spin down tests. At 20 rad·s^{-1} rotational speed, the frictional torque of the turbine installed with 4 pads thrust bearing is 2.68 μNm; the frictional torque rises up to 4.32 μNm when 6 pads thrust bearing is used on the turbine; the frictional torque ascends further to 4.75 μNm when 8 pads thrust bearing is installed on the turbine. At 400 rad·s^{-1} rotational speed, however, the correlation between the frictional torque and the pad number of the thrust bearings installed on the micro energy harvesting turbine is reversed. The measured frictional torque when the turbine is installed with 4 pads thrust bearing is 22.94 μNm; it declines to 19.95 μNm when replacing the 4 pads bearing with the 6 pads bearing; the frictional torque can be further reduced to 17.35 μNm when 8 pads bearing is used.

From figure 7-25 (a) and figure 7-25 (b) it can be concluded that when the turbine operates in low speed range within which the lubrication of the thrust bearing is in boundary or mixed regime, the frictional torque increases with the increasing pad number of the thrust bearing. Based on this observations, it can be deduced that the load carrying capacity of the 4 pads thrust bearing is the highest among the three thrust bearings tested on the micro turbine whereas the load carrying capacity of the 8 pads thrust bearing is the lowest. That is because the frictional torque decreases with increasing load carrying capacity in the boundary and mixed lubrication regimes.

As the load carrying capacity of the 4 pads bearing is the highest, it would enter full film hydrodynamic lubrication regime at lower rotational speed. On the contrary, the 8 pads thrust

bearing which has the lowest load carrying capacity would operate in the low-friction coefficient mixed lubrication regime for a wider speed range, it would start to operate in the full film hydrodynamic lubrication regime at larger rotational speed. For micro scale thrust bearings, the friction coefficient would increase drastically with ascending rotational speed once the bearing enters full-film hydrodynamic lubrication regime as the viscous drag becomes dominant for small scale bearings at high rotational speed. The friction coefficient of the hydrodynamic lubrication regime at high rotational speed would even be higher than the friction coefficient of the mixed lubrication regime. Therefore, lower frictional torque results from micro thrust bearing with lower load capacity at high rotational speeds as the friction coefficient of the thrust bearing starts to increase drastically at larger rotational speed. So, the frictional torque is negatively correlated with the pad number of the thrust bearing.

7.4.6. Validation of the Load Carrying Capacity and Pad Number of the Thrust Bearing in Trend by the Numerical Model

As deduced from the experimental results demonstrated in **section 7.4.5**, the 4 pads thrust bearing has the highest load carrying capacity among the three tested thrust bearings whereas the 8 pads thrust bearing has the lowest load carrying capacity. That can be validated through simulation using the model developed in this research.

When the three thrust bearings operates under same conditions (942.5 $rad \cdot s^{-1}$ speed/ 400 nm minimum film thickness), the integrated hydrodynamic force of the 4 pads thrust bearing is 0.3257 N, the load carrying capacity of the 6 pads thrust bearing is 0.3141 N and the load carrying capacity of the 8 pads thrust bearing is 0.3047 N. That agrees with the experimental obtained results that the load carrying capacity decreases with increasing pad number of the thrust bearing.

The film thickness distribution contours of three thrust bearings are demonstrated in figure 7-26 (a) and the pressure distribution contours of the three thrust bearings are demonstrated in figure 7-26 (b).

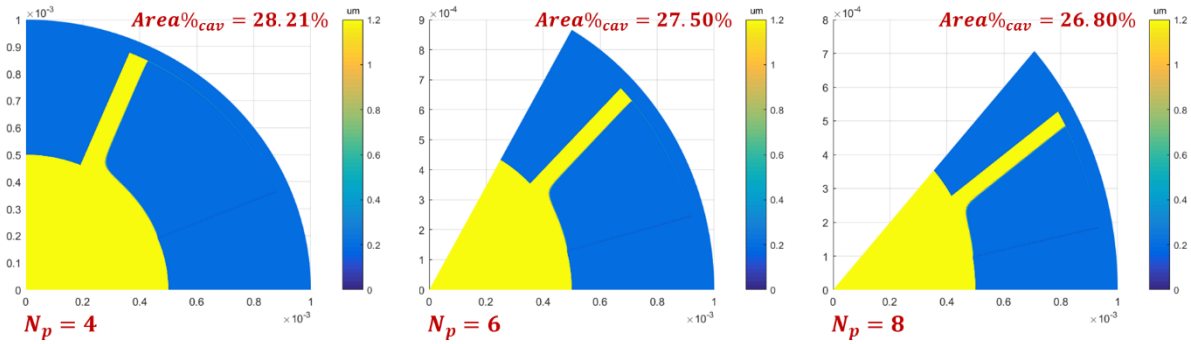

Figure 7-26 (a). Film thickness distribution Contours of Micro Pocketed Parallel Thrust Bearings Recessed with Different Patterns

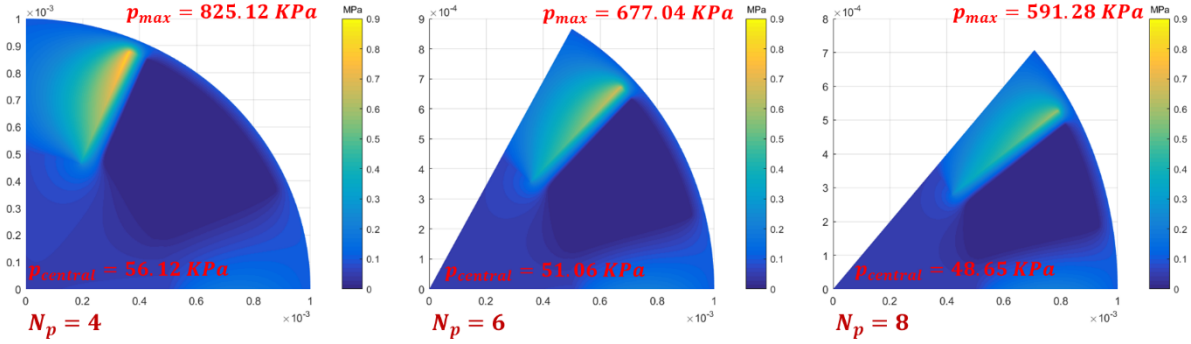

Figure 7-26 (b). Pressure Distribution Contours of Micro Pocketed Parallel Thrust Bearings Recessed with Different Patterns

It can be seen from figure 7-26 (a) that the percentages that the cavitation area occupies the total bearing area of the 4 pads, 6 pads and 8 pads thrust bearings are in similar values which are 28.21%, 27.50% and 26.80% respectively. Therefore, the area of the pressurized regions of three thrust bearings are almost equal. It can be observed from figure 7-26 (b), the hydrodynamic pressure generated around the leading step of the thrust bearing drops with increasing pad number of the thrust bearing. In addition, the pressure in the central flat region also declines with increasing pad number of the thrust bearing. Therefore, the load carrying capacity drops with increasing pad number of the bearing for the micro parallel pocketed thrust bearing, which agrees with the experimental results.

7.5. Comparison between the Performance of the Developed Micro Liquid Bearings and the Performance of the Commercial V Bearings

Previously, two commercial V bearings (pivot bearings) were used in the sliding contacts of the prototype micro turbine [1]. As discussed in Chapter 1, one of the most important objectives of this research is to reduce the power loss of the sliding contacts by replacing the V bearings with liquid journal bearings and thrust bearings. In addition, the wear rate of the pivot bearing is high as the contact of the pivot bearing is just a tip (contact pressure is high) and no lubricant is used for the surface protection, the high wear rate results in increasingly higher friction coefficient with sliding being continually applied; whereas the wear rate of the liquid bearings is much smaller since the bearing surfaces are separated by the pressurized liquid and the bearing contact is conformal (contact pressure is small). Therefore, the liquid bearings are more reliable after large amount of sliding is applied compared to the dry contact pivot bearings. A simplified diagram of the V bearing and tipped shaft setup is demonstrated in figure 7-27 below.

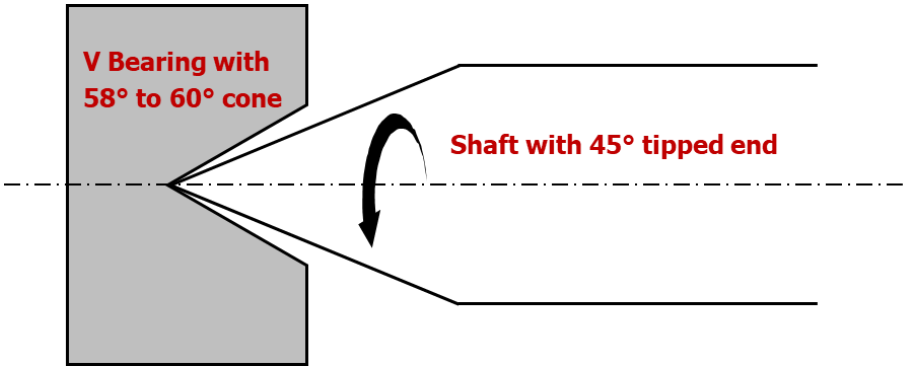

Figure 7-27. Setup of the Commercial V Bearing and the Tipped Rotor Shaft

Comparisons of the frictional torque and power loss of the dry contact pivot bearings and liquid bearings are demonstrated in figures 7-28 to 7-31 below. The thrust bearing selected for the comparison in this section is the eight pad thrust bearing and the lubricant used in the liquid bearings is 0.1%wt ODA mixed hexadecane.

7.5.1. Turbine Operates Vertically in the Vacuum Chamber

Figure 7-28 below demonstrates the frictional torque and power loss comparisons of the two types of bearings operating vertically in the vacuum chamber.

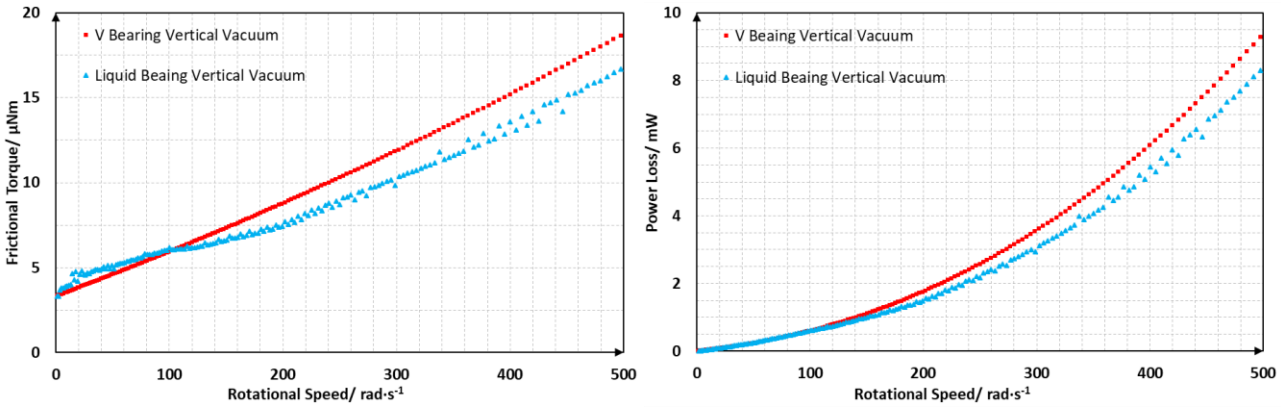

Figure 7-28. Frictional Torque and Power Loss Comparisons of the Two Types of Micro Bearings Operating Vertically in the Vacuum Chamber

It can be seen that the when the speed is close to zero, the frictional torque of the turbine installed with liquid bearings is 3.5 μNm which is slightly higher than that of the dry contact V bearings. That is because the radius of the liquid bearings is much larger than that of the V bearings (the contact is just a tip, so the radius is tiny). Therefore, the frictional torque from the V bearings would be smaller when the friction coefficient of the liquid bearings is not lower enough compared to that of the V bearings.

When the rotational speed exceeds 100 rad·s^{-1}, the frictional torque of the turbine installed with liquid bearings is smaller than that of the V bearings. At 200 rad·s^{-1} rotational speed, the frictional torque of the liquid bearings is 7.40 μNm, the frictional torque of the V bearing is 8.83 μNm. At 400 rad·s^{-1} rotational speed, the frictional torque of the liquid bearings is 13.11 μNm, the frictional torque of the V bearing is 15.19 μNm. When the rotational speed reaches 500 rad·s^{-1} rotational speed, the frictional torque of the liquid bearings is 16.67 μNm, the frictional torque of the V bearing is 18.66 μNm.

As demonstrated in figure 7-28, even though the frictional torque of the turbine installed with liquid bearings is smaller than that of the V bearings at low rotational speeds, the power loss curves of the two types of bearing in low speed range almost coincide with each other. Considerable power loss reduction is achieved by replacing the V bearings with liquid bearings when the speed is higher than 200 rad·s^{-1}. At 200 rad·s^{-1} speed, the power loss of the V bearings is 1.75 mW, the power loss of the liquid bearings is 1.48 mW, 15.4% power loss reduction is achieved. At 400 rad·s^{-1} speed, the power loss of the V bearings is 5.09 mW, the power loss of the liquid bearings is 6.08 mW, 16.3% power loss reduction is achieved. When the speed

reaches 500 rad·s^{-1}, the power loss of the V bearings is 9.30 mW, the power loss of the liquid bearings is 8.30 mW, 10.8% power loss reduction is achieved.

7.5.2. Turbine Operates Horizontally in the Vacuum Chamber

The frictional torque and power loss comparisons of the two types of bearings operating horizontally in the vacuum chamber are presented in figure 7-29. The speed range within which the frictional torque of the turbine installed with liquid bearings is larger than that of the V bearings is much wider in this case. However, considerable power loss reduction is still achived when the rotaional speed is higher than 400 rad·s^{-1}.

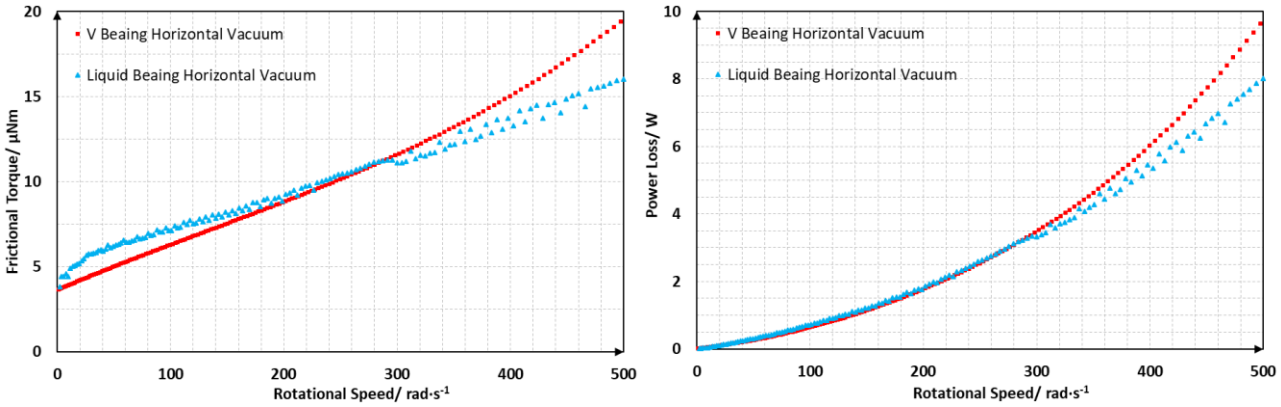

Figure 7-29. Frictional Torque and Power Loss Comparisons of the Two Types of Micro Bearings Operating Horizontally in the Vacuum Chamber

7.5.3. Turbine Operates Vertically in Air

Figure 7-30 below demonstrates the frictional torque and power loss comparisons of the two types of bearings operating vertically in air. This group of comparison is more important as pratically, the turbine must operates in air to harvester energy from air flow.

It can be seen from figure 7-30 that, the frictional torque versus rotational speed curves of the two types of bearings almost coincides with each other when the rotational speed is lower than 100 rad·s^{-1}. When the rotational speed of the turbine exceeds 200 rad·s^{-1}, the frictional torque of the turbine installed with liquid bearings are smaller than that of the V bearings hence resulting in less power loss. The power loss of the liquid bearings at 400 rad·s^{-1} is 7.30 mW whereas the power loss of the V bearings is 9.37 mW, 22.1% power loss reduction is achieved by using liquid bearings. At 500 rad·s^{-1} speed, the power loss reduction is 22.7%.

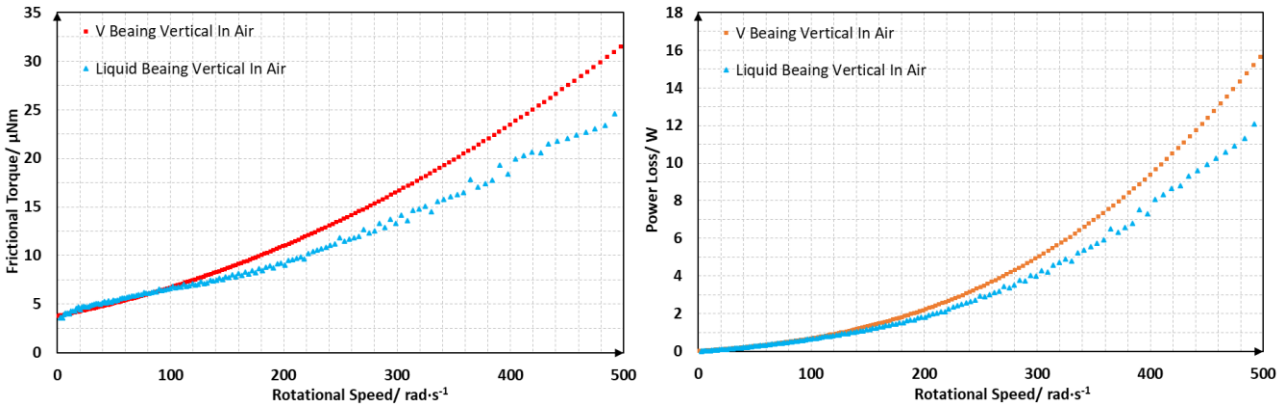

Figure 7-30. Frictional Torque and Power Loss Comparisons of the Two Types of Micro Bearings Operating Vertically in Air

7.5.4. Turbine Operates Horizontally in Air

Figure 7-31 below shows the frictional torque and power loss comparisons of the two types of bearings operating horizontally in air. Similarly, the power loss of two different types of bearings are almost equal to the same value when the turbine rotational speed is lower than 220 rad·s^{-1}.

The power loss of the liquid bearings at 300 rad·s^{-1} is 3.94 mW whereas the power loss of the V bearings is 5.04 mW, 21.8% power loss reduction is achieved by using liquid bearings. At 400 rad·s^{-1} speed, the power loss of the liquid bearings is 6.98 mW whereas the power loss of the V bearings is 9.40 mW, 25.8% power loss reduction is achieved. When the rotational speed reaches 500 rad·s^{-1} speed, 29.3% less power is consumed at the sliding contact when liquid bearings are used.

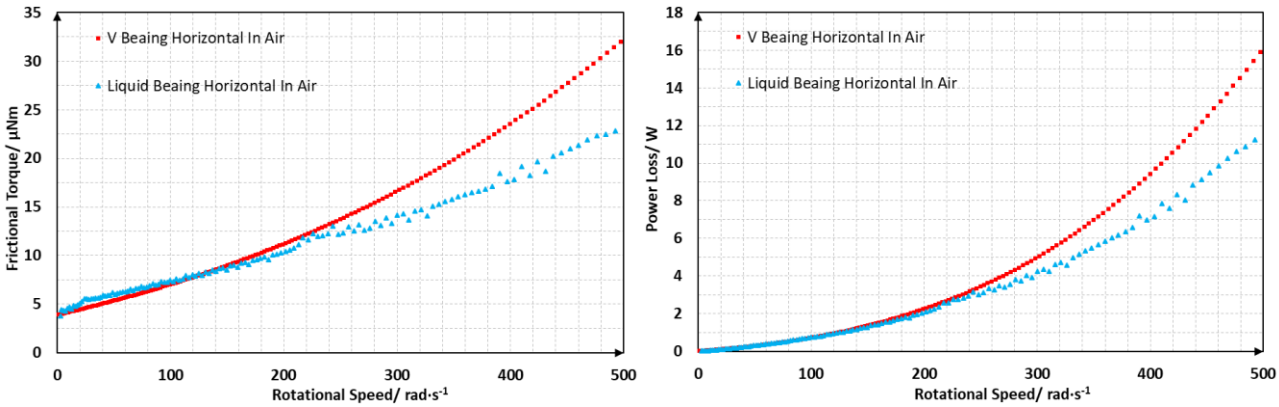

Figure 7-31. Frictional Torque and Power Loss Comparisons of the Two Types of Micro Bearings Operating Horizontally in Air

7.6. Conclusions

The performance of the liquid bearings developed in this research operating on the micro energy harvesting turbine is assessed through turbine spin-down tests under different operation conditions.

It can be concluded from the tests results that the developed silicon micro thrust bearing operates in the mixed and boundary lubrication regimes when the rotational speed is lower than 200 rad·s^{-1} and it operates in full film hydrodynamic lubrication regime when the speed exceeds 200 rad·s^{-1}. However, the micro journal bearing which consists of a ruby ring and stainless-steel rotor shaft operates in boundary and mixed lubrication regime in the whole tested speed range. Therefore, further modification for the micro journal bearing is required in the future.

Lower frictional torque at high rotational speed can be achieved by using liquid with lower dynamic viscosity, whereas adding friction modifier (ODA) helps to reduce frictional torque at low turbine rotational speeds.

Thrust bearings with lower load capacity has higher friction coefficient at low rotational speeds and lower friction coefficient at higher rotational speeds. Correspondingly, thrust bearings with higher load capacity has lower friction coefficient at low rotational speeds and higher friction coefficient at higher rotational speeds. It has also been found that the load carrying capacity of the micro thrust bearing is negatively correlated to the number of pads of the thrust bearing.

Over 20% power loss at the sliding contact is reduced by replacing the dry contact V bearings with the liquid bearings developed in this research when the turbine operates with speed higher than 200 rad·s^{-1}. Therefore, more mechanical power from the rotor can be delivered to the generator implicated within the turbine hence outputting more electrical power in high turbine rotation speed range (200 rad·s^{-1} to 400 rad·s^{-1}).

Chapter 8: Effects of Surface Texture on the Micro Thrust Bearing Performance

The results presented in this chapter demonstrate the effects of the surface texture on the micro pocketed parallel thrust bearing performance are presented. The stator pads of the micro thrust bearing are partially textured with circular dimples by reactive ion etching different regions. Stribeck curves of the partially textured thrust bearings are obtained on the MEMS tribometer, with speeds ranging from 1 rad·s^{-1} to 1000 rad·s^{-1}, which covers boundary, mixed and hydrodynamic lubrication regimes. A preliminary investigation into the feasibility of reducing frictional coefficient of the micro thrust bearing using partial surface texture is conducted by comparing the Stribeck curves for the textured and untextured micro thrust bearing. Pure hexadecane and hexadecane with 0.1%wt Octadecylamine added are selected as the lubricants in this series of tests because lowest friction coefficient of the micro thrust bearing is achieved by using these two lubricants, as presented in previous chapters.

8.1. Brief Introduction of Surface Texture

Surface texture comprises small features (dimples, bumps, grooves, shaped pockets, etc.) with pre-designed geometric parameters which are intentionally introduced on the surfaces of mechanical parts. The size scale of surface texture discussed here is much larger than that of surface roughness. Texturing surfaces to achieve some special functions is not a new idea, for example, it has been used to increase surface adhesion in some cases, and to reduce the air drag of the surfaces in other cases [111].

In the tribology field, surface texture has been introduced on the surfaces of mechanical parts that are used in contacts with relative motion to improve their performance since 1966 [161]. It has been shown in many studies that surface textures are able to improve the tribological performance of rotating shaft seals, thrust bearings, journal bearings, piston rings and piston liners by increasing the load carrying capacity or reducing the friction coefficient [162-164].

It has been found in many experimental and modelling investigations that surface texture is able to provide additional load support when the contact operates in mixed or hydrodynamic lubrication regimes. The expansion of the hydrodynamic lubrication speed range might lead to friction coefficient reduction. However, the mechanism behind the load support increase by texturing the surfaces is still not fully understood and the effects of a certain surface texture design on the tribological performances of the contacts (load carrying capacity, friction coefficient, etc.) could be either positive or negative depending on the operation conditions [165].

Depending the extent of the textured area, surface texture can be divided into two categories which are full texture and partial texture [111]. The surfaces would be uniformly and completed textured for full texture cases whereas only selected areas (e.g. regions close to inlet or outlet) would be textured for partial texture cases. It has been found in many studies that partial surface texture is much more efficient in load support improvement and friction reduction compared to full surface texture especially when surface textures are applied on parallel contacts [166,167].

A very good literature review of surface texture used in tribology field within which the key findings of the effects of surface texture over decades are summarized has been conducted by Gropper and Wang [111].

In this project, two different partial surface texture layouts have been introduced on the micro parallel pocketed thrust bearing to investigate the effects of partial surface texture on micro parallel bearing performance and the feasibility of using surface texture is an efficient method to reduce micro bearings. The friction reduction ability of surface texture and friction modifier are also compared in this series of investigation. Friction reduction achieved by the combination of friction modifier and surface texture has also been assessed in this contribution of work.

8.2. Tests Setups of the Surface Texture on Micro Bearing Investigation

Detailed information on the test conditions, graphic parameters of the partially textured micro pocketed parallel thrust bearings, properties of the lubricants and friction modifier are given in the following sections.

8.2.1. MEMS Tribometer

This series of tests investigating the effect of partial surface texture on the micro pocketed parallel thrust bearing performance are conducted on the MEMS tribometer which has been introduced with all details in Chapter 5. Stribeck curves under fixed applied load can be obtained from the MEMS tribometer. The frictional torque is obtained by knowing the rotational stiffness of the test platform (by calibration) and measuring the rotational displacements (by light lever). The load is controlled by knowing the vertical deformation stiffness of the test placement (by calibration) and controlling the vertical displacement of the test platform (by using laser displacement measurement). The partially textured pad of the micro parallel bearing is fixed stationary on the test platform whereas the smooth flat pad of the bearing is driven by the high-speed step motor to rotate against the stationary textured pad in parallel.

8.2.2. Graphic Parameters of Textured Thrust Bearings

Smooth and Flat Rotor Pad of the Micro Pocketed Parallel Thrust Bearing

The contact surface of the rotor pad of the micro pocketed parallel thrust bearing is smooth and flat, holes which are used to assemble the rotating shaft are deeply etched on the backside of the rotor pad. A thin nickel layer is uniformly coated on the backside of the rotor pad, it is used to hold the rotor pad on the shaft in the tests. Drawings of the front side, back side and the 3D views of the rotor pad are demonstrated in figure 8-1 (a), figure 8-1 (b) and figure 8-1 (c) respectively.

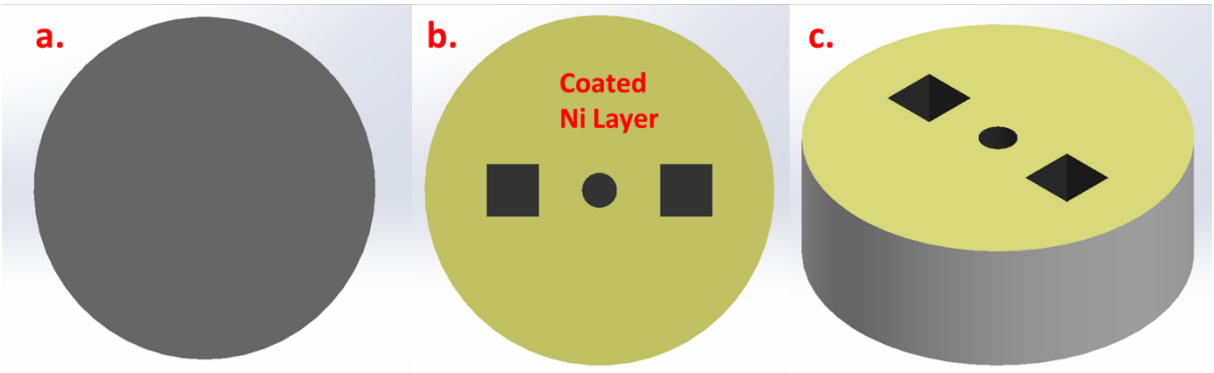

Figure 8-1. (a) Front Side of the Rotor Pad; (b) Back Side of the Rotor Pad; (c) 3D View of the Rotor Pad

Drawing that is labelled with key dimensions of the rotor pad is demonstrated in figure 8-2

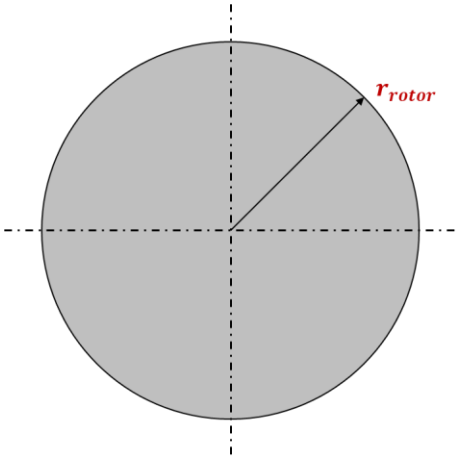

Figure 8-2: Graphics of the Rotor Pad of the Thrust Bearing

The material of the rotor pad of the thrust bearing is silicon. The surface of the rotor pad is flat and smooth, the surface roughness is: $R_a = 5$ nm. The diameter of the thrust bearing rotor pad, r_{rotor} is 1 mm.

Partially Textured Stator Pads of the Micro Pocketed Parallel Thrust Bearings

There are two different types of partially textured stator pads which are demonstrated in figure 8-3 and figure 8-4 below. As shown in figure 8-3 and figure 8-4, the contact surfaces of the stator pads of the micro pocketed parallel thrust bearings are etched with pocket patterns and textures by reactive ion etching technique. It can be seen that the shape of the surface textures are circular dimples with vertical cylindrical side walls and flat smooth bottom surfaces. The texture patterns etched on the two types of bearing stator pads are the same but the regions of the micro thrust bearing stator pads where the partial surface textures are applied are different. For the stator pad A, the partial surface texture patterns are applied in the downstream region of the leading steps of the thrust bearing stator pad, which is shown in figure 8-3 (c). For the stator pad B, the partial surface texture patterns are applied in the upstream region of the trailing steps of the thrust bearing stator pad, which is displayed in figure 8-4 (c). These types of texture were selected in an attempted to utilize a specific friction reduction mechanism associated with surface texture known as “Inlet Suction”. As described by Olver and co-workers, inlet suction occurs when pocket at the inlet of a contact cause cavitation due to the expansion of fluid into the increasing gap [168]. This locally reduces the pressure which acts to suck addition fluid into the contact, and this has an overall effect of increasing entrainment so as to increase film thickness for a given load hence friction is reduced. The effectiveness of this method in

reducing friction will depend on the location of the location of the pockets in relation inlet of the contact and hence the choice of the two pad configurations use in this study.

The blue arrows on figure 8-3 (c) and figure 8-4 (c) shows the directions in which the lubricant travels within the thrust bearings. There are four pins on the back side of the stator pads which are used to install the stator pads on the test platform and to fix the stator pads on the platform from any movement in the tests.

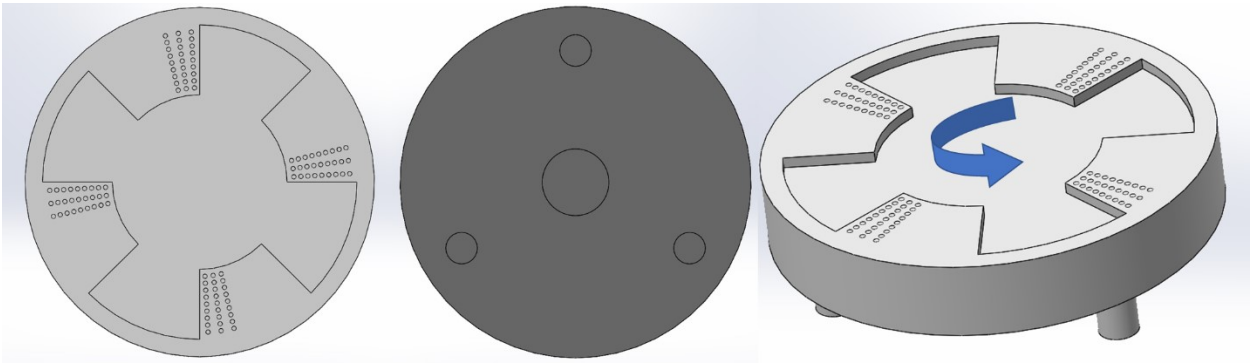

Figure 8-3. (a) Front Side of the Partially Textured Stator Pad A; (b) Back Side of the Partially Textured Stator Pad A; (c) 3D View of the Partially Textured Stator Pad A

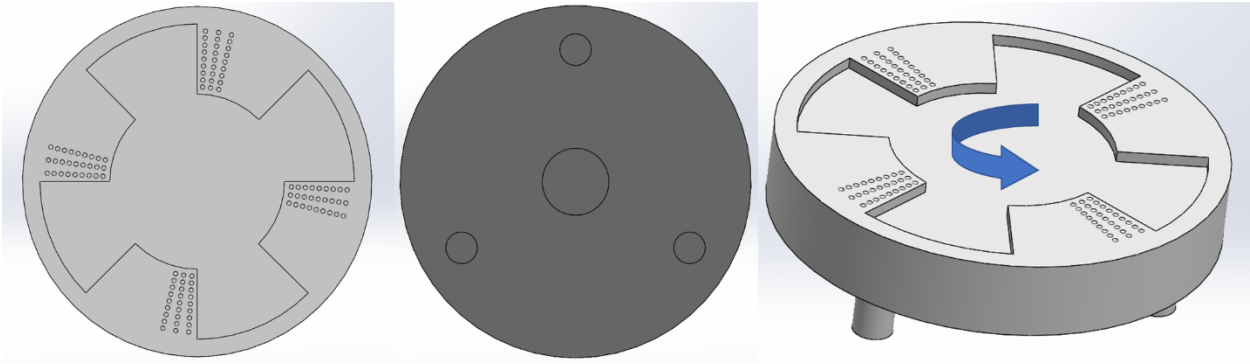

Figure 8-4. (a) Front Side of the Partially Textured Stator Pad B; (b) Back Side of the Partially Textured Stator Pad B; (c) 3D View of the Partially Textured Stator Pad B

Drawing that is labelled with key dimensions of the untextured stator pad is demonstrated in figure 8-5 below.

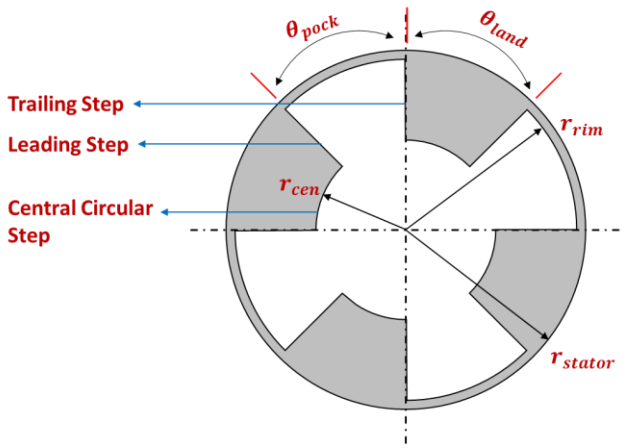

Figure 8-5: Graphics of the Untextured Stator Pad of the Thrust Bearing

The material of the stator pad of the thrust bearing is also silicon. The surface of the stator pad is etched with a pocket pattern using deep reactive ion etching technique. The surface roughness of the land region (the region where etching is not conducted) is also: $R_a = 5$ nm, the surface roughness of the etched pocket region is $R_a = 7$ nm.

The diameter of the stator pad, r_{stator} is 1 mm, the inner radius of the etched pocket, r_{inner} is 0.5 mm, the rim radius of the etched pocket, r_{rim} is 0.95 mm. The angular width of the etched pocket, θ_{pocket} is $\frac{\pi}{2}$, the angular width of the land region, θ_{land} is also $\frac{\pi}{2}$. The depth of the etched pocket, h_{pocket} is 1 μm.

For the partially textured stator pad A, the textures are applied in the downstream region of the leading steps of the pocketed stator pad. As shown in figure 8-3, the texture pattern is a circular dimple matrix consisting of 8 rows and 3 columns. The angular distance between the leading step of stator pad and the first column of textured dimples is 3.2 °, the radial distance between the central circular step and the first row of the textured dimples is 40 μm. The angular width of the textured region is 10 °, the angular interval between each columns of dimples is 5 °. The radial width of the texture region is 320 μm, the distance in radial direction between each rows of dimples is 40 μm. The diameter of each single circular dimple is 25 μm, the depth of the dimple is also 1 μm, which is the same with the etched pocket pattern. The surface roughness of the bottoms surfaces of the dimples constructed by reactive ion etching is: $R_a < 10$ nm.

For the partially textured stator pad B, the textures are applied in the upstream region of the trailing steps of the pocketed stator pad. As shown in figure 8-4, the texture pattern of textured pad B is the same with that of the stator pad A. The angular distance between the trailing step of stator pad and the first column of textured dimples is also 3.2 °, the radial distance between

the central circular step and the first row of the textured dimples is 40 μm as well. The angular width of the textured region is 10 °, the angular interval between each columns of dimples is 5 °. The radial width of the texture region is 320 μm, the distance in radial direction between each rows of dimples is 40 μm. The parameters of each single circular dimple on stator pad B are the same with those of the stator pad A.

8.2.3. Test Conditions

Temperature

This series of tests are all conducted in room temperature: 25 ℃.

Ambient Pressure

This series of tests are all conducted under atmosphere pressure which is 1.01×10^{5} Pa.

Rotational Speed

In this series of tests, the speed ranges from 1 $rad\cdot s^{-1}$ to 1000 $rad\cdot s^{-1}$. Therefore, the performance of the 1-mm diameter MEMS thrust bearing in all lubrication regimes (boundary regime/ mixed regime/ hydrodynamic regime) can be investigated.

Applied Load

Applied load for all the tests conducted in this series of investigation is 9.80×10^{-2} N. That is equal to the weight of 10 gram mass.

Properties of Tested Lubricant

The base oil used in this series of tests is hexadecane. The density of hexadecane under room temperature (25 ℃) and low pressure (below 1 MPa) is 0.77 $g\cdot cm^{-3}$, the viscosity of hexadecane under room temperature (25 ℃) and low pressure (below 1MPa) is 3.02 cP.

The friction modifier selected for the investigation of this research is octadecylamine ($C_{18}H_{39}N$). It consists of an 18-carbon straight chain and an amine group at the end of the carbon chain. The molecular weight of this additive is 269.5 $g\cdot mol^{-1}$. The chemical structure of this molecule is demonstrated in figure 8-6.

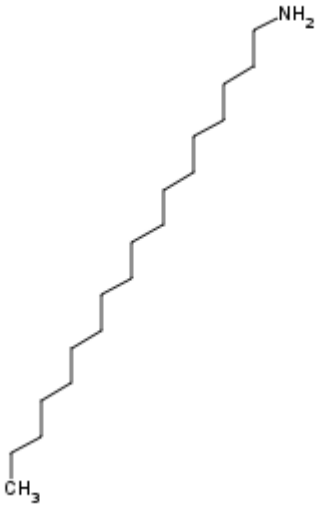

Figure 8-6. Chemical Structure of Octadecylamine

The amine group of the ODA molecule enables the molecule with straight chain attach to the silicon surfaces and form a slippery thin film which helps friction reduction in boundary and mixed lubrication regimes.

8.3. Results and Discussion

8.3.1. Performance of the Thrust Bearings with Partial Surface Texture on Different Regions

The friction coefficient versus rotational speed curves of the 2-mm diameter pocketed parallel thrust bearing with no surface texture, the bearing with partial surface texture in the downstream region of the leading steps where hydrodynamic pressure develops and the bearing with partial surface texture in the upstream region of the trailing steps where cavitation occurs are shown in figure 8-7 below. All the bearings are lubricated with pure hexadecane in this group of tests.

It can be indicated from the shapes of the stribeck curves illustrated in figure 8-7 that all three types of bearings experience boundary, mixed and full-film hydrodynamic lubrication regimes when the rotational speed of the rotor pad is increased from 1 $rad{\cdot}s^{-1}$ to 1000 $rad{\cdot}s^{-1}$. The Stribeck curves of all three types of thrust bearings fluctuate slightly with increasing rotational speed in the low speed range (boundary lubrication regime), then declines with rising rotational

speed (mixed lubrication regime) and eventually climbs with increasing speed in the high speed range (hydrodynamic lubrication regime).

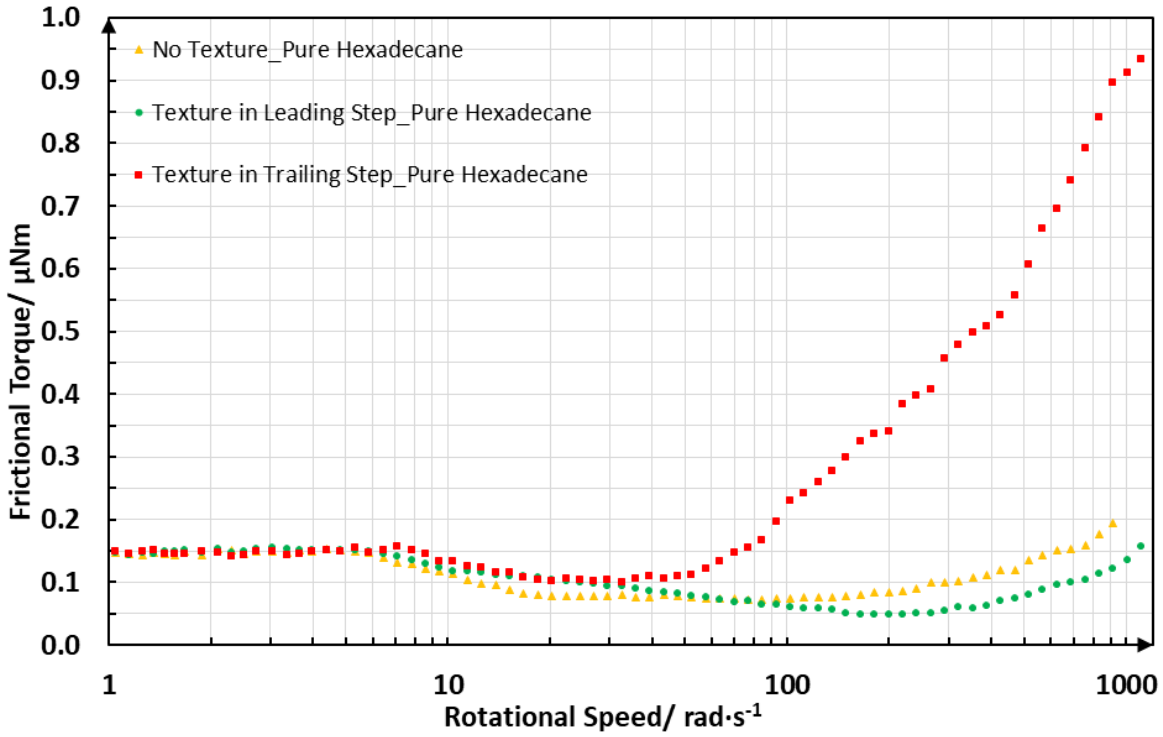

Figure 8-7. Friction Coefficient versus Rotational Speed Curves of Partially Textured and Non-textured Micro Pocketed Parallel Thrust Bearings Lubricated by Hexadecane

It can be concluded by comparing the Stribeck curves of the two micro pocketed parallel thrust bearings with partial surface texture located in different regions to the Stribeck curve with the untextured pocketed parallel thrust bearing that the effects of the partial surface texture on the bearing performance are totally different when the same surface texture pattern is located in different regions of the micro thrust bearing.

It can be seen from figure 8-7 that, when the rotational speed of the rotor pad is lower than 5 $rad{\cdot}s^{-1}$, all three types of micro thrust bearings operate in boundary lubrication regime. The friction coefficient of all three bearings are in the same value, 0.15. This is because the lubricant, material and surface roughness of all three bearings are the same.

When the rotational speed is increased from 5 $rad{\cdot}s^{-1}$, all three bearings enters mixed lubrication regime within which the friction coefficient decreases with rising rotational speed. However, the speeds at which the lubrication regime transfers to full-film hydrodynamic

lubrication regime are different for the three different thrust bearings. The bearings with partial surface texture located in the upstream region of the trailing steps of the micro pocketed parallel thrust bearing enters the full-film lubrication regime at the lowest speed, around 32.6 $rad{\cdot}s^{-1}$. The bearing with no surface texture enters hydrodynamic lubrication regime at around 102.3 $rad{\cdot}s^{-1}$ speed. The bearing with partial surface texture located in the downstream region of the leading steps of the bearing enters hydrodynamic lubrication regime at the highest speed, 200 $rad{\cdot}s^{-1}$. Therefore, it is reasonable to deduce that load carrying capacity of the micro pocketed parallel thrust bearing can be improved by adding surface texture in the upstream region of the trailing steps of the pocketed parallel thrust bearing. This improvement may be explained by the inlet suction mechanisms described above. An alternative hypothesis that could explain the load carrying capacity is proposed as follows. For the untextured pocketed parallel thrust bearing, the pressure in the upstream region of the trailing steps are close to the low cavitation pressure of the hexadecane as cavitation occurs in the downstream region of the trailing steps. Adding partial surface texture in this region could be viewed as constructing another leading step around which high hydrodynamic pressure develops. Therefore, the load carrying capacity is improved.

It is also reasonable to deduce that load carrying capacity of the thrust bearing would be weakened by adding surface texture in the downstream region of the leading steps of the pocketed parallel thrust bearing. For the untextured pocketed parallel thrust bearing, the pressure in the downstream region of the leading steps of the bearing is high as hydrodynamic pressure develops around this step (see modelling chapter). When the partial surface texture is added in the down stream region of the leading steps, additional cavitation might develop in this region hence damaging the load carrying capacity. However, for micro-scale thrust bearings, improvement of load carrying capacity does not necessarily means that the friction coefficient of the bearing would be reduced as the friction coefficient would increase drastically once the micro bearing enters hydrodynamic lubrication regime. This is shown clearly in figure 8-7. When the rotational speed is high (400 $rad{\cdot}s^{-1}$), the friction coefficient of the bearing with the highest load carrying capacity (surface texture in the upstream region of the trailing step) is about 0.51 which is highest. The friction coefficient of the bearing with the lowest load carrying capacity (surface texture in the downstream region of the leading step) is around 0.07 which is the lowest. The friction coefficient of the non-textured bearing at 400 $rad{\cdot}s^{-1}$ rotational speed is approximately 0.12. Therefore, friction coefficient reduction of the micro pocketed parallel thrust bearing in the speed range within which the speed is higher than 100 $rad{\cdot}s^{-1}$ can

be achieved by adding partial surface texture in the downstream region of the leading steps of micro bearing. It can be seen from figure 8-7 that, when the non-textured bearing enters full film lubrication region and its friction coefficient reaches the minimum value (0.06), the bearing with surface texture in the downstream region of the leading steps still operates in mixed lubrication regime, the friction coefficient of the partially textured bearing still decreases with increasing rotational speed and reaches the lowest value (0.048) at 200 $rad{\cdot}s^{-1}$. However, when both bearings operate in the mixed lubrication regime in the speed range [6 $rad{\cdot}s^{-1}$, 100 $rad{\cdot}s^{-1}$], the friction coefficient of the non-textured bearing is slightly lower than that of the textured bearing as more load is supported by the pressurized film hence reducing the load supported by the asperity contact which resulting in high friction.

8.3.2. Comparing the Friction Reduction Abilities of the Friction Modifier and Partial Surface Texture

Friction reduction abilities of the friction modifier and the partial surface texture are compared in this section. The friction coefficient versus rotational speed curve of the non-textured micro thrust bearing lubricated by pure hexadecane, the curve of the micro thrust bearing with surface textured in the downstream region of the leading steps lubricated by pure hexadecane and the curve of the non-textured bearing lubricated by the 0.1%wt octadecylamine added hexadecane are demonstrated in figure 8-8 below.

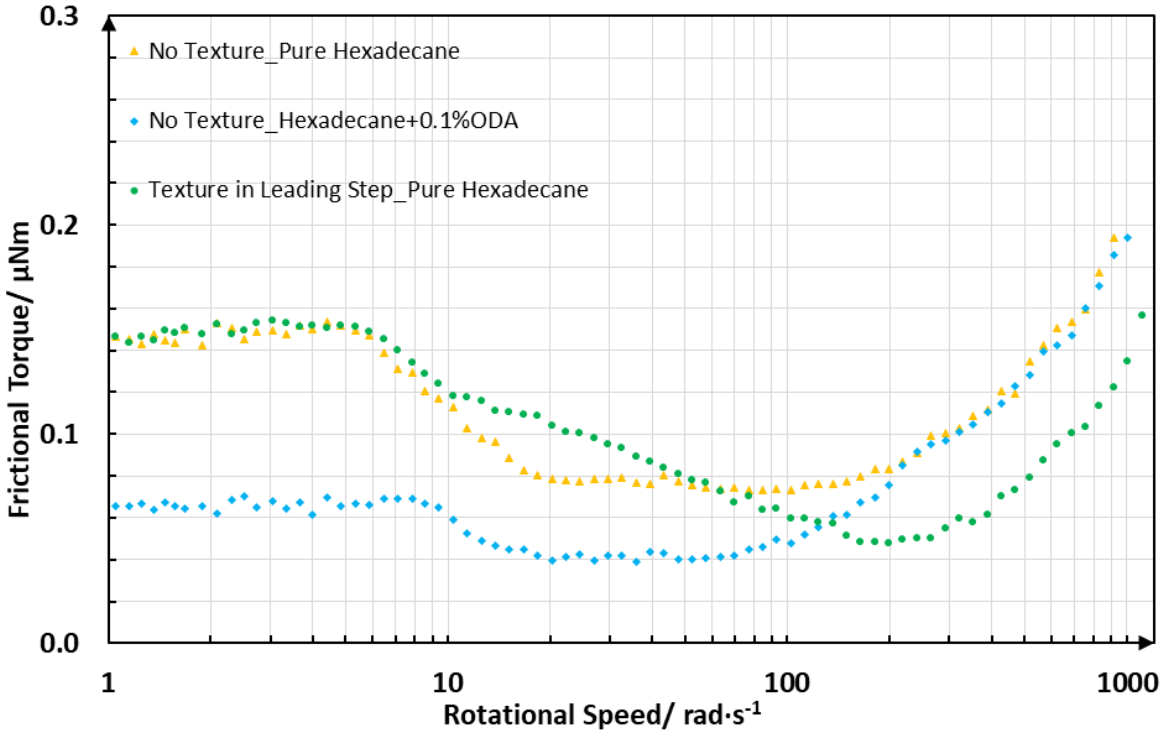

Figure 8-8. Friction Coefficient versus Rotational Speed Curves of Partially Textured and Non-textured Micro Pocketed Parallel Thrust Bearings Lubricated by Hexadecane and the Curve of the Non-textured Bearing Lubricated by ODA Added Hexadecane

It can be observed clearly that when the rotational speed is lower than 5 $rad{\cdot}s^{-1}$ and the micro pocketed parallel thrust bearing operates in the boundary lubrication regime, and the curves of the non-textured bearing and the partially textured bearing lubricated both by pure hexadecane coincide with each other. However, the friction coefficient of the non-textured bearing can be reduced in this speed range by adding friction modifier, and the friction coefficient is reduced from 0.15 to 0.07. Over 55% friction reduction is achieved by adding friction modifier in the low speed range whereas no friction reduction can be achieved by adding texture in the bearing surface in this speed range.

When the rotational speed is higher than 200 $rad{\cdot}s^{-1}$, the friction reduction ability of the friction modifier totally disappears and the friction coefficient versus rotational speed curves of the non-textured micro bearing lubricated by pure hexadecane and lubricated by the 0.1%wt ODA added hexadecane coincide with other. However, friction reduction can be achieved by adding partial surface texture on the micro pocketed parallel thrust bearing in this speed range. At 200 $rad{\cdot}s^{-1}$ speed, the friction coefficient of the non-textured thrust bearing is 0.08 whereas the friction coefficient of the partially textured thrust bearing is 0.048, over 42% friction reduction

is reduced at this speed. At 400 $rad{\cdot}s^{-1}$ speed, the friction coefficient of the non-textured thrust bearing is 0.11 whereas the friction coefficient of the partially textured thrust bearing is 0.06, over 43% friction reduction is reduced at this speed. It can be then be concluded that in the high speed range within which the rotational speed is higher than 200 $rad{\cdot}s^{-1}$, over 42% friction reduction can be achieved by adding surface texture whereas no friction reduction can be achieved in this speed range.

8.3.3. Further Friction Reduction by Combining Usage of Friction Modifier and Partial Surface Texture

In this section, the friction reduction ability of the partial surface texture when using friction modifier simultaneously is investigated. The Stribeck curve of the non-textured micro pocketed parallel thrust bearing lubricated by pure hexadecane and the Stribeck curve of the partially textured micro pocketed parallel thrust bearing lubricated by 0.1%wt ODA added hexadecane is demonstrated in figure 8-9 below.

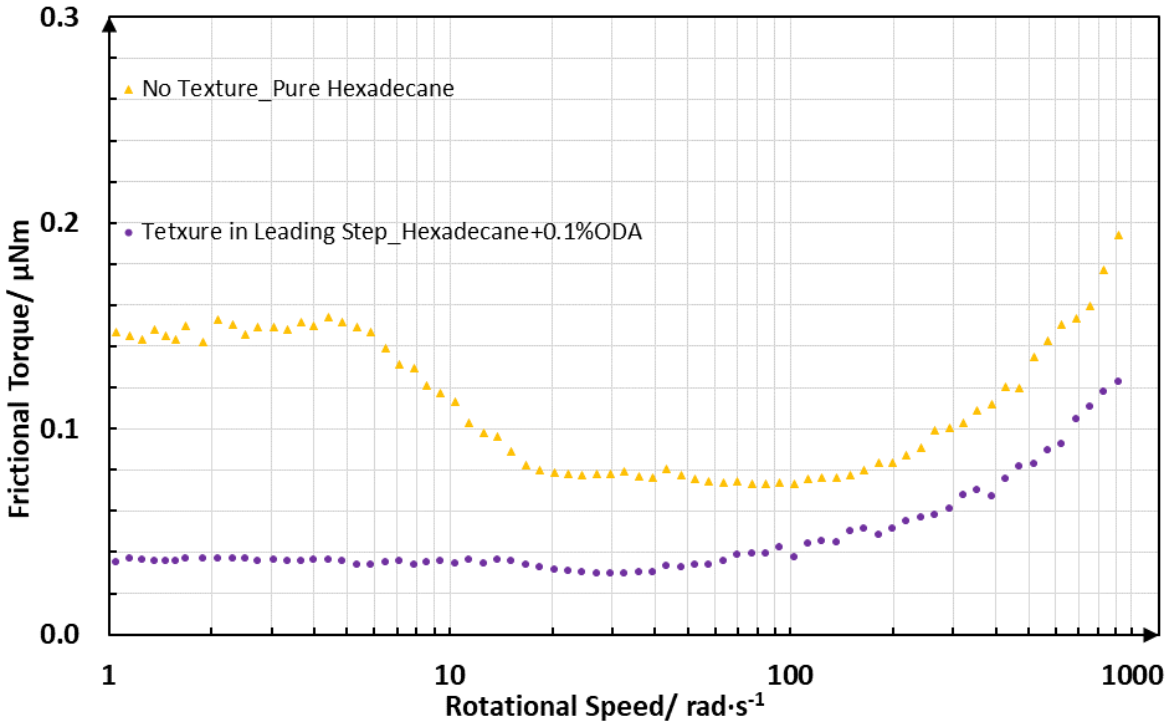

Figure 8-9. Friction Coefficient versus Rotational Speed Curve of Partially Textured Micro Pocketed Parallel Thrust Bearings Lubricated by ODA Added Hexadecane and the Curve of the Non-textured Bearing Lubricated by Pure Hexadecane

It can be seen from figure 8-9 that friction reduction can be achieved in the whole speed range when using partial surface texture and friction modifier simultaneously. This is because the friction reduction mechanisms of the friction modifier and partial surface texture are independent of each other. The friction modifier reduces the friction coefficient of the micro bearing in the low speed boundary and mixed lubrication region by forming a slippery monolayer on the silicon-made bearing surfaces. The partial surface texture reduces the friction coefficient of the micro bearing in the high speed hydrodynamic lubrication region by increasing the load carrying capacity of the bearing. As the load capacity is reduced, the speed range within which the micro thrust bearing operates in low friction coefficient mixed lubrication regime would be extended to higher speed. In addition, as the partially textured bearing enters the hydrodynamic lubrication regime at higher speed, the high viscous drag effect which results in high friction coefficient also occurs at higher rotational speed.

Another phenomenon which requires attention is that the boundary friction coefficient of the partially textured micro bearing lubricated by ODA added hexadecane at low speed is slightly **lower than 0.04 (from figure 8-9)**, which is even lower than the boundary friction coefficient of the non-textured micro bearing lubricated by ODA added hexadecane which is slightly **higher than 0.06 (from figure 8-8)**. Therefore, it is reasonable to deduce that partial surface texture could boost the friction reduction ability of the friction modifier in the boundary and lubrication regime. As suggested by Hamilton and Wakuda [169], the micro dimples which consisting the surface texture pattern might function as liquid reservoirs. Therefore, more friction modifier molecules together with the base lubricant might be provided to the contact from the micro dimples hence resulting in higher friction reduction.

8.4. Summary

Experiments results showing the effects of partial surface texture on the micro pocketed parallel thrust bearing performances are presented in this section. Three types of bearings: non-textured pocketed bearing, pocketed bearing with partial surface texture in the downstream region of the leading steps, pocketed bearing with partial surface texture in the upstream region of the trailing steps are tested on the MEMS tribometer to obtain their Stribeck curves that covers all lubrication regimes. The pocket patterns for all three bearings are the same; the partial texture

pattern for the two types of textured bearings are the same as well. The key findings are listed as follows:

- Adding surface texture in the upstream region of the trailing steps can improve the load carrying capacity of the micro pocketed parallel thrust bearing.
- Adding surface texture in the downstream region of the leading steps can reduce the load carrying capacity of the micro pocketed parallel thrust bearing.
- The friction coefficient of the micro bearing with higher load carrying capacity could be high especially when the rotational speed is high. The bearing would operate in the full-film hydrodynamic lubrication region at a low speed from which the viscous drag increases drastically with increasing speed.
- Friction reduction can be achieved at high rotational speeds by adding surface texture in the downstream region of the leading steps. The friction reduction is suggested to result from the load carrying capacity reduction. As the load capacity is reduced, the speed range within which the micro thrust bearing operates in low friction coefficient mixed lubrication regime would be extended to higher speed. In addition, as the partially textured bearing enters the hydrodynamic lubrication regime at higher speed, the high viscous drag effect which results in high friction coefficient also occurs at higher rotational speed.
- Partial surface texturing seems to boost the friction reduction ability of the friction modifier in the low speed boundary lubrication regime. Results show that the boundary friction coefficient of the bearing with partial texture located close to the leading steps (lower than 0.04) is slightly lower than that of the bearing with no texture (higher than 0.06) when both of them are lubricated with 0.1%wt ODA added hexadecane. A possible explanation is that micro dimples can function as liquid reservoirs. More friction modifier molecules together with the base lubricant would be provided to the contact from the micro dimples hence resulting in greater friction reduction. [169]
- Friction reduction can be achieved in the whole speed range by using the friction modifier and partial surface texture simultaneously.

Chapter 9: Conclusions and Future Work

A brief summary of the achievements of this work, which focuses on implementing liquid lubrication on micro-electro-mechanical devices (MEMS) with high sliding contacts, is given in the first part of the chapter. Important findings obtained in this research are reported in the second part of this chapter. In the third part of this chapter, suggestions on the future work are proposed.

9.1 Summary of Completed Tasks

As stated in the Chapter 1 of this thesis, the overall aims of this research are to conduct miniaturization of liquid hydrodynamic bearings and investigations of the appropriate geometry and liquid phase lubricants for the micro hydrodynamic bearings. Eventually, the developed micro bearings with appropriate geometric design and lubricating fluid are expected to be implemented on the micro scale contacts with high sliding to achieve low friction coefficient and wear rate, thereby improving the performance of MEMS devices encouraging the commercialization of this kind of MEMS devices.

It can be concluded from this thesis that the proposed overall aims of this research have been achieved successfully by completing the following tasks.

i. A literature review has been conducted and presented in the second chapter of this thesis. It shows the advantages of MEMS devices with rotating or sliding contacts. It also illustrates that micro liquid bearings have some advantages that cannot be achieved by coatings and vapour phase lubrication which are: (*i*) liquid bearings are capable of providing stable and reliable lubrication and surface protection for the micro contacts with large amount of applied sliding; (*ii*) it is viable, relatively simple and inexpensive to miniaturize the liquid bearings and to adapt the micro liquid bearings to be practically installed on MEMS devices. In addition, the details of a wide range of commonly used micro fabrication techniques are summarized in the final part of the literature review.

ii. A finite volume model based on the solution of the mass-conservation considering Reynold's equation has been successfully developed. Understanding of the lubrication

behaviours of the micro thrust bearings – in particular the unexpected role of cavitation - has been gained through simulations using this model. In addition, geometry optimization of the micro thrust bearing aiming to achieve higher bearing load carrying capacity and higher bearing transmission efficiency has also been achieved with this model.

iii. Fabrication recipes for the micro thrust bearings have been successfully developed. Micro thrust bearings with 500 μm-radius have been manufactured using the developed recipe. Bearing features with dimensions below 1 μm have all been constructed and the surface finish of the micro thrust bearing is below 7 nm.

iv. The performance of the 500 μm-radius micro thrust bearing lubricated by liquids with different viscosities has been tested on a MEMS tribometer. Results show that the shape of the stribeck curve of the micro thrust bearing is similar to that of a typical stribeck curve of macro hydrodynamic bearing. As rotational speed rises from 0 $rad \cdot s^{-1}$ to over 733.0 $rad \cdot s^{-1}$, the lubrication regime experiences boundary lubrication, mixed lubrication and full film hydrodynamic lubrication in order. The friction coefficient of the micro thrust bearing decreases with decreasing viscosity of the lubricant. It has been found through tests on the tribometer that, the friction coefficient of the micro thrust bearing can reach below 0.04 at very high rotational speed (over 314.2 $rad \cdot s^{-1}$) when the micro thrust bearing is lubricated by liquids with low polarity and low viscosity (pure hexadecane).

v. After designing and fabricating some assisting parts, the micro hydrodynamic thrust bearing and micro journal bearing are assembled together into one bearing housing which can be easily installed on the small-scale micro contacts of a prototype micro energy harvesting turbine. The practical performance of the developed hydrodynamic liquid bearings when they operate on the micro turbine is assessed. Results demonstrates the efficiency of the micro energy harvesting turbine has been significantly improved by using the micro hydrodynamic liquid bearings developed in this research as much less power is consumed on the micro sliding contacts especially when the turbine operates at high speeds. The power loss on the micro sliding contacts have been reduced by over 20%.

vi. The effects of micro surface texture and friction modifier additives – *i.e.* commonly used methods for further friction reduction of the macro-scale hydrodynamic liquid bearings – have also been examined when they are applied on the micro liquid bearings developed in this research. Results illustrate that both methods are still effective in friction reduction for the micro liquid bearings.

9.2 Summary of Key Findings and Achievements

Important knowledge on the miniaturization the liquid bearings and on the implementation of micro liquid bearings on micro-scale sliding contacts has been obtained in this research and the summary of the key findings are summarized as follows.

i. **The pocketed parallel thrust bearing is suitable for small scale applications (MEMS), but it is necessary to design the thrust bearing with appropriate pocket patterns.** Simulation results show that if the circumferential direction pocket extent is below 40% or above 80%, or the radial direction pocket extent is below 40%, no load support can be generated by the micro thrust bearing even at high rotational speeds. Experimental results show that if the micro bearing is lubricated by liquid with viscosity that is not sufficiently low (*e.g.* squalane), the friction coefficient of the micro bearing at high rotational speed can be very high (higher than 0.2) as viscous drag dominates.

ii. **Liquids such as squalane and water are not appropriate to be selected as the lubricant for micro-scale liquid bearings.** Experimental results show that if the micro bearing is lubricated by squalane, the friction coefficient of the micro bearing at high rotational speed can be very high (higher than 0.2) as viscous drag resulted from the high viscosity of squalane dominates. Test results indicates that friction coefficient of the micro bearings lubricated with water is even much higher than that of the bearing lubricated by high viscosity lubricants especially when the bearing operates in the boundary or mixed lubrication regimes at low speeds.

iii. **Hexadecane is appropriate to be selected as the lubricant for micro-scale liquid bearings.** Results from both tests on the MEMS tribometer and tests on the micro energy harvesting turbine indicate that the friction coefficient and power loss of the micro bearings are pretty low when the micro bearings are lubricated by hexadecane.

iv. **Cavitation can occur within the micro pocketed parallel thrust bearing when the rotational speed is high, or the minimum film thickness is low and largely affects the bearing performance (load carrying capacity and frictional torque).** Expansion of the cavitation leads to two phenomena which generate different effects on the load carrying capacity: (*i*) cavitation area increase which acts to decrease load support and (*ii*) pressure increase in the pressure active region which acts to increase load support. The overall load

support behaviour of the micro pocketed parallel thrust bearing is therefore determined by which effect outweighs the other.

v. **Implementing partial surface texture in the downstream region of the leading steps where high hydrodynamic pressure is developed can significantly reduce the friction coefficient of the micro thrust bearings at high speed range (in the hydrodynamic lubrication regime).** A possible hypothesis explaining the friction reduction at high speeds is that the load carrying capacity of the micro thrust bearings is reduced by implementing partial surface texture in the bearing region where hydrodynamic pressure develops as additional cavitation is introduced in this region hence reducing the bearing load carrying capacity.

vi. **Fabrication recipe for the micro bearings has been successfully developed.** With the developed recipe, features with dimensions as small as 1 micron can be precisely implemented on the micro bearings.

vii. **Methods to assemble the micro bearings and to install the micro bearings in the micro energy harvesting turbine has been successfully developed.**

9.3 Future Work of the Research

The following tasks are suggested as part of future work.

i. Add load balance loop in the developed model.

ii. Upgrade the model by integrating an energy equation-based thermal model into the bearing model so that temperature contour of the bearing can be generated by the model and the thermal effects can be further investigated.

iii. Conduct experiments on the MEMS tribometer, measurements of the contact angel of the liquids on bearing surface and observations of the meniscus shape at the bearing-liquid interface to further assess the effects of the lubricant viscosity and the effects of the lubricant surface tension on the micro bearing performance.

iv. Install the partially surface textured bearings on the micro turbine and use octadecylamine added hexadecane as the micro bearing lubricants and test the turbine performance in this case to see whether further energy harvesting efficiency improvement can be achieved.

v. In the current research, attention is mainly focused on the development and modification of the micro thrust bearing whereas little attention has been paid on the modification of the micro journal bearing. In the future, the micro journal bearings are required to be modified as centrifugal force of the rotor which is supported by the micro journal bearing is much bigger than the gravity of the rotor and the windage thrust force.

vi. Investigate the feasibility of combining liquid lubrication with self-assembled monolayers or solid film coatings to achieve superlubricity of micro bearings in a wide speed range. Theoretically, this might be viable as the micro bearing developed in the current research is silicon, techniques to coat SAM films or solid films on this material are relatively mature.

vii. Upgrade the MEMS tribometer used in this research by adding functions of observing the film thickness distributions of the micro thrust bearings. Simulation results indicate that the size of the cavitation occurs within the micro parallel thrust bearing is relatively large, so it would be interesting to observe the actual film thickness distributions of the micro bearings to validate or improve the mass-conserved numeric model for the micro parallel thrust bearings.

References

[1] P. Wang, J. Zhang and A. S. Holmes, "Development of hydrodynamic micro-bearings", Journal of Physics, Conf. Ser. 773, p. 012020, 2016.

[2] K. Deng, G. Ramanathan and M. Mehregany, "Micromotor dynamics in lubricating fluids", Journal of Micromechanics and Microengineering, vol. 4, no. 4, pp. 266-269, 1994.

[3] I. Ku, T. Reddyhoff, R. Wayte, J. Choo, A. Holmes and H. Spikes, "Lubrication of Microelectromechanical Devices Using Liquids of Different Viscosities", Journal of Tribology, vol. 134, no. 1, p. 012002, 2012.

[4] A. Ghosal, "A Review of Fluid Film Bearing", Proceedings of the 13th Asian Congress of Fluid Mechanics, pp. 723-728, 2010.

[5] S. Nabavi and L. Zhang, "Portable Wind Energy Harvesters for Low-Power Applications: A Survey", Sensors, vol. 16, no. 7, p. 1101, 2016.

[6] D. Howey, A. Bansal and A. Holmes, "Design and Performance of A Centimetre-scale Shrouded Wind Turbine for Energy Harvesting", Smart Materials and Structures, vol. 20, no. 8, p. 085021, 2011.

[7] M. Fesanghary and M. M. Khonsari, "Topological and Shape Optimization of Thrust Bearings for Enhanced Load-carrying Capacity", Tribology International, vol. 53, pp. 12-21, 2012.

[8] J Li, C. Zhang and J. Luo, "Investigations of the Superlubricity of Sapphire against Ruby under Phosphoric Acid Lubrication", Friction, vol. 2, pp. 164-172, 2014.

[9] P. Baillio, "Jewel Bearings Solve Light Load Problems", web resource:

http://cdn.thomasnet.com/ccp/00400419/38874.pdf

[10] "An Introduction to MEMS (Micro-Electromechanical Systems)", 2017. [Online]. Available: http://www.lboro.ac.uk/microsites/mechman/research/ipm-ktn/pdf/Technology_review/an-introduction-to-mems.pdf.

[11] M. Gad-el-Hak, MEMS, 1st ed. Boca Raton: CRC/Taylor & Francis, 2006, pp. 1-1 - 1-4.

[12] J. Waldner, Nanocomputers and swarm intelligence, 1st ed. London: ISTE, 2008, p. 205.

[13] J. Anglel and S. Terry, Silicon micromechanical devices, 1st ed. pp. 42-56.

[14] E. Mounier, "Future of MEMS: a Market & Technologies Perspective", 2014.

[15] C. Nguyen, "Frequency-selective MEMS for miniaturized low-power communication devices", IEEE Transactions on Microwave Theory and Techniques, vol. 47, no. 8, pp. 1486-1503, 1999.

[16] "Sandia National Laboratories: MicroElectroMechanical Systems, Mems.sandia.gov., 2017. [Online]. Available: http://www.mems.sandia.gov. [Accessed: 25- Feb- 2017].

[17] N. Yamazoe and Y. Shimizu, "Humidity sensors: Principles and applications", Sensors and Actuators, vol. 10, no. 3-4, pp. 379-398, 1986.

[18] G. T. A. Kovacs, Micromachined Transducers Sourcebook, New York: McGraw-Hill, 1998, pp. 614–623.

[19] S. E. Lyshevski, Mems and Nems: systems, devices and structures: CRC Press LLC, USA, 2002, pp. 120-124.

[20] N. Maluf, An Introduction to Microelectromechanical Systems Engineering, Second Edition, 2004, pp. 82-84.

[21] P.W. Barth, C.C. Beatty and L.A. Field, Baker, "A robust normally-closed silicon microvalve", Solid-State Sensor and Actuator Workshop 1994, 248-250.

[22] N. Kabei, M. Kosuda, H. Kagamibuchi, R. Tashiro, H. Mizuno, Y. Ueda and K. Tsuchiya, "A Thermal-Expansion-Type Microactuator with Paraffin as the Expansive Material. (Basic Performance of a Prototype Linear Actuator).", JSME International Journal Series C, vol. 40, no. 4, pp. 736-742, 1997.

[23] W. Riethmuller and W. Benecke, "Thermally excited silicon microactuators", IEEE Transactions on Electron Devices, vol. 35, no. 6, pp. 758-763, 1998.

[24] P. Osterberg and S. Senturia, "M-TEST: A test chip for MEMS material property measurement using electrostatically actuated test structures", Journal of Microelectromechanical Systems, vol. 6, no. 2, pp. 107-118, 1997.

[25] S. Masmanidis, R. Karabalin, I. De Vlaminck, G. Borghs, M. Freeman and M. Roukes, "Multifunctional Nanomechanical Systems via Tunably Coupled Piezoelectric Actuation", Science, vol. 317, no. 5839, pp. 780-783, 2007.

[26] C. Enz, A. El-Hoiydi, J. Decotignie and V. Peiris, "An ultralow-power wireless sensor network solution", Computer, vol. 37, no. 8, pp. 62-70, 2004.

[27] R. O'Donnell, "Prolog to Energy Harvesting From Human and Machine Motion for Wireless Electronic Devices", Proceedings of the IEEE, vol. 96, no. 9, pp. 1455-1456, 2008.

[28] S. Beeby, M. Tudor and N. White, "Energy harvesting vibration sources for microsystems applications", Measurement Science and Technology, vol. 17, no. 12, pp. R175-R195, 2006.

[29] R. Miles, K. Hynes and I. Forbes, "Photovoltaic solar cells: An overview of state-of-the-art cell development and environmental issues", Progress in Crystal Growth and Characterization of Materials, vol. 51, no. 1-3, pp. 1-42, 2005.

[30] J. Simon and T. Caroff, "Device for Generating Current and/or Voltage Based on a Thermoelectric Module Placed in a Flowing Fluid", US9099942 B2. U.S. Patent. 2015 Aug 4

[31] J. Chen, Z. Yan and L. Wu, "The influence of Thomson effect on the maximum power output and maximum efficiency of a thermoelectric generator", Journal of Applied Physics, vol. 79, no. 11, pp. 8823-8828, 1996.

[32] A. Deivasigamani, J. McCarthy, S. John, S. Watkins, P. Trivailo and F. Coman, "Piezoelectric Energy Harvesting from Wind Using Coupled Bending-Torsional Vibrations", Modern Applied Science, vol. 8, no. 4, 2014.

[33] J. McCarthy, S. Watkins, A. Deivasigamani and S. John, "Fluttering energy harvesters in the wind: A review", Journal of Sound and Vibration, vol. 361, pp. 355-377, 2016.

[34] S. Priya, C. Chen, D. Fye and J. Zahnd, "Piezoelectric Windmill: A Novel Solution to Remote Sensing", Japanese Journal of Applied Physics, vol. 44, no. 3, pp. L104-L107, 2004.

[35] M. Perez, S. Boisseau, P. Gasnier, J. Willemin, M. Geisler and J. Reboud, "A cm scale electret-based electrostatic wind turbine for low-speed energy harvesting applications", Smart Materials and Structures, vol. 25, no. 4, p. 045015, 2016.

[36] M. Gad-el-Hak, MEMS, 1st ed. Boca Raton: CRC/Taylor & Francis, 2006, pp. 80-85.

[37] R. Maboudian and C. Carraro, "SURFACE CHEMISTRY AND TRIBOLOGY OF MEMS", Annual Review of Physical Chemistry, vol. 55, no. 1, pp. 35-54, 2004.

[38] N. Tas, T. Sonnenberg, H. Jansen, R. Legtenberg and M. Elwenspoek, "Stiction in surface micromachining", Journal of Micromechanics and Microengineering, vol. 6, no. 4, pp. 385-397, 1996.

[39] W. Van Spengen, R. Puers and I. De Wolf, "On the physics of stiction and its impact on the reliability of microstructures", Journal of Adhesion Science and Technology, vol. 17, no. 4, pp. 563-582, 2003.

[40] M. de Boer, P. Clews, B. Smith and T. Michalske, "Adhesion of Polysilicon Microbeams in Controlled Humidity Ambients", MRS Proceedings, vol. 518, 1998.

[41] K. Deng and W. Ko, "A study of static friction between silicon and silicon compounds", Journal of Micromechanics and Microengineering, vol. 2, no. 1, pp. 14-20, 1992.

[42] C. Mastrangleo and C. Hsu, "Mechanical stability and adhesion of microstructures under capillary forces. II. Experiments", Journal of Microelectromechanical Systems, vol. 2, no. 1, pp. 44-55, 1993.

[43] J. Israelachvili and D. Tabor, "The Measurement of Van Der Waals Dispersion Forces in the Range 1.5 to 130 nm", Proceedings of the Royal Society A: Mathematical, Physical and Engineering Sciences, vol. 331, no. 1584, pp. 19-38, 1972.

[44] S. G. A. C. M. pierings and J. Haisma, "Diversity and interfacial phenomena in direct bonding" Proceedings of 1st International Symposium on Semiconductor Wafer Bonding, Science,Technology and Applications, pp. 18–32, 1991.

[45] P. Scheeper, J. Voorthuyzen, W. Olthuis and P. Bergveld, "Investigation of attractive forces between PECVD silicon nitride microstructures and an oxidized silicon substrate", Sensors and Actuators A: Physical, vol. 30, no. 3, pp. 231-239, 1992.

[46] G. T. Mulhern, D. S. Soane, and R. T. Howe, "Supercritical carbon dioxide drying of microstructures" Proceedings of 7th International Conference on Solid-State Sensors and Actuators, pp 296–9, 1993

[47] T. Abe, W. Messner and M. Reed, "Effects of elevated temperature treatments in microstructure release procedures", Journal of Microelectromechanical Systems, vol. 4, no. 2, pp. 66-75, 1995.

[48] H. Hwang and J. Song, "An effective method to prevent stiction problems using a photoresist sacrificial layer", Journal of Micromechanics and Microengineering, vol. 17, no. 2, pp. 245-249, 2006.

[49] P. Grunthaner, F. Grunthaner, R. Fathauer, T. Lin, M. Hecht, L. Bell, W. Kaiser, F. Schowengerdt and J. Mazur, "Hydrogen-terminated silicon substrates for low-temperature molecular beam epitaxy", Thin Solid Films, vol. 183, no. 1-2, pp. 197-212, 1989.

[50] B. Arkles, "Hydrophobicity, hydrophilicity and silanes", Paint Coatings Industry Magazine, October, 2006.

[51] O. M. R. Chyan, J. Wu, J, Chen, "Comparative Studies of Hydrogen Termination on Single-Crystal Silicon Surfaces by FT-IR and Contact-Angle Measurements", Applied Spectroscopy, vol. 51, no. 12, pp. 1905-1909, 1997.

[52] M. Barisik, A. Beskok, "Wetting characterization of silicon (1,0,0) surface", Molecular Simulation, vol. 39, no. 9, pp. 700-709, 2013.

[53] K. Hermansson, U. Lindberg and G. Palmskog, "Wetting properties of silicon surfaces", Proceedings of the IEEE International Conference on Solid-State Sensors Actuators, pp. 193-196, 1991.

[54] N. Martinez, "Wettability of silicon, silicon dioxide, and organo-silicate glass", Master of science thesis, University of North Texas, 2009.

[55] P. Jakob, and Y. J. Chabal, "Chemical Etching of Vicinal Si (111): Dependence of the Surface Structure and the Hydrogen Termination on the pH of the Etching Solutions", The Journal of Chemical Physics, no. 95, pp. 2897-2909, 1991.

[56] G. J. Pietsch, G. S. Higashi, and Y. J. Chabal, "Chemomechanical polishing of silicon: Surface termination and mechanism of removal", Applied Physics Letters, vol. 64, p. 3115, 1994.

[57] V. A. Burrows, Y. J. Chabal and S. B. Christman, "Infrared spectroscopy of Si (111) surfaces after HF treatment: Hydrogen termination and surface morphology", Applied Physics Letters, vol. 53, p. 998, 1988.

[58] M. Houston, R. Howe and R. Maboudian, "Effect of hydrogen termination on the work of adhesion between rough polycrystalline silicon surfaces", Journal of Applied Physics, vol. 81, no. 8, pp. 3474-3483, 1997.

[59] X. Zhu, Y. Jun, V. Boiadjiev, R. Major, H. Kim and J. Houston, "Novel Chemistry for Surface Engineering in Mems", MRS Proceedings, vol. 657, 2000.

[60] M. Houston and R. Maboudian, "Stability of ammonium fluoride-treated Si (100)", Journal of Applied Physics, vol. 78, no. 6, pp. 3801-3808, 1995.

[61] X. Zhang, Y, Dong and J. A. Schaefer, "Effect of micro-dimple patterns on capillary pull-off force and friction force of silicon surface", Chinese Physics B, vol. 18, no. 1, pp. 231-237, 2009.

[62] L. S. Fan, Y. C. Tai and R. S. Muller, "IC-Processed Electrostatic Micromotors", International Electron Devices Meeting, pp. 666-669, 1988.

[63] Y. S. Allison and A. A. Polycarpou, "Adhesion and Pull-Off Forces for Polysilicon MEMS Surfaces Using the Sub-Boundary Lubrication Model", Journal of Tribology, vol. 125, pp. 193-199, 2003.

[64] Y. Ando, "Wear Tests and Pull-Off Force Measurements of Single Asperities by Using Parallel Leaf Springs Installed on an Atomic Force Microscope", Journal of Tribology, vol. 122, pp. 639–645, 2000.

[65] J. C. Love, L. A. Estroff and G. M. Whitesudes, "Self-Assembled Monolayers of Thiolates on Metals as a Form of Nanotechnology", Chemical Reviews, vol. 105, no. 4, pp. 1103-1169, 2005.

[66] S. M. Barlow and R. Raval, "Complex organic molecules at metal surfaces: bonding, organization and chirality", Surface Science Reports, vol. 50, no. 6-8, pp. 201-341, 2003.

[67] D. K. Aswal, S. Lenfant and D. Vuillaume, "Self assembled monolayers on silicon for molecular electronics", Analytica Chimica Acta, no. 568, pp. 84-108, 2006.

[68] A. Ulman, "Formation and Structure of Self-Assembled Monolayers", Chemical Reviews, vol. 96, no. 4, pp. 1533-1554, 1996.

[69] P. Silberzan, L. Leger and J. J. Benattar, " Silanation of Silica Surfaces. A New Method of Constructing Pure or Mixed Monolayers", Langmuir, vol. 7, pp. 1647-1651, 1991.

[70] S. Onclin, B. J. Ravoo and D. N. Reinhoudt, " Engineering Silicon Oxide Surfaces Using Self-Assembled Monolayers", Angewandte Chemie, vol. 44, pp. 6282-6304, 2005.

[71] R. R. Rye, G. C. Nelson, and M. T. Dugger, " Mechanistic Aspects of Alkylchlorosilane Coupling

Reactions", Langmuir, vol. 13, pp. 2965-2972, 1997.

[72] M. P. de Boer, J. A. Knapp, M. M. Thomas and M. Terry, "Role of Interfacial Properties on MEMS Performance and Reliability", Proc. SPIE 3825, Microsystems Metrology and Inspection, 2, 1999.

[73] K. Oguri and T. Arai, "Low friction coatings of diamond-like carbon with silicon prepared by plasma-assisted chemical vapor deposition", Journal of Materials Research, vol. 5, no. 11, pp. 2567-2571, 1990.

[74] K. Oguri and T. Arai, " Tribological properties and characterization of diamond-like carbon coatings with silicon prepared by plasma-assisted chemical vapor deposition ", Surface and Coatings Technology, vol. 47, no. 1-3, pp. 710-721, 1991.

[75] J. K. Luo, Y. K. Fu, H. R. Le, and W. I. Milne, "Diamond and diamond-like carbon MEMS", Journal of Micromechanics and Microengineering, vol. 17, pp. S147-S163, 2007.

[76] Y. Zhou, B. Wang and H. Yan, " Control over the Wettability of Amorphous Carbon Films in a Large Range from Hydrophilicity to Superhydrophobicity ", Applied Surface Science, vol. 253, pp. 2690-2694, 2006.

[77] A. Erdemir, O. Eryilmaz, I. Nilufer and G. Fenske, "Synthesis of superlow-friction carbon films from highly hydrogenated methane plasmas", Surface and Coatings Technology, vol. 133-134, pp. 448-454, 2000.

[78] J. Robertson, " Diamond-like Amorphous Carbon ", Materials Science and Engineering: Reports, vol. 37, pp. 129-281, 2002.

[79] S. T. Patton, W. D. Cowan, K. C. Eapen and J. S. Zabinski, J. S, "Effect of Surface Chemistry on the Tribological Performance of a MEMS Electrostatic Lateral Output Motor", Tribology Letters, 9, pp. 199-209, 2000.

[80] K. Strawhecker, D. Asay, J. McKinney and S. Kim, "Reduction of adhesion and friction of silicon oxide surface in the presence of n-propanol vapor in the gas phase", Tribology Letters, vol. 19, no. 1, pp. 17-21, 2005.

[81] D. Asay, M. Dugger and S. Kim, "In-situ Vapor-Phase Lubrication of MEMS", Tribology Letters, vol. 29, no. 1, pp. 67-74, 2007.

[82] D. Asay, M. Dugger, J. Ohlhausen and S. Kim, "Macro- to Nanoscale Wear Prevention via Molecular Adsorption", Langmuir, vol. 24, no. 1, pp. 155-159, 2008.

[83] A. Barnette, D. Asay, D. Kim, B. Guyer, H. Lim, M. Janik and S. Kim, "Experimental and Density Functional Theory Study of the Tribochemical Wear Behavior of SiO2in Humid and Alcohol Vapor Environments", Langmuir, vol. 25, no. 22, pp. 13052-13061, 2009.

[84] A. Barnette, D. Asay, M. Janik and S. Kim, "Adsorption Isotherm and Orientation of Alcohols on Hydrophilic SiO2under Ambient Conditions", The Journal of Physical Chemistry C, vol. 113, no. 24, pp. 10632-10641, 2009.

[85] T. D. Michael, "Tribological Challenges in MEMS and Their Mitigation Via Vapor Phase Lubrication", Sandia National Laboratories.

[86] S. Bart, M. Mehregany, L. Tavrow, J. Lang and S. Senturia, "Electric micromotor dynamics", IEEE Transactions on Electron Devices, vol. 39, no. 3, pp. 566-575, 1992.

[87] T. Reddyhoff, I. Ku, A. Holmes and H. Spikes, "Friction Modifier Behaviour in Lubricated MEMS Devices", Tribology Letters, vol. 41, no. 1, pp. 239-246, 2010.

[88] M. Liu, P. Jin and C. Chen, "Two-dimensional modelling of the self-limiting oxidation in silicon and tungsten nanowires", Theoretical and Applied Mechanics Letters, vol. 6, no. 5, pp. 195-199, 2016.

[89] D. E. Bruce, "Highlights of silicon thermal oxidation technology", Silicon materials science and technology, pp. 183, 1998.

[90] J. Tavares, E. J. Swanson and S. Coulombe, "Plasma synthesis of coated metal nanoparticles with surface properties tailored for dispersion", Plasma Processes and Polymers, vol. 5, no. 8, pp. 759-769, 2008.

[91] K. K. S. Lau, J. A. Caulfield and K. K. Gleason, "Structure and morphology of fluorocarbon films grown by hot filament chemical vapor deposition", Chemistry of Materials, vol. 12, no. 10, pp. 3032-3037, 2000.

[92] A. André, "Handbook of plasma immersion ion implantation and deposition", Third Edition, 2000.

[93] L. Christophe, "Makers of the microchip: a documentary history of fair child semiconductor", The MIT Press, 2010.

[94] J. L. Wasserman, K. Lucas and A. Ashton, "Fabrication of one-dimensional programmable-height nanostructures via dynamic stencil deposition", Review of Scientific Instruments, vol. 79, no. 7, p. 073909, 2008.

[95] Web source, link:

https://www.purdue.edu/discoverypark/birck/files/Plasma_RIE_Etching_Fundamentals_and_Applications.pdf

[96] Web source, link:

http://www.freepatentsonline.com/5501893.html

[97] Web source, link:

http://www.freepatentsonline.com/6531068.html

[98] X. Mu, Q. Liang and G. Luo, "Laminar flow used as ‘liquid etch mask’ in wet chemical etching to generate glass microstructures with an improved aspect ratio", Lab on a Chip, no. 9, pp. 1994-1996, 2009.

[99] D. V. De Pellegrin and D. J. Hargreaves, "An isoviscous, isothermal model investigating the influence of hydrostatic recess on a spring-supported tilting pad thrust bearing", Tribology International, vol. 51, pp. 25-35, 2012.

[100] T. H. Yu and F. Sadeghi, "Groove effect on thrust washer lubrication", Journal of Tribology, vol. 123, pp. 295-304, 2001.

[101] D. G. Fouflias, A. G. Charitopoulos and M. Fillon, "Performance comparison between textured, pocket, and tapered-land sector-pad thrust bearings using computational fluid dynamics thermohydrodynamic analysis", Proc IMechE Part J: J Engineering Tribology, 0 (0), pp. 1-22, 2014.

[102] V. Zouzoulas and C. I. Papadopoulos, "3-D Therohydrodynamic analysis of textured, grooved, pocketed and hydrophobic pivoted-pad thrust bearing", Tribology International, vol. 110, pp. 426-440, 2017.

[103] V. Brizmer, Y. Kligerman and I. Etsion, "A laser surface textured parallel thrust bearing", Tribology of Transactions, 46 (3), pp. 397-403, 2003.

[104] A. M. Mikula and R. S. Gregory, "A comparison of tilting pad thrust bearing lubricant supply methods", Journal of Lubrication Technology, vol. 105, pp. 39-45, 1983.

[105] L. Zhai, Y. Luo and Y. Xiao, "A review on the large tilting pad thrust bearings in the hydropower units", Renewable and Sustainable Energy Reviews, vol. 69, pp. 1182-1198, 2017.

[106] C. P. Chaudhali, B.B. Thakare and S. U. Gunjal, "A study of bearing and its types", International Journal of Advance Research In Science and Engineering, vol. 4, Special issue (01), pp. 1674-1681, 2015.

[107] J. Han, L. Fang and S. Ge, "Hydrodynamic Lubrication of microdimple textured surface using three-dimensional CFD", Tribology Transactions, vol. 53, pp. 860-870, 2010.

[108] M. Z. Hossain and M. Z. Razzaque, "Load Capacity of Grooved Circular Thrust Bearing", Journal of Tribology, vol. 136, pp. (011705)1-(011705)8, 2014.

[109] H. Yu, X. Wang and F. Zhou, "Geometric shape effects of surface texture on the generation of hydrodynamic pressure between conformal contacting surfaces", Tribology Letters, vol. 37, pp. 123-130, 2010.

[110] A. Dadouche, M. Fillon and W. Dmochowski, "Performance of a hydrodynamic fixed geometry thrust bearing: comparison between experimental data and numeric results", Tribology Transactions, vol. vol. 49 (3), pp. 419-426, 2006.

[111] D. Gropper, L. Wang and T. J. Harvey, "Hydrodynamic lubrication of textured surfaces: A review of modelling techniques and key findings", Tribology International, vol. 94, pp. 509-529, 2016.

[112] X. Wang, K. Kato and K. Aizawa, "Loads carrying capacity map for the surface texture design of SiC thrust bearing sliding in water", Tribology International, vol. 36, pp. 189-197, 2003.

[113] B. Schweizer, "Numeric approach for solving Reynolds equation with JFO boundary conditions incorporating ALE techniques", Journal of Tribology, vol. 131, pp. (011702)1-(011702)14, 2009.

[114] M. Fesanghary and M. M. Khonsari, "On the optimum grooves shapes for load-carrying capacity enhancement in parallel flat surface bearings: theory and experiment", Tribology International, vol. 67, pp. 254-262, 2013.

[115] I. Etsion, G. Halperin and Y. Kligerman, "Experimental investigation of laser surface textured parallel thrust bearings", Tribology Letters, vol. 17, pp. 295-300, 2004.

[116] A. G. Charitopoulos, D. G. Fouflias and M. Fillon, "Thermohydrodynamic analysis of a textured sector-pad thrust bearing: effects on mechanical deformations", Mechanics and Industry, vol. 15, pp. 403-411, 2014.

[117] L. Wang, W. Wang and Y. Hu, "Numeric analysis of the factors affecting the hydrodynamic performance for the parallel surfaces with microtextures", Journal of Tribology, vol. 136, pp. (021702)1-(021702)8, 2014.

[118] Y. Henry, J. Bouyer and M. Fillon, "An experimental analysis of the hydrodynamic contribution with the untextured parallel surface configuration", Proceedings of the Institution of Mechanical Engineers, Part J: Journal of Engineering Tribology, vol. 229, pp. 362-375, 2014.

[119] C. Gachot, A. Rosenkranz and H. L. Costa, "A critical assessment of surface texturing for friction and wear improvement", Wear, vol. 372-373, pp. 21-41, 2017.

[120] U. Sudeep, N. Tandon and R. K. Pandy, "Performance of lubricated rolling-sliding concentrated contacts with surface textures: a review", Journal of Tribology, vol. 137, pp. (031501)1-(031501)11, 2015.

[121] Y. Qiu and M. M. Khonsari, "On the prediction of cavitation in dimples using a mass-conservative algorithm", Journal of Tribology, vol. 131, pp. (041702)1-(041702)11, 2009.

[122] C. Shen and M. M. Khonsari, "Effect of dimples internal structure on hydrodynamic lubrication", Tribology Letters, vol. 52, pp. 415-430, 2013.

[123] N. Brunettiere, "A general model for liquid and gas lubrication including cavitation", Journal of Tribology, vol. 140, pp. (021702)1-(021702)10, 2018.

[124] M. Giacopini, M. T. Fowell and A. Strozzi, "A mass-conserving complementarity formulation to study lubricant films in the presence of cavitation", Journal of Tribology, vol. 132, pp. (041702)1-(041702)12, 2010.

[125] A. Almqvist, J. Fabricius and P. Wall, "A new approach for studying cavitation in lubrication", Journal of Tribology, vol. 136, pp. (011706)1-(011706)7, 2014.

[126] L Bertocchi, D Dini and A Baldini, "s ", Tribology International, vol. 67, pp. 61-71, 2013.

[127] F. J. Profito, M. Giacopini and D. Dini, "A general finite volume method for the solution of the Reynolds lubrication equation with a mass-conserving cavitation model", Tribology Letters, vol. 60(18), pp. 1-21, 2015.

[128] M. Scaraggi, "Textured surface hydrodynamic lubrication: discussion", Tribology Letters, vol. 48 (3), pp. 375-391, 2012.

[129] L. Biancofiore, M. Giacopini and D. Dini, "Interplay between wall slip and cavitation: a complementary variable approach", Tribology International, vol. 137, pp. 324-339, 2019.

[130] S. Boedo, "Mass conserving cavitation effects in squeeze-film journal bearings subjected to sinusoidal loads", Tribology Transactions, vol. 54(1), pp. 21-35, 2010.

[131] A. D. Kraker, R. V. Ostayen, and D. Rixen "Development of a texture averaged Reynolds equation", Tribology International, vol. 43(11), pp. 2100-2109, 2010.

[132] T. Woloszynski, P. Podsiadlo, and G. W. Stachowiak, "Efficient solution to the cavitation problem in hydrodynamic lubrication" Tribology Letters, vol. 58(18), pp. 1-11, 2015.

[133] L. Bai, Y. Meng and V. Zhang, "Experimental study on transient behavior of cavitation phenomenon in textured thrust bearings", Tribology Letters, vol. 63(27), pp. 1-15, 2016.

[134] F. J. Profito, S. C. Vlădescu, and D. Dini, "Transient experimental and modelling studies of laser-textured micro-grooved surfaces with a focus on piston-ring cylinder liner contacts", Tribology International, vol. 113, pp. 125-136, 2017.

[135] F. J. Profito, S. C. Vlădescu, and D. Dini, "Experimental validation of a mixed-lubrication regime model for textured piston-ring-liner contacts", Material Performance and Characterization, vol. 6(2), pp. 112-129, 2017.

[136] S. C. Vlădescu, S. Medina and T. Reddyhoff, "Lubricant film thickness and friction force measurements in a laser surface textured reciprocating line contact simulating the piston ring–liner pairing", Tribology International vol. 98, pp. 317-329, 2016.

[137] R. Rahmani and H. Rahnejat, "Enhanced performance of optimised partially textured load bearing surfaces", Tribology International, vol. 117, pp. 272-282, 2018.

[138] N. Tala-Ighil, M. Fillon and P. Maspeyrot, "Effect of textured area on the performances of a hydrodynamic journal bearing", Tribology International, vol. 44(3), pp. 211-219, 2011.

[139] A.B. Shinde and P.M. Pawar, "Multi-objective optimization of surface textured journal bearing by Taguchi based Grey relational analysis", Tribology International, vol. 114, pp. 349-357, 2017.

[140] C. Shen and M. M. Khonsari, "Numerical optimization of texture shape for parallel surfaces under unidirectional and bidirectional sliding", Tribology International, vol. 82, pp. 1-11, 2015.

[141] L. Floberg, "Cavitation boundary conditions with regard to the number of streamers and tensile strength of the liquid" Cavitation and Related Phenomena in Lubrication, IMechE, England, pp. 31-36, 1974.

[142] B. Jacobsson and L. Floberg, "The finite journal bearing, considering vaporization", Transactions of Chalmers University of Technology, Gothenburg, Report 190, 1957.

[143] K. Olsson, "Cavitation in dynamically loaded bearings", Transactions of Chalmers University of Technology, Gothenburg, Report 308, 1965.

[144] R. F. Ausas, P. Ragot and G. C. Buscaglia, "The impact of the cavitation model in the analysis of microtextured lubricated journal bearings", Journal of Tribology, vol. 129, pp. 868-875, 2007.

[145] H. G. Elrod and M. Adams, "A Computer Program for Cavitation and Starvation Problems", Proceedings of the First LEEDS-LYON Symposium on Cavitation and Related Phenomena in Lubrication, Leeds, UK, pp. 37–41, 1974.

[146] M. J. Braun and W. M. Hannon, "Cavitation formation and modelling for fluid film bearings: a review", Proceedings of the Institution of Mechanical Engineers, Part J: Journal of Engineering Tribology, vol. 224, pp. 839-863, 2014.

[147] J. Zhang and Y. Meng, "Direct observation of cavitation phenomenon and hydrodynamic lubrication analysis of textured surfaces", Tribology Letters, vol. 46, pp. 147-158, 2012.

[148] X. Meng, S. Bai and X. Peng, "Lubrication film flow control by oriented dimples for liquid lubricated mechanical seals", Tribology International, vol. 77, pp. 132-141, 2014.

[149] O. C. Zienkiewicz and R. L. Taylor, The Finite Volume Method Volume 3: Fluid Dynamics, Oxford, 2000.

[150] Y. Song, X. Ren, C. Gu and X. Li, "Experimental and numerical studies of cavitation effects in a tapered land thrust bearing", Journal of Tribology, vol. 137, pp. (011701)1 – (011701)9, 2014.

[151] R. F. Ausas, J. Mohammed and G. C. Buscaglia, "A mass-conserving algorithm for dynamical lubrication lubrication problems with cavitation", Journal of Tribology, vol. 131, pp. (031702)1-(031702)7, 2009.

[152] H. Tseng, J. Wu and R. Chang, "Shear thinning and shear dilatancy of liquid n-hexadecane via equilibrium and nonequilibrium molecular dynamics simulations: Temperature, pressure, and density effects", Journal of Chemical Physics, vol. 129, pp. (014502)1-(014502)20, 2008.

[153] D. Gropper, T. J. Harvey and L. Wang, "A numerical model for design and optimization of surface textures for tilting thrust bearings", Tribology International, vol. 119, pp. 190-207, 2018.

[154] D. Gropper, T. J. Harvey and L. Wang, "Numerical studies and optimization of surface textures for a tilting thrust bearing", Tribology International, vol. 124, pp. 134-144, 2018.

[155] S. B. Glavatskih, M. Fillon and R. Larsson, "The significance of oil thermal properties on the performance of a tilting-pad thrust bearing", Journal of Tribology, vol. 124, pp. 377-385, 2001.

[156] I. S. Y. Ku, T. Reddyhoff and H. A. Spikes, "A novel tribometer for the measurement of friction in MEMS", vol. 43, pp. (1087)1-(1090)4, 2010.

[157] J. Sotres and T. Arnebrant, "Experimental Investigations of Biological Lubrication at the Nanoscale: The Cases of Synovial Joints and the Oral Cavity", Lubricants, vol. 1, no. 4 pp. 102-131, 2013.

[158] J. Douglas, Fluid Mechanics, 5th edition (Harlow: Pearson Prentice Hall), 2005.

[159] CIBSE Concise Handbook ed J Armstrong (London: The Chartered Institution of Building Services Engineers), 2008.

[160] Web source, Link: https://birdprecision.com/wp-content/uploads/Ring_jewel.pdf

[161] D. B. Hamilton, J. A. Walowit and C. M. Allen, "A theory of lubrication by micro-irregularities", Journal of Fluids Engineering, vol. 88, pp. 177-185, 1966.

[162] J. N. Anno, J. A. Walowit and C. M. Allen, "Microasperity lubrication", Journal of Tribology, vol. 90, pp. 351-355, 1968.

[163] E.Willis, "Surface finish in relation to cylinder liners", Wear, vol. 109, pp. 351-366, 1986.

[164] I. Etsion, "State of the art in laser textureing", Journal of Tribology, vol. 127, pp. 248-253, 2005.

[165] S. C. Vladescu, A. V. Pegg and T. Reddyhoff, "The effects of surface texture in reciprocating contacts–An experimental study", Tribology International, vol. 82, pp. 28-42, 2015.

[166] M. B. Dobrica, M. Fillon and T. Cicone, "Optimizing surface texture for hydrodynamic lubricated contacts using a mass-conserving numerical approach", Journal of Engineering Tribology, vol.224, pp. 737-750, 2010.

[167] M. T. Fowell, S. Medina and I. G. Pegg, "Parametric study of texturing in convergent bearings", Tribology International, vol. 52, pp. 7-16, 2012.

[168] A. V. Olver, M. T. Fowell, and I. G. Pegg, "'Inlet suction', a load support mechanism in non-convergent, pocketed, hydrodynamic bearings", Proceedings of the Institution of Mechanical Engineers, Part J: Journal of Engineering Tribology, vol. 220, no. 2, pp. 105-108, 2006.

[169] M. Wakuda and Y. Yasuda, "Effect of surface texturing on friction reduction between ceramic and steel materials under lubricated sliding contact", Wear, vol. 254, pp. 356-363, 2003.

List of Published Work

Published Articles

P. Wang, J. Zhang and A. S. Holmes, "Development of hydrodynamic micro-bearings", Journal of Physics, Conf. Ser. 773, p. 012020, 2016.

Articles Submitted and Being Corrected in the Moment

P. Wang, F. Profito, T. Reddyhoff, D. Dini, A. S. Holmes and H. A. Spikes, "Numerical optimization of circular pocketed thrust bearings: the role of cavitation and scaling effects", Submitted to Tribology International.

Presentations in the Academic Conferences

P. Wang, T. Reddyhoff and A. S. Holmes, "Implementing Lubrication in Micro-Electro-Mechanical Systems", *PowerMEMS 2016: The 16th International Conference on Micro and Nanotechnology for Power Generation and Energy Conversion Applications*, Paris, France, 06/December/2016 to 09/December/2016, Presentation.

P. Wang, F. Profito, T. Reddyhoff, D. Dini and A. S. Holmes, "Implementing Lubrication in Micro-Electro- Mechanical Systems", *The 45th Leeds-Lyon Symposium on Tribology*, Leeds, UK, 04/September/2018 to 07/ September /2018, Presentation.

P. Wang, F. Profito, T. Reddyhoff, D. Dini and A. S. Holmes, "Numerical & Experimental Investigation of Micro Pocketed Parallel Thrust Bearing Performance", *The 74th STLE Annual Meeting & Exhibition*, Nashville, USA, 19/May/2019 to 23/May/2019, Presentation.

Appendix A: Code of the FVM Model

```
t_input = 298.15;     % input initial temperature (Unit K)
T_tolerance = 5e-3;   % tolerance value of temperature loop
T_error = 1;          % input initial temperature loop error value
ti = 0;               % set temperature loop initial counting number
% p_inital = zeros(Np_r,Np_xta);
% S_initial = ones(Np_r,Np_xta);
gama = 0.7;           % fraction of the heat transfered by convection;
cp = 2187;            % set pressure specific heat for hexadecane (2087 J/(kg K))

while  (T_error >= T_tolerance)
   ti = ti+1;
   t_eff(ti,1) = t_input;



% clear
% clc


% % Bearing geometry and mesh (patterned thrust bearing)
%     % Geometry Parameters in r direction
%     rad1 = 5e-7;                % fictional radius of centre circle [m]
%     rad2 = 3.5e-4;                % radius of inner recessed circle   [m]
%     rad3 = 9.5e-4;               % radius of rim                     [m]
%     rad = 1e-3;                 % outter radius of thrust bearing   [m]
%
%     % Geometry Parameters in xita direction
%     xita1 = (pi*3/40);              % angle of pad region_1             [rad]
%     xita2 = (pi*14/40);              % angle of recessed region          [rad]
%     xita3 = (pi*3/40);              % angle of pad region_2             [rad]
%     xita  = xita1+xita2+xita3;    % angle of the whole modelled region   [rad]
%
%     % Geometry Parameters in z direction
%     h_step = 1e-6;              % step height of the parallel bearing   [m]

   %Position of pivot point
   rad_p = 0;                  % radial position of pivot            [m]
   xita_p = 0;                 % tangential position of pivot        [rad]

   %Film thickness/ pitch angle/ roll angle of pivot
   h_p = 0;                    % film thickness at pivot point       [m]
   Alpha_r = 0;                % pitch angle                         [rad]
   Alpha_x = 0;                % roll angle                          [rad]

   %Suraface textures Parameters
   TE_x = 0;                   % Texture extend in xita direxion
   TE_r = 0;                   % Texture extend in radial direction
   D_x = 0;                    % Texture density in xita direction
   D_r = 0;                    % Texture density in radial direction
   h_t = 0;                    % Texture depth       [m]
   n_tx = 0;                   % Number of texture in xita direction
   n_tr = 0;                   % Number of texture in radial direction

%     R_ts = rad1+(rad2-rad1)*((1-TE_r)/2);       % Starting point of texture in radial direction
```

```
%     R_tw = ((rad2-rad1)*TE_r)/((n_tr-1)+D_r);   % Texture width in radial direction
%
%     Xita_ts = 0;                          % Starting point of texture in xira direction
%     Xita_tw = (xita*TE_x)/((n_tx-1)+D_x);       % Texture width in xita direction



    % Mesh generation

    % Macro discontinuity mesh preparation in radial direction
    R_ds = zeros(1,2);
    Dis_r = zeros(1,3);
    R_ds(1,1) = rad2;
    R_ds(1,2) = rad3;
    Dis_r(1,1) = 1/20;
    Dis_r(1,2) = 1/20;
    Dis_r(1,3) = 1/20;

    % Macro discontinuity mesh preparation in xita direction
    Xita_ds = zeros(1,2);
    Dis_x = zeros(1,2);
    Xita_ds(1,1) = xita1;
    Xita_ds(1,2) = xita1 + xita2;
    Dis_x(1,1) = 1/8;
    Dis_x(1,2) = 1/8;

    % Texture discontinuity mesh preparation in radial direction
    R_ts = zeros(1,n_tr);
    R_te = zeros(1,n_tr);
    R_tw = ((rad2-rad1)*TE_r)/((n_tr-1)+D_r);   % Texture width in radial direction
    R_pw = R_tw*D_r;                          % Pocket width in radial direction

%     R_ts(1,1) = rad1+(rad-rad1)*((1-TE_r)/2);
    for i=2:1:n_tr
        R_ts(1,i) = R_ts(1,i-1)+R_tw;
    end
    clear i

    for i=1:1:n_tr
        R_te(1,i) = R_ts(1,i)+R_pw;
    end
    clear i

    % Texture discontinuity mesh preparation in xita direction
    Xita_ts = zeros(1,n_tx);
    Xita_te = zeros(1,n_tx);
    Xita_tw = (xita*TE_x)/((n_tx-1)+D_x);       % Texture width in xita direction
    Xita_pw = Xita_tw*D_x;                    % Pocket width in xita direction

    % Xita_ts(1,1) = 0;
    for i=2:1:n_tx
        Xita_ts(1,i) = Xita_ts(1,i-1)+Xita_tw;
    end
    clear i

    for i=1:1:n_tx
        Xita_te(1,i) = Xita_ts(1,i)+Xita_pw;
    end
    clear i
```

```
%     NVX_ut1 = 21;
%     NVX_ut2 = 18;
%     NVX_ut3 = 42;
%     NVX_ut4 = 42;
%     NVX_ut5 = 18;
%     NVX_ut6 = 42;
%     NVX_ut7 = 18;
%     NVX_ut8 = 42;
%     NVX_ut9 = 42;
%     NVX_ut10 = 18;
%     NVX_ut11 = 21;

    NVX_ut =1;
    NVX_t = 0;
    NVX_ta = 0;

%     NVR_ut1 = 16;          %fine
%     NVR_ut2 = 13;          %varing
%     NVR_ut3 = 12;          %coarse
%     NVR_ut4 = 13;          %varying
%     NVR_ut5 = 8;           %fine
%     NVR_ut6 = 8;           %fine
%     NVR_ut7 = 13;          %varying
%     NVR_ut8 = 40;          %coarse
%     NVR_ut9 = 13;          %varying
%     NVR_ut10 = 8;          %fine
%     NVR_ut11 = 16;         %fine


    NVR_t = 0;
    NVR_ta = 0;

    NVX = NVX_ut1 + NVX_ut2 + NVX_ut3 + NVX_ut4 + NVX_ut5 + NVX_ut6 + NVX_ut7 + NVX_ut8
+ NVX_ut9 + NVX_ut10 + NVX_ut11 + NVX_t * (n_tx) + NVX_ta * (n_tx-1);
    NVR = NVR_ut1 + NVR_ut2 + NVR_ut3 + NVR_ut4 + NVR_ut5 + NVR_ut6 + NVR_ut7 + NVR_ut8
+ NVR_ut9 + NVR_ut10 + NVR_ut11 + NVR_t * (n_tr) + NVX_ta * (n_tr-1);

    NVX_s = zeros(NVR,NVX);
    NVX_e = zeros(NVR,NVX);

    NVR_s = zeros(NVR,NVX);
    NVR_e = zeros(NVR,NVX);


%    % Mesh ratio values in xita direction
%     Ratio1 = 100/112;
%     Ratio2 = 112/100;


  % Unequal Mesh setup in Xita direction

    %Region1 in Xita Direction: Coarse Mesh
    dt = (xita*(Dis_x(1,1)/2)/NVX_ut3)*Coe_t1;
    aa = 1;
    bb = aa+NVX_ut1-1;
    for i = aa:1:bb
        NVX_s(1,i) = (i-aa)*dt;
        NVX_e(1,i) = NVX_s(1,i) + dt;
    end
```

```
clear n dt aa bb i

%Region2 in Xita Direction: Gradually Finner Mesh
aa = NVX_ut1+1;
bb = aa+NVX_ut2-1;
n =0;
for i = aa:1:bb
    dt = ((xita*(Dis_x(1,1)/2)/NVX_ut3)*Coe_t2) * (Ratio1^n);
    NVX_s(1,i) = NVX_e(1,NVX_ut1+n);
    NVX_e(1,i) = NVX_s(1,i) + dt;
    n = n+1;
end
clear n dt aa bb i

%Region3 in Xita Direction: Fine Mesh
aa = NVX_ut1+NVX_ut2+1;
bb = aa+NVX_ut3-1;
for i = aa:1:bb
    dt = (Xita_ds(1,1) - NVX_e(1,NVX_ut1+NVX_ut2))/NVX_ut3;
    NVX_s(1,i) = NVX_e(1,NVX_ut1+NVX_ut2) +(i-aa)*dt;
    NVX_e(1,aa+bb-i) = (Xita_ds(1,1))-(i-aa)*dt;
end
clear n dt aa bb i

%Region4 in Xita Direction: Fine Mesh
aa = NVX_ut1+NVX_ut2+NVX_ut3+1;
bb = aa+NVX_ut4-1;
for i = aa:1:bb
    dt = (Xita_ds(1,1) - NVX_e(1,NVX_ut1+NVX_ut2))/NVX_ut3;
    NVX_s(1,i) = Xita_ds(1,1) + (i-aa)*dt;
    NVX_e(1,i) = NVX_s(1,i) + dt;
end
clear n dt aa bb i

%Region5 in Xita Direction: Gradually Coarser Mesh
aa = NVX_ut1+NVX_ut2+NVX_ut3+NVX_ut4+1;
bb = aa+NVX_ut5-1;
n =0;
for i = aa:1:bb
    dt = (NVX_e(1,NVX_ut1+NVX_ut2+NVX_ut3+NVX_ut4)-
NVX_s(1,NVX_ut1+NVX_ut2+NVX_ut3+NVX_ut4))  * (Ratio2^n);
    NVX_s(1,i) = NVX_e(1,NVX_ut1+NVX_ut2+NVX_ut3+NVX_ut4+n);
    NVX_e(1,i) = NVX_s(1,i) + dt;
    n = n+1;
end
clear n dt aa bb i

%Region6 in Xita Direction: Coarse Mesh
dt = ((xita/2)-NVX_e(1,NVX_ut1+NVX_ut2+NVX_ut3+NVX_ut4+NVX_ut5)) / (NVX_ut6/2);
aa = NVX_ut1+NVX_ut2+NVX_ut3+NVX_ut4+NVX_ut5+1;
bb = aa+NVX_ut6-1;
for i = aa:1:bb
    NVX_s(1,i) = NVX_e(1,NVX_ut1+NVX_ut2+NVX_ut3+NVX_ut4+NVX_ut5) + (i-aa)*dt;
    NVX_e(1,i) = NVX_s(1,i) + dt;
end
clear n dt aa bb i

%Region7 in Xita Direction: Gradually Finner Mesh
aa = NVX_ut1+NVX_ut2+NVX_ut3+NVX_ut4+NVX_ut5+NVX_ut6+1;
bb = aa+NVX_ut7-1;
```

```
    n =0;
    for i = aa:1:bb
        dt = (NVX_e(1,NVX_ut1+NVX_ut2+NVX_ut3+NVX_ut4)-
NVX_s(1,NVX_ut1+NVX_ut2+NVX_ut3+NVX_ut4))  * (Ratio2^(NVX_ut5-1)) * (Ratio1^n);
        NVX_s(1,i) = NVX_e(1,NVX_ut1+NVX_ut2+NVX_ut3+NVX_ut4+NVX_ut5+NVX_ut6+n);
        NVX_e(1,i) = NVX_s(1,i) + dt;
        n = n+1;
    end
    clear n dt aa bb i

    %Region8 in Xita Direction: Fine Mesh
    aa = NVX_ut1+NVX_ut2+NVX_ut3+NVX_ut4+NVX_ut5+NVX_ut6+NVX_ut7+1;
    bb = aa+NVX_ut8-1;
    for i = aa:1:bb
        dt = (Xita_ds(1,2) -
NVX_e(1,NVX_ut1+NVX_ut2+NVX_ut3+NVX_ut4+NVX_ut5+NVX_ut6+NVX_ut7))/NVX_ut8;
        NVX_s(1,i) = NVX_e(1,NVX_ut1+NVX_ut2+NVX_ut3+NVX_ut4+NVX_ut5+NVX_ut6+NVX_ut7)
+(i-aa)*dt;
        NVX_e(1,aa+bb-i) = (Xita_ds(1,2))-(i-aa)*dt;
    end
    clear n dt aa bb i

    %Region9 in Xita Direction: Fine Mesh
    aa = NVX_ut1+NVX_ut2+NVX_ut3+NVX_ut4+NVX_ut5+NVX_ut6+NVX_ut7+NVX_ut8+1;
    bb = aa+NVX_ut9-1;
    for i = aa:1:bb
        dt = (Xita_ds(1,2) -
NVX_e(1,NVX_ut1+NVX_ut2+NVX_ut3+NVX_ut4+NVX_ut5+NVX_ut6+NVX_ut7))/NVX_ut8;
        NVX_s(1,i) = Xita_ds(1,2) + (i-aa)*dt;
        NVX_e(1,i) = NVX_s(1,i) + dt;
    end
    clear n dt aa bb i

    %Region10 in Xita Direction: Gradually Coarser Mesh
    aa =
NVX_ut1+NVX_ut2+NVX_ut3+NVX_ut4+NVX_ut5+NVX_ut6+NVX_ut7+NVX_ut8+NVX_ut9+1;
    bb = aa+NVX_ut10-1;
    n =0;
    for i = aa:1:bb
        dt = ((xita*(Dis_x(1,1)/2)/NVX_ut3)*Coe_t2) * (Ratio1^(NVX_ut2-1)) * (Ratio2^n);
        NVX_s(1,i) =
NVX_e(1,NVX_ut1+NVX_ut2+NVX_ut3+NVX_ut4+NVX_ut5+NVX_ut6+NVX_ut7+NVX_ut8+NVX_ut9
+n);
        NVX_e(1,i) = NVX_s(1,i) + dt;
        n = n+1;
    end
    clear n dt aa bb i

    %Region11 in Xita Direction: Coarse Mesh
    dt = (xita-
NVX_e(1,NVX_ut1+NVX_ut2+NVX_ut3+NVX_ut4+NVX_ut5+NVX_ut6+NVX_ut7+NVX_ut8+NVX_ut9
+NVX_ut10))/(NVX_ut11);
    aa =
NVX_ut1+NVX_ut2+NVX_ut3+NVX_ut4+NVX_ut5+NVX_ut6+NVX_ut7+NVX_ut8+NVX_ut9+NVX_ut
10+1;
    bb = aa+NVX_ut11-1;
    for i = aa:1:bb
        NVX_s(1,i) =
NVX_e(1,NVX_ut1+NVX_ut2+NVX_ut3+NVX_ut4+NVX_ut5+NVX_ut6+NVX_ut7+NVX_ut8+NVX_ut9
+NVX_ut10) + (i-aa)*dt;
```

```
        NVX_e(1,aa+bb-i) = xita-(i-aa)*dt;
    end
    clear n dt aa bb i


%     % Mesh setup in xita direction when surface texture applies
%     for n = 1:1:n_tx
%         dt = (Xita_te(1,n)-Xita_ts(1,n))/NVX_t;
%         aa = (n-1)*(NVX_t+NVX_ta)+1;
%         bb = aa+NVX_t-1;
%         for i=aa:1:aa+(NVX_t-1)
%             NVX_s(1,i) = Xita_ts(1,n) + (i-aa)*dt;
%             NVX_e(1,aa+bb-i) = Xita_te(1,n) - (i-aa)*dt;
%         end
%     end
%     clear n dt aa bb i
%
%
%     for n = 1:1:n_tx-1
%         dt = (Xita_ts(1,n+1)-Xita_te(1,n))/NVX_ta;
%         aa = (n-1)*(NVX_t+NVX_ta)+NVX_t+1;
%         bb = aa+NVX_ta-1;
%         for i=aa:1:aa+(NVX_ta-1)
%             NVX_s(1,i) = Xita_te(1,n) + (i-aa)*dt;
%             NVX_e(1,aa+bb-i) = Xita_ts(1,n+1) - (i-aa)*dt;
%         end
%     end
%     clear n dt aa bb i
%
%
%     for i = 1+(n_tx-1)*(NVX_t+NVX_ta)+NVX_t:1:NVX
%         dt = (xita-Xita_te(1,n_tx))/NVX_ut;
%         aa = 1+(n_tx-1)*(NVX_t+NVX_ta)+NVX_t;
%         NVX_s(1,i) = Xita_te(1,n_tx)+(i-aa)*dt;
%         NVX_e(1,NVX+aa-i) = xita-(i-aa)*dt;
%     end
%     clear n dt aa bb i


    Coe_a = 0.5;


    niter = 0;
    for i = 1:1:NVX
        niter = niter+1;
        aa = niter;
        for n = 1:1:2
            if NVX_s(1,i)==Xita_ds(1,n)
                A_dt = Coe_a * ( min( (NVX_s(1,i+1)-NVX_s(1,i)), (NVX_s(1,i)-NVX_s(1,i-1)) ) );
                temp_xs(1,niter) = NVX_s(1,i)-A_dt;
                niter = niter+1;
                temp_xs(1,niter) = NVX_s(1,i);
                niter = niter+1;
                temp_xs(1,niter) = NVX_s(1,i)+A_dt;
            end
        end

        if niter == aa
            temp_xs(1,niter) = NVX_s(1,i);
        end
```

```
    end
    clear m n dt aa bb i niter


    niter=0;
    for i = 1:1:NVX
        niter = niter+1;
        aa = niter;
        for n = 1:1:2
            if NVX_e(1,i)==Xita_ds(1,n)
                A_dt = Coe_a * ( min( (NVX_e(1,i+1)-NVX_e(1,i)), (NVX_e(1,i)-NVX_e(1,i-1)) ) );
                temp_xe(1,niter) = NVX_e(1,i)-A_dt;
                niter = niter+1;
                temp_xe(1,niter) = NVX_e(1,i);
                niter = niter+1;
                temp_xe(1,niter) = NVX_e(1,i)+A_dt;
            end
        end

        if niter == aa
            temp_xe(1,niter) = NVX_e(1,i);
        end

    end
    clear m n dt aa bb i niter

%     %Additional points adding when surface texture is applied
%     niter = 0;
%     for i = 1:1:NVX
%         niter = niter+1;
%         aa = niter;
%         for n = 2:1:n_tx
%             if NVX_s(1,i)==Xita_ts(1,n)
%                 A_dt = Coe_a * ( min( (NVX_s(1,i+1)-NVX_s(1,i)), (NVX_s(1,i)-NVX_s(1,i-1)) ) );
%                 temp_xs(1,niter) = NVX_s(1,i)-A_dt;
%                 niter = niter+1;
%                 temp_xs(1,niter) = NVX_s(1,i);
%                 niter = niter+1;
%                 temp_xs(1,niter) = NVX_s(1,i)+A_dt;
%             end
%         end
%
%         for m = 1:1:n_tx
%             if NVX_s(1,i)==Xita_te(1,m)
%                 A_dt = Coe_a * ( min( (NVX_s(1,i+1)-NVX_s(1,i)), (NVX_s(1,i)-NVX_s(1,i-1)) ) );
%                 temp_xs(1,niter) = NVX_s(1,i)-A_dt;
%                 niter = niter+1;
%                 temp_xs(1,niter) = NVX_s(1,i);
%                 niter = niter+1;
%                 temp_xs(1,niter) = NVX_s(1,i)+A_dt;
%             end
%         end
%
%         if niter == aa
%             temp_xs(1,niter) = NVX_s(1,i);
%         end
%
%     end
%     clear m n dt aa bb i niter
```

```
%
%
%    niter=0;
%    for i = 1:1:NVX
%        niter = niter+1;
%        aa = niter;
%        for n = 2:1:n_tx
%            if NVX_e(1,i)==Xita_ts(1,n)
%                A_dt = Coe_a * ( min( (NVX_e(1,i+1)-NVX_e(1,i)), (NVX_e(1,i)-NVX_e(1,i-1)) ) );
%                temp_xe(1,niter) = NVX_e(1,i)-A_dt;
%                niter = niter+1;
%                temp_xe(1,niter) = NVX_e(1,i);
%                niter = niter+1;
%                temp_xe(1,niter) = NVX_e(1,i)+A_dt;
%            end
%        end
%
%        for m = 1:1:n_tx
%            if NVX_e(1,i)==Xita_te(1,m)
%                A_dt = Coe_a * ( min( (NVX_e(1,i+1)-NVX_e(1,i)), (NVX_e(1,i)-NVX_e(1,i-1)) ) );
%                temp_xe(1,niter) = NVX_e(1,i)-A_dt;
%                niter = niter+1;
%                temp_xe(1,niter) = NVX_e(1,i);
%                niter = niter+1;
%                temp_xe(1,niter) = NVX_e(1,i)+A_dt;
%            end
%        end
%
%        if niter == aa
%            temp_xe(1,niter) = NVX_e(1,i);
%        end
%
%    end
%    clear m n dt aa bb i niter


%    % Mesh ratio values in radial direction
%    clear Ratio1 Ratio2
%    Ratio1 = 100/110;
%    Ratio2 = 110/100;

    % Unequal Mesh setup in Radial direction
    % Region 1 mesh (Fine mesh)
    dr = (rad*Dis_r(1,1))/NVR_ut1;
    aa = 1;
    bb = aa+NVR_ut1-1;
    for i = aa:1:bb
        NVR_s(i,1) = rad1+(i-aa)*dr;
        NVR_e(i,1) = NVR_s(i,1)+dr;
    end
    clear n dr aa bb i

    % Region 2 mesh (Varying mesh)
    aa = NVR_ut1+1;
    bb = aa+NVR_ut2-1;
    n=0;
    for i = aa:1:bb
        dr = ((rad*Dis_r(1,1))/NVR_ut1)*(Ratio4^n);
        NVR_s(i,1) = NVR_e(NVR_ut1+n,1);
        NVR_e(i,1) = NVR_s(i,1) + dr;
```

```
    n = n+1;
end
clear n dr aa bb i

% Region 5 mesh (Fine mesh)
aa = NVR_ut1+NVR_ut2+NVR_ut3+NVR_ut4+1;
bb = aa+NVR_ut5-1;
dr = (rad*(Dis_r(1,2)/2))/NVR_ut5;
for i = aa:1:bb
    NVR_e(aa+bb-i,1) = R_ds(1,1) - (i-aa)*dr;
    NVR_s(aa+bb-i,1) = NVR_e(aa+bb-i,1) - dr;
end
clear n dr aa bb i

% Region 4 mesh (Varying mesh)
aa = NVR_ut1+NVR_ut2+NVR_ut3+1;
bb = aa+NVR_ut4-1;
n=0;
for i = aa:1:bb
    dr = ((rad*(Dis_r(1,2)/2))/NVR_ut5)*(Ratio4^n);
    NVR_e(aa+bb-i,1) = NVR_s(NVR_ut1+NVR_ut2+NVR_ut3+NVR_ut4+1-n,1);
    NVR_s(aa+bb-i,1) = NVR_e(aa+bb-i,1) - dr;
    n = n+1;
end
clear n dr aa bb i

% Region 3 mesh (Coarse mesh)
dr = (NVR_s(NVR_ut1+NVR_ut2+NVR_ut3+1) - NVR_e(NVR_ut1+NVR_ut2))/NVR_ut3;
aa = NVR_ut1+NVR_ut2+1;
bb = aa+NVR_ut3-1;
for i = aa:1:bb
    NVR_s(i,1) = NVR_e(NVR_ut1+NVR_ut2)+(i-aa)*dr;
    NVR_e(i,1) = NVR_s(i,1)+dr;
end
clear n dr aa bb i

 % Region 6 mesh (Fine mesh)
dr = (rad*(Dis_r(1,2)/2))/NVR_ut6;
aa = NVR_ut1+NVR_ut2+NVR_ut3+NVR_ut4+NVR_ut5+1;
bb = aa+NVR_ut6-1;
for i = aa:1:bb
    NVR_s(i,1) = R_ds(1,1)+(i-aa)*dr;
    NVR_e(i,1) = NVR_s(i,1)+dr;
end
clear n dr aa bb i

% Region 7 mesh (Varying mesh)
aa = NVR_ut1+NVR_ut2+NVR_ut3+NVR_ut4+NVR_ut5+NVR_ut6+1;
bb = aa+NVR_ut7-1;
n=0;
for i = aa:1:bb
    dr = ((rad*(Dis_r(1,2)/2))/NVR_ut6)*(Ratio4^n);
    NVR_s(i,1) = NVR_e(NVR_ut1+NVR_ut2+NVR_ut3+NVR_ut4+NVR_ut5+NVR_ut6+n,1);
    NVR_e(i,1) = NVR_s(i,1) + dr;
    n = n+1;
end
clear n dr aa bb i

% Region 10 mesh (Fine mesh)
```

```
    aa =
NVR_ut1+NVR_ut2+NVR_ut3+NVR_ut4+NVR_ut5+NVR_ut6+NVR_ut7+NVR_ut8+NVR_ut9+1;
    bb = aa+NVR_ut10-1;
    dr = (rad*(Dis_r(1,3)/2))/NVR_ut10;
    for i = aa:1:bb
        NVR_e(aa+bb-i,1) = R_ds(1,2) - (i-aa)*dr;
        NVR_s(aa+bb-i,1) = NVR_e(aa+bb-i,1) - dr;
    end
    clear n dr aa bb i

    % Region 9 mesh (Varying mesh)
    aa = NVR_ut1+NVR_ut2+NVR_ut3+NVR_ut4+NVR_ut5+NVR_ut6+NVR_ut7+NVR_ut8+1;
    bb = aa+NVR_ut9-1;
    n=0;
    for i = aa:1:bb
        dr = ((rad*(Dis_r(1,3)/2))/NVR_ut10)*(Ratio4^n);
        NVR_e(aa+bb-i,1) =
NVR_s(NVR_ut1+NVR_ut2+NVR_ut3+NVR_ut4+NVR_ut5+NVR_ut6+NVR_ut7+NVR_ut8+NVR_ut9
+1-n,1);
        NVR_s(aa+bb-i,1) = NVR_e(aa+bb-i,1) - dr;
        n = n+1;
    end
    clear n dr aa bb i

    % Region 8 mesh (Coarse mesh)
    dr = (NVR_s(NVR_ut1+NVR_ut2+NVR_ut3+NVR_ut4+NVR_ut5+NVR_ut6+NVR_ut7+NVR_ut8+1)
- NVR_e(NVR_ut1+NVR_ut2+NVR_ut3+NVR_ut4+NVR_ut5+NVR_ut6+NVR_ut7))/NVR_ut8;
    aa = NVR_ut1+NVR_ut2+NVR_ut3+NVR_ut4+NVR_ut5+NVR_ut6+NVR_ut7+1;
    bb = aa+NVR_ut8-1;
    for i = aa:1:bb
        NVR_s(i,1) =
NVR_e(NVR_ut1+NVR_ut2+NVR_ut3+NVR_ut4+NVR_ut5+NVR_ut6+NVR_ut7)+(i-aa)*dr;
        NVR_e(i,1) = NVR_s(i,1)+dr;
    end
    clear n dr aa bb i

    % Region 11 mesh (Fine mesh)
    aa =
NVR_ut1+NVR_ut2+NVR_ut3+NVR_ut4+NVR_ut5+NVR_ut6+NVR_ut7+NVR_ut8+NVR_ut9+NVR_u
t10+1;
    bb = aa+NVR_ut11-1;
    dr = (rad-R_ds(1,2))/NVR_ut11;
    for i = aa:1:bb
        NVR_s(i,1) = R_ds(1,2) + (i-aa)*dr;
        NVR_e(i,1) = NVR_s(i,1) + dr;
    end
    clear n dr aa bb i


%     % Mesh setup in radial direction when surface texture applies
%     for n = 1:1:n_tr
%         dr = (R_te(1,n)-R_ts(1,n))/NVR_t;
%         aa = (n-1)*(NVR_t+NVR_ta)+NVR_ut1+1;
%         bb = aa+NVR_t-1;
%         for i=aa:1:aa+(NVR_t-1)
%             NVR_s(i,1) = R_ts(1,n) + (i-aa)*dr;
%             NVR_e(aa+bb-i,1) = R_te(1,n) - (i-aa)*dr;
%         end
%     end
%     clear n dr aa bb i
```

```
%
%
%    for n = 1:1:n_tr-1
%       dr = (R_ts(1,n+1)-R_te(1,n))/NVR_ta;
%       aa = (n-1)*(NVR_t+NVR_ta)+NVR_t+NVR_ut1+1;
%       bb = aa+NVR_ta-1;
%       for i=aa:1:aa+(NVR_ta-1)
%          NVR_s(i,1) = R_te(1,n) + (i-aa)*dr;
%          NVR_e(aa+bb-i,1) = R_ts(1,n+1) - (i-aa)*dr;
%       end
%    end
%    clear n dr aa bb i
%
%
%    for i = 1+NVR_ut1+(n_tr-1)*(NVR_t+NVR_ta)+NVR_t:1:NVR
%       dr = (rad2-R_te(1,n_tr))/NVR_ut2;
%       aa = 1+NVR_ut1+(n_tr-1)*(NVR_t+NVR_ta)+NVR_t;
%       NVR_s(i,1) = R_te(1,n_tr)+(i-aa)*dr;
%       NVR_e(NVR+aa-i,1) = rad2-(i-aa)*dr;
%    end
%    clear n dr aa bb i
%
%
%    for i = 1:1:NVR_ut1
%       dr = (R_ts(1,1)-rad1)/NVR_ut1;
%       aa = 1;
%       NVR_s(i,1) = rad1+(i-aa)*dr;
%       NVR_e(NVR_ut1+aa-i,1) = R_ts(1,1)-(i-aa)*dr;
%    end
%    clear n dr aa bb i


   Coe_a = 0.5;

   niter = 0;
   for i = 1:1:NVR
      niter = niter+1;
      aa = niter;
      for n = 1:1:2
         if NVR_s(i,1)==R_ds(1,n)
            A_dr = Coe_a * ( min( (NVR_s(i+1,1)-NVR_s(i,1)), (NVR_s(i,1)-NVR_s(i-1,1)) ) );
            temp_rs(niter,1) = NVR_s(i,1)-A_dr;
            niter = niter+1;
            temp_rs(niter,1) = NVR_s(i,1);
            niter = niter+1;
            temp_rs(niter,1) = NVR_s(i,1)+A_dr;
         end
      end

      if niter == aa
         temp_rs(niter,1) = NVR_s(i,1);
      end

   end
   clear m n dr aa bb i niter


   niter = 0;
   for i = 1:1:NVR
      niter = niter+1;
```

```
        aa = niter;
        for n = 1:1:2
            if NVR_e(i,1)==R_ds(1,n)
                A_dr = Coe_a * ( min( (NVR_e(i+1,1)-NVR_e(i,1)), (NVR_e(i,1)-NVR_e(i-1,1)) ) );
                temp_re(niter,1) = NVR_e(i,1)-A_dr;
                niter = niter+1;
                temp_re(niter,1) = NVR_e(i,1);
                niter = niter+1;
                temp_re(niter,1) = NVR_e(i,1)+A_dr;
            end
        end

        if niter == aa
            temp_re(niter,1) = NVR_e(i,1);
        end

    end
    clear m n dr aa bb i niter


%     %Additional points adding when surface texture is applied
%     niter = 0;
%     for i = 1:1:NVR
%         niter = niter+1;
%         aa = niter;
%         for n = 1:1:n_tr
%             if  NVR_s(i,1)==R_ts(1,n)
%                 A_dr = Coe_a * ( min( (NVR_s(i+1,1)-NVR_s(i,1)), (NVR_s(i,1)-NVR_s(i-1,1)) ) );
%                 temp_rs(niter,1) = NVR_s(i,1)-A_dr;
%                 niter = niter+1;
%                 temp_rs(niter,1) = NVR_s(i,1);
%                 niter = niter+1;
%                 temp_rs(niter,1) = NVR_s(i,1)+A_dr;
%             end
%         end
%
%         for m = 1:1:n_tr
%             if  NVR_s(i,1)==R_te(1,m)
%                 A_dr = Coe_a * ( min( (NVR_s(i+1,1)-NVR_s(i,1)), (NVR_s(i,1)-NVR_s(i-1,1)) ) );
%                 temp_rs(niter,1) = NVR_s(i,1)-A_dr;
%                 niter = niter+1;
%                 temp_rs(niter,1) = NVR_s(i,1);
%                 niter = niter+1;
%                 temp_rs(niter,1) = NVR_s(i,1)+A_dr;
%             end
%         end
%
%         if niter == aa
%             temp_rs(niter,1) = NVR_s(i,1);
%         end
%
%     end
%     clear m n dr aa bb i niter
%
%
%     niter=0;
%     for i = 1:1:NVR
%         niter = niter+1;
%         aa = niter;
%         for n = 1:1:n_tr
```

```
%            if  NVR_e(i,1)==R_ts(1,n)
%               A_dr = Coe_a * ( min( (NVR_e(i+1,1)-NVR_e(i,1)), (NVR_e(i,1)-NVR_e(i-1,1)) ) );
%               temp_re(niter,1) = NVR_e(i,1)-A_dr;
%               niter = niter+1;
%               temp_re(niter,1) = NVR_e(i,1);
%               niter = niter+1;
%               temp_re(niter,1) = NVR_e(i,1)+A_dr;
%            end
%        end
%
%        for m = 1:1:n_tr
%            if  NVR_e(i,1)==R_te(1,m)
%               A_dr = Coe_a * ( min( (NVR_e(i+1,1)-NVR_e(i,1)), (NVR_e(i,1)-NVR_e(i-1,1)) ) );
%               temp_re(niter,1) = NVR_e(i,1)-A_dr;
%               niter = niter+1;
%               temp_re(niter,1) = NVR_e(i,1);
%               niter = niter+1;
%               temp_re(niter,1) = NVR_e(i,1)+A_dr;
%            end
%        end
%
%        if niter == aa
%            temp_re(niter,1) = NVR_e(i,1);
%        end
%
%    end
%    clear m n dr aa bb i niter

    temp_pr = (temp_re+temp_rs)/2;
    temp_px = (temp_xe+temp_xs)/2;

    Np_r = 2+length(temp_pr);
    Np_x = 2+length(temp_px);

    Xta = zeros(Np_r,Np_x);
    R   = zeros(Np_r,Np_x);

    Xta(1,1)=0;
    Xta(1,end)=xita;
    Xta(1,2:end-1)=temp_px;
    for i=2:1:Np_r
        Xta(i,:)=Xta(1,:);
    end
    clear i

    R(1,1)=rad1;
    R(end,1)=rad;
    R(2:end-1,1)=temp_pr;
    for i=2:1:Np_x
        R(:,i)=R(:,1);
    end
    clear i


    R_n = zeros(Np_r,Np_x);
    for i=2:1:Np_r-1
        R_n(i,2)=temp_re(i-1,1);
    end
    for j=3:1:Np_x-1
        R_n(:,j)=R_n(:,2);
```

```
    end
    clear i j

    R_s = zeros(Np_r,Np_x);
    for i=2:1:Np_r-1
        R_s(i,2)=temp_rs(i-1,1);
    end
    for j=3:1:Np_x-1
        R_s(:,j)=R_s(:,2);
    end
    clear i j

    Xta_e = zeros(Np_r,Np_x);
    for i=2:1:Np_x-1
        Xta_e(2,i)=temp_xe(1,i-1);
    end
    for j=3:1:Np_r-1
        Xta_e(j,:)=Xta_e(2,:);
    end
    clear i j

    Xta_w = zeros(Np_r,Np_x);
    for i=2:1:Np_x-1
        Xta_w(2,i)=temp_xs(1,i-1);
    end
    for j=3:1:Np_r-1
        Xta_w(j,:)=Xta_w(2,:);
    end
    clear i j


%     % Z direction values for nodal points of the tilting bearing without pockets
%     Z_ut = zeros(Np_r,Np_x);
%     for i=1:1:Np_r
%         for j = 1:1:Np_x
%           Z_ut(i,j) = R(i,j).*sin(xita_p-Xta(i,j)).*sin(Alpha_r) + (rad_p-(R(i,j).*cos(xita_p-
Xta(i,j)))).*sin(Alpha_x);
%         end
%     end
%     clear i j


    % Z direction values for nodal points of the tilting bearing without pockets
    Z_ut = zeros(Np_r,Np_x);
    for i=1:1:Np_r
        for j=1:1:Np_x
            if ((R(i,j)<R_ds(1,1)) || (Xta(i,j)>Xita_ds(1,1) && Xta(i,j)<Xita_ds(1,2) && R(i,j)<R_ds(1,2)))
                Z_ut(i,j) = h_step;
            end
        end
    end


%     % Z direction values for nodal points of the pockets distribution and depth
%     Texture = zeros(Np_r,Np_x);
%     for i=1:1:Np_r
%         for j=1:1:Np_x
%           for m=1:1:n_tr
%               for n=1:1:n_tx
```

```
%                 if (R(i,j)>=R_ts(1,m)&&R(i,j)<=R_te(1,m)) &&
(Xta(i,j)>=Xita_ts(1,n)&&Xta(i,j)<=Xita_te(1,n))
%                     Texture(i,j) = h_t;
%                 end
%             end
%         end
%       end
%   end
%
%   % Z direction values for nodal points of the bearing with pockets
%   Z_t = Z_ut+Texture;


   Z = Z_ut;

   clear i j


% Operational conditions, SI units
  % Operational conditions, SI units

   rho   = 770;                % density of lubricant                    [Kg/m3]

   T_sup = 298.15;

   T_eff = t_eff(ti,1);

   ki = 10^(10^(10.2177-4.201*log10(T_eff))) - 0.7;
   mi    = ki*(rho/1000)*(1e-3);          % dynamic viscosity of lubricant            [Pa.s]

   ome_t = (15000*2*pi)/60;       % top surface rotational speed              [rad/s]
   ome_b = (0*2*pi)/60;          % bottom suface rotational speed            [rad/s]
   ome   = ome_t + ome_b;        % total rotational speed of both syrfaces   [rad/s]
   ps    = 1.015e5;              % boundary pressure on the side edge        [Pa]
   pcav  = 1;                    % cavitation pressure                       [Pa] This setup is doubious
%    h_min  = 0.5e-6;            % minimum film thickness                    [m]


% Parameters for SOR algorithm
   w_p    = 1.8;   % over-relaxation parameter (1 <= w_p <= 2), depend on the mesh size (w_p = 1.7
is a good educated guess)
   w_s    = 1;

   w_t    = 0.4;   % under-relaxation parameter (0.2<= w_t <= 0.6)

   tol    = 5e-9;  % tolerance error for convergence
   maxIter = 600000000; % maximum number of iterations


% Calculate local lubricant film thickness
   h = (h_min+Z);


% % Calculate squeeze velocity (IGNORED for now)
%    dt        = 0;
%    dhdt      = 0;
%    theta_prev = (0*h)+1;


% Dimensionless parameters
```

```
    Ro  = rad;
    Ho  = h_min;
    MIo = mi;
    Rho = rho;
    Omeo  = ome;
    Po  = (Omeo*(Ro^2)*MIo) / (Ho^2);
    %   To  = Lo/Vo;


% Calculate dimensionless values
    R_dim    = (R/Ro);
    R_ndim = (R_n/Ro);
    R_sdim = (R_s/Ro);
    Xta_dim    = Xta;
    Xta_wdim = Xta_w;
    Xta_edim = Xta_e;
    H_dim    = (h/Ho);
    ps_dim   = (ps/Po);
    pcav_dim = (pcav/Po);
    Mi_dim   = (mi/MIo);
    Ome_dim    = (ome/Omeo);
    Rho_dim = ((Rho*Omeo*(Ho^2))/(MIo));     %Here is the Modified Reynolds Number
    %     dt_dim   = (dt/H0To);
    %     dhdt_dim = (dhdt/(Ho/To));


% % Calculate CFD coefficient matrices
%     [AXTA, AR, AC, B, C, D] = FVM_Matrix(Np_x, Np_r, Xta_wdim, Xta_edim, Xta_dim, R_dim,
R_ndim, R_sdim, H_dim, Ome_dim, Mi_dim, Rho_dim);




%  FVM_Matrix: Function for coefficient matrices
%  Calculate coefficients matrix in the FVM governing equations for p and s computation for solver


% Initialize FVM coefficients matrices
    AXTA = zeros(Np_r,Np_x,3);
    AR   = zeros(Np_r,Np_x,3);
    AC   = zeros(Np_r,Np_x,3);
    B    = zeros(Np_r,Np_x,3);
    C    = zeros(Np_r,Np_x);
    D    = zeros(Np_r,Np_x);
    ZERO = zeros(Np_r,Np_x);
    Hw_dim = zeros(Np_r,Np_x);
    He_dim =zeros(Np_r,Np_x);
    Hs_dim =zeros(Np_r,Np_x);
    Hn_dim =zeros(Np_r,Np_x);


    for i = 2:1:Np_r-1
        Hw_dim(i,2) = H_dim(i,1);
        for j =3:1:Np_x-1
            Hw_dim(i,j) = ((Xta_dim(i,j)-Xta_wdim(i,j))/(Xta_dim(i,j)-Xta_dim(i,j-1)))*H_dim(i,j-1)...
                +((Xta_wdim(i,j)-Xta_dim(i,j-1))/(Xta_dim(i,j)-Xta_dim(i,j-1)))*H_dim(i,j);
        end
    end
    clear i j
```

```
    for i = 2:1:Np_r-1
        He_dim(i,Np_x-1) = H_dim(i,Np_x);
        for j =2:1:Np_x-2
            He_dim(i,j) = ((Xta_dim(i,j+1)-Xta_edim(i,j))/(Xta_dim(i,j+1)-Xta_dim(i,j)))*H_dim(i,j)...
                +((Xta_edim(i,j)-Xta_dim(i,j))/(Xta_dim(i,j+1)-Xta_dim(i,j)))*H_dim(i,j+1);
        end
    end
    clear i j

    for j = 2:1:Np_x-1
        Hs_dim(2,j) = H_dim(1,j);
        for i =3:1:Np_r-1
            Hs_dim(i,j) = ((R_dim(i,j)-R_sdim(i,j))/(R_dim(i,j)-R_dim(i-1,j)))*H_dim(i-1,j)...
                +((R_sdim(i,j)-R_dim(i-1,j))/(R_dim(i,j)-R_dim(i-1,j)))*H_dim(i,j);
        end
    end
    clear i j

    for j = 2:1:Np_x-1
        Hn_dim(Np_r-1,j) = H_dim(Np_r,j);
        for i =2:1:Np_r-2
            Hn_dim(i,j) = ((R_dim(i+1,j)-R_ndim(i,j))/(R_dim(i+1,j)-R_dim(i,j)))*H_dim(i,j)...
                +((R_ndim(i,j)-R_dim(i,j))/(R_dim(i+1,j)-R_dim(i,j)))*H_dim(i+1,j);
        end
    end
    clear i j


% Coefficients of the Reynolds equation
    GAMA_dimensionless = (H_dim.^3)/(12*Mi_dim);
    GAMA_dimensionless_w = (Hw_dim.^3)/(12*Mi_dim);
    GAMA_dimensionless_e = (He_dim.^3)/(12*Mi_dim);
    GAMA_dimensionless_s = (Hs_dim.^3)/(12*Mi_dim);
    GAMA_dimensionless_n = (Hn_dim.^3)/(12*Mi_dim);
    PHI_dimensionless  = (Ome_dim/2).*(R_dim);
    H_dimensionless    = ((H_dim));
    Hw_dimensionless    = ((Hw_dim));
    He_dimensionless    = ((He_dim));
    Cenf_dimensionless = zeros(Np_r,Np_x);
    Cenf_dimensionless(1:Np_r,1:Np_x) = ((3/10)*((Ome_dim)^2)*(Rho_dim));


% Calculate [AXTA] - Diffusive term in xita direction (simple averaging approach)
    % Coefficients Aw
    AXTA(2:(Np_r-1),2:(Np_x-1),1) = ( (((GAMA_dimensionless_w(2:(Np_r-1),2:(Np_x-1)))) ./
((Xta_dim(2:(Np_r-1),2:(Np_x-1))-Xta_dim(2:(Np_r-1),1:(Np_x-2))) .* (R_dim(2:(Np_r-1),2:(Np_x-
1))))) .* (((R_ndim(2:(Np_r-1),2:(Np_x-1))-R_sdim(2:(Np_r-1),2:(Np_x-1))))));

    % Coefficients Ae
    AXTA(2:(Np_r-1),2:(Np_x-1),3) = ( (((GAMA_dimensionless_e(2:(Np_r-1),2:(Np_x-1)))) ./
((Xta_dim(2:(Np_r-1),3:(Np_x))-Xta_dim(2:(Np_r-1),2:(Np_x-1))) .* (R_dim(2:(Np_r-1),2:(Np_x-1))))) .*
(((R_ndim(2:(Np_r-1),2:(Np_x-1))-R_sdim(2:(Np_r-1),2:(Np_x-1))))));

    % Coefficients Ap
    AXTA(2:(Np_r-1),2:(Np_x-1),2) = -(AXTA(2:(Np_r-1),2:(Np_x-1),1) + AXTA(2:(Np_r-1),2:(Np_x-
1),3));


    % Calculate [AR] - Diffusive term in r direction (simple averaging approach)
    % Coefficients As
```

```
    AR(2:(Np_r-1),2:(Np_x-1),1) = ( (((GAMA_dimensionless_s(2:(Np_r-1),2:(Np_x-1)))) ./
((R_dim(2:(Np_r-1),2:(Np_x-1))-R_dim(1:(Np_r-2),2:(Np_x-1))))) .* ((((R_sdim(2:(Np_r-1),2:(Np_x-
1)))))).* ((Xta_edim(2:(Np_r-1),2:(Np_x-1))-Xta_wdim(2:(Np_r-1),2:(Np_x-1))))));

    % Coefficients An
    AR(2:(Np_r-1),2:(Np_x-1),3) = ( (((GAMA_dimensionless_n(2:(Np_r-1),2:(Np_x-1)))) ./
((R_dim(3:(Np_r),2:(Np_x-1))-R_dim(2:(Np_r-1),2:(Np_x-1))))) .* ((((R_ndim(2:(Np_r-1),2:(Np_x-
1)))))).* ((Xta_edim(2:(Np_r-1),2:(Np_x-1))-Xta_wdim(2:(Np_r-1),2:(Np_x-1))))));

    % Coefficients Ap
    AR(2:(Np_r-1),2:(Np_x-1),2) = -(AR(2:(Np_r-1),2:(Np_x-1),1) + AR(2:(Np_r-1),2:(Np_x-1),3));


% Calculate [B] - Convective term in x direction (currently only apply speed in x direction)
    % Coefficients Bw
    B(2:(Np_r-1),2:(Np_x-1),1) = ((-max(PHI_dimensionless(2:(Np_r-1),1:(Np_x-2)),ZERO(2:(Np_r-
1),1:(Np_x-2)))).*Hw_dimensionless(2:(Np_r-1),2:(Np_x-1)).*(((R_ndim(2:(Np_r-1),2:(Np_x-1))-
R_sdim(2:(Np_r-1),2:(Np_x-1))))));
    % Coefficients Be
    B(2:(Np_r-1),2:(Np_x-1),3) = ((min(PHI_dimensionless(2:(Np_r-1),3:(Np_x)),ZERO(2:(Np_r-
1),3:(Np_x)))).*He_dimensionless(2:(Np_r-1),2:(Np_x-1)).*(((R_ndim(2:(Np_r-1),2:(Np_x-1))-
R_sdim(2:(Np_r-1),2:(Np_x-1))))));
    % Coefficients Bp
    B(2:(Np_r-1),2:(Np_x-1),2) = ((abs(PHI_dimensionless(2:(Np_r-1),2:(Np_x-
1)))).*He_dimensionless(2:(Np_r-1),2:(Np_x-1)).*(((R_ndim(2:(Np_r-1),2:(Np_x-1))-R_sdim(2:(Np_r-
1),2:(Np_x-1))))));


% Calculate [AC] - Diffusive term in r direction (simple averaging approach)
    % Coefficients As
    AC(2:(Np_r-1),2:(Np_x-1),1) = 0.*(((-1*GAMA_dimensionless(1:(Np_r-2),2:(Np_x-
1))).*Cenf_dimensionless(1:(Np_r-2),2:(Np_x-1)).*R_dim(1:(Np_r-2),2:(Np_x-1)) .* (((R_dim(2:(Np_r-
1),2:(Np_x-1))+R_dim(1:(Np_r-2),2:(Np_x-1)))/2).*((Xta_dim(2:(Np_r-1),3:(Np_x))-Xta_dim(2:(Np_r-
1),1:(Np_x-2)))/2))) / 2);

    % Coefficients An
    AC(2:(Np_r-1),2:(Np_x-1),3) = 0.*(((GAMA_dimensionless(3:(Np_r),2:(Np_x-
1))).*Cenf_dimensionless(3:(Np_r),2:(Np_x-1)).*R_dim(3:(Np_r),2:(Np_x-1)) .* (((R_dim(2:(Np_r-
1),2:(Np_x-1))+R_dim(3:(Np_r),2:(Np_x-1)))/2).*((Xta_dim(2:(Np_r-1),3:(Np_x))-Xta_dim(2:(Np_r-
1),1:(Np_x-2)))/2))) / 2);

    % Coefficients Ap
    AC(2:(Np_r-1),2:(Np_x-1),2) = 0.*( (((-1*GAMA_dimensionless(2:(Np_r-1),2:(Np_x-
1))).*Cenf_dimensionless(2:(Np_r-1),2:(Np_x-1)).*R_dim(2:(Np_r-1),2:(Np_x-1)) .* (((R_dim(2:(Np_r-
1),2:(Np_x-1))+R_dim(1:(Np_r-2),2:(Np_x-1)))/2).*((Xta_dim(2:(Np_r-1),3:(Np_x))-Xta_dim(2:(Np_r-
1),1:(Np_x-2)))/2))) / 2)...
                        + (((GAMA_dimensionless(2:(Np_r-1),2:(Np_x-
1))).*Cenf_dimensionless(2:(Np_r-1),2:(Np_x-1)).*R_dim(2:(Np_r-1),2:(Np_x-1)) .* (((R_dim(2:(Np_r-
1),2:(Np_x-1))+R_dim(3:(Np_r),2:(Np_x-1)))/2).*((Xta_dim(2:(Np_r-1),3:(Np_x))-Xta_dim(2:(Np_r-
1),1:(Np_x-2)))/2))) / 2) );


% Calculate [C] - Matrix store the coefficients multiplied with the pressure at the centre:P(i,j)
  C(1:Np_r,1:Np_x) = (AXTA(1:Np_r,1:Np_x,2) + AR(1:Np_r,1:Np_x,2));


% Calculate [D] - Matrix store the coefficients multiplied with the film fraction at the centre:S(i,j)
  D(1:Np_r,1:Np_x) = 0.*AC(1:Np_r,1:Np_x,2);
```

```
% Calculate temporal term
%     cp1 =  ((1/2)*(X_dim(1,3:(Np))-X_dim(1,1:(Np-2))).*(dhdt_dim + (h_dim(1,2:(Np-
1))*((dt_dim)/(((1e-30)+dt_dim)^2)))));
%     cp2 = -((1/2)*(X_dim(1,3:(Np))-X_dim(1,1:(Np-2))).*(h_dim(1,2:(Np-1))*((dt_dim)/(((1e-
30)+dt_dim)^2))));
%     B(2,2:(Np-1)) = B(2,2:(Np-1)) + cp1;
%     b(1,2:(Np-1)) = cp2.*theta_prev(1,2:(Np-1));

% Impose boundary conditions
   % First pressure condition
%        A(2,1) = 1;
%        B(2,1) = 1;
%        b(1,1) = p1_dim-1;
   % Second pressure condition
%        A(2,Np) = 1;
%        B(2,Np) = 1;
%        b(1,Np) = p2_dim-1;









% Calculate fluid pressure and film fraction fields
   Np_xta = Np_x;

   if ti ==1
      p_initial = zeros(Np_r,Np_xta);
      S_initial = ones(Np_r,Np_xta);
   end

   P_initial = p_initial./Po;
   P = P_initial;
   S = S_initial;


% Initialization
   epsilon   = 1e-30;
   convFlag  = false;
   numIter   = 0;
   SZ = size(P);
   num_R_nodes = SZ(1,1);
   num_XTA_nodes = SZ(1,2);
   P_OLD    = P;
   S_OLD = S;


% Boundary Condition definition (According to P_side and it is always full film)
   P(num_R_nodes,:) = ps_dim;
   P(:,1) = ((P(:,2)+P(:,num_XTA_nodes-1))/2);
   P(:,num_XTA_nodes) = P(:,1);
%     aa = mean(P(2,:));
   P(1,:) = P(2,:);   %This place there might be a centrifugal term and the pressure gradient term
balances the centrifugal term rather than the pressure gradient is zero

   S(num_R_nodes,:) = 1;
```

```
    S(:,1) = ((S(:,2)+S(:,num_XTA_nodes-1))/2);
    S(:,num_XTA_nodes) = S(:,1);
    S(1,:) = 1;

    P_OLD    = P;
    S_OLD = S;

    maxError = 1;
    numIter = 1;

% Start iterations
    while  (max(maxError) >= tol)
        for or = 1 : 2
            for i = (or+1) : 2 : (num_R_nodes-1)
                for oxta = 1:2
                    for j = (oxta+1) : 2 : (num_XTA_nodes-1)
                    % CALCULATIONS FOR HYDRODYNAMIC PRESSURE in full film region



                    if (P(i,j) > pcav_dim) || (S(i,j) >= 1)
                            % Calculate hydrodynamic pressure residue
                            pH_res = ((B(i,j,1)*S(i,j-1) + B(i,j,2)*S(i,j) + B(i,j,3)*S(i,j+1) + AC(i,j,1)*((S(i-1,j))^2)
+ D(i,j)*((S(i,j))^2) + AC(i,j,3)*((S(i+1,j))^2) - AXTA(i,j,1)*P(i,j-1) - AXTA(i,j,3)*P(i,j+1) -AR(i,j,1)*P(i-1,j) -
AR(i,j,3)*P(i+1,j)) / (C(i,j)));
                            % Update hydrodynamic pressure
                            P(i,j) = ((w_p)*pH_res + (1-w_p)*P(i,j));
                            % Cavitation checks
                            if (P(i,j) >= pcav_dim)


                                S(i,j) = 1;
                            else
                                P(i,j) = pcav_dim;
                            end
                        end

                    % CALCULATION FOR FILM FRACTION in cavitation region
                        if (P(i,j) <= pcav_dim) || (S(i,j) < 1)
%                           % Calculate factor a for the second order equation as^2 + bs + c = 0
%                               ea = D(i,j);
%                           % Calculate factor b for the second order equation as^2 + bs + c = 0
%                               eb = B(i,j,2);
%                           % Calculate factor c for the second order equation as^2 + bs + c = 0
%                               ec = B(i,j,1)*S(i,j-1) + B(i,j,3)*S(i,j+1) + AC(i,j,1)*((S(i-1,j))^2) +
AC(i,j,3)*((S(i+1,j))^2) - AXTA(i,j,1)*P(i,j-1) - AXTA(i,j,3)*P(i,j+1) -AR(i,j,1)*P(i-1,j) - AR(i,j,3)*P(i+1,j) -
C(i,j)*P(i,j);
                            % Calculate film fraction residue
                            s_res = ((AXTA(i,j,1)*P(i,j-1) + AXTA(i,j,3)*P(i,j+1) + AR(i,j,1)*P(i-1,j) +
AR(i,j,3)*P(i+1,j) + C(i,j)*P(i,j) - B(i,j,1)*S(i,j-1) - B(i,j,3)*S(i,j+1)) / (B(i,j,2)));
                            % Update film fraction
                            S(i,j)  = ((w_s)*s_res + (1-w_s)*S(i,j));
                            % Cavitation checks
                            if (S(i,j) < 1)
                                P(i,j) = pcav_dim;
                            else
                                S(i,j) = 1;
                            end
                        end
                    end
```

```
            end
        end
    end

    % Update P and S values at perimeter boundaries
        P(num_R_nodes,:) = ps_dim;
        P(:,1) = ((P(:,2)+P(:,num_XTA_nodes-1))/2);
        P(:,num_XTA_nodes) = P(:,1);

        P(1,:) = P(2,:);

        S(num_R_nodes,:) = 1;
        S(:,1) = ((S(:,2)+S(:,num_XTA_nodes-1))/2);
        S(:,num_XTA_nodes) = S(:,1);
        S(1,:) = 1;

    % Compute error (relative error 1, more accurate and slower)
        Error_p    = max(abs((P-P_OLD).*((P)./((P+epsilon).^2))));
        Error_s    = max(abs((S-S_OLD).*((S)./((S+epsilon).^2))));
        maxError   = Error_p + Error_s;

        Residual(numIter,1) = max(maxError);
        Sum_P(numIter,1) = sum(sum(P));

%       % Compute error (relative error 2, less accurate and faster)
%           Error_p     = ((norm(p-p_OLD))       *((norm(p))    /((norm(p)+epsilon)    ^2)));
%           Error_theta = ((norm(theta-theta_OLD))*((norm(theta))/((norm(theta)+epsilon)^2)));
%           maxError    = Error_p + Error_theta;

     % Check error
        if (max(maxError) <= tol)
            convFlag = true;
%               return
        else
            P_OLD  = P;
            S_OLD  = S;
        end

        if (numIter >maxIter)
            conFlag = false;
            return
        end

        numIter = numIter+1;
    end

    clear i j



    p = (P*Po);


    % record p and S as initial values
    p_initial = p;
    S_initial = S;

    % compute torque
    dpdt = zeros(Np_r,Np_x);
        for i=2:1:Np_r-1
```

```
            for j=2:1:Np_x-1
                dpdt(i,j)=(p(i,j+1)-p(i,j-1))/(Xta(i,j+1)-Xta(i,j-1));
            end
            dpdt(i,1)= (p(i,2)-p(i,Np_x))/(Xta(i,2)+2*pi-Xta(i,Np_x));
            dpdt(i,Np_x)= (p(i,1)-p(i,Np_x-1))/(Xta(i,1)+2*pi-Xta(i,Np_x-1));
        end
        tau=zeros(Np_r,Np_x);
        tau_c=zeros(Np_r,Np_x);
        tau_p=zeros(Np_r,Np_x);
        for i=2:1:Np_r-1
            for j= 1:1:Np_x
                tau(i,j)=(0.5*h(i,j)*dpdt(i,j)/R(i,j)+ome*mi*R(i,j)/h(i,j))*S(i,j);
                tau_c(i,j)=(ome*mi*R(i,j)/h(i,j))*S(i,j);
                tau_p(i,j)=(0.5*h(i,j)*dpdt(i,j)/R(i,j))*S(i,j);
            end
        end
        sumt=0;
        sumt_c=0;
        sumt_p=0;
        for i=2:1:Np_r-1
            for j=1:1:Np_x
                sumt = sumt +tau(i, j)* (R(i, j)^2)*(Xta_e(i,j)-Xta_w(i,j))*(R_n(i,j)-R_s(i,j)) ;
                sumt_c = sumt_c +tau_c(i, j)* (R(i, j)^2)*(Xta_e(i,j)-Xta_w(i,j))*(R_n(i,j)-R_s(i,j)) ;
                sumt_p = sumt_p +tau_p(i, j)* (R(i, j)^2)*(Xta_e(i,j)-Xta_w(i,j))*(R_n(i,j)-R_s(i,j)) ;
            end
        end
        torque=4*sumt*1e6;
        torque_c=4*sumt_c*1e6;
        torque_p=4*sumt_p*1e6;

    clear i j



    % compute power loss
    PL = torque*(1e-6)*ome;



    % compute boundary flow rate
    Q_boundary = zeros(1,Np_x);
    Q_boundary(1,2:1:Np_x-1) = (((h(end,2:1:Np_x-1)).^3)./(12*mi)) .* ((p(end,2:1:Np_x-1)-p(end-
1,2:1:Np_x-1)) ./ (R_n(end-1,2:1:Np_x-1)- R(end-1,2:1:Np_x-1))) .* (rad.*(Xta_e(end-1,2:1:Np_x-1) -
Xta_w(end-1,2:1:Np_x-1)));



    % compute supply and leakage flow rate
    Q_supply = 0;
    Q_leakage = 0;

    for i = 1:1:Np_x
        if Q_boundary(1,i) >= 0
            Q_supply = Q_supply + Q_boundary(1,i);
        end

        if Q_boundary(1,i) < 0
            Q_leakage = Q_leakage + Q_boundary(1,i);
        end
    end
```

```
    clear i j

    Q_supply = 4*Q_supply;
    Q_leakage = 4*Q_leakage;
    Q_net = Q_supply+Q_leakage;


    % compute effective temperature
    t_temp = T_sup + (gama*PL)/(Q_supply*rho*cp);

    % relaxation and error computation
    T_old = T_eff;
    T_effective = T_old + w_t*(t_temp-T_old);

    T_error = (abs(T_effective-T_old))/T_effective;

    t_input = T_effective;



end
```